

AD-A037 098

AGBABIAN ASSOCIATES EL SEGUNDO CALIF

F/G 19/4

GROUT/SOIL INTERACTION AND VELOCITY GAGE EMPLACEMENT FOR GROUND--ETC(U)

AUG 76 M B BALACHANDRA, J A MALTHAN

DNA001-74-C-0100

UNCLASSIFIED

AA-R-7364-7-4265

DNA-4089F

NL

1 OF 3
AD
A037098



1 OF 3
AD
A037098



ADA 037098

(12) DNA 4089F

GROUT/SOIL INTERACTION AND VELOCITY GAGE EMPLACEMENT FOR GROUND-SHOCK MEASUREMENT

Agbabian Associates
250 North Nash Street
El Segundo, California 90245

18 August 1976

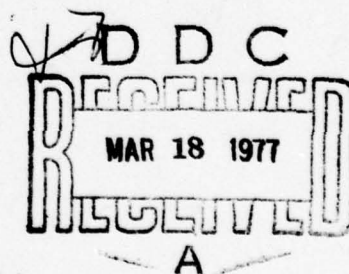
Final Report for Period September 1975—July 1976

CONTRACT No. DNA 001-74-C-0100

APPROVED FOR PUBLIC RELEASE;
DISTRIBUTION UNLIMITED.

THIS WORK SPONSORED BY THE DEFENSE NUCLEAR AGENCY
UNDER RDT&E RMSS CODE B344074462 L11CAXSX35233 H2590D.

Prepared for
Director
DEFENSE NUCLEAR AGENCY
Washington, D. C. 20305



Destroy this report when it is no longer
needed. Do not return to sender.



UNCLASSIFIED

SECURITY CLASSIFICATION OF THIS PAGE (When Data Entered)

19 REPORT DOCUMENTATION PAGE		READ INSTRUCTIONS BEFORE COMPLETING FORM	
1. REPORT NUMBER DNA 4089F	2. GOVT ACCESSION NO.	3. RECIPIENT'S CATALOG NUMBER	
4. TITLE (and Subtitle) GROUT/SOIL INTERACTION AND VELOCITY GAGE EMPLACEMENT FOR GROUND-SHOCK MEASUREMENT.		5. TYPE OF REPORT & PERIOD COVERED Final Report, Sept 1975 - Jul 1976	
6. AUTHOR(s) Mysore B. Balachandra James A. Malthan		7. PERFORMING ORG. REPORT NUMBER R-7364-7-4265	
8. PERFORMING ORGANIZATION NAME AND ADDRESS Agabian Associates 250 North Nash Street El Segundo, California 90245		9. CONTRACT OR GRANT NUMBER(s) DNA 001-74-C-0100	
10. CONTROLLING OFFICE NAME AND ADDRESS Director Defense Nuclear Agency Washington, D.C. 20305		11. PROGRAM ELEMENT, PROJECT, TASK AREA & WORK UNIT NUMBERS NWET Subtask L11CAXSX352-33	
12. MONITORING AGENCY NAME & ADDRESS (if different from Controlling Office) 201 p.		13. REPORT DATE 18 Aug 1976	
		14. NUMBER OF PAGES 208	
		15. SECURITY CLASS (of this report) UNCLASSIFIED	
		15a. DECLASSIFICATION/DOWNGRADING SCHEDULE	
16. DISTRIBUTION STATEMENT (of this Report) Approved for public release; distribution unlimited.			
17. DISTRIBUTION STATEMENT (of the abstract entered in Block 20, if different from Report)			
18. SUPPLEMENTARY NOTES This work sponsored by the Defense Nuclear Agency under RDT&E RMSS Code B344074462 L11CAXSX35233 H2590D.			
19. KEY WORDS (Continue on reverse side if necessary and identify by block number) Velocity Measurement Experimental/Analytical Correlations Emplacement Techniques Grouting Recommendations Laboratory Ground-Shock Tests Sensitivity Studies Finite Element Calculations Slip Interfaces			
20. ABSTRACT (Continue on reverse side if necessary and identify by block number) Analytical work aimed at establishing velocity gage emplacement procedures for ground-shock measurement is reported. Finite element calculations were performed using nonlinear, inelastic material models, in support of experiments at WES using artificial soil specimens in the Small Blast Load Generator. The investigations covered a wide range of borehole/free-field impedances under a variety of interface conditions.			

DD FORM 1473
1 JAN 73

EDITION OF 1 NOV 65 IS OBSOLETE

UNCLASSIFIED

SECURITY CLASSIFICATION OF THIS PAGE (When Data Entered)

407844

UNCLASSIFIED

SECURITY CLASSIFICATION OF THIS PAGE(When Data Entered)

20. ABSTRACT (Continued)

Interface bond rather than impedance matching was identified as the principal requirement for fidelity of velocity measurement. Velocity gage canisters are, therefore, recommended to be locked to the free field with an expansive grout in the vicinity of the gage.

UNCLASSIFIED

SECURITY CLASSIFICATION OF THIS PAGE(When Data Entered)

SUMMARY

Proper emplacement of velocity sensors in field tests in order to ensure accurate measurement of ground motions in soils is a long-standing problem. This report discusses analytical work addressing the question of interaction between the free-field material and the grout used to fill instrumentation boreholes. The analysis is in support of experiments conducted at WES.

The analysis and the tests both show that good interface bond is the primary requirement for assuring that the sensor follows free-field motion faithfully. Furthermore, the velocity measurement fidelity is achieved even in the presence of large impedance mismatches between borehole and free-field materials.

It is recommended that velocity gage canisters be locked into the free-field material by using a stiff, expansive grout locally around the canister in the borehole. The remaining regions of the borehole may be filled with grouts that only crudely approximate the free-field material properties. This procedure greatly reduces the expense and effort involved in preparing borehole grouts that carefully match the native soil properties.

ACCESSION for	
NTS	✓
DDC	
UNANIMOUS	
JUSTIFICATION	
BY	
DATE	
A	

PREFACE

The work reported in this document was supported by the Defense Nuclear Agency under Contract No. DNA001-74-C-0100, NWE T, Subtask Code L11CAXSX352, Work Unit Code 33. Mr. T.E. Kennedy was the Contracting Officer's Representative (COR) for DNA; his active interest and careful guidance are gratefully acknowledged.

Also, special thanks are extended to the personnel of the Waterways Experiment Station, especially to Mr. J.K. Ingram and Dr. J.S. Zelasko, who jointly participated in the project, for a most pleasant working relationship. Their support, comments, and recommendations throughout the project were highly valued.

Agbabian Associates personnel who participated in the project were J.A. Malthan, Program Manager; M.B. Balachandra, Project Engineer; and J.W. Workman and D.P. Reddy who participated as staff consultants.

CONTENTS

<u>Section</u>	<u>Page</u>
1 INTRODUCTION	13
2 BACKGROUND AND SCOPE OF CURRENT WORK	15
2.1 Parametric Analysis at AA	15
2.2 Scope of Present Work	16
2.3 Experiments at WES	18
2.4 Calculations of the CBMI Test Series	21
3 GENERAL DESCRIPTION OF COMPUTER CODE USED FOR THE CALCULATIONS	25
3.1 Brief Description of FEDRC Code	25
3.2 Damping and Material Model	26
3.3 Slip Element	30
4 CALCULATION OF TEST CBMI-10 (CONTROL TEST)	37
4.1 Review of Previous Calculation of Test CBMI-10	37
4.2 Recalculation of Test CBMI-10 (CBMI-10-1)	39
4.3 Results of CBMI-10-1 Calculations	43
4.4 Auxiliary Calculations	47
4.5 Final Recalculation of Test CBMI-10 (CBMI-10-2)	55
4.6 Results of CBMI-10-2 Calculations and Discussion	57
5 OVERVIEW OF TESTS CBMI-12, -13, AND -14	61
5.1 Brief Review of Test Results	61
5.2 Material Properties	63
5.3 Anomalies in Test CBMI-12	66
5.4 Order of Performance of Calculations	67
5.5 Organization of Sections 6 through 8	67

CONTENTS (CONTINUED)

<u>Section</u>		<u>Page</u>
6	CALCULATION OF TEST CBMI-13	69
6.1	Finite-Element Mesh	69
6.2	Material Models	69
6.3	Interface Conditions and Slip Models . . .	78
6.4	Input Pulse and Schedule of Integration .	83
6.5	Results of CBMI-13 Calculations	83
6.6	Interpretation of the Results	94
6.7	Conclusions from CBMI-13 Calculations . .	98
6.8	CBMI-13-1 Calculations	99
6.9	Conclusions and Discussion	112
7	CALCULATION OF TEST CBMI-14	115
7.1	Finite Element Mesh	115
7.2	Generation of Matrix Material Properties .	115
7.3	Other Material Properties Used in CBMI-14 Calculations	128
7.4	Input Pulse and Integration Schedule . . .	132
7.5	Results of the CBMI-14 Calculations . . .	132
7.6	Interpretation of CBMI-14 Calculations . .	137
7.7	Conclusions and Discussion	148
8	CALCULATION OF TEST CBMI-12	149
8.1	Finite Element Mesh	149
8.2	Material Models	149
8.3	Preliminary Calculations	153
8.4	Input Pulse and Integration Schedule . . .	158
8.5	Results of the CBMI-12 Calculations . . .	158
8.6	Interpretation of the CBMI-12 Calculations	164
8.7	Conclusions and Discussion	177

CONTENTS (CONTINUED)

<u>Section</u>		<u>Page</u>
9	FREQUENCY ANALYSIS	179
	9.1 Description of Analyses Performed	179
	9.2 Frequency Analysis of CBMI-14 Calculation	180
	9.3 Frequency Analysis of CBMI-12 Calculation	184
10	OBLIQUE INCIDENCE	189
	10.1 Development of Elastic Analysis	190
	10.2 Description of Calculations Performed and Results	192
	10.3 Conclusions and Limitations of Analysis	193
11	CONCLUSIONS AND GAGE EMPLACEMENT RECOMMENDATIONS	197
	11.1 Grout and Matrix Stiffness Considerations	197
	11.2 Grout/Matrix Stiffness Comparisons in CBMI Test Series	197
	11.3 Conclusions from CBMI Test Series	198
	11.4 Gage Emplacement Recommendations	200
12	REFERENCES	203

ILLUSTRATIONS

<u>Figure</u>		
2-1	Typical Small Blast Load Generator (SBLG) Schematic	19
2-2	Surface Pressure Measured during CBMI Test Series	22
3-1	Variable Modulus Model Used in the Calculations	28
3-2	Geometry of Slip Element	31
3-3	Slip Model Yield Surface	34

ILLUSTRATIONS (CONTINUED)

<u>Figure</u>		<u>Page</u>
4-1	Comparison of Velocity Histories at $R = 0$ and $D = 18$ in. for Test CBMI-10	38
4-2	Comparison of Velocity Histories at $R = 0$ and $D = 54$ in. for Test CBMI-10	38
4-3	Finite Element Mesh Used for CBMI-10-1 Calculations	40
4-4	Soil Properties for Test CBMI-10-1	42
4-5	Input Pulse Used in the CBMI-10-1 Calculation	45
4-6	Comparison of Velocity Histories from CBMI-10-1 and CBMI-10 Calculations with CBMI-10 Test at 18-in. Depth	46
4-7	Comparison of Velocity Histories from CBMI-10-1 and CBMI-10 Calculations with CBMI-10 at 54-in. Depth	46
4-8	Finite Element Mesh for Column Run	48
4-9	Comparison of Velocities from 1-D Calculation with CBMI-10 Test	48
4-10	Finite Element Mesh for Parametric Study of Slip Model	51
4-11	Slip (Relative) Displacement (Top Surface)	54
4-12	Vertical Velocity at Node Point 1 (Top Surface)	54
4-13	Vertical Stress in Element 3 (Midheight)	54
4-14	Comparison of Matrix Material Model for CBMI-10-2 Calculations with Data	56
4-15	Comparison of CBMI-10-2 and 1-D Calculations	58
4-16	Comparison of Velocities in CBMI-10-2 Calculations with Test	59

ILLUSTRATIONS (CONTINUED)

<u>Figure</u>		<u>Page</u>
4-17	Comparison of Displacement at 18-in. Depth in CBMI-10-2 Calculations with Test	60
4-18	Vertical Stress at 36-in. Depth in CBMI-10-2 Calculations	60
5-1	Velocity Time Histories at 18-in. Depth Measured in CBMI-12, -13, and -14 Tests	62
5-2	Recommended Material Properties for CBMI-12 Matrix and Borehole Filler	64
6-1	Finite Element Mesh for CBMI-13 Calculations . .	70
6-2	Recommended Properties for Free-Field Matrix for Test CBMI-13	72
6-3	Model of Matrix for CBMI-13 Calculations Compared with Data	73
6-4	Model for Soft Borehole Filler Grout for CBMI-13 Calculations Compared against Data	75
6-5	Recommended Material Properties for Canister Locking Grout, CBMI-13	76
6-6	Model of Canister Locking Grout Used in CBMI-13 Calculations Compared with Data	77
6-7	One-Dimensional Column Run on CBMI-13 Matrix . .	79
6-8	Double Column Calculation to Test Matrix/SBLG Slip	82
6-9	Input Pulse and Schedule of Integration Used in CBMI-13 Calculations	84
6-10	Velocities Measured during Test CBMI-13	85
6-11	Displacements in Test CBMI-13	86
6-12	Accelerations in Test CBMI-13	87
6-13	Free-Field Stresses in Test CBMI-13	88

ILLUSTRATIONS (CONTINUED)

<u>Figure</u>		<u>Page</u>
6-14	Comparison of CBMI-13 Calculations and Test at 18-in. Depth	89
6-15	Comparison of CBMI-13 Calculation with Test at 36-in. Depth	90
6-16	Comparison of CBMI-13 Calculations and Test at 54-in. Depth	91
6-17	Comparison of CBMI-13 Calculations with Test, Stresses	92
6-18	Comparison of Velocity in the Gage and Neighboring Matrix, CBMI-13 Calculations	95
6-19	Calculated Response of Borehole Filler Grout at Top (2-in. Depth).	97
6-20	Finite Element Mesh used for CBMI-13-1 Calculation	100
6-21	Comparison of Gage and Free-Field Motion at 18-in. Depth, CBMI-13-1 Calculation	102
6-22	Comparison of Gage and Free-Field Motion at 36-in. Depth, CBMI-13-1 Calculations	103
6-23	Comparison of Gage and Free-Field Motion at 54-in. Depth, CBMI-13-1 Calculations	104
6-24	Acceleration at 18-in. Depth, CBMI-13-1 Calculations	105
6-25	Acceleration at 36-in. Depth, CBMI-13-1 Calculations	106
6-26	Acceleration at 54-in. Depth, CBMI-13-1 Calculations	107
6-27	Stresses, CBMI-13-1 Calculations	108
6-28	Response of Borehole Filler Grout, CBMI-13-1 Calculations	110

ILLUSTRATIONS (CONTINUED)

<u>Figure</u>		<u>Page</u>
7-1	Finite Element Mesh Used in CBMI-14 Calculations	116
7-2	Comparison of Stiffened CBMI-13 Matrix with Original Properties	120
7-3	Uniaxial Behavior of CBMI-14 Matrix Compared with Original Properties	123
7-4	Comparison of 1-D Calculation on Matrix Column with CBMI-14 Test Data	125
7-5	One-Dimensional Calculation with Layered Matrix	126
7-6	Recommended Properties for Hard Borehole Grout for CBMI-14 Calculations	129
7-7	Comparison of Model and Data for Borehole Grout--CBMI-14 Calculations	130
7-8	One-Dimensional Calculation with CBMI-14 Borehole Grout	131
7-9	Input Pulse and Integration Schedule Used in CBMI-14 Calculations	133
7-10	Velocities from Test CBMI-14	134
7-11	Displacements from Test CBMI-14	135
7-12	Accelerations from Test CBMI-14	136
7-13	Stress from Test CBMI-14	136
7-14	Comparison of CBMI-14 Calculations and Test at 18-in. Depth	138
7-15	Comparison of CBMI-14 Calculations and Test at 36-in. Depth	139
7-16	Comparison of CBMI-14 Calculations and Test at 54-in. Depth	142
7-17	Accelerations at 18-in. Depth CBMI-14 Calculations	141

ILLUSTRATIONS (CONTINUED)

<u>Figure</u>		<u>Page</u>
7-18	Accelerations at 36-in. Depth CBMI-14 Calculations	142
7-19	Accelerations at 54-in. Depth--CBMI-14 Calculations	143
7-20	Stresses from CBMI-14 Calculations	144
8-1	Finite Element Mesh Used in CBMI-12 Calculations	150
8-2	Recommended Properties for Layers 1 and 3 of CBMI-12 Free-Field Material	151
8-3	Material Model for Layers 1 and 3 Compared with Data--CBMI-12 Calculations	154
8-4	One-Dimensional Calculation on CBMI-12 Matrix Column	156
8-5	One-Dimensional Calculation on Grout Column . .	156
8-6	Input Pulse and Schedule of Integration Used in CBMI-12 Calculations	159
8-7	Velocities from Test CBMI-12	160
8-8	Displacements from Test CBMI-12	161
8-9	Accelerations from Test CBMI-12	162
8-10	Stresses from Test CBMI-12	163
8-11	Comparison of CBMI-12 Calculations and Test at 18-in. Depth	165
8-12	Comparison of CBMI-12 Calculations and Test at 36-in. Depth	166
8-13	Comparison of CBMI-12 Calculation and Test at 54-in. Depth	167
8-14	Acceleration at 18-in. Depth--CBMI-12 Calculations	168

ILLUSTRATIONS (CONCLUDED)

<u>Figure</u>		<u>Page</u>
8-15	Acceleration at 36-in. Depth--CBMI-12 Calculations	169
8-16	Acceleration at 54-in. Depth--CBMI-12 Calculations	170
8-17	Comparison of Calculated Stresses with Test Data--CBMI-12 Calculations	171
8-18	Punch Down of Borehole Grout in CBMI-12 Calculations	173
9-1	Velocity Response in Frequency Domain-- 18-in. Depth, CBMI-14 Calculation	181
9-2	Velocity Response in Frequency Domain-- 36-in. Depth, CBMI-14 Calculation	182
9-3	Velocity Response in Frequency Domain-- 54-in. Depth, CBMI-14 Calculation	183
9-4	Velocity Response in Frequency Domain-- 18-in. Depth, CBMI-12 Calculation	185
9-5	Velocity Response in Frequency Domain-- 36-in. Depth, CBMI-12 Calculation	186
9-6	Velocity Response in Frequency Domain-- 54-in. Depth, CBMI-12 Calculation	187
10-1	Geometry of Moving Point Load on Half Plane . .	191
10-2	Typical Pressure Pulse	191
10-3	Plot of Maximum $\sqrt{J_2^I}$ vs. Peak Overpressure . .	195

SI CONVERSION TABLE

For English Units Used in This Report

To Convert English Units	To SI Units	Multiply By
fps	m/s	0.3048
ft	m	0.3048
g	m/s/s	9.807
in.	m	0.0254
in./sec/sec	m/s/s	0.0254
ips	m/s	0.0254
ksi	MPa	6.8948
lb-sec ² /in. ⁴	kg/m ³	1.069 x 10 ⁷
pcf	N/m ³	1.571 x 10 ²
psi	kPa	6.8948

SECTION 1

INTRODUCTION

The long-standing problems associated with accurately measuring free-field response and interpreting signals obtained from field tests remain only partially solved. Agbabian Associates, under contract to DNA, has been studying the effect of two aspects of gage emplacement--bond strength and impedance mismatch--on the motion of instrumentation canisters grouted in place. This report covers simulation calculations for a series of instrumentation canister experiments conducted at WES. The calculations of instrumentation canister response are directed at the evaluation and interpretation of the experiments and the development of simpler, less costly, and more effective canister placement procedures.

The main finding of this investigation is that good interface bond is the primary requirement for ensuring the fidelity of velocity measurement. Even considerable mismatch in the impedances of the borehole grouts and the free-field materials can be tolerated if a nonslip interface between them can be maintained. Consequently, it is recommended that velocity canisters be locked in place by using a stiff, expansive grout in the region surrounding the canister. The remainder of the borehole may be filled with other grouts that only grossly approximate the properties of the free-field materials at the site. Thus, elaborate procedures for grout preparation are circumvented.

SECTION 2

BACKGROUND AND SCOPE OF CURRENT WORK

Free-field response of a soil medium to ground shock has traditionally been measured using an array of ground motion gages located at various ranges and depths from ground zero. Dynamic transient response was originally measured with accelerometers. Currently, accelerometers and velocity gages are in common use. Occasional attempts have been made to obtain direct measurements of transient displacement.

Accurate measurement of ground response requires (1) an accurate transducer (with the associated transmission and recording system), (2) a means of coupling the transducer to the ground, and (3) a means of evaluating and accounting for the disturbing effect of the transducer package on local ground motion. Velocity gages are customarily housed in instrumentation canisters both for protection and for ease of orientation control. The canisters, which may contain a number of transducers, are placed in boreholes at their designated locations and grouted in place. Accumulated experience and analytical studies of the response of inclusions in simple linear elastic media have led to approximate density matching. The grout column and canister do, however, present discontinuities in strength and stiffness. The discontinuities and the indirect coupling of the ground motion transducer through the canisters and grout to the soil give rise to two questions: What are the qualitative changes of the local free-field motion introduced by the canister and grout-filled borehole, and are the quantitative differences between the free-field and recorded motion sufficient to require correction?

2.1 PARAMETRIC ANALYSIS AT AA

Analytical work was carried out at Agbabian Associates (AA) during 1972-73 addressing the above two questions (Ref. 1). The goal of the analyses was to determine how the local free field is modified by the presence of the canister and how faithfully the canister records the motion. The analysis was made partly by using a finite element model of the soil, grout, and canister

including inelastic properties of the soil and grout that were measured for a MIDDLE GUST event. Slip between the soil and grout was also considered. In addition to the finite element studies, an existing theory of dynamic interaction between an idealized, rigid spherical canister and elastic soil was used to define the range of accurate frequency response in terms of engulfment times for the canister.

The finite element analyses indicated that the interface bond between the grout surrounding the canister and the free field might be more important than the ratio of the stiffnesses of the grout and the free field. However, the study was not detailed enough to be conclusive on this point.

2.2 SCOPE OF PRESENT WORK

As an outcome of the above study, a combined experimental and analytical investigation was begun in 1974. This project was designed to compare the response of the gage and the free field at several ratios of the grout stiffness to that of the free field varying over a range of 0.5 to 2.0 and at different bond strengths at the grout/matrix interface. In this context, it must be noted that the term stiffness is ambiguous since the materials in question generally exhibit nonlinear stress/strain behavior. It is possible to define the stiffness ratio precisely by referring to the secant or tangent moduli at specified stress levels. This point is discussed in more detail in Section 11.

Test cases originally proposed are shown in Table 2-1. Test No. 6 was later omitted.

The experimental part of the project was carried out at the U.S. Army Engineer Waterways Experiment Station (WES), Vicksburg, Mississippi, using the Small Blast Load Generator (SBLG) and is described briefly in Section 2.3. Analytical studies were performed using finite element calculations at AA. These calculations used material properties and input pulses supplied by WES and are discussed in Section 2.4.

TABLE 2-1. SUMMARY OF TESTS ORIGINALLY PROPOSED

Original Test No.	Type of Calculations	Stiffness of Grout Stiffness of Soil	Bond Between Grout and Soil	Density of Grout Density of Soil
1	Parametric calculations using a coarse mesh and a calculation using a detailed mesh	1.0	Perfect	1.0
2	One with a coarse mesh and one with a detailed mesh	0.5	Weak	1.0
3	One with a coarse mesh and one with a detailed mesh	0.5	Strong	1.0
4	One with a coarse mesh and one with a detailed mesh	2.0	Weak	1.0
6	One with a coarse mesh and one with a detailed mesh	0.5	Strong	2.0

2.3 EXPERIMENTS AT WES

This section presents a very brief description of the general test environment and individual tests conducted for this program. A more detailed explanation may be found in References 2 and 3.

2.3.1 TEST ENVIRONMENT

All tests were conducted in the Small Blast Load Generator at WES (Fig. 2-1). The matrix specimens were 6 ft high by 4 ft in diameter and were made of artificial soil material. Boreholes of 5-in. diameter were placed in the center in the specimen and extended up to within 6 in. of the base of the SBLG.

The loading in each test was applied by detonating primacord in the firing chamber above the specimen. A neoprene diaphragm was used at the top of the specimen to ensure a uniform pressure distribution. Overpressures were nominally 250 psi in all the tests.

Gages were placed at 18-in., 36-in., and 54-in. depths in the borehole as well as in the "free field," at a radial distance of 12 in. These gages were placed in position as the specimen was built up. The primary sensors were velocity gages. Each gage was a piezoelectric accelerometer with a built-in electronic integrator and was housed in aluminum canisters 3-in. diameter by 2-3/4 in. high. The canister density was approximately 100 lb/cu ft.

Stress measurements were made in some of the tests using WES SE soil stress gages. These gages were placed in the free field at depths of 18 in., 36 in., 54 in., and 72 in. at a distance of approximately 1 ft from the borehole. Displacements were derived by digital integration of the velocity signals.

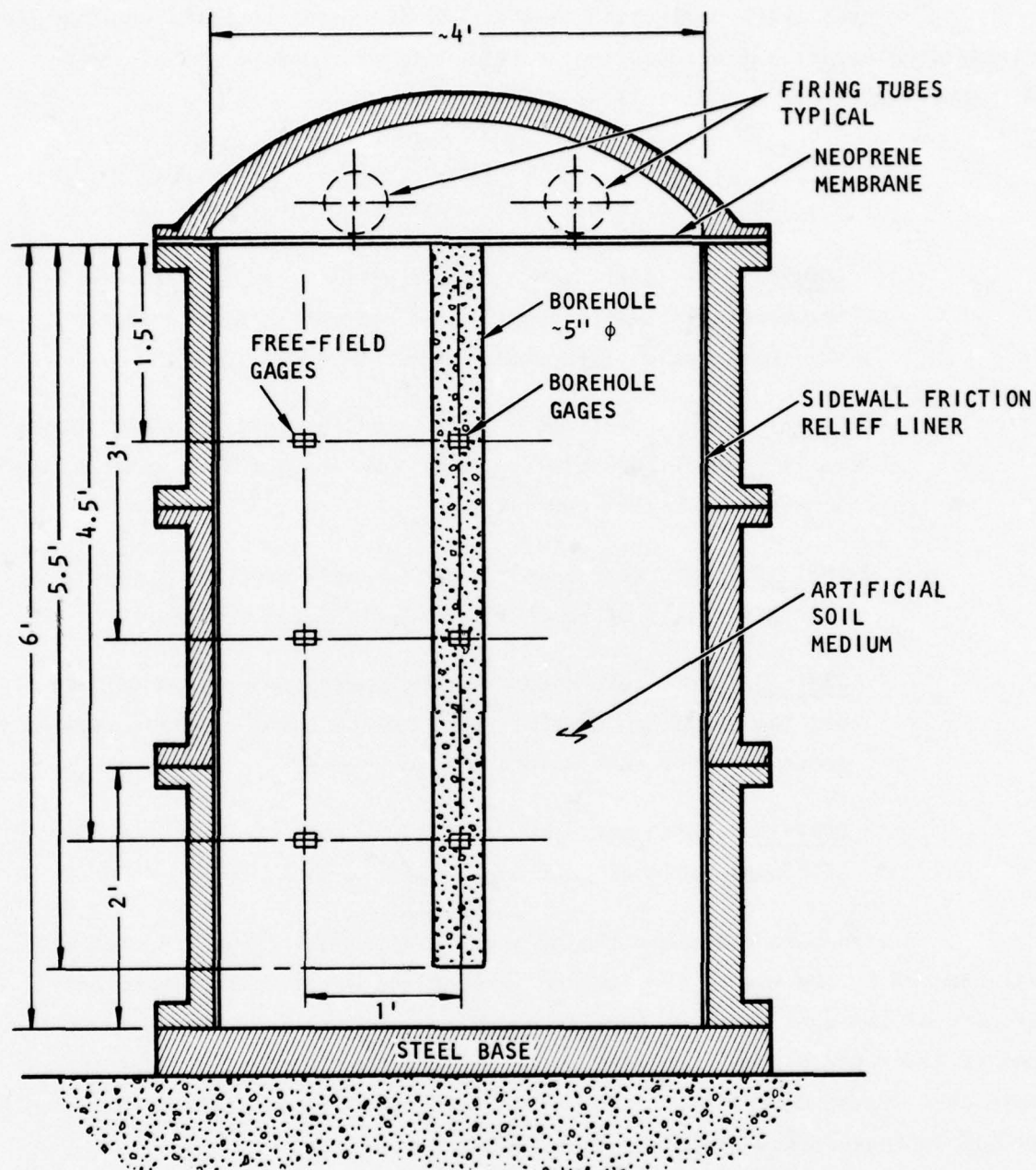


FIGURE 2-1. TYPICAL SMALL BLAST LOAD GENERATOR (SBLG) SCHEMATIC

2.3.2 DESCRIPTION OF INDIVIDUAL TESTS

Several tests designated as the CBMI (Canister-Backfill-Medium-Interaction) series, were conducted by WES. Six of these were analyzed by AA. These six tests are as follows:

CBMI-1. This test was conducted with a homogeneous matrix specimen to serve as the Control Test. There was no borehole.

CBMI-5. This test used a borehole filler grout with nearly the same stiffness properties as the matrix to simulate a stiffness ratio of borehole to matrix equal to 1.

CBMI-10. This test was a second control test with a homogeneous matrix and no borehole, performed because of some internal inconsistencies in Test CBMI-1.

CBMI-12. This test used a soft borehole grout to simulate a stiffness ratio of borehole to matrix equal to 0.5.

CBMI-13. This test used the same borehole grout as CBMI-12, but the canisters were locked in place using a stiff, expansive grout in order to simulate a strong bond.

CBMI-14. This test used a stiff borehole grout to simulate a stiffness ratio of borehole to matrix equal to 2.

A strong bond between the canister and the matrix was ensured in Test CBMI-13 by the use of the locking (expansive) grout in the immediate vicinity of the canister. No special measures were taken to provide a weak bond in Tests CBMI-12 and CBMI-14, which corresponded to Nos. 2 and 4 in Table 2-1. Based on the test data, it is felt that a moderately strong bond existed in these tests also (see Secs. 8 and 9).

Tests CBMI-1, -5, -10, and -12 were conducted on virgin specimens of the matrix material. Tests CBMI-13 and -14 reused the specimen used for CBMI-12. This specimen was made of expansive cement. The matrix in Tests CBMI-13 and -14 was in a relatively stiff condition as a result of the stress history of CBMI-12 and additional aging. It was also thought to be subjected to large radial stresses arising from the use of expansive cement.

The pressure-time histories measured during the above tests are shown in Figure 2-2.

2.4 CALCULATIONS OF THE CBMI TEST SERIES

Calculations were performed at AA for Tests CBMI-1, -5, and -10 during 1974-75. The CBMI-5 calculation is reported in Reference 4 and the other two in Reference 5. While the CBMI-5 calculation showed reasonably good correlation with the test results, the other two did not. Specific points of disagreement between the CBMI-10 calculations and test data are listed in Section 5. The discrepancies were attributed to incorrect material property data.

Revised material properties for the matrix in Test CBMI-10 were supplied by WES. A new calculation was made with these properties during 1975-76 along with calculations for the Tests CBMI-12, -13, and -14.

In each of these calculations, a finite element mesh was prepared to represent the test configuration. The canisters containing velocity gages were not explicitly modeled. Instead, the calculated time histories of the quantities of interest were obtained from the borehole and free-field regions of the mesh corresponding to the locations where test measurements were made.

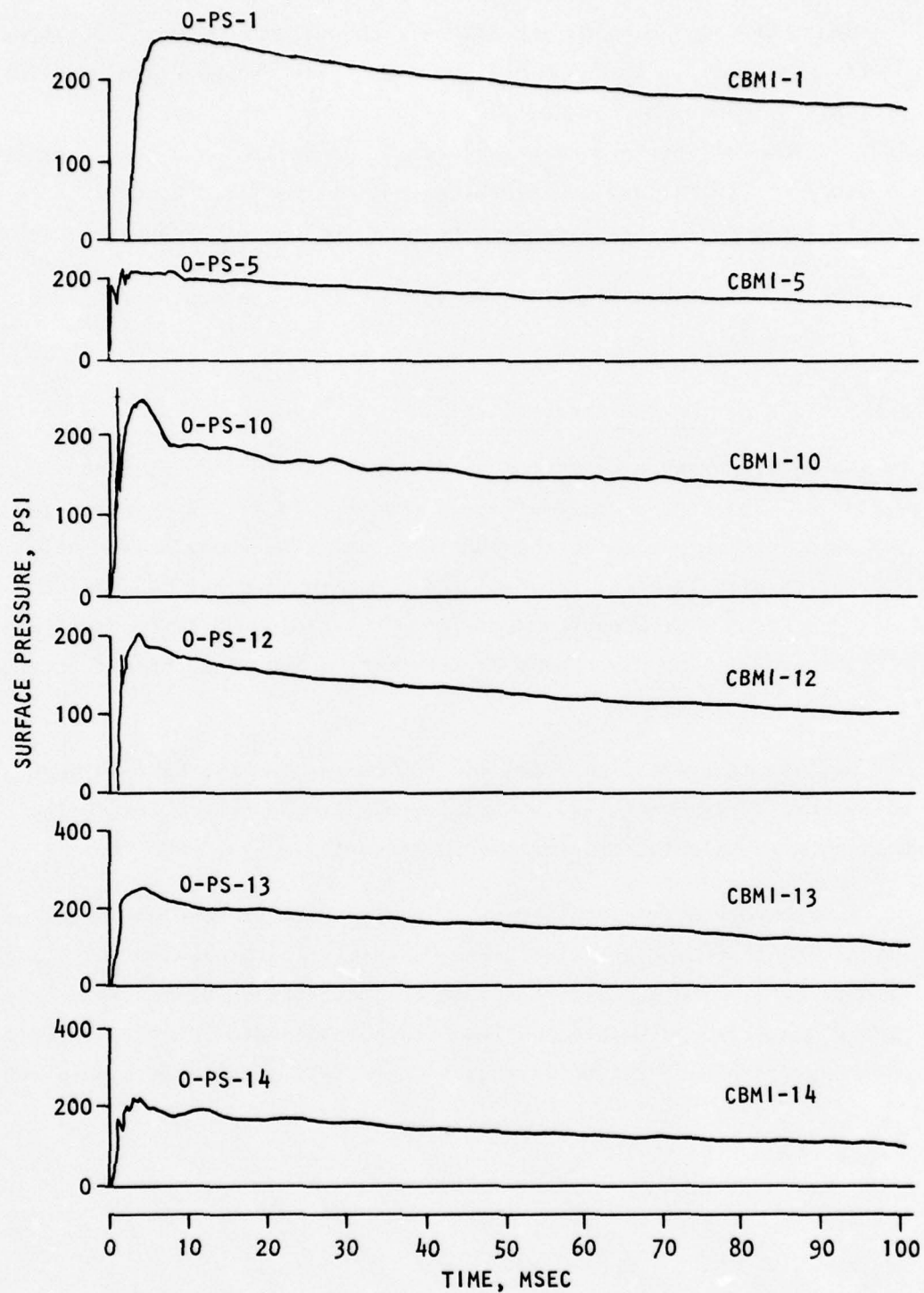


FIGURE 2-2. SURFACE PRESSURE MEASURED DURING CBMI TEST SERIES

The finite-element computer code used for the calculations is described in Section 3. The details of the input parameters used in these calculations are discussed in Sections 4 through 8, and the results obtained from the calculations are presented, interpreted, and compared with test data. Overall conclusions from the tests and tentative recommendations for gage placement are presented in Section 9. Section 9 also describes proposed analytical work from which recommendations for gage placement would be finalized and presented in the final report.

SECTION 3

GENERAL DESCRIPTION OF COMPUTER CODE
USED FOR THE CALCULATIONS

The calculations described in this report were performed on a UNIVAC 1108 Computer using the FEDRC computer code. A brief description of this code follows, along with a more detailed discussion of the features of particular relevance to the present calculations.

3.1 BRIEF DESCRIPTION OF FEDRC CODE

FEDRC is a two-dimensional, axisymmetric, nonlinear finite element code that can be used for both static and dynamic calculations (Ref. 6). The dynamic solution is obtained by an implicit integration technique using either the Newmark β -method or the Wilson θ -method.

The code permits long calculations to be performed in segments using several intermediate restart runs. Each such run generates three tapes: a restart tape to continue the run, a plot data tape, and a data tape containing time histories of all the quantities calculated during the run. The plot data tape may be used to generate time history plots of quantities selected at the beginning of the calculation. Additional plots may also be obtained using the data tape.

In a nonlinear calculation, the global stiffness matrix must be reformulated as frequently as necessary in order to retain accuracy, but as infrequently as possible in order to minimize the economic burden. The interval in number of steps after which the global stiffness matrix is reformulated and the time step of integration can be changed during the course of the run. In the present calculations, the stiffness matrix was reformulated after every step. The schedule of variation of the integration time step followed in each calculation is indicated in the section describing the calculation.

3.2 DAMPING AND MATERIAL MODEL

The global damping matrix C is taken in the FEDRC code as

$$C = \alpha K + \beta M$$

where K , M are the global stiffness and mass matrixes, respectively, and α , β are user specified constants. In a linear system, this formulation would imply that a normal mode with a frequency ω would experience a damping factor

$$\zeta = \frac{1}{2} (\alpha\omega + \beta/\omega)$$

In each of the present calculations, except that of Test CBMI-10, the values chosen were:

$$\alpha = 0.00005 \quad \beta = 0$$

With $\beta = 0$ the damping factor ζ is directly proportional to the frequency and the above value of α is such that the damping factor is 1.57% at 100 Hz. This value of the damping factor was chosen as being large enough to control possible numerical oscillations and yet, not so large as to distort the calculated response substantially.

By far the greatest source of energy dissipation in real soil materials occurs as the result of hysteresis in the stress/strain relationship and because of irreversible deformations resulting from inelastic behavior, in general, and yielding in particular. Because of their importance to these calculations, material model representations and large, discontinuous deformations resulting from debonding and slip are discussed in detail in the following two subsections.

The FEDRC code has an extensive library of nonlinear, inelastic material models. For soil or earth materials, these include the so-called cap and variable modulus type models.

All the present calculations employed an isotropic, variable modulus model, defined by a bulk modulus and Poisson's ratio. The model assumes both the volumetric strain/pressure relation and the uniaxial stress path to be piecewise linear (Figs. 3-1a, b).

Loading

The bulk modulus can have up to four different values and Poisson's ratio, up to three different values. The changes from one value to another occur at designated values of the elastic component of volumetric strain in the case of the bulk modulus, and of the mean pressure, in the case of Poisson's ratio. The bulk modulus K_L and Poisson's ratio ν_L for virgin loading are given by the following expressions:

$$K_L = \begin{cases} B_4 & B_1 \leq \mu \leq 0 \\ B_5 & B_2 \leq \mu < B_1 \\ B_6 & B_3 \leq \mu < B_1 \\ B_7 & \mu < B_3 \end{cases} \quad (3-1)$$

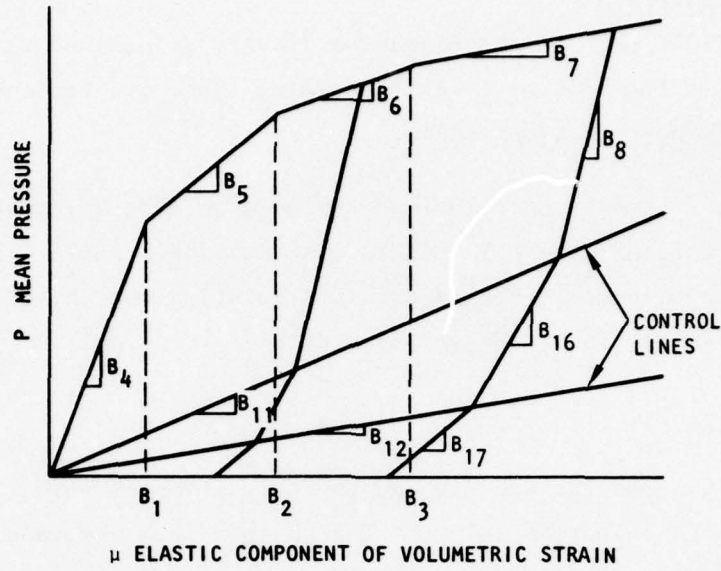
$$\nu_L = \begin{cases} G_1 & G_6 \leq P \leq 0 \\ G_{11} & G_7 \leq P < G_6 \\ G_{12} & P < G_7 \end{cases} \quad (3-2)$$

where

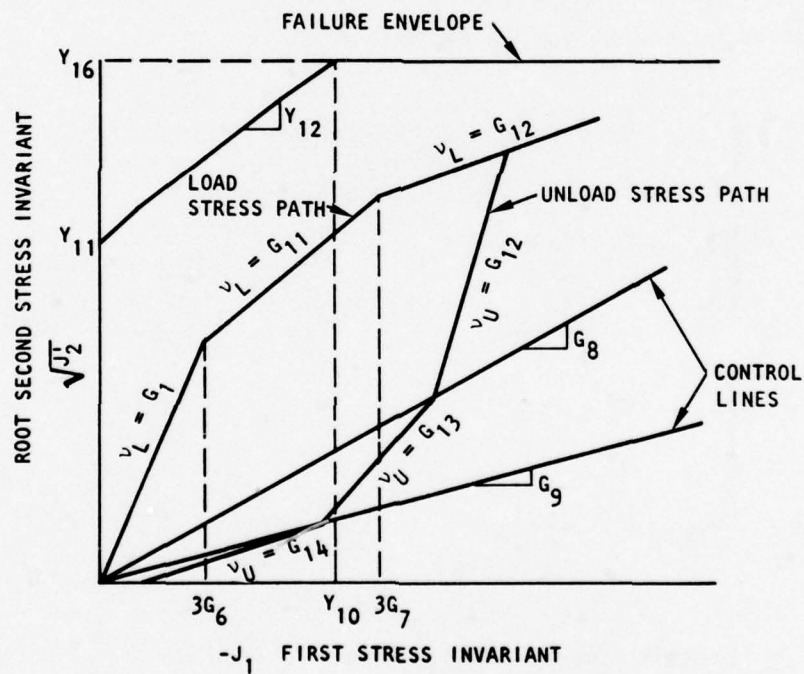
μ = Elastic component of volumetric strain

P = Mean pressure = $1/3 J_1$

J_1 = First invariant of stress tensor



(a) Pressure versus volumetric strain



(b) Stress path and failure envelope

FIGURE 3-1 VARIABLE MODULUS MODEL USED IN THE CALCULATIONS

Unloading/Reloading

The bulk modulus and Poisson's ratio are each permitted to have three different values in unloading. A change in these values is triggered whenever the unloading path (in the $P - \mu$ space for the bulk modulus and the $J_1 - \sqrt{J_2^I}$ space for Poisson's ratio) intersects one of the "control lines" as indicated in Figure 3-1. The bulk modulus K_U and Poisson's ratio ν_U for unloading are given by the following expressions:

$$K_U = \begin{cases} B_8 & P < B_{11}\mu \\ B_{16} & B_{11}\mu \leq P < B_{12}\mu \\ B_{17} & P \geq B_{12}\mu \end{cases} \quad (3-3)$$

$$\nu_U = \begin{cases} G_2 & \sqrt{J_2^I} > G_8 J_1 \\ G_{13} & G_9 J_1 < \sqrt{J_2^I} \leq G_8 J_1 \\ G_{14} & \sqrt{J_2^I} \leq G_9 J_1 \end{cases} \quad (3-4)$$

where J_2^I is the second invariant of the deviatoric stress tensor.

Reloading is assumed to take place along the unloading path till the volumetric elastic strain exceeds the highest value previously attained during the loading history; at which stage, the properties corresponding to virgin loading take effect.

Inelasticity

The model also incorporates a failure envelope defined by

$$F = \begin{cases} \sqrt{J_2^I} - Y_{11} - Y_{12}J_1 & Y_{10} \leq J_1 \\ \sqrt{J_2^I} - Y_{16} & J_1 < Y_{10} \end{cases} \quad (3-5)$$

$F < 0$ Elastic

$F \geq 0$ Inelastic

Tension

When the volumetric elastic strain μ is positive, the bulk modulus and the shear modulus are assumed to have the constant values B_{10} and G_{10} , respectively.

Tension Cutoff

If J_1 exceeds a specified positive value Y_{25} , tension cutoff is assumed to have been reached and all components of stress are set to zero.

The model requires the user to specify the mass density ρ and the coefficients B_1 through B_7 , B_8 , B_{10} , B_{11} , B_{12} , B_{16} , B_{17} , G_1 , G_2 , G_6 through G_{14} , Y_{10} , Y_{11} , Y_{12} , Y_{16} , and Y_{25} . The values of these coefficients for each material used in the calculations are indicated in the sections detailing the calculations.

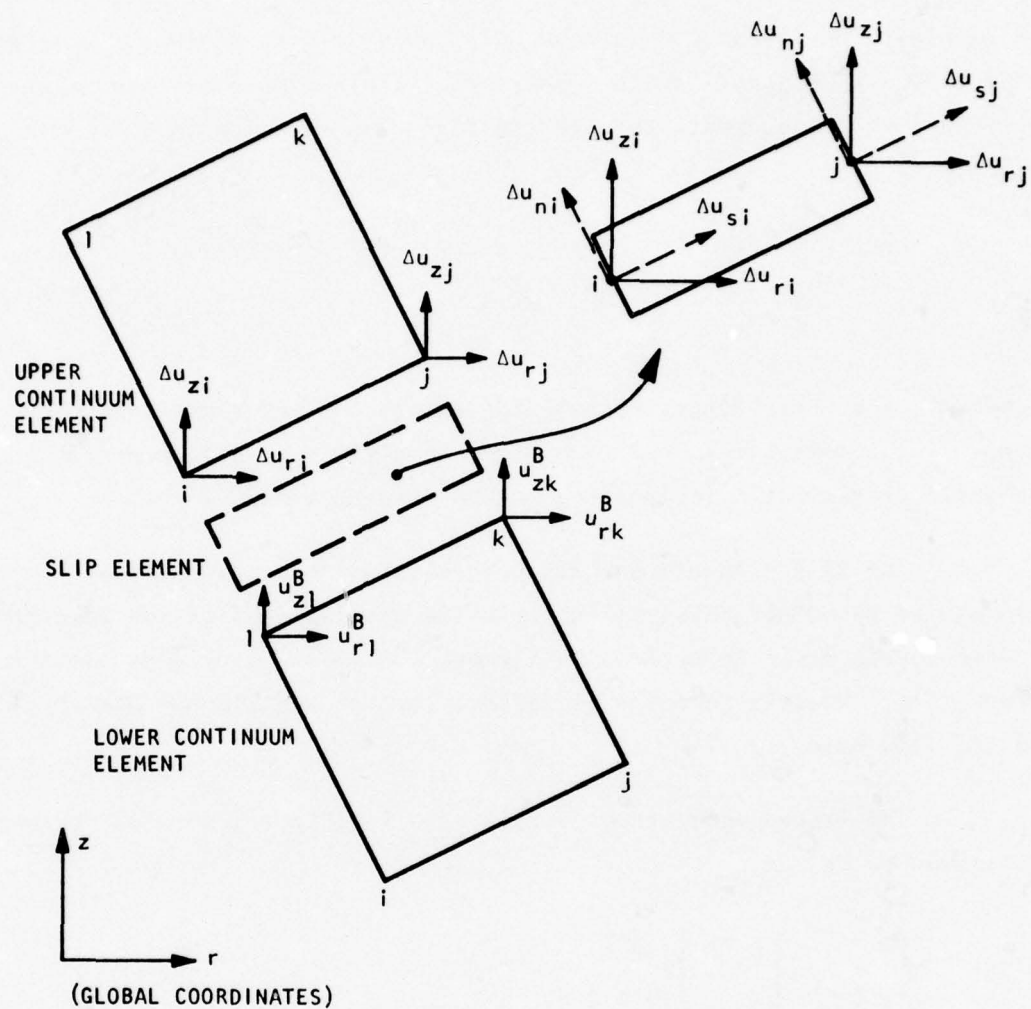
3.3 SLIP ELEMENT

The slip element is intended to represent interfaces between dissimilar materials and other discontinuities in continuum systems, and allows for behavior such as debonding and slip. The term debonding means the ability of two blocks of continuum, initially in contact, to separate. Subsequent contact can develop by the movement of the two blocks towards each other. The term slip means the relative motion along the slip surface when the shearing force exceeds the shear strength of the interface.

The slip element in the FEDRC code employs the relative displacements at the slip surface as the degrees of freedom. Thus, the slip element has four degrees of freedom (Fig. 3-2). The relative normal and tangential displacements, Δu_n and Δu_s , are assumed to vary linearly along the element as follows:

$$\Delta u_n = h_i \Delta u_{ni} + h_j \Delta u_{nj} \quad (3-6)$$

$$\Delta u_s = h_i \Delta u_{si} + h_j \Delta u_{sj}$$



$$u_{ri}^T = u_{ri}^B + \Delta u_{ri}$$

$$u_{zi}^T = u_{zi}^B + \Delta u_{zi}$$

$$u_{rj}^T = u_{rk}^B + \Delta u_{rj}$$

$$u_{zj}^T = u_{zk}^B + \Delta u_{zj}$$

FIGURE 3-2. GEOMETRY OF SLIP ELEMENT

where h_i and h_j are linear interpolation functions and Δu_{ni} , Δu_{nj} , Δu_{si} and Δu_{sj} are the nodal point values of the relative displacements. The slip element is assumed to have only two strain components; ϵ_n = normal strain, and ϵ_s = shear strain. These two strain components are related to the relative displacements through the following relations.

$$\epsilon_n = \frac{1}{t} \Delta u_n$$

$$\epsilon_s = \frac{1}{t} \Delta u_s$$

The normal and shear forces transmitted across the interface are computed from these using stress/strain relations that involve input parameters chosen on the basis of available information on the interface behavior.

The slip elements are assigned elastoplastic properties. Slippage, accompanied by comparatively large relative displacement at the interface, is intended to occur when the slip element yields and undergoes plastic deformation. Plastic behavior is defined through a yield surface and a plastic flow rule.

The incremental stress/strain relationship for the slip elements is assumed to be

$$\begin{Bmatrix} d\sigma \\ d\tau \end{Bmatrix} = \begin{bmatrix} c_\sigma & 0 \\ 0 & c_\tau \end{bmatrix} \begin{Bmatrix} d\epsilon^{el} \\ d\gamma^{el} \end{Bmatrix} \quad (3-7)$$

where

$d\sigma$ = Normal stress increment

$d\tau$ = Shear stress increment

c_σ = Normal elastic stiffness (tangent modulus)

c_τ = Shear Elastic stiffness (tangent modulus)

$d\epsilon^{el}$ = Elastic part of normal strain increment

$d\gamma^{el}$ = Elastic part of shear strain increment

During elastic deformations, the plastic part of the strain increment is zero and the total strain increments are used in Equation 3-7.

The onset of plastic behavior is determined through a yield function $f(\sigma, \tau)$. Thus

$$f(\sigma, \tau) \quad \begin{cases} = 0 & \text{plastic} \\ < 0 & \text{elastic} \end{cases} \quad (3-8)$$

The flow rule is chosen to be

$$\begin{Bmatrix} d\epsilon^{pl} \\ d\gamma^{pl} \end{Bmatrix} = \eta \begin{Bmatrix} \frac{\partial f}{\partial \sigma} \\ \frac{\partial f}{\partial \tau} \end{Bmatrix} \quad (3-9)$$

where η is a scalar quantity to be determined, and $\partial f/\partial \sigma$ and $\partial f/\partial \tau$ are the derivatives of the yield function with respect to the stress components (Ref. 7).

In the present model, the yield function has the form

$$f = \begin{cases} |\tau| - Y_{11} - Y_{12}\sigma & \sigma \geq Y_{10} \\ |\tau| - Y_{16} & \sigma < Y_{10} \end{cases} \quad (3-10)$$

and is illustrated in Figure 3-3.

Using this explicit form of f , after some manipulation, the inelastic stress/strain relationship is obtained as

$$\begin{Bmatrix} d\sigma \\ d\tau \end{Bmatrix} = \begin{bmatrix} C_\sigma \left(1 - \frac{Y_{12}^2 C_\sigma}{Y_{12}^2 C_\sigma + C_\tau} \right) & \pm \frac{Y_{12} C_\sigma C_\tau}{Y_{12}^2 C_\sigma + C_\tau} \\ \pm \frac{Y_{12} C_\sigma C_\tau}{Y_{12}^2 C_\sigma + C_\tau} & C_\tau \left(1 - \frac{C_\tau}{Y_{12}^2 C_\sigma + C_\tau} \right) \end{bmatrix} \begin{Bmatrix} d\epsilon \\ d\gamma \end{Bmatrix} \quad (3-11)$$

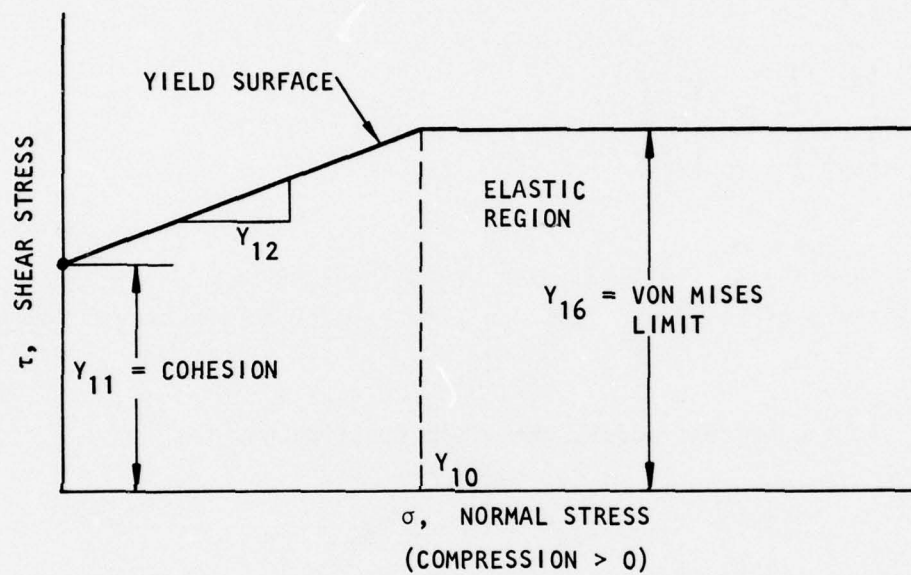


FIGURE 3-3. SLIP MODEL YIELD SURFACE

Introducing the dimensionless parameter

$$\lambda = \frac{c_{\tau}}{\gamma_{12}^2 c_{\sigma}} \quad (3-12)$$

Equation 3-11 may be written as

$$\begin{Bmatrix} d\sigma \\ d\tau \end{Bmatrix} = \begin{bmatrix} c_{\sigma} \frac{\lambda}{1 + \lambda} & \pm c_{\sigma} \frac{\gamma_{12}^{\lambda}}{1 + \lambda} \\ \pm c_{\sigma} \frac{\gamma_{12}^{\lambda}}{1 + \lambda} & c_{\tau} \frac{1}{1 + \lambda} \end{bmatrix} \begin{Bmatrix} d\epsilon \\ d\gamma \end{Bmatrix} \quad (3-13)$$

SECTION 4

CALCULATION OF TEST CBMI-10 (CONTROL TEST)

This section presents a review of work previously completed on the Control Test and describes the recalculated results performed to identify the source of problems that led to relatively poor quality in the predictions.

4.1 REVIEW OF PREVIOUS CALCULATION OF TEST CBMI-10

Finite-element calculations were performed earlier at AA on the Test CBMI-10 and have been reported in Reference 5. The results of these calculations did not correlate well with the test data. The following specific points of disagreement existed between the calculated results and test data:

- a. Calculated peak velocities were higher, sometimes by a factor of 2.
- b. Peak velocities in the calculations showed considerably more attenuation with depth.
- c. Calculated velocities attained their peak values earlier than the test velocities.
- d. Calculated velocities returned to zero considerably earlier than the test velocities.
- e. The calculations showed more rebound, i.e., when the velocities reversed direction, the calculated velocities attained higher peak values in the upward direction than the test velocities.

Velocities at two locations, at depths of 18 and 54 in. in the calculations and test are compared in Figures 4-1 and 4-2. More comparisons may be found in Reference 5.

Reference 5 concluded that the differences were due to incorrect representation of material properties in the calculations and recommended that the material properties be determined again by WES and that a new calculation be performed.

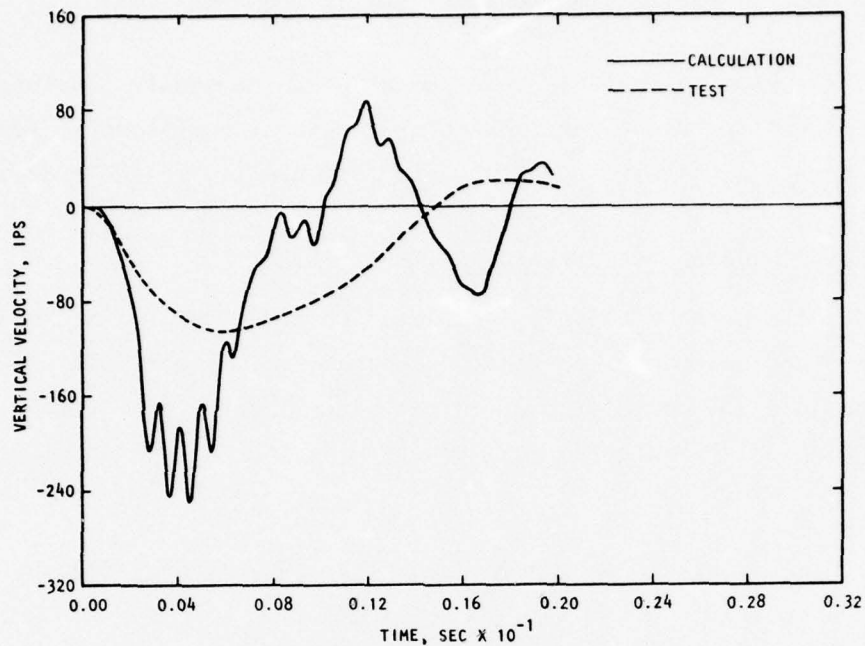


FIGURE 4-1. COMPARISON OF VELOCITY HISTORIES AT $R = 0$ AND $D = 18$ IN. FOR TEST CBMI-10

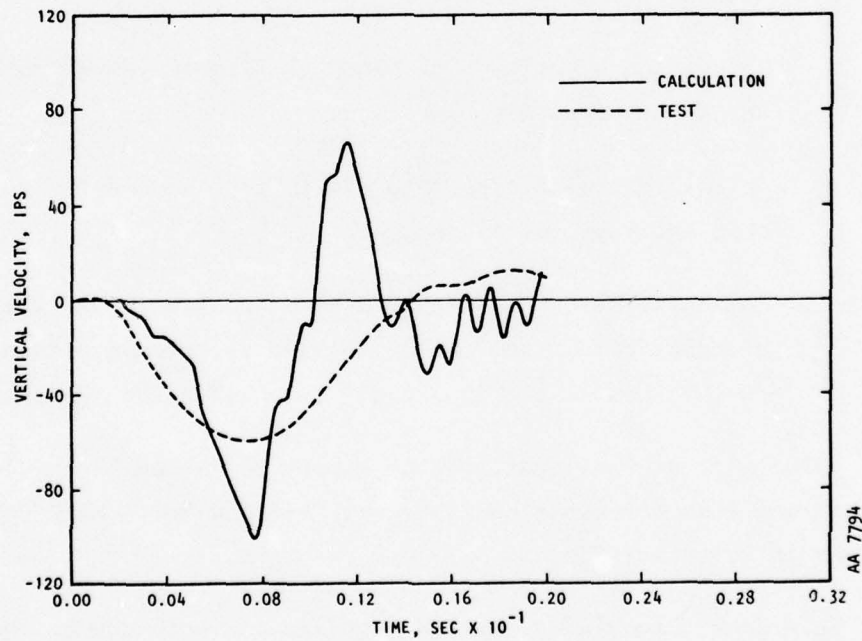


FIGURE 4-2. COMPARISON OF VELOCITY HISTORIES AT $R = 0$ AND $D = 54$ IN. FOR TEST CBMI-10

4.2 RECALCULATION OF TEST CBMI-10 (CBMI-10-1)

A new set of material property data was supplied by WES (Ref. 8), and new calculations were performed with these properties. These calculations are designated as CBMI-10-1 for clarity.

4.2.1 MESH

The finite-element mesh used for the calculations was exactly identical to the one used in the earlier calculations (Ref. 5) and is shown in Figure 4-3. An axisymmetric formulation was used, and one side of the axis of symmetry was modeled. The wall of the SBLG was included in the mesh, and slip elements were used at the interface between the wall and the soil. A tensile (upward) equilibrating load was applied to the SBLG wall as in Reference 5. The wall was modeled using quadrilateral elements.

4.2.2 MATERIAL MODELS

Initially, it was intended to use a cap-type model for the soil. However, after several attempts it was found that although the model matched the uniaxial stress/strain data quite well, it was impossible to get a good match for the stress path. Therefore, it was decided to adopt a variable modulus model of the type described in Section 3.2.

The numerical values of the parameters of the model used in the calculations are shown in Table 4-1. In this calculation the unloading bulk modulus was assumed to be constant. Poisson's ratio was also assumed constant, with one value for loading and another for unloading. The uniaxial stress/strain behavior of the model and the supplied data are shown in Figure 4-4.

The elements in the SBLG wall were assigned elastic properties corresponding to steel, namely, an elastic modulus of 30×10^6 psi and a shear modulus of 12×10^6 psi.

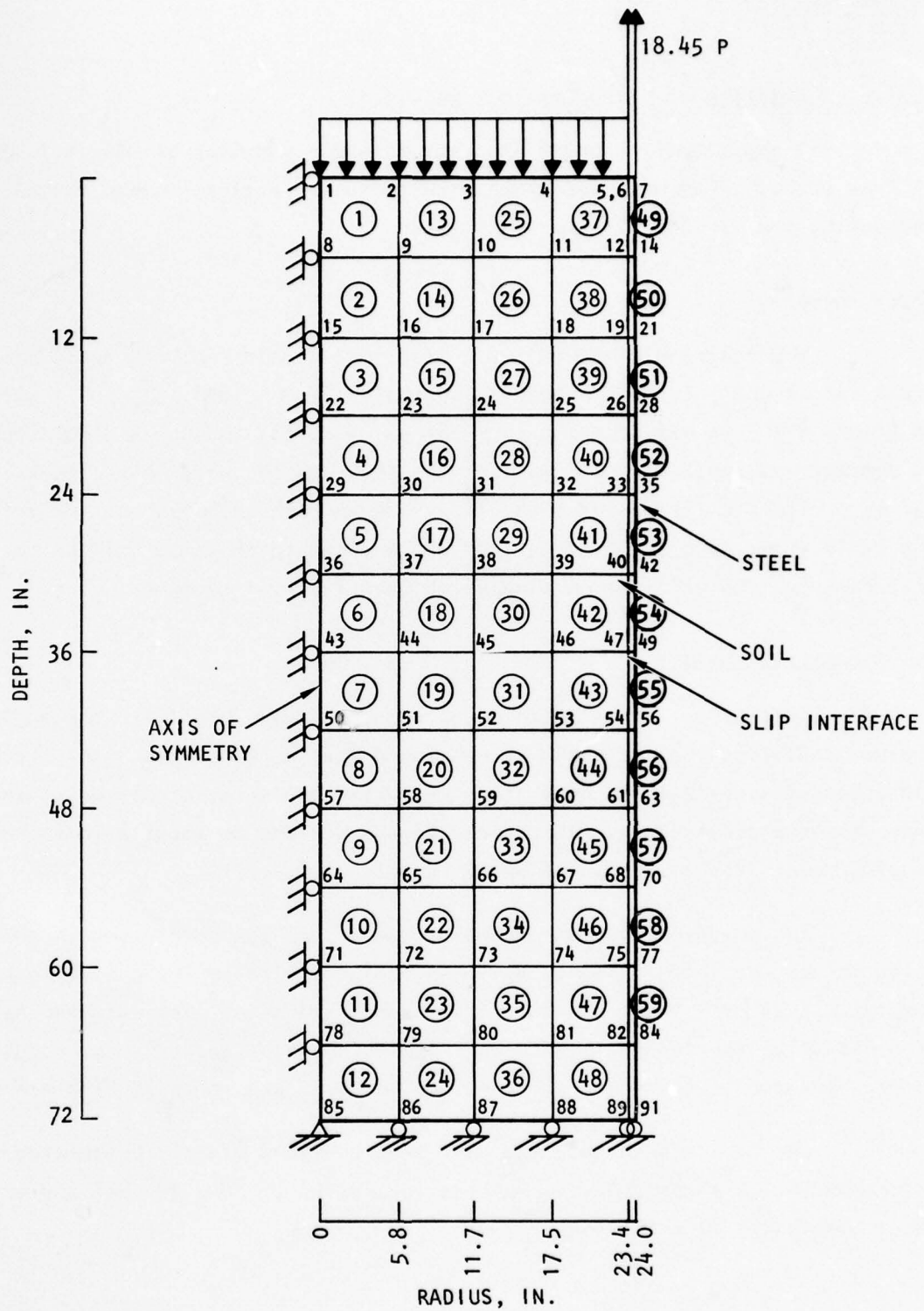
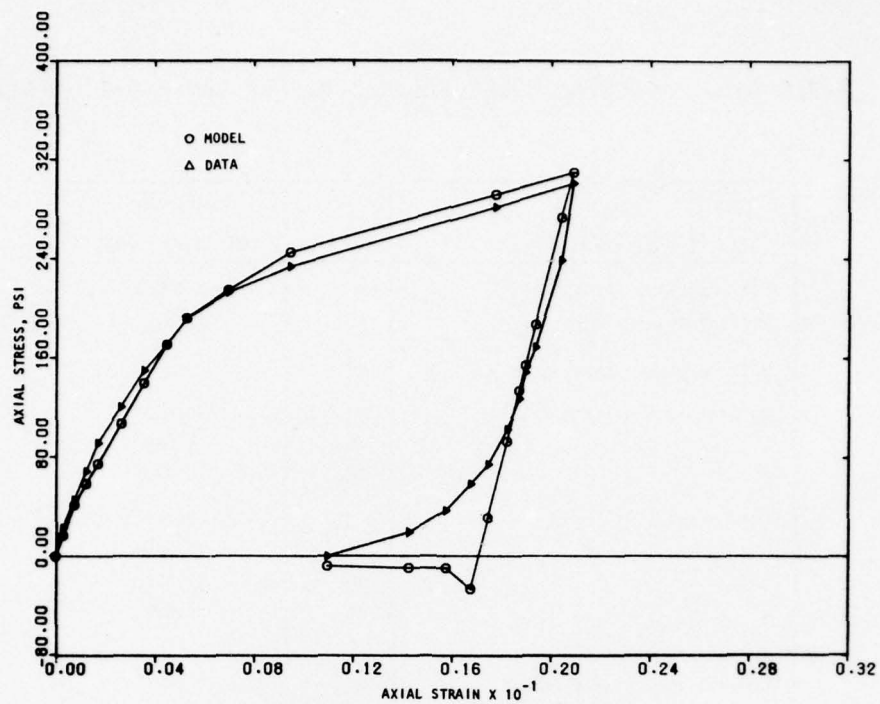


FIGURE 4-3. FINITE ELEMENT MESH USED FOR CBMI-10-1 CALCULATIONS

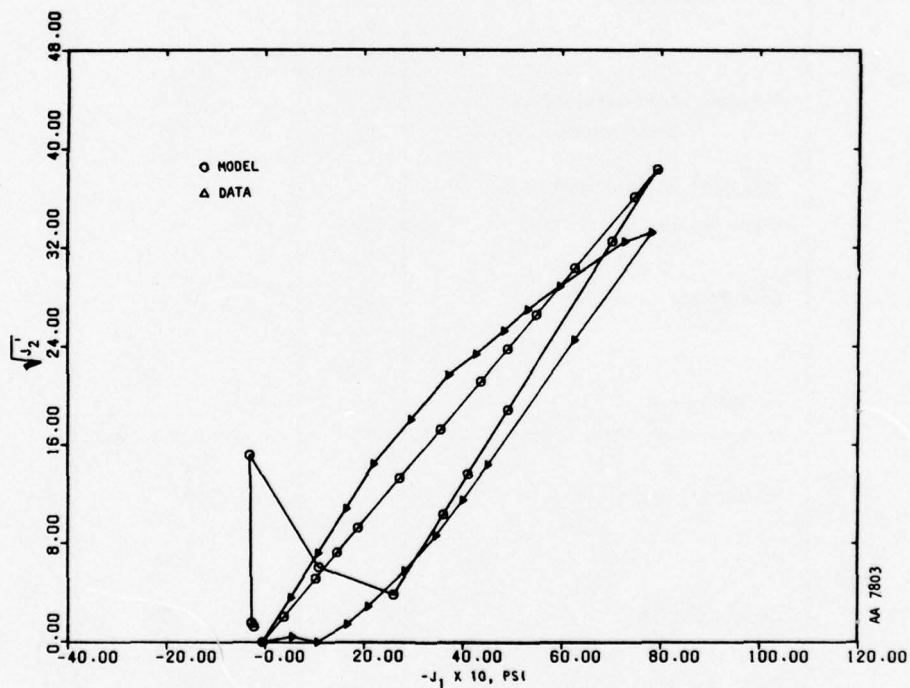
TABLE 4-1. MATERIAL MODEL PARAMETERS FOR CBMI-10-1 MATRIX

Quantity and Units	Symbol	Material CBMI-10-1 Matrix
Mass Density, lb-sec ² /in. ⁴	ρ	0.000131
Unit Weight, pcf	γ	87.5
<u>Bulk Modulus: Loading</u>		
Strain break points, in./in.	B_1	-0.0008
	B_2	-0.005
	B_3	-0.0091
Load moduli, psi	B_4	45,701
	B_5	29,676
	B_6	11,357
	B_7	4,800
<u>Unload/reload:</u>		
Control line slopes, psi	B_{11}	--
	B_{12}	--
Unload moduli, psi	B_8	66,900
	B_{16}	--
	B_{17}	--
Tension: Bulk modulus, psi	B_{10}	5,000
	Shear modulus, psi	G_{10} 845
<u>Poisson's Ratio: Loading</u>		
Break points, psi	G_6	--
	G_7	--
Load Poisson's ratio	G_1	0.44
	G_{11}	--
	G_{12}	--
<u>Unload/reload</u>		
Control line slope, dimensionless	G_8	--
	G_9	--
Unload Poisson's ratio	G_2	0.42
	G_{13}	--
	G_{14}	--
<u>Yield Parameters</u>		
Cohesion, psi	Y_{10}	-600.0
	Y_{11}	43.3
Slope	Y_{12}	-0.024
von Mises limit, psi	Y_{16}	57.74
Tension cutoff, psi	Y_{25}	30.0

AA8192



(a) Uniaxial stress/strain curve



(b) Uniaxial stress path

FIGURE 4-4. SOIL PROPERTIES FOR TEST CBMI-10-1

Slip elements of the type described in Section 3.3 were used at the wall interface. Properties had been chosen so as to simulate a coefficient of friction of 0.3 in Reference 5. From discussions with WES personnel, it appeared that a considerably lower value was more appropriate in order to take into account the presence of the sidewall friction relief liner in the SBLG. Therefore, the properties were altered so as to simulate a coefficient of friction of 0.1. The parameters used in the CBMI-10-1 calculations are shown in Table 4-2. In reality, however, the properties assumed for the slip elements resulted in much higher frictional resistance at the interface than intended. This point is discussed in more detail in Section 4.4.2.

4.2.3 INPUT PULSE AND INTEGRATION SCHEDULE

The input pulse for the CBMI-10-1 calculations was the same one used in Reference 5 and was obtained from the measurements made during the CBMI-10 test. The pulse is shown in Figure 4-5. The schedule according to which the integration time step Δt was varied, is also shown in Figure 4-5. The global stiffness matrix was reformulated after every step. No damping was used in this calculation, and therefore the constants α and β were both zero in this case. The entire calculation took 250 steps and was terminated after encompassing a real-time duration of 16.5 msec.

4.3 RESULTS OF CBMI-10-1 CALCULATIONS

The results of the CBMI-10-1 calculations showed no appreciable improvement over the CBMI-10 calculations. The velocities obtained from the new calculations are shown in Figures 4-6 and 4-7. Overlaid on the plots are the velocities obtained in the original CBMI-10 calculations and the test (shown earlier in Figs. 4-1 and 4-2). It is seen that the discrepancies listed in Section 4.1 persist although there is some improvement in the peak values. The velocities at other locations exhibited the same lack of improvement.

In order to pinpoint the cause of this discrepancy, some auxiliary calculations were performed. These are described in the next subsection.

TABLE 4-2. SLIP MODEL PARAMETERS: CBMI-10-1
MATRIX/SBLG INTERFACE

Parameter	Numerical Value Used in Calculation
Normal Stiffness C_{σ} , psi	50,000
Shear Stiffness C_{τ} , psi	2,000
Y_{10} , psi	150
Cohesion Y_{11} , psi	35
Coefficient of Friction Y_{12} , psi	0.1
Y_{16} , psi	50

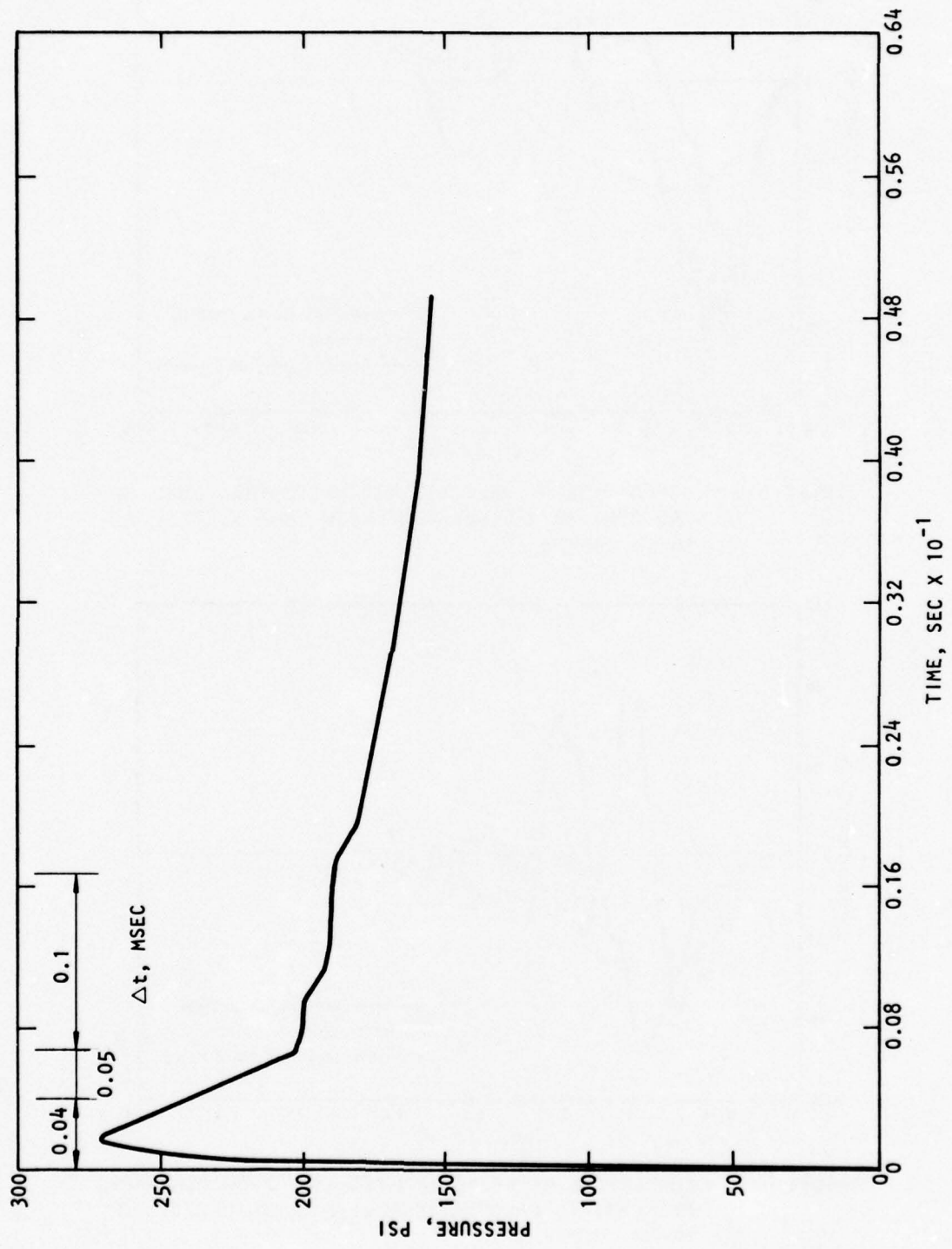


FIGURE 4-5. INPUT PULSE USED IN THE CBMI-10-1 CALCULATION

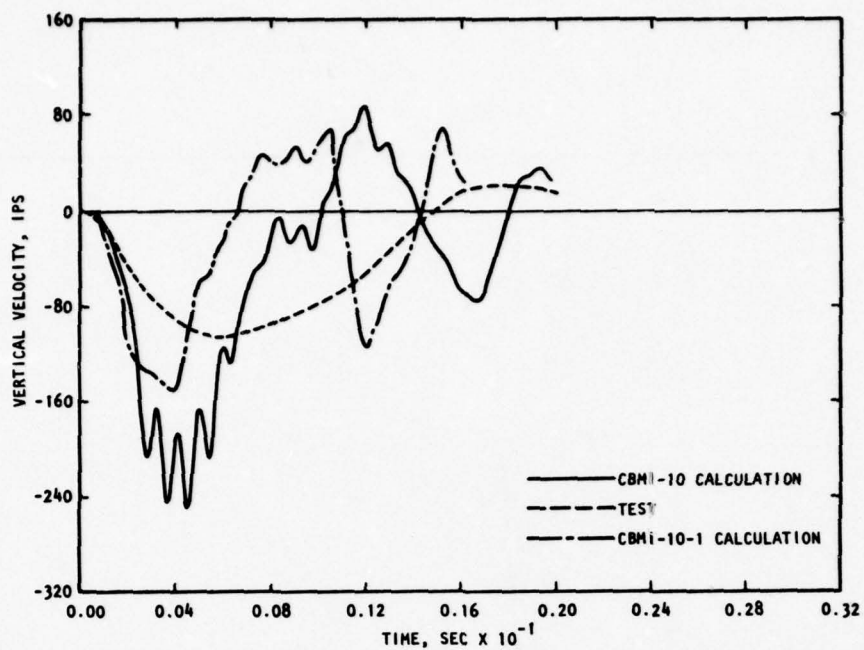


FIGURE 4-6. COMPARISON OF VELOCITY HISTORIES FROM CBMI-10-1 AND CBMI-10 CALCULATIONS WITH CBMI-10 TEST AT 18-IN. DEPTH

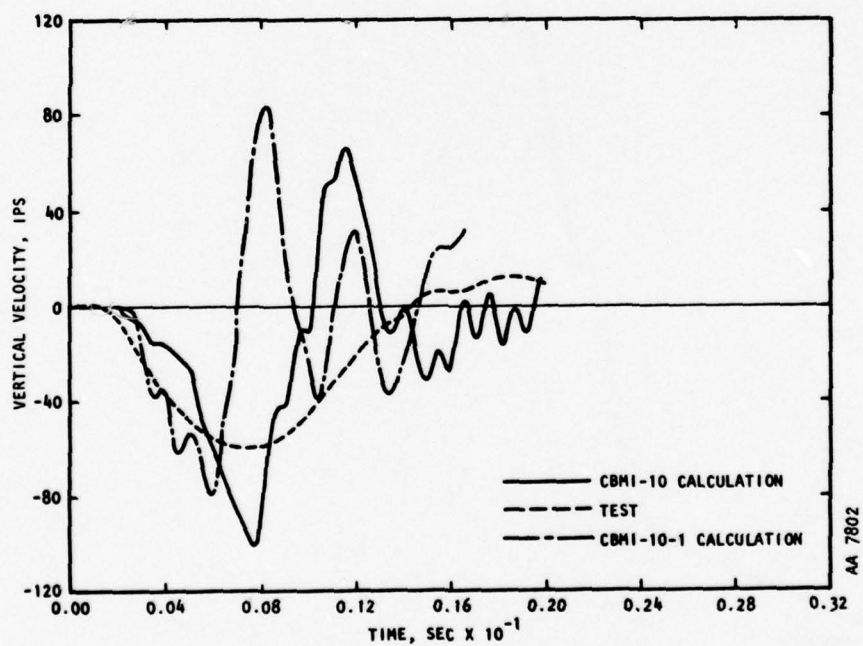


FIGURE 4-7. COMPARISON OF VELOCITY HISTORIES FROM CBMI-10-1 AND CBMI-10 CALCULATIONS WITH CBMI-10 TEST AT 54-IN. DEPTH

4.4 AUXILIARY CALCULATIONS

7 A one-dimensional calculation and a parametric series of two-dimensional calculations were performed to provide insight on the selection of interface slip parameters.

4.4.1 ONE-DIMENSIONAL CALCULATION

If the friction at the SBLG wall is small, then it is to be expected that the response of the soil is essentially one-dimensional. Pilot calculations by WES, in fact, confirmed this. Therefore, it was decided to perform one-dimensional calculations using the new material properties for the soil.

The mesh used for the one-dimensional calculation simulated the two-dimensional mesh closely, being made of a 72-in. long column of 6-in. deep elements and is shown in Figure 4-8. Both sides were rollered to simulate uniaxial conditions, and the bottom was rollered as in the two-dimensional calculation. The same input pulse used in the two-dimensional calculation was applied at the top, and the integration time step was changed according to the same schedule.

The velocities from the one-dimensional calculation at three different depths are compared with the test velocities in Figure 4-9, and it is seen that the agreement with the test result is quite close. This confirmed the speculation that the response of the soil column is essentially one-dimensional and indicates that the discrepancy in the two-dimensional calculation is due to the modeling of the interface effects at the SBLG wall.

4.4.2 PARAMETRIC STUDY OF THE BEHAVIOR OF THE SLIP MODEL

In order to choose the slip model properties so as to simulate interface effects more accurately, it was decided to gain a better understanding of the influence of the parameters of the slip model on the overall response by conducting a parametric study.

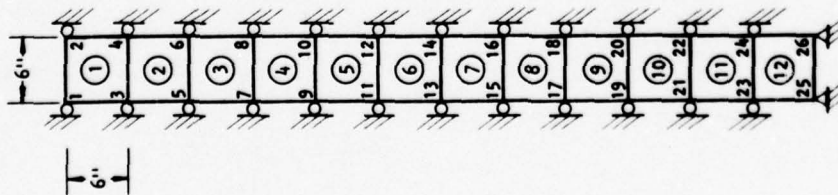


FIGURE 4-8. FINITE ELEMENT MESH FOR COLUMN RUN

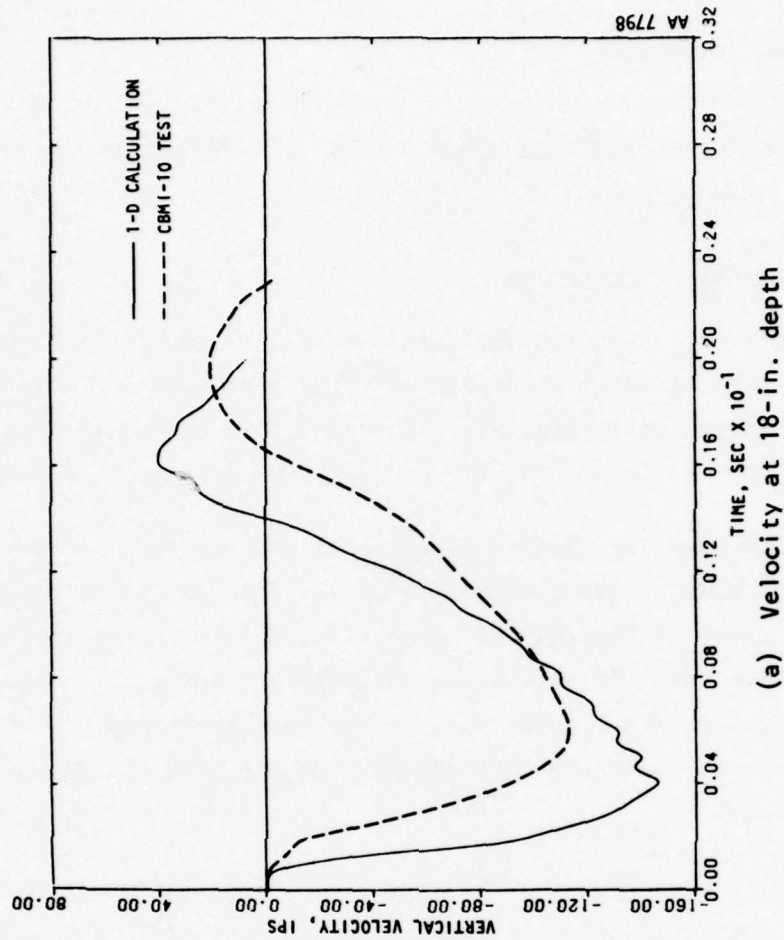
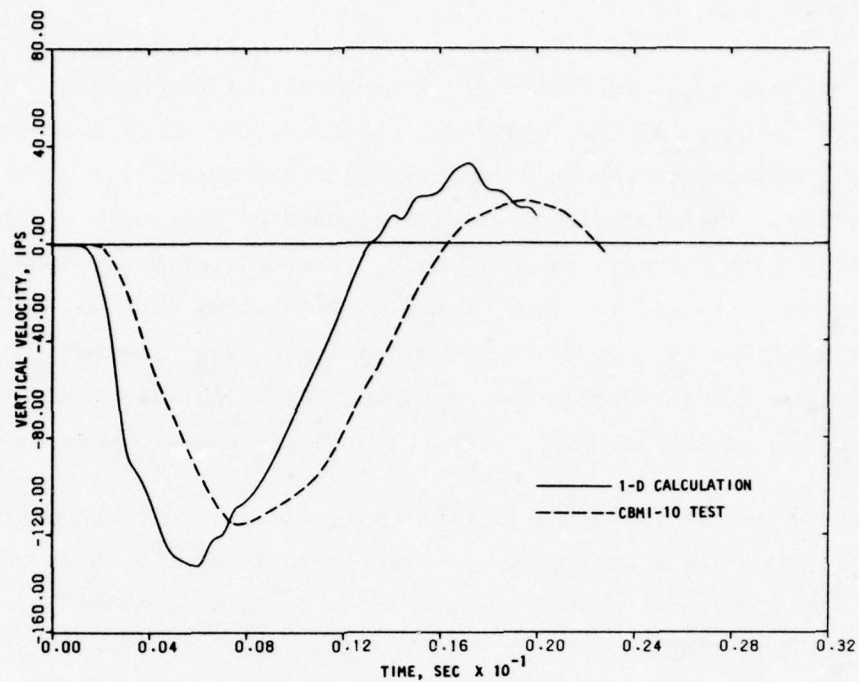
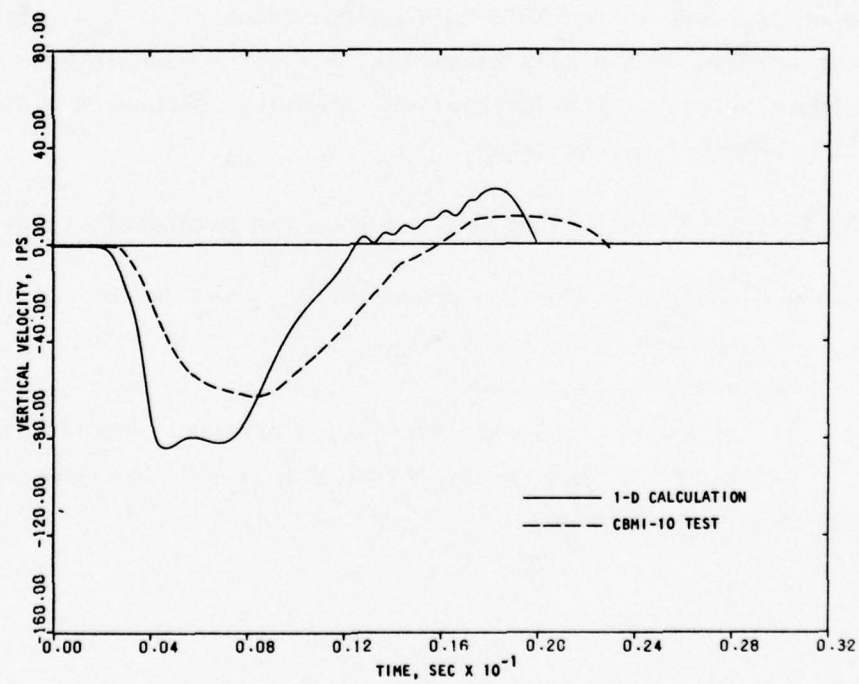


FIGURE 4-9. COMPARISON OF VELOCITIES FROM 1-D CALCULATION WITH CBMI-10 TEST



(b) Velocity at 36-in. depth



(c) Velocity at 54-in. depth

FIGURE 4-9. (CONCLUDED)

The slope Y_{12} in Figure 3-1 is generally identified as the coefficient of friction at the interface. However, the model used here is considerably more complex than a straightforward representation of interface sliding friction. Therefore, the overall response of a structural system employing these slip elements is influenced by several of the parameters entering into the slip model. Thus, Equation 3-10 shows that not only Y_{12} but also the cohesion Y_{11} and the von Mises limit Y_{16} control the maximum shear that can be transmitted across the interface. This is because appreciable slip displacement occurs only when the slip element yields.

In the parametric study, dynamic calculations were performed using a soil column and a steel column 36 in. long arranged side by side with slip elements at the interface. The mesh used for the study is shown in Figure 4-10. The following parameters were varied: elastic normal stiffness, C_σ ; cohesion, Y_{11} ; slope Y_{12} ; and von Mises limit, Y_{16} . The matrix of cases studied is shown in Table 4-3. It may be noted that Case 1 is identical with the properties used in the CBMI-10-1 calculations. Six runs were made with different choices of the slip properties but no changes in material properties, input pulse, or the integration schedule, which were all the same as in the CBMI-10-1 calculations.

The following conclusions emerged from the parametric study:

- a. A higher value for the cohesion Y_{11} and, more importantly, for the von Mises limit Y_{16} , signifies an increased capability to transmit shear across the interface. In such a case, even if the slope Y_{12} , and hence, the apparent "coefficient of friction" is low, the effective frictional resistance at the interface is high.

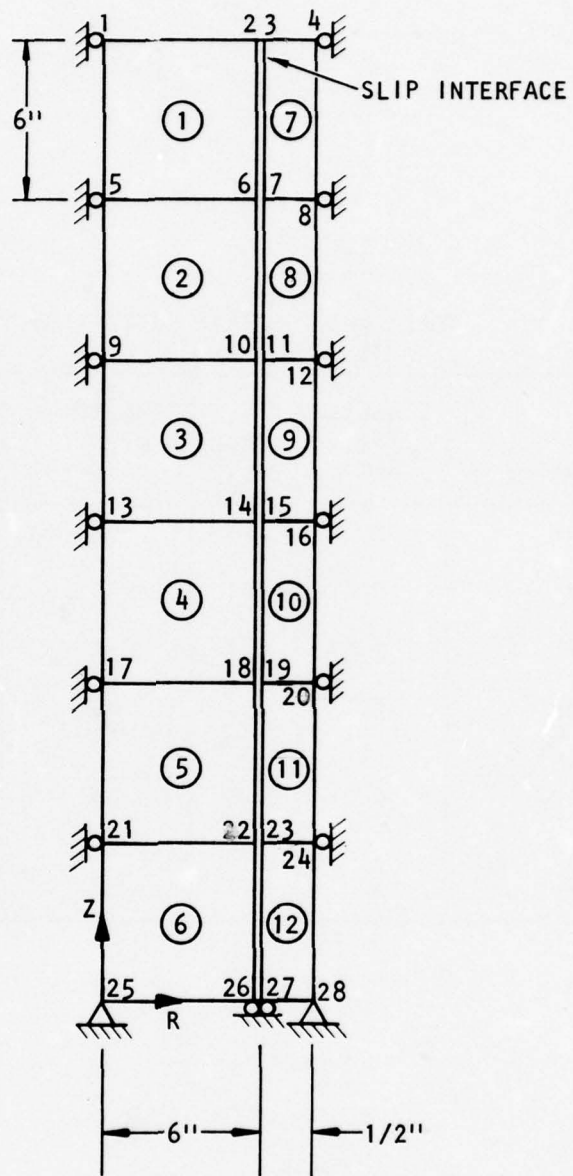


FIGURE 4-10. FINITE ELEMENT MESH FOR PARAMETRIC STUDY OF SLIP MODEL

TABLE 4-3. MATRIX OF TEST CASES

Case No.	Description	Cohesion γ_{11} , psi	Slope γ_{12}	von Mises Limit γ_{16} , psi	C_σ , psi	$\lambda = \frac{C_\tau}{\gamma_{12}^2 C_\sigma}$
1	High Shear	35	0.1	50	50,000	4
2	Low Shear	0.01	0.1	2	50,000	4
3	Low Shear	0.01	0.1	2	2,000	100
4	High Shear	35	0.1	50	2,000	100
5	High Coefficient of Friction	0.01	0.5	50	2,000	4
6	High Coefficient of Friction	35	0.5	50	2,000	4

$C_\tau = 2000 \text{ psi}$

- b. Under the above conditions, the slip displacement at the interface is obviously lower. The calculations also show that higher interface friction results in an early and rapid unloading pulse that completely masks the true reflection from the lower boundary. Thus, the vertical velocity returns to zero much earlier and the vertical stress does not show the expected increase from the reflected compression wave. Peak velocities and peak stresses (other than the discrepancy produced by subdued reflection) are not much influenced.
- c. An increase in the value of the parameter λ defined in Section 3.3, with yield properties unaltered, results in delaying the return of the velocity to zero and significantly increasing the peak velocity and slip displacement. There is not much influence on wave reflection from the lower boundary.

The relative displacement between the two columns at the top, the vertical velocity at the top, and the vertical stress at midheight for the six cases studied are shown in Figures 4-11 through 4-13.

Based on these observations, the following guidelines were adopted to govern the selection of slip model parameters:

- a. To simulate an interface with low frictional resistance, the coefficients Y_{11} and Y_{16} should be chosen very small in addition to taking the slope Y_{12} equal to the estimated coefficient of friction.
- b. To simulate a high friction interface, Y_{11} and Y_{16} should be chosen high. It should be noted that a von Mises limit Y_{16} equal to the shear limit of the weaker of the two materials at the interface signifies perfect bonding. This provides a guideline to choosing an appropriate value for Y_{16} . The slope Y_{12} may be chosen equal to the estimated coefficient of friction, but it is desirable to keep it under 0.3.

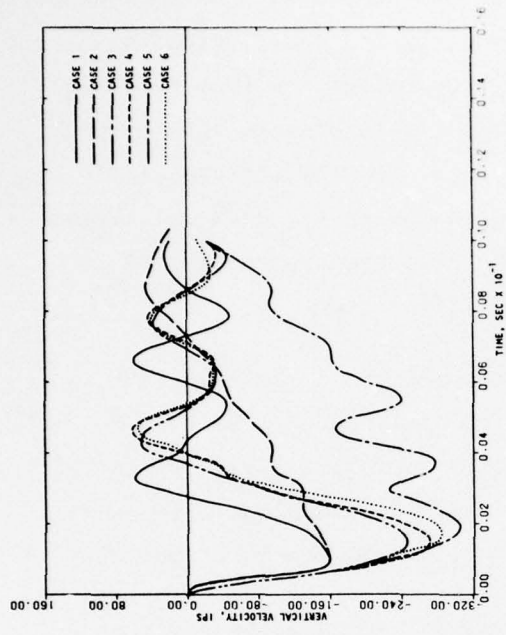


FIGURE 4-11. SLIP (RELATIVE) DISPLACEMENT (TOP SURFACE)

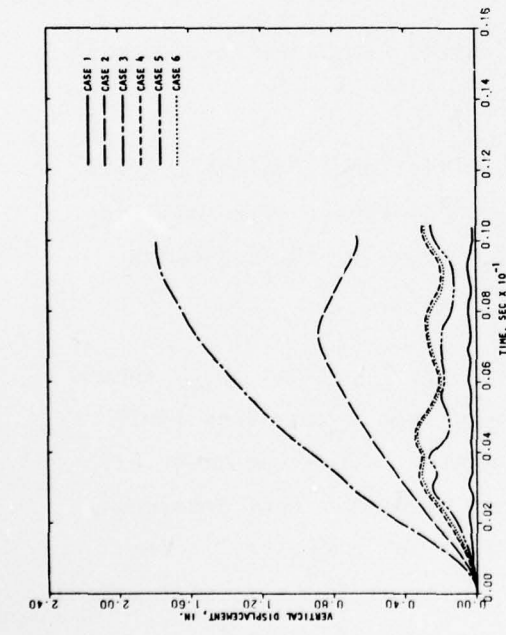


FIGURE 4-12. VERTICAL VELOCITY AT NODE POINT 1 (TOP SURFACE)

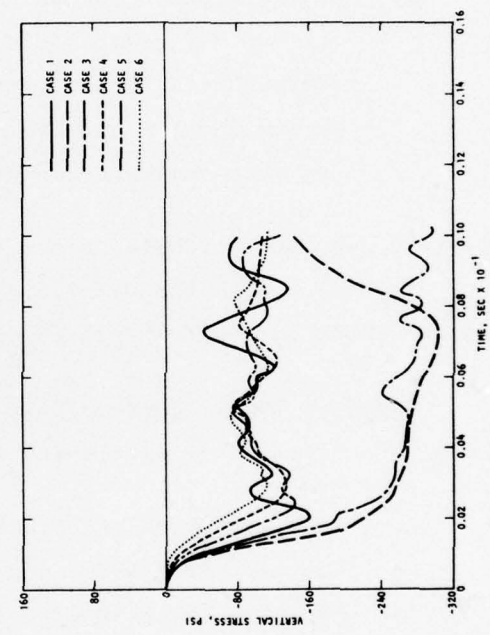


FIGURE 4-13. VERTICAL STRESS IN ELEMENT 3 (MIDHEIGHT)

4.5 FINAL RECALCULATION OF TEST CBMI-10 (CBMI-10-2)

Another calculation of the CBMI-10 test was made introducing the modifications of the slip model suggested by the above study. This calculation is designated as CBMI-10-2 for reference.

8

The following values were chosen for the slip model (these correspond to Case 2 in the parametric study):

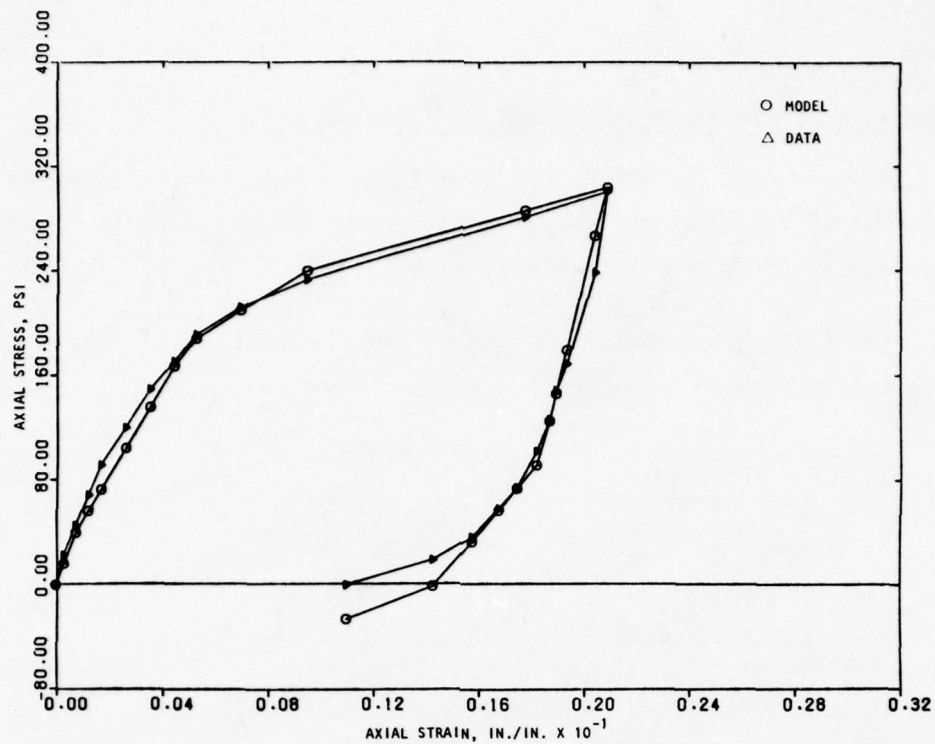
Normal Stiffness	=	50,000 psi
Shear Stiffness	=	2,000 psi
Cohesion Y_{11}	=	0.01 psi
Slope, Y_{12}	=	0.1 psi
von Mises Limit Y_{16}	=	2 psi

In addition, it was also decided to modify the soil model to introduce three bulk moduli instead of one during unloading. The properties of the matrix remained as in Table 4-1 except for the following modifications:

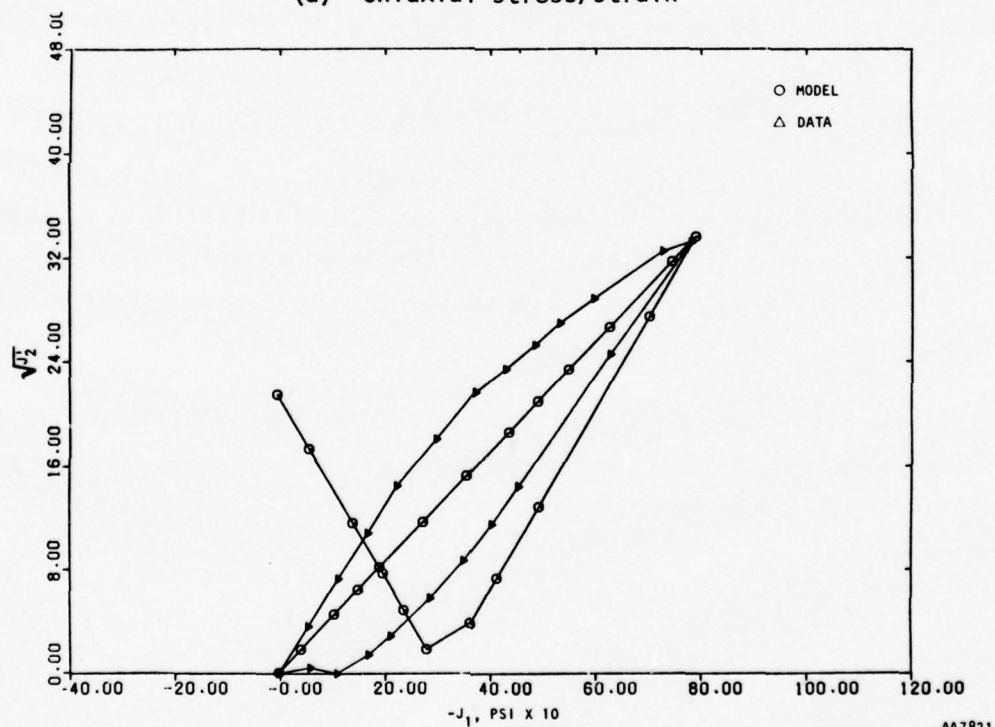
$$B_{11} = 5260.3 \quad B_{12} = 1398.6 \quad B_{16} = 19,240 \quad B_{17} = 6061$$

The resulting match between the model and supplied material data is much improved, as shown in Figure 4-14. One-dimensional calculations made with this improved soil model showed, however, that the response was affected very little by this modification.

The mesh shown in Figure 4-3 was used for the CBMI-10-2 calculations. The input pulse and the integration schedule were also identical with the CBMI-10-1 calculations (Sec. 4.2.3).



(a) Uniaxial stress/strain



AA7821

(b) Uniaxial stress path

FIGURE 4-14. COMPARISON OF MATRIX MATERIAL MODEL FOR CBMI-10-2 CALCULATIONS WITH DATA

4.6 RESULTS OF CBMI-10-2 CALCULATIONS AND DISCUSSION

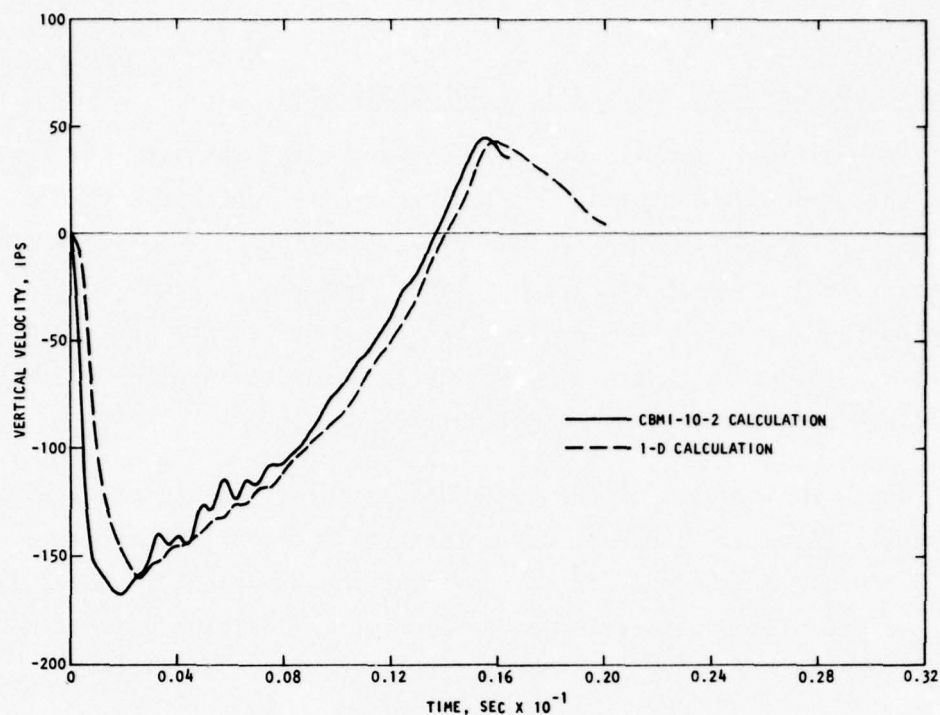
The vertical velocity at the top surface and the vertical stress at midheight obtained in the CBMI-10-2 calculations are compared with the corresponding quantities obtained in the one-dimensional calculation shown in Figure 4-15. It is seen that the two calculations are extremely close, thus showing that the parameters chosen for the slip model in the CBMI-10-2 calculations do indeed simulate a low-friction interface at the SBLG wall and hence lead to a nearly one-dimensional response.

Next, the results of the CBMI-10-2 calculations are compared with the test data. Figures 4-16a, b, and c show the vertical velocities at depths of 18 in., 36 in., and 54 in. It is seen that the agreement is quite close although the calculated velocities have somewhat larger peak values and attain the peak value and return to zero earlier than the test velocities.

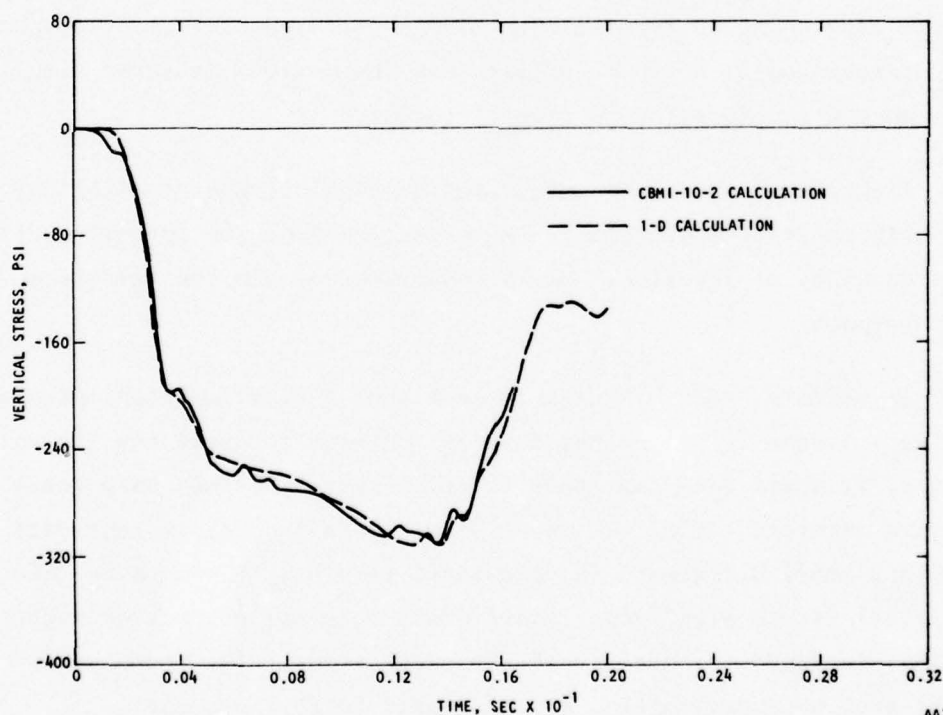
Figure 4-17 compares the calculated displacement at a depth of 18 in. against the corresponding test result. The calculated maximum displacement is about 20% larger and is reached earlier than the maximum measured displacement, in consistency with the velocity time histories.

Figure 4-18 shows the calculated vertical stress at midheight compared with the test measurement. A reflection from the bottom resulting in a near doubling of the stress may be observed in both the calculated and measured stresses.

In summary, these results suggest that a very important parameter in SBLG tests is the friction that develops between the soil and the wall. Furthermore, it would seem that this friction must have been very small. While a more accurate fit of the material model to laboratory test data resulted in a small difference in calculated results, it cannot be inferred that a nominal fit to significantly different material properties might not have further improved the quality of the predictions. This remains an unresolved area of investigation not addressed in this project.



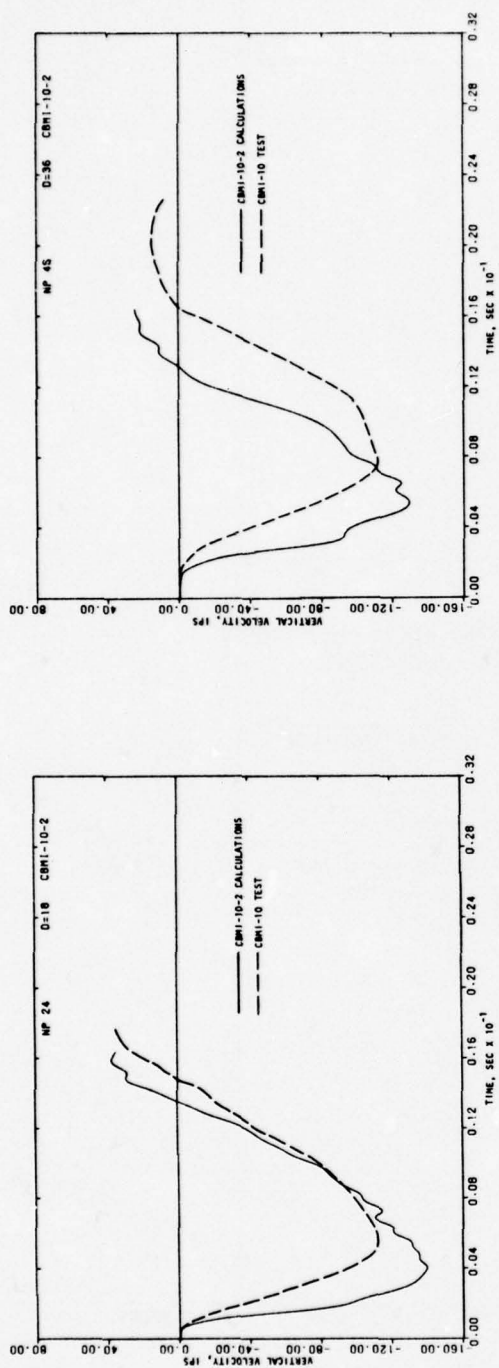
(a) Vertical velocity at surface



(b) Vertical stress at midheight

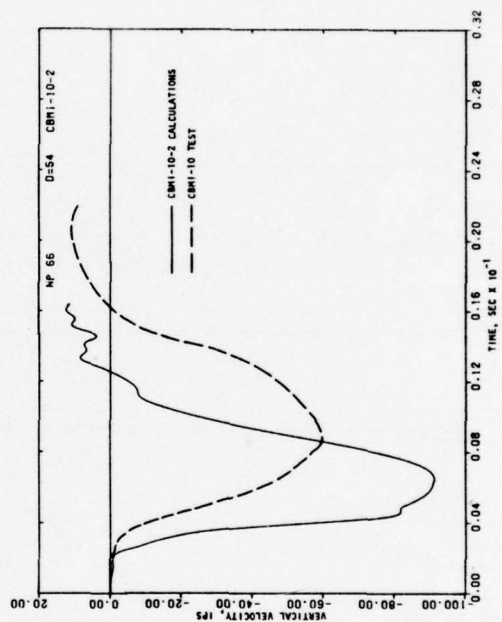
AA7823

FIGURE 4-15. COMPARISON OF CBMI-10-2 AND 1-D CALCULATIONS



(a) Velocity at 18-in. depth

(b) Velocity at 36-in. depth



(c) Velocity at 54-in. depth

FIGURE 4-16. COMPARISON OF VELOCITIES IN CBMI-10-2 CALCULATIONS WITH TEST

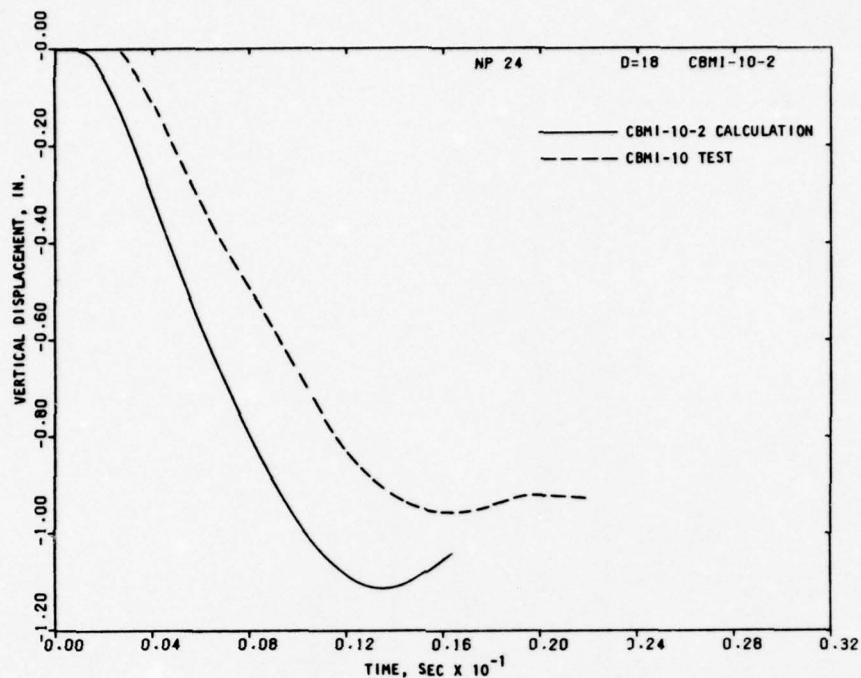


FIGURE 4-17. COMPARISON OF DISPLACEMENT AT 18-IN. DEPTH IN CBMI-10-2 CALCULATIONS WITH TEST

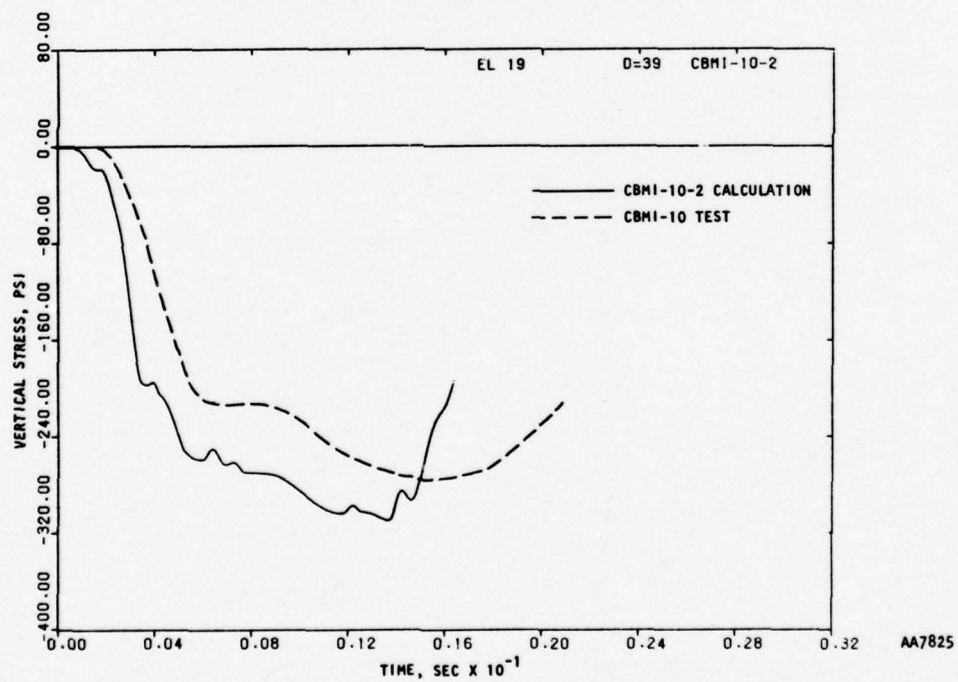


FIGURE 4-18. VERTICAL STRESS AT 36-IN. DEPTH IN CBMI-10-2 CALCULATIONS

SECTION 5

OVERVIEW OF TESTS CBMI-12, -13, AND -14

Tests CBMI-12, 13, and 14 were conducted at WES with three different borehole filler conditions. The tests had many features in common, and therefore, this section gives a general view of all three tests and their calculations. Common ideas underlying the three calculations are discussed and the organization of the sections detailing the calculations is described.

- a. CBMI-12. This test was conducted with a virgin matrix specimen of an artificial soil made with expansive cement and a borehole filler grout whose stiffness was nominally one-half of that of the matrix (Refs. 2 and 3).
- b. CBMI-13. The same specimen that had been subjected to the CBMI-12 test was used for this test. The borehole was cored out and refilled with the same filler grout as in the CBMI-12 test, but an expansive, stiff grout was used in the immediate vicinity of the canisters to lock them in position.
- c. CBMI-14. This test was also conducted on the same matrix specimen as the two above. The borehole in this case was filled with a grout nominally having twice the stiffness of the matrix.

5.1 BRIEF REVIEW OF TEST RESULTS

The vertical velocity time histories measured at 18-in. depth in the three tests are shown in Figure 5-1. Considering just the free-field velocities for the moment, it is observed that in going from CBMI-12 to -14--

- a. The peak value decreases
- b. The velocity returns to zero sooner

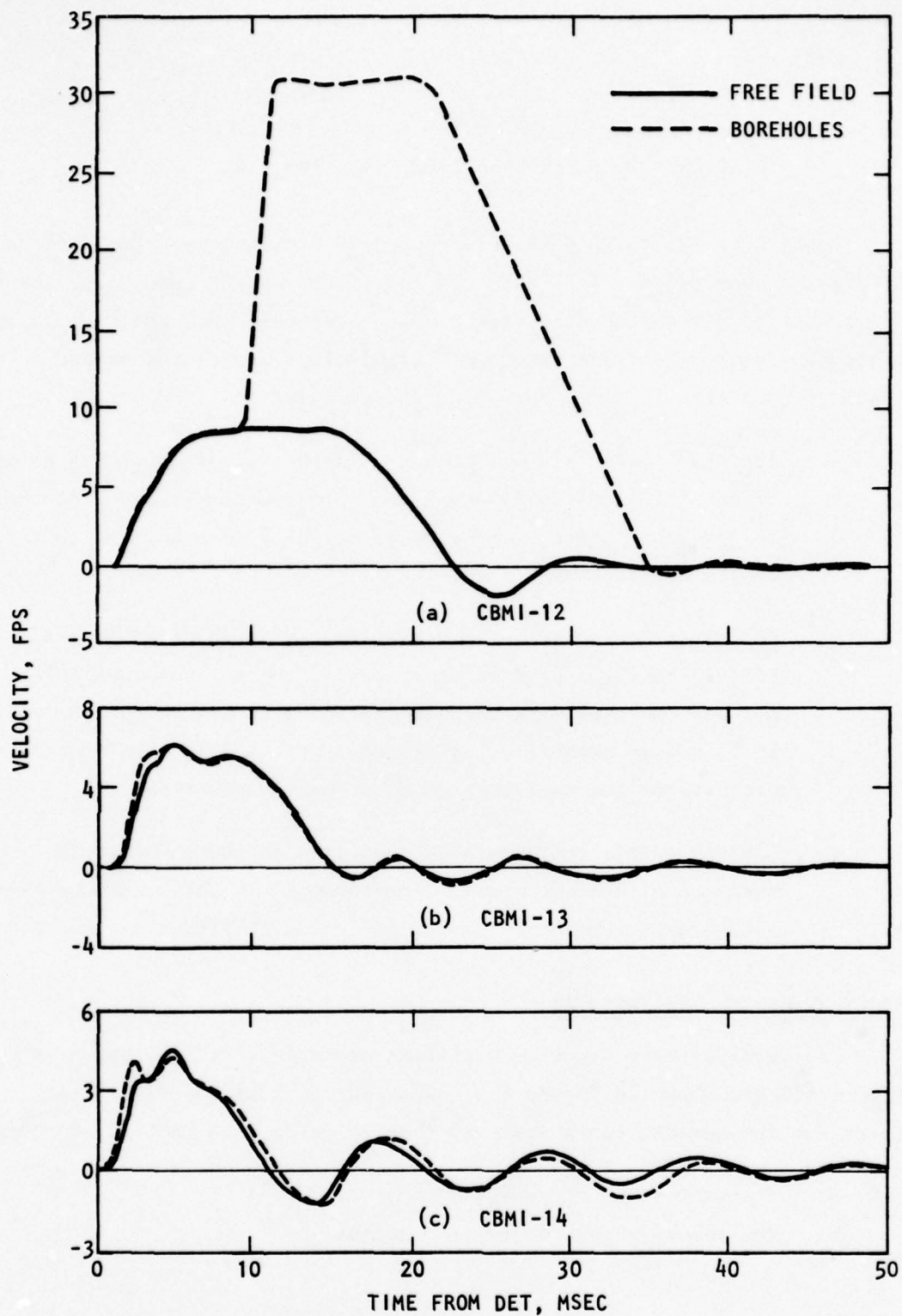


FIGURE 5-1. VELOCITY TIME HISTORIES AT 18-IN. DEPTH MEASURED IN CBMI-12, -13, AND -14 TESTS

These observations may be explained by recalling that the same matrix was used for all three tests. The repeated use of the matrix may be expected to have two effects on the later tests:

- a. The matrix is stiffer because of (1) aging and (2) shock-hardening effect of the earlier tests.
- b. The matrix, being composed of expansive cement, has large radial stresses, possibly resulting in high frictional resistance at the SBLG wall.

Both the above effects would give rise to the features noted in the velocity plots. ~~Neither effect~~ was amenable to direct measurement in the tests, and therefore allowances based on judgment had to be made during the calculations.

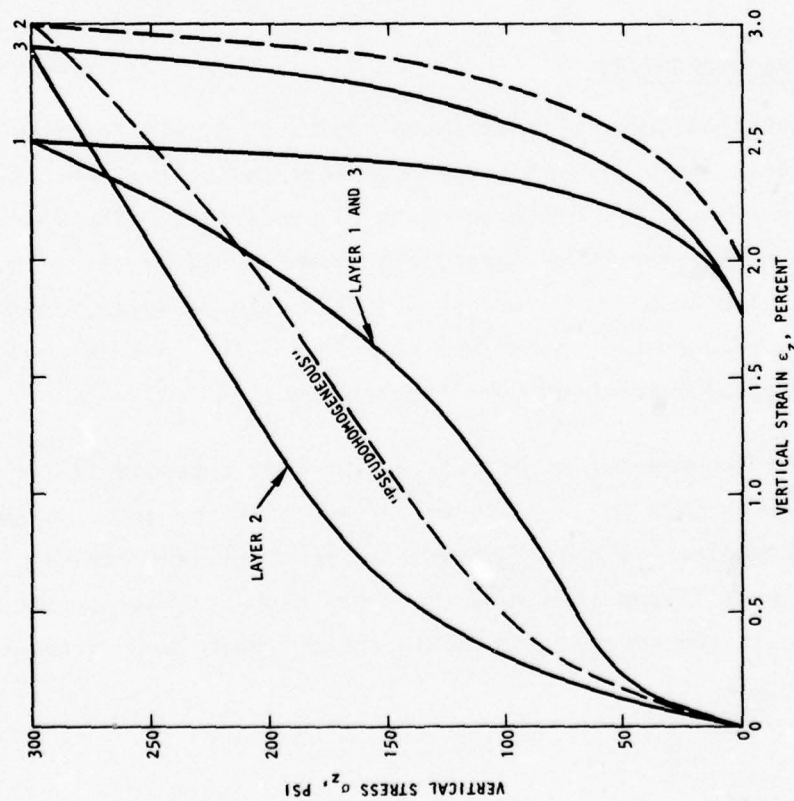
It will be demonstrated that matrix stiffening was probably the only significant result achieved from repeated use of the test specimens.

5.2 MATERIAL PROPERTIES

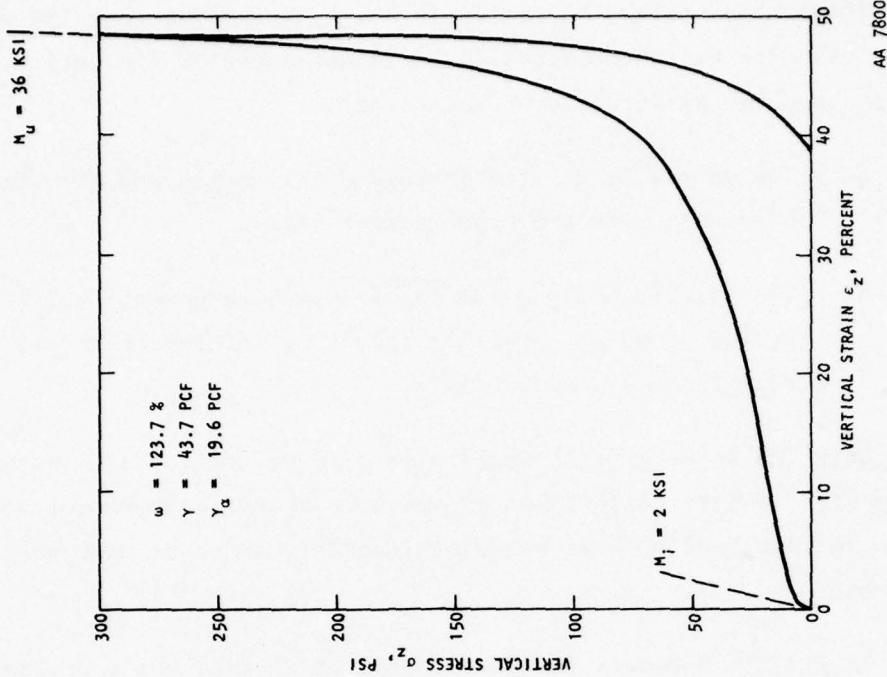
Material property tests were conducted by WES for the matrix used in Test CBMI-12 (Ref. 9). It turned out that the matrix exhibited three distinct layers with two different sets of properties. The material properties recommended by WES for these layers are shown in Figures 5-2a, c, and d. Figure 5-2a also shows an "average" stress/strain relation recommended by WES for use if a homogeneous matrix was planned for the calculation. This curve is labeled "pseudohomogeneous" in Figure 5-2a.

The recommended properties of the soft borehole filler grout are shown in Figures 5-2b and e. It may be seen that the grout is extremely soft at intermediate values of strain and then stiffens rapidly. The uniaxial stress/strain relations also show that very high strains, of the order of 50%, are attained in the stress range of interest. Such large strains raise

CURVE NO.	CURVE IDENTIFICATION	WATER CONTENT, %	DRY DENSITY, PCF	WET DENSITY, PCF	INITIAL CONSTRAINED MODULUS, M_i , KSI	LAYER NO.	DEPTH RANGE, IN.
1	LAYERS 1 AND 3	139.0	35.0	84.0	30	1	0 TO 33
2	AVERAGE	132.0	36.5	85.0	40	2	33 TO 57
3	LAYER 2	125.0	38.0	87.5	56	3	57 TO 72

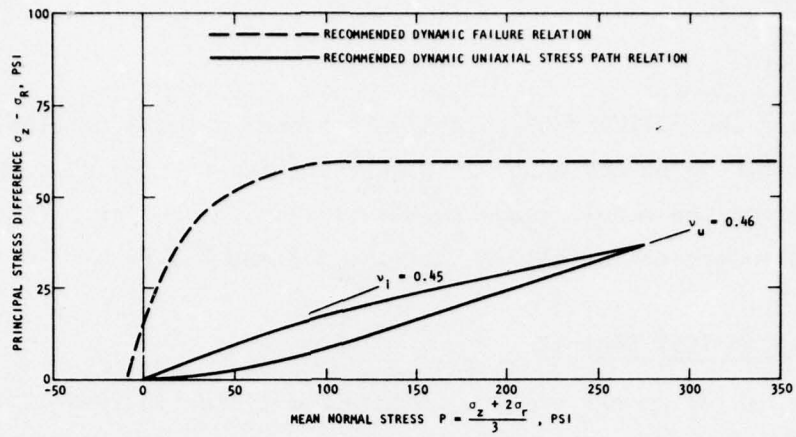


(a) Uniaxial stress/strain relations for CBMI-12 matrix

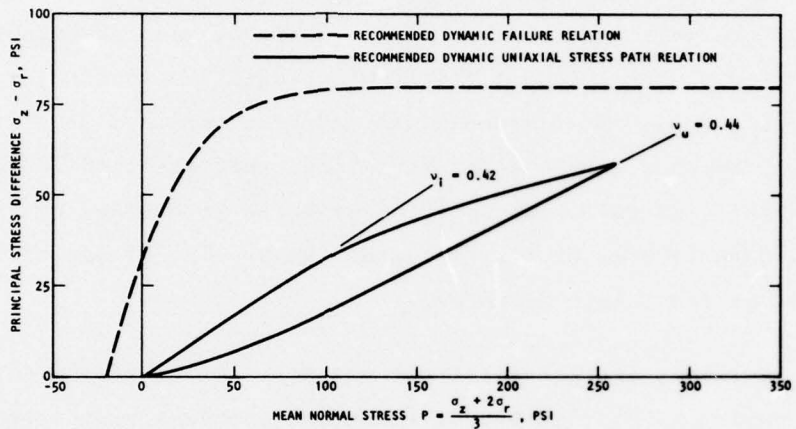


(b) Uniaxial stress/strain relations for CBMI-12 borehole

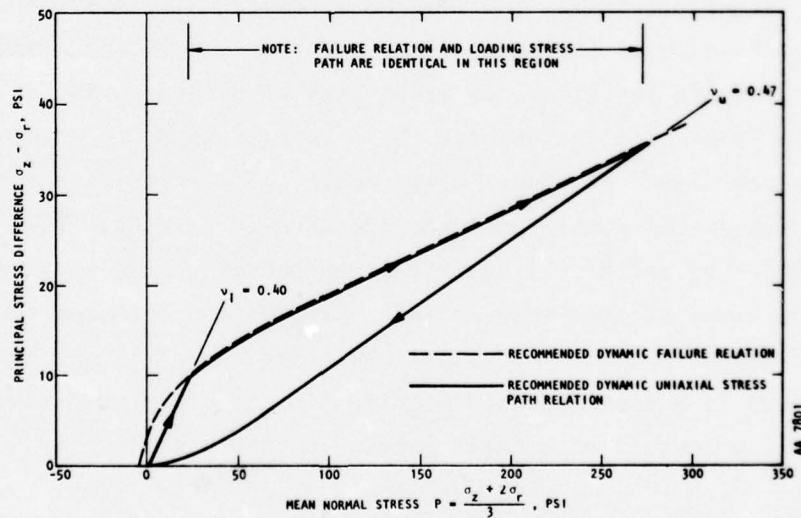
FIGURE 5-2. RECOMMENDED MATERIAL PROPERTIES FOR CBMI-12 MATRIX AND BOREHOLE FILLER



(c) Failure envelope and uniaxial stress path for CBMI-12 layers 1 and 3



(d) Failure envelope and uniaxial stress path for CBMI-12 layer 2



(e) Failure envelope and uniaxial stress path for CBMI-12 borehole filler grout

FIGURE 5-2. (CONCLUDED)

questions about the validity of an analysis based on small strains. The degree of stiffening of the grout at higher strains and the discrepancy between loading and unloading moduli leads to numerical difficulties. These problems are discussed in greater detail in Sections 5.3 and 8.3.2.

5.3 ANOMALIES IN TEST CBMI-12

The use of an extremely soft borehole filler in CBMI-12 led to some difficulties during the test. The neoprene membrane separating the surface of the specimen from the detonation chamber ruptured during the test, allowing explosive gases to vent into the borehole. Postshot measurements showed that the upper portion of the borehole filler grout experienced strains of the order of 50% (Refs. 2 and 3). As a result, the velocity measured at the 18-in. depth in the borehole reached a peak about four times that attained in the free field (Fig. 5-1a). Calculations could be expected to deviate considerably from the test data in view of the fact that the precise effect of the venting of gases would be impossible to model.

In addition, the stress/strain characteristics of the soft borehole grout led to numerical difficulties. These are problems associated with the propagation of waves through finite element meshes of rapidly hardening media. Material models that represent the loading stress/strain behavior with a number of linear segments introduce local oscillations in the element stresses as the element strain passes values associated with corners in the stress/strain curve. These oscillations are the result of updating strains on the basis of previous values of moduli while computing stress increments on the basis of modulus values consistent with the updated strains. This problem can be controlled by artificial damping or by reducing time step and element size, but reductions of time step and element size are accompanied by proportional increases in computing costs, while the use of large, artificial damping may lead to a substantial distortion in the calculated response. This subject is discussed at greater length in Reference 10.

5.4 ORDER OF PERFORMANCE OF CALCULATIONS

One-dimensional calculations made with a column of the soft grout revealed a highly oscillatory response with unrealistically high peak values of stresses and velocities. It was expected that in the main two-dimensional calculation, the relatively large mass of the matrix material would help keep these problems under control. However, in view of the uncertainties associated with interface effects and the anomalous nature of the CBMI-12 test results, it was decided to defer the CBMI-12 calculations to the last and perform the relatively straightforward calculations of CBMI-13 and -14 first. The experience gained from these two calculations would then be used to prepare the input parameters to the CBMI-12 calculations in an optimal manner.

Accordingly, the CBMI-13, -14, and -12 calculations were performed in that order. Several technical decisions relating to interface effects, material properties, integration schedules, and such other matters had to be revised time and again in the light of calculations made up to that point. For this reason, it was felt that the rationale underlying the calculations would be most clearly brought out by describing the calculations in chronological order. Therefore, calculations of Tests CBMI-13, -14, and -12 are described in Section 6, 7, and 8, respectively. Section 5.5 outlines the organization of these sections and some of the notation followed therein.

5.5 ORGANIZATION OF SECTIONS 6 THROUGH 8

Sections 6 through 8 describe the CBMI-13, -14, and -12 calculation in that order. Each section begins by describing the input parameters used in the appropriate calculation. Particular emphasis is placed on discussing the rationale governing the selection of material and interface properties because of their great influence on the calculated response.

The results obtained from each calculation are presented in the form of time history plots, along with similar data obtained from the corresponding test. Velocity and displacement plots at the three gage levels, i.e., depths of 18, 36, and 54 in. are shown overlaid with test data. A two-fold comparison

is made, bringing out (1) the agreement between the motion response at the gage and free-field locations within the calculations themselves and (2) the agreement between the calculated response and the test measurements.

Acceleration time histories are shown from both the calculations and the tests. Acceleration plots generally exhibit considerable high-frequency response. Therefore, these plots are not overlaid, so that details of each time history plot are clearly preserved.

Vertical stresses were monitored during the calculations at depths of 0, 18, 36, 54, and 72 in. at both the gage and free-field locations. In the test, stress gages were set up in the free field only at the last four of the above depths. Not all of the gages remained functional through the duration of the three tests. The available data from these gages are compared with the corresponding calculated free-field stresses. Calculated stresses at the gage and free-field locations are compared as a prelude to developing recommendations for stress gage placement, which are indicated to be drastically different from those for velocity gages.

The axisymmetrical formulation of the problem makes use of a radial R-axis pointing toward the right, and an axial Z-axis pointing upward. Thus, a displacement, velocity, or acceleration component is considered positive when pointing toward the right or upward. Normal stresses and strains are considered positive when tensile. However, in the test data from WES and in the material property plots, compressive stresses are considered positive. Similarly, the WES motion plots show downward displacement, velocity, and acceleration as positive. The common factors indicated along the axes of the plots are to be multiplied by the values obtained from the scales to obtain final amplitudes; (e.g., on Fig. 6-19a the ordinate common factor = 10; therefore, each scale division = $20 \times 10 = 200$ ips. The abscissa common factor = 10^{-1} ; therefore, each scale division = $0.04 \times 10^{-1} = 0.004$ sec).

SECTION 6

CALCULATION OF TEST CBMI-13

The CBMI-13 test, as described briefly in Section 5, involved the matrix that had previously been used for the CBMI-12 Test along with the same soft borehole filler material as in CBMI-12. In contrast to the CBMI-12 test, the canisters were embedded in a hard, expansive grout with a view to binding them to the surrounding matrix material. Also, in order to prevent a rupture of the neoprene membrane at the bottom of the detonation chamber as in CBMI-12, a 2-in. deep layer of the matrix material was used at the top of the borehole.

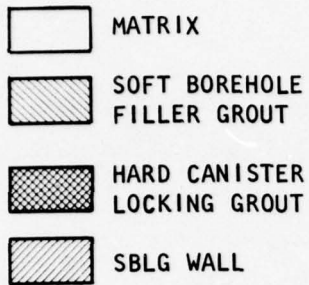
6.1 FINITE-ELEMENT MESH

The finite-element mesh used for the CBMI-13 calculation is shown in Figure 6-1. This mesh is somewhat less uniform than the one used for the CBMI-10-1 calculations (Fig. 4-3) in order to account for the locking grout around each canister and the top layer of matrix material. Slip interfaces are introduced at the SBLG/matrix and matrix/borehole interfaces. As in the CBMI-10-1 calculations, the axis of symmetry and the bottom edge of the mesh were rollered, a downward pressure-time history was applied to the top edge of the mesh over the matrix, and an equilibrating upward load was applied to the SBLG wall. The outer edge of the SBLG wall was left free.

6.2 MATERIAL MODELS

This subsection describes the material properties recommended by WES on the basis of laboratory tests and the models constructed therefrom for use in the calculations.

LEGEND



SLIP INTERFACE

SLIP INTERFACE

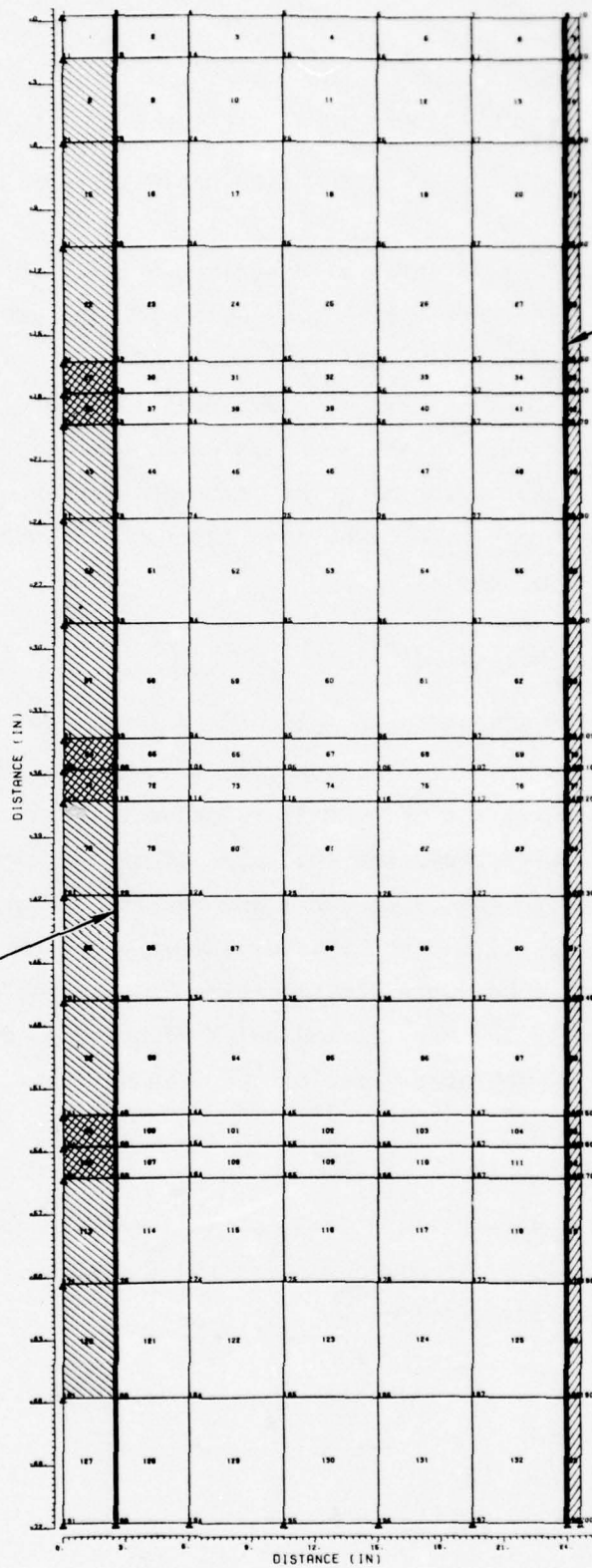


FIGURE 6-1. FINITE ELEMENT MESH FOR CBMI-13 CALCULATIONS

6.2.1 MATRIX

10 As noted in Section 5, the specimen for Test CBMI-13 was believed to have stiffened through aging and shock hardening from the CBMI-12 test and to perhaps have developed significant radial stresses because of the use of expansive cement. There was no way of estimating the residual stresses and attempts by WES to perform material property tests on the matrix led to highly questionable results on account of stress relief in the test specimens (Ref. 9). Therefore, WES recommended probable upper- and lower-bound uniaxial stress/strain relations and a failure envelope with the suggestion that it might be modified within $\pm 15\%$ in shear if shear failure was considered important (Ref. 9). These recommended properties are shown in Figure 6-2.

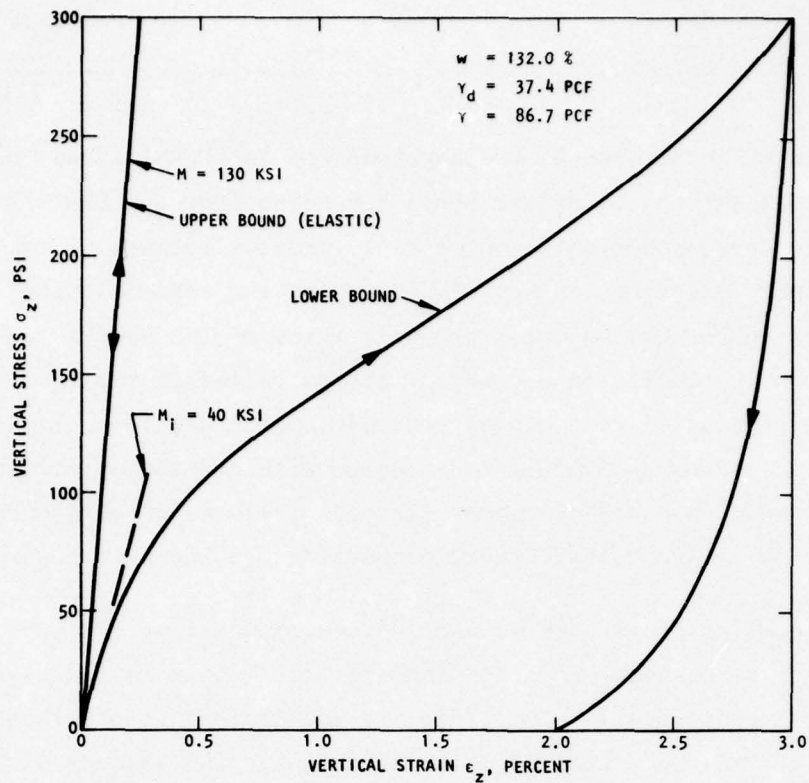
In choosing properties to use in the calculations, it was observed that the properties of Layer 2 in the CBMI-12 test (shown in Fig. 5-2) lay within the above constraints. Therefore, it was decided to use these properties for the matrix in the CBMI-13 calculations. In the absence of specific information regarding layering, it was also decided to use a homogeneous, rather than a layered configuration for the matrix. The material model for the matrix is compared against data in Figure 6-3, and the parameters of the model (see Sec. 3.2) are shown in Table 6-1.

6.2.2 BOREHOLE FILLER GROUT

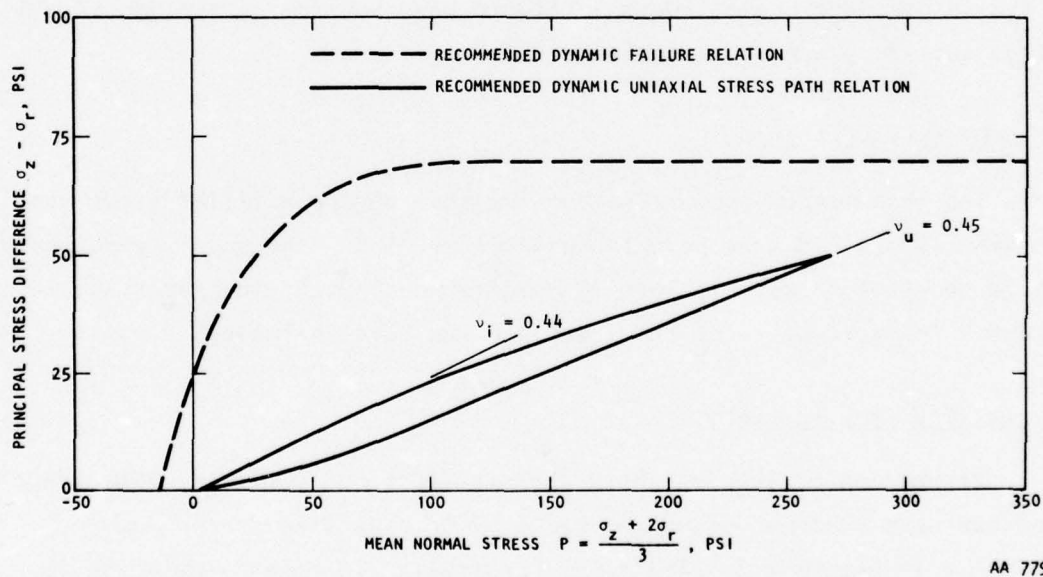
The recommended properties for the soft borehole filler grout used in both CBMI-12 and -13 have been shown in Figure 5-2. The model constructed for use in the CBMI-13 calculations is compared against these properties in Figure 6-4. The parameters of the model are included in Table 6-1.

6.2.3 CANISTER LOCKING GROUT

Properties of the very hard canister locking grout were not directly measured but were recommended on the basis of some earlier tests (Ref. 9) and are shown in Figure 6-5. The model constructed for the calculation is compared against these data in Figure 6-6 and the parameters of the model are included in Table 6-1.

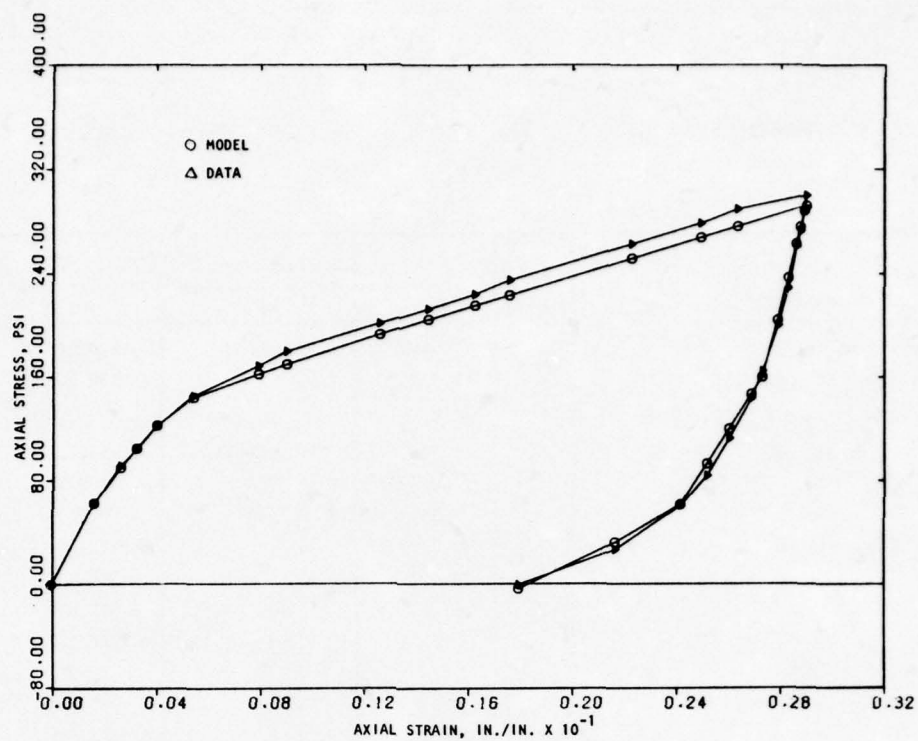


(a) Recommended upper and lower bound uniaxial stress/strain relations

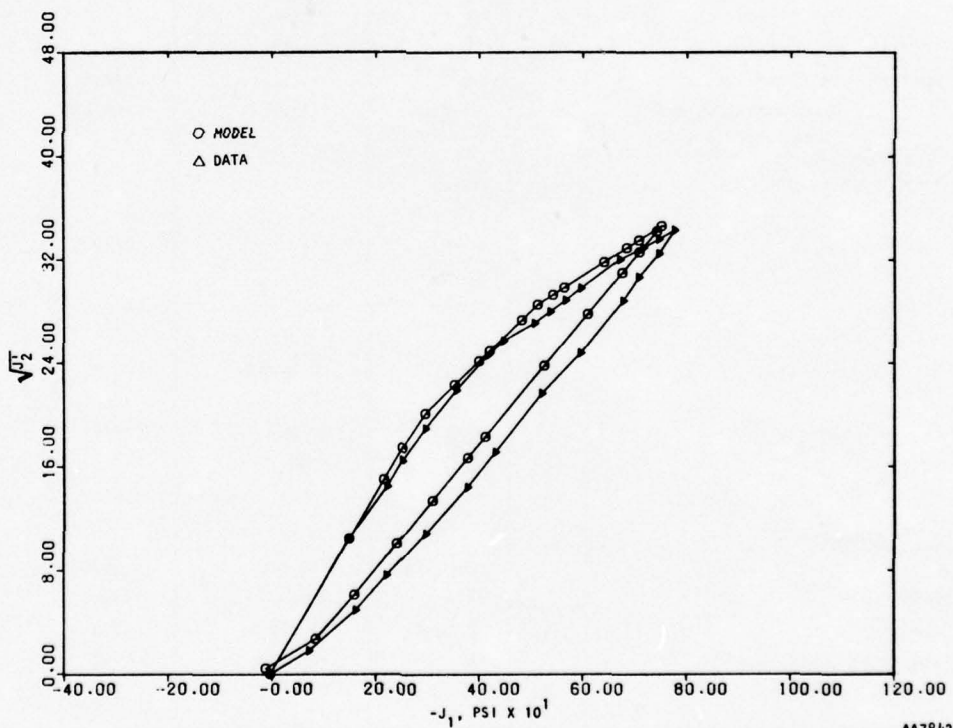


(b) Recommended average dynamic failure and uniaxial stress path relations

FIGURE 6-2. RECOMMENDED PROPERTIES FOR FREE-FIELD MATRIX FOR TEST CBMI-13



(a) Uniaxial stress/strain



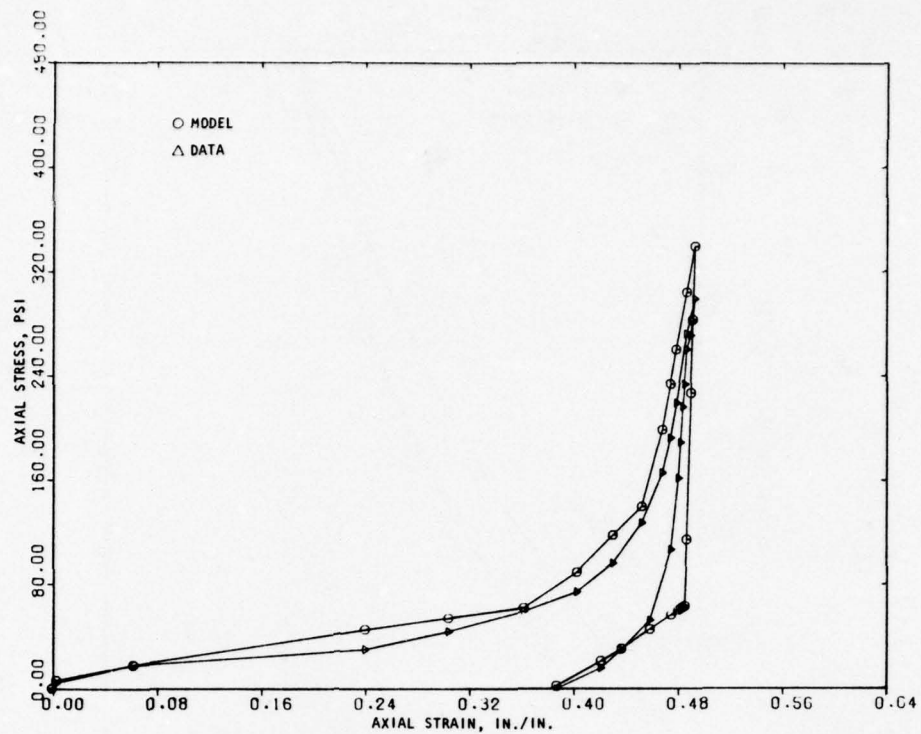
(b) Uniaxial stress path

FIGURE 6-3. MODEL OF MATRIX FOR CBMI-13 CALCULATIONS COMPARED WITH DATA

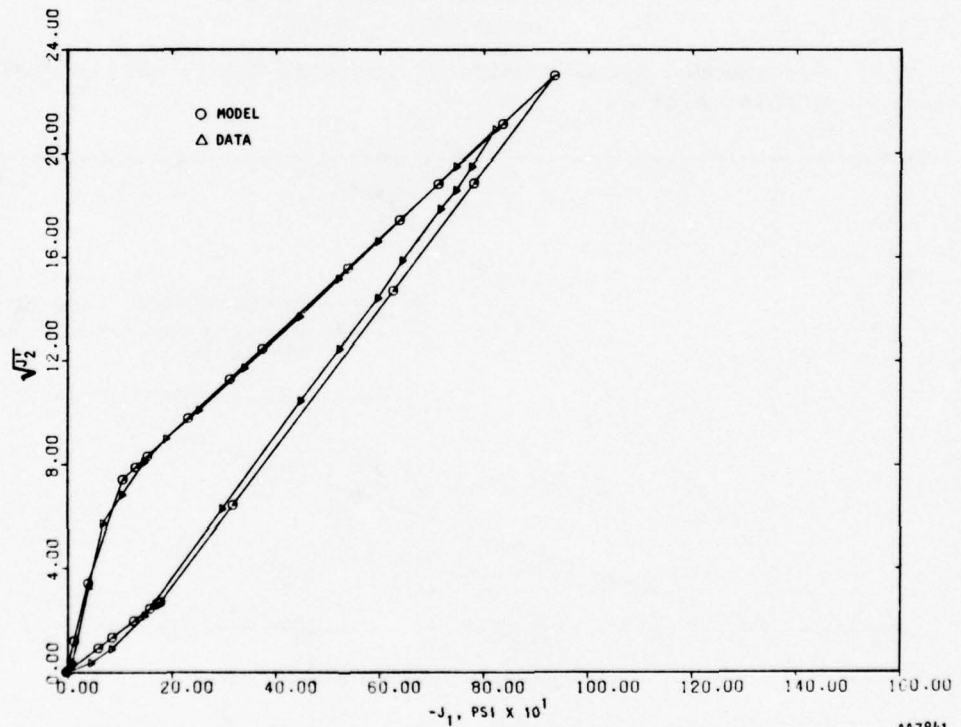
TABLE 6-1. PARAMETERS OF MATERIAL MODELS USED IN CBMI-13 CALCULATIONS

Quantity and Units	Symbol	Matrix	Material	
			Borehole Filler Grout	Canister Locking Grout
Mass density, lb-sec ² /in. ⁴	ρ	0.00013105	0.00006545	0.00018676
Unit weight, pcf	γ	87.5	43.7	124.7
<u>Bulk Modulus: Loading</u>				
Strain break points, in./in.	B ₁	-0.001875	-0.0046875	-0.00016
	B ₂	-0.004843	-0.3781	-0.00024
	B ₃	-0.009844	-0.4594	-0.0003
	B ₄	30,982	1,552	424,632
Load moduli, psi	B ₅	19,107	124	566,177
	B ₆	6,284	905	808,824
	B ₇	5,477	5,022	924,370
	B ₇	5,477	5,022	924,370
<u>Unload/reload:</u>				
Control line slopes, psi	B ₁₁	5,036	122.8	388,235
	B ₁₂	2,000	59.45	323,529
Unload moduli, psi	B ₈	71,143	32,945	2,588,235
	B ₁₆	25,905	644	650,756
	B ₁₇	8,512	528	432,373
	B ₁₀	3,500	1,000	400,000
Tension: Bulk modulus, psi	B ₁₀	3,500	1,000	400,000
Shear modulus, psi	G ₁₀	300	100	163,634
<u>Poisson's Ratio: Loading</u>				
Break points, psi	G ₆	-94	--	--
	G ₇	-173	--	--
Load Poisson's ratio	G ₁	0.416	0.4	0.32
	G ₁₁	0.453	--	--
	G ₁₂	0.458	--	--
<u>Unload/reload:</u>				
Control line slopes, dimensionless	G ₈	-0.03	-0.014838	--
	G ₉	--	--	--
Unload Poisson's ratio	G ₂	0.44	0.466	0.32
	G ₁₃	0.46	0.48	--
	G ₁₄	--	--	--
<u>Yield Parameters</u>				
Cohesion, psi	Y ₁₀	-162.175	-10,000	-2020
	Y ₁₁	19.4	5.4	145
Slope	Y ₁₂	-0.16402	-0.01875	-0.5
von Mises limit, psi	Y ₁₆	46	185	1155
Tension cutoff, psi	Y ₂₅	61	14	300

AA8191

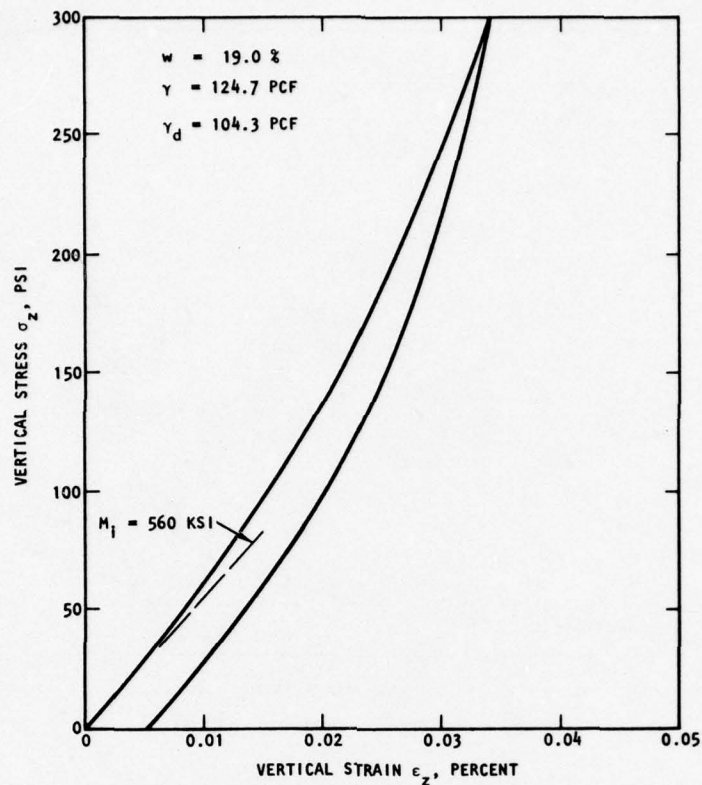


(a) Uniaxial stress/strain

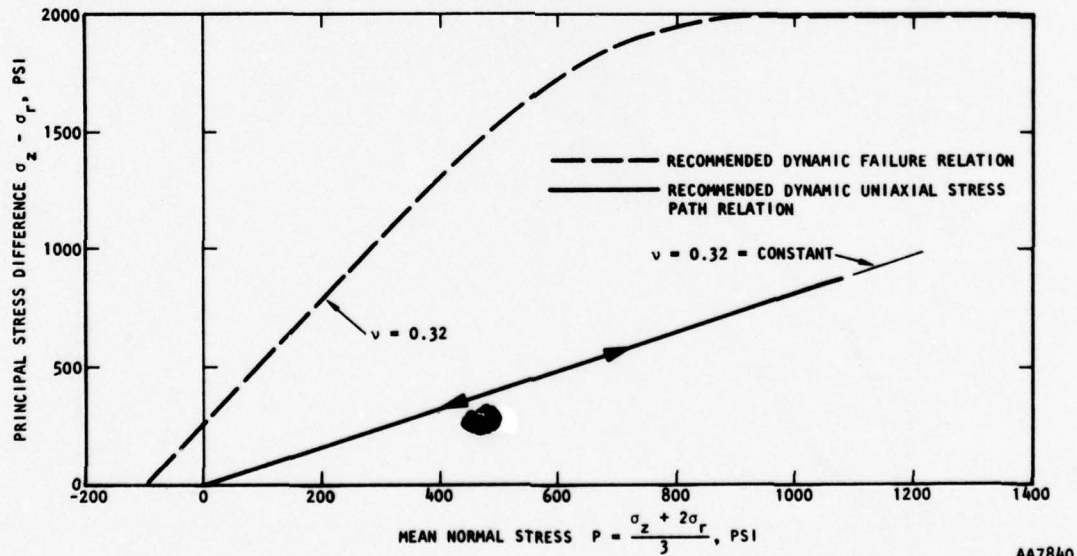


(b) Uniaxial stress path

FIGURE 6-4. MODEL FOR SOFT BOREHOLE FILLER GROUT FOR CBMI-13 CALCULATIONS COMPARED AGAINST DATA

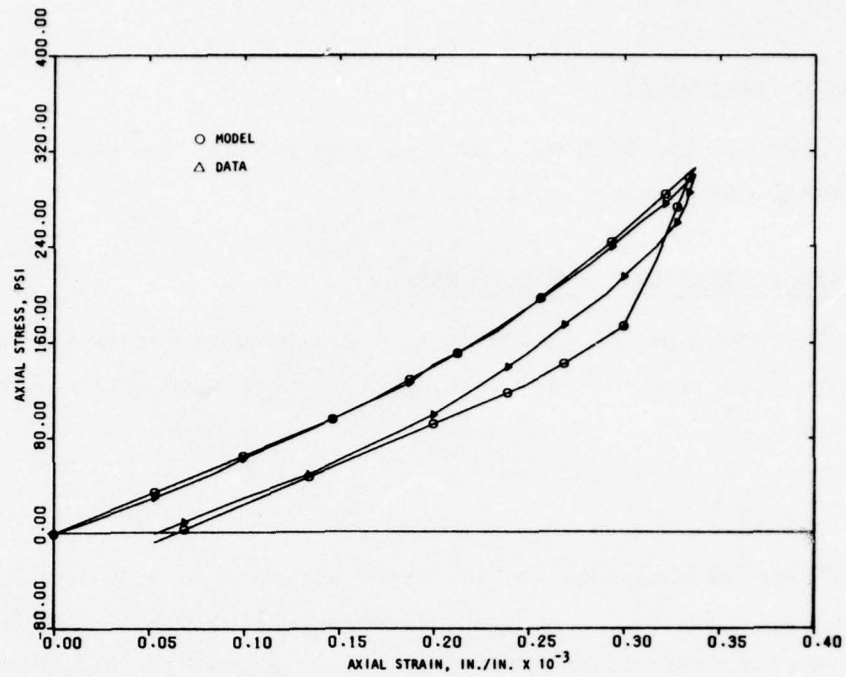


(a) Recommended dynamic uniaxial vertical stress versus vertical strain relation

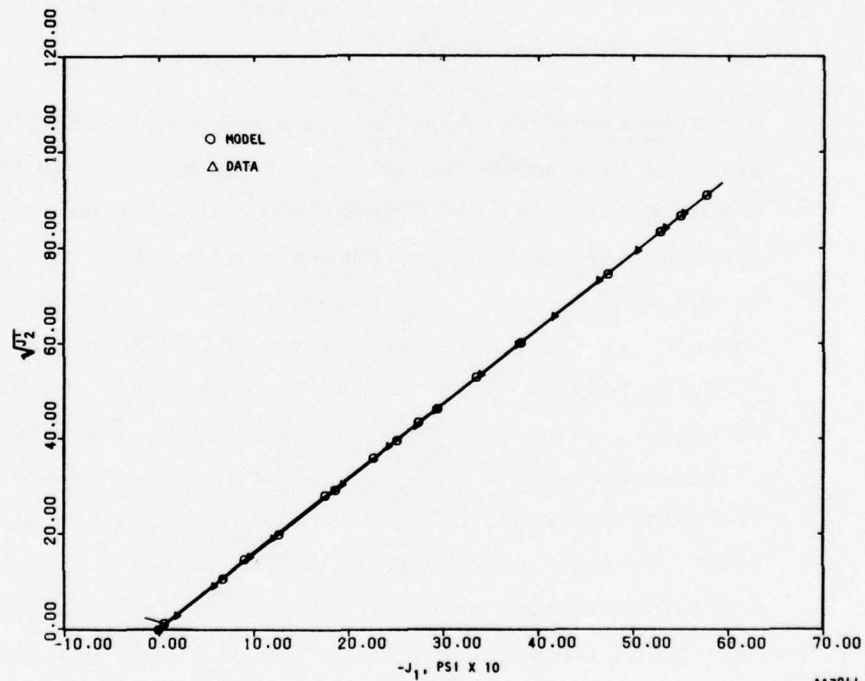


(b) Recommended dynamic failure and uniaxial stress path

FIGURE 6-5. RECOMMENDED MATERIAL PROPERTIES FOR CANISTER LOCKING GROUT, CBMI-13



(a) Uniaxial stress/strain



(b) Uniaxial stress path

FIGURE 6-6. MODEL OF CANISTER LOCKING GROUT USED IN CBMI-13 CALCULATIONS COMPARED WITH DATA

6.2.4 STEEL (SBLG WALL)

Steel in the SBLG wall was assigned exactly the same properties as in the CBMI-10 calculations (Sec. 4.2.2).

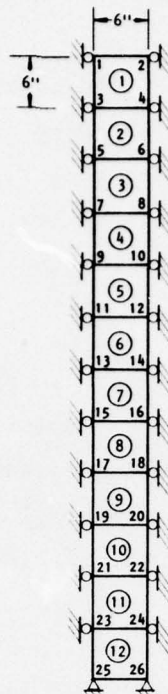
6.3 INTERFACE CONDITIONS AND SLIP MODELS

The selection of the parameters of the slip models used at the various interfaces and the rationale governing their selection are discussed in this subsection.

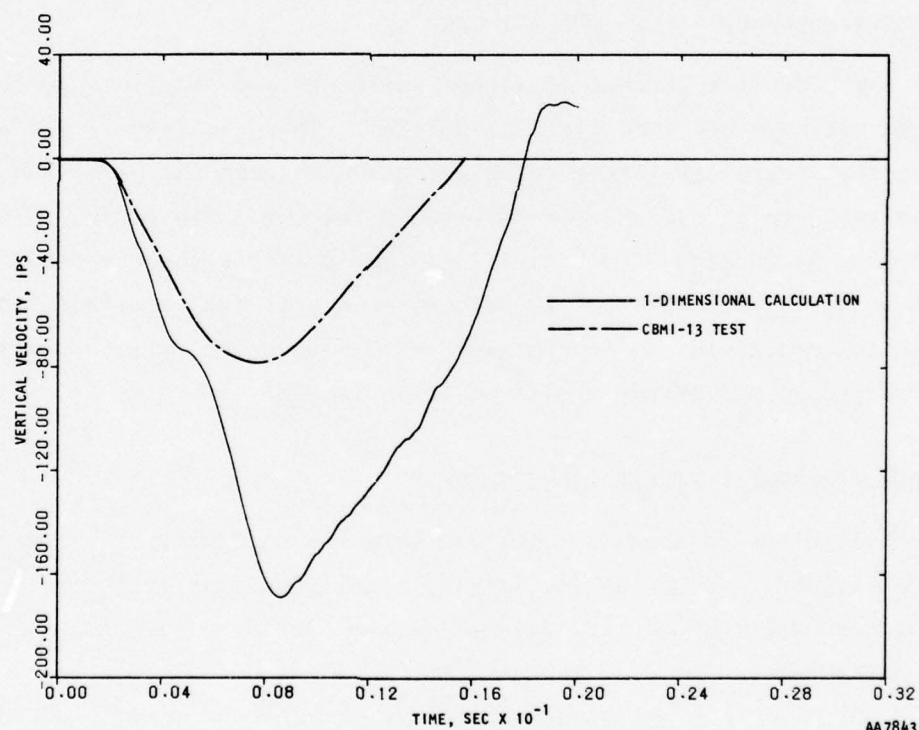
6.3.1 MATRIX/SBLG INTERFACE

There were no data available directly on the frictional effects at the matrix/SBLG interface. However, it was speculated that in contrast to the CBMI-10 test, significant frictional resistance might be present in this test because of the radial stresses believed to be present in the matrix. It was decided to perform some preliminary calculations to help select a suitable slip model for this interface.

- a. One-Dimensional Calculation. A one-dimensional calculation was made on a column of the matrix material using the mesh shown in Figure 6-7a. Figure 6-7b shows the velocity obtained from the calculation at middepth compared with the velocity in the CBMI-13 test. It is seen that the calculated peak velocity is about two times larger and that the calculated velocity returns to zero later than the test. Based on the parametric study conducted earlier on the slip model (Sec. 4.4.2), it was reasonable to expect that both these features could be improved by increasing shear transfer capability at the matrix/SBLG interface. Therefore, the discrepancies between the one-dimensional column calculations and the test results were attributed (incorrectly, as it turned out later) to friction at the SBLG wall.



(a) Finite element mesh used for the calculation



(b) Velocity at midheight compared with test

FIGURE 6-7. ONE-DIMENSIONAL COLUMN RUN ON CBMI-13 MATRIX

- b. Slip Model Parameters. The parameters of the slip model at the matrix/SBLG interface were chosen to represent a moderate amount of shear transfer capability. This was done by assigning to the slip elements a shear limit of about one-third of that of the matrix material (Ref. 11). The parameters chosen are shown in Table 6-2.
- c. Double Column Calculation. In order to assess the dynamic behavior of the above slip model, a calculation was made on a simple double column configuration shown in Figure 6-8a. Two columns of matrix and steel were considered with a slip interface in between, the slip elements being assigned the properties shown in Table 6-2. The columns were taken to be 36 in. deep to economize on computer time. The velocity obtained at middepth is shown in Figure 6-8b.

6.3.2 MATRIX/BOREHOLE FILLER GROUT INTERFACE

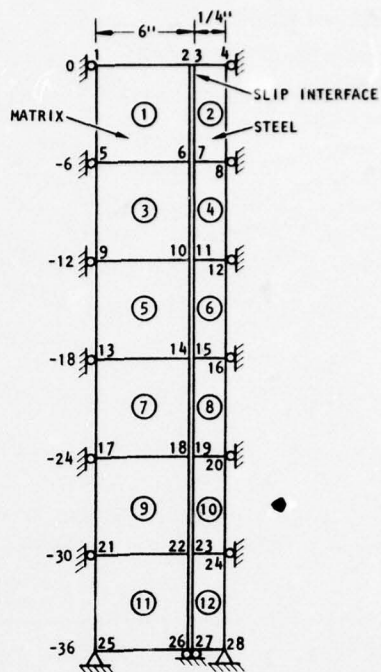
The CBMI-12 test data at larger depths showed excellent agreement between the borehole and free-field velocities. This was interpreted as indicating that there was little relative motion between the grout and the matrix and thus implying perfect bond between the two. Therefore, this slip interface was designed to have its maximum possible shear capability. Since the grout is the weaker of the two materials at the interface, the slip elements were assigned shear properties based on the failure envelope of the grout. The properties are shown in Table 6-2.

6.3.3 MATRIX/BOREHOLE FILLER GROUT INTERFACE

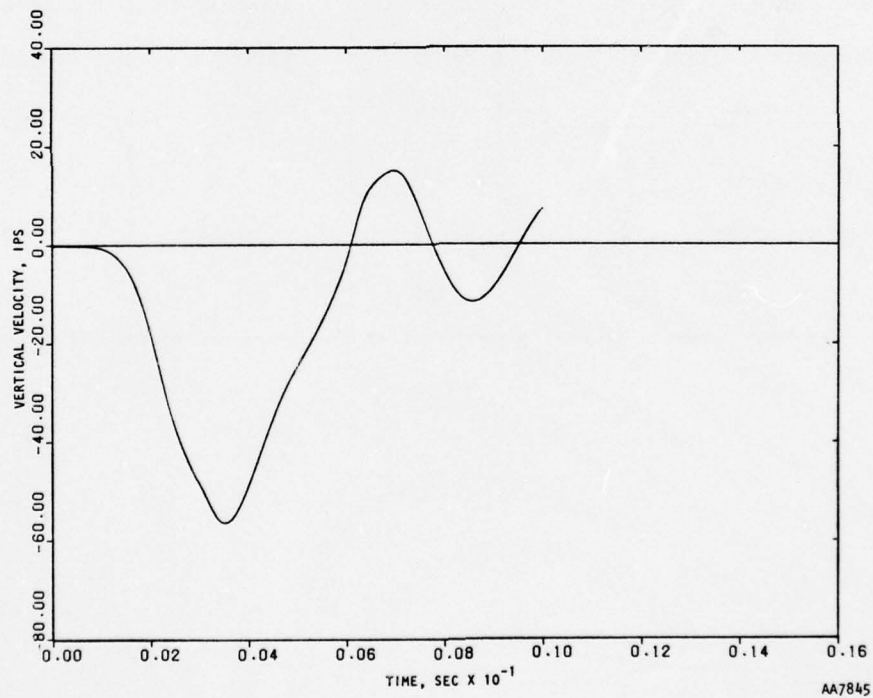
Slip elements at this interface were assigned properties corresponding to the failure envelope of the matrix, signifying a perfect bond and thus simulating the "locking" of the canister to the matrix. The properties are shown in Table 6-2.

TABLE 6-2. SLIP MODEL PARAMETERS AT VARIOUS INTERFACES IN CBMI-13 CALCULATIONS

Slip Model Parameters	Matrix/ SBLG	Matrix/ Borehole Filler Grout	Matrix/ Canister Locking Grout
Normal Stiffness C_o , psi	5000	5000	5000
Shear Stiffness C_T , psi	5000	5000	5000
Y_{10}	128	437	184
Cohesion Y_{11} , psi	18	9.4	33
Coefficient of Friction Y_{12}	0.25	0.093	0.25
Shear Limit Y_{16} , psi	50	50	79



(a) Finite element mesh used in the calculation



(b) Velocity at midheight (Node Point 13)

FIGURE 6-8. DOUBLE COLUMN CALCULATION TO TEST MATRIX/SBLG SLIP

The calculational code required that the slip interface at the edge of the borehole extend all the way from top to bottom. As seen in the mesh used for the calculations (Fig. 6-1), the top and bottom elements of the borehole are composed of the matrix material. The slip elements at the top and bottom, therefore, form an interface between identical materials. These slip elements had to be assigned properties based on the failure envelope of the matrix and thus were identical with the slip elements at the canister locking grout interface.

6.4 INPUT PULSE AND SCHEDULE OF INTEGRATION

The input pulse used in the CBMI-13 calculations is shown in Figure 6-9 along with the schedule of variation of the time step, Δt . The calculations were carried through a real-time duration of 20 msec in a total of 650 time steps. The average computational time was 11.6 sec/step.

6.5 RESULTS OF CBMI-13 CALCULATIONS

Several time histories of motion and stresses obtained from the CBMI-13 test and calculations are presented in this subsection, and the discrepancies between test data and calculations are pointed out.

6.5.1 TEST DATA

The measured data obtained from the CBMI-13 test are shown in Figures 6-10 through 6-13. Motion data include the velocities, displacements, and accelerations at each of the gage locations, i.e., at 18-in., 36-in., and 54-in. depths both in the borehole and the free field. Stresses shown in Figure 6-13 were measured in the free field at depths of 18 in., 54 in., and 72 in.

6.5.2 RESULTS OF CBMI-13 CALCULATIONS

The velocities and displacements obtained from the calculations are compared with the test data in Figures 6-14 through 6-16. Stresses at two depths are compared in Figure 6-17.

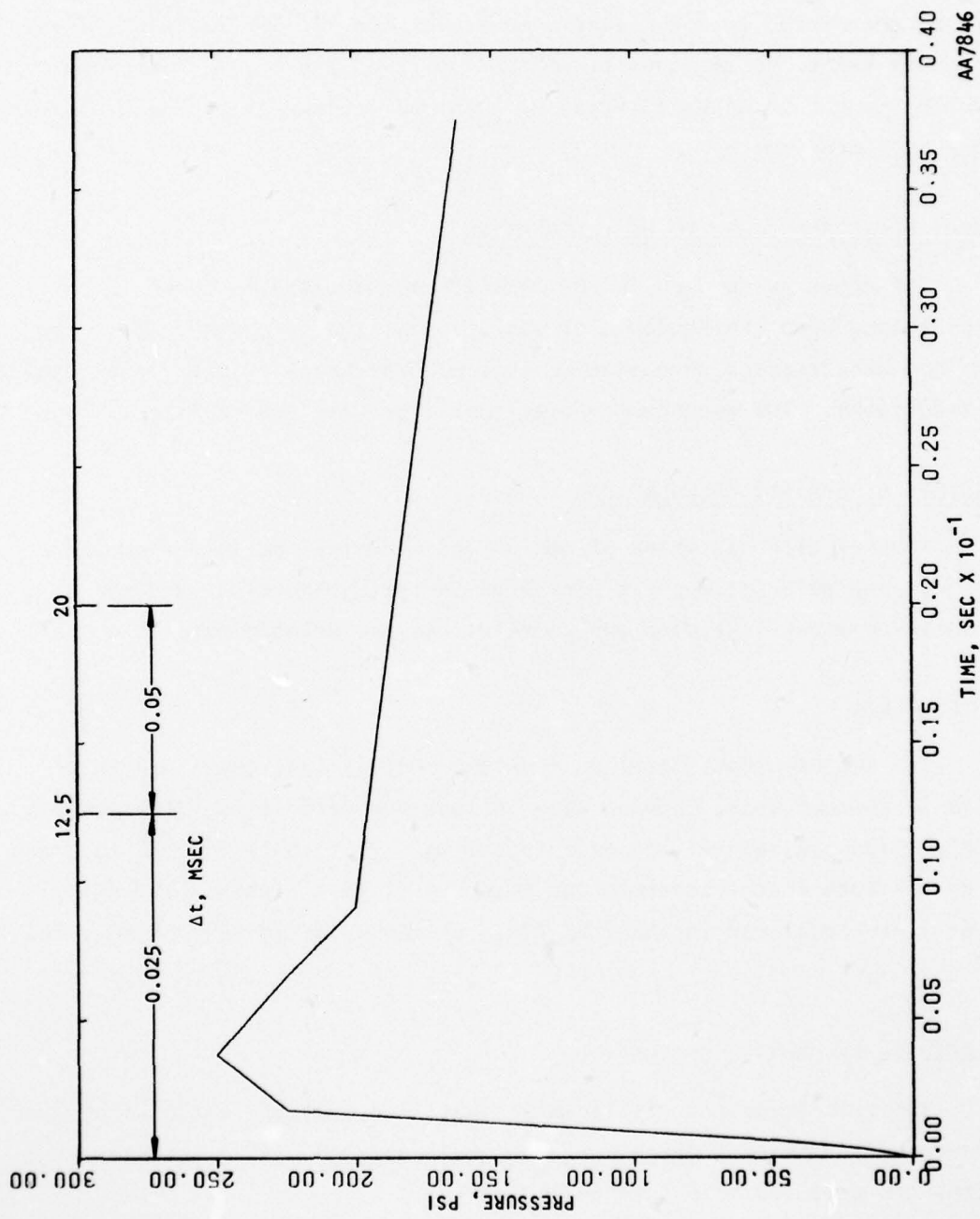


FIGURE 6-9. INPUT PULSE AND SCHEDULE OF INTEGRATION USED IN CBMI-13 CALCULATIONS

AA7846

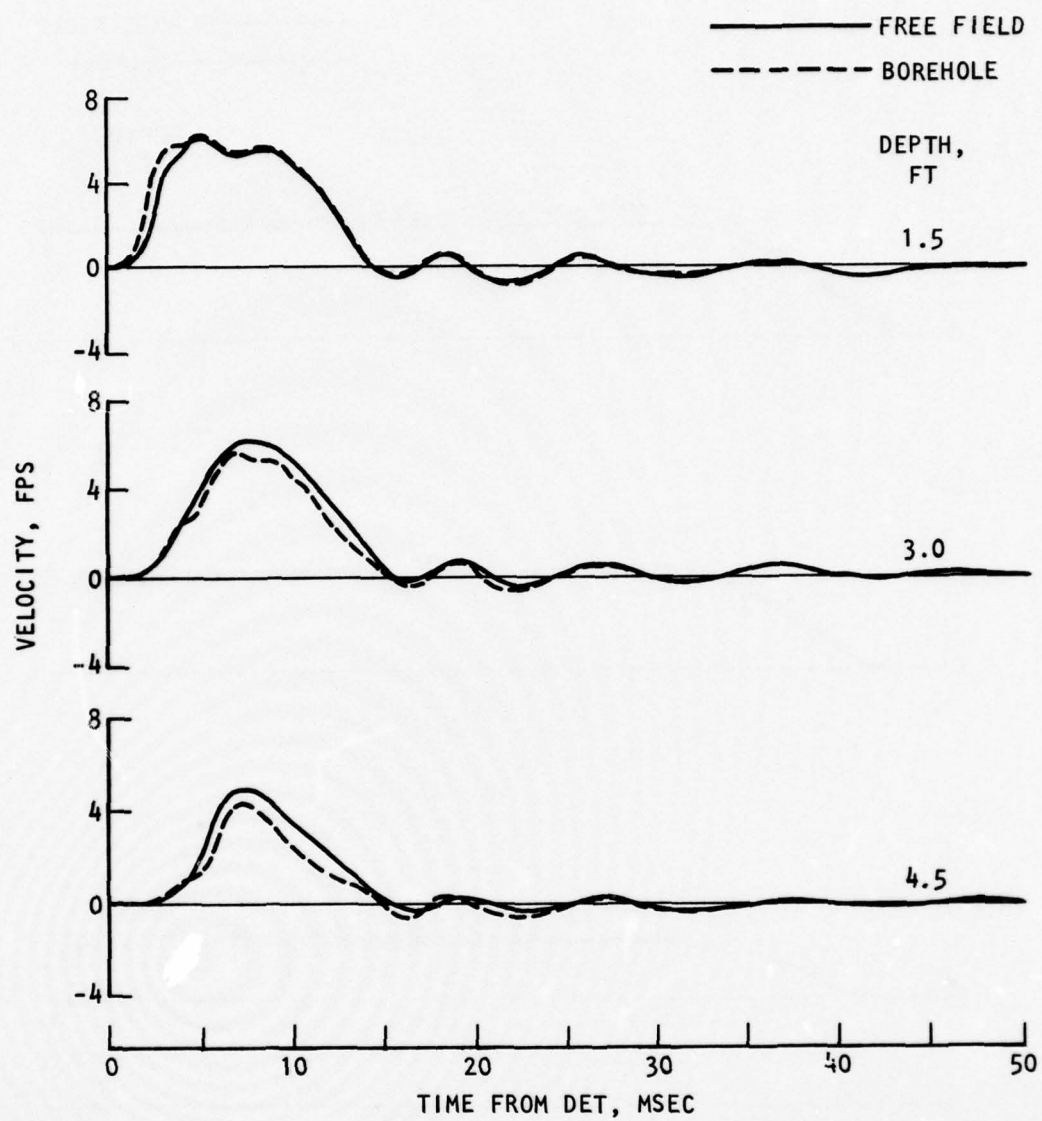


FIGURE 6-10. VELOCITIES MEASURED DURING TEST CBMI-13

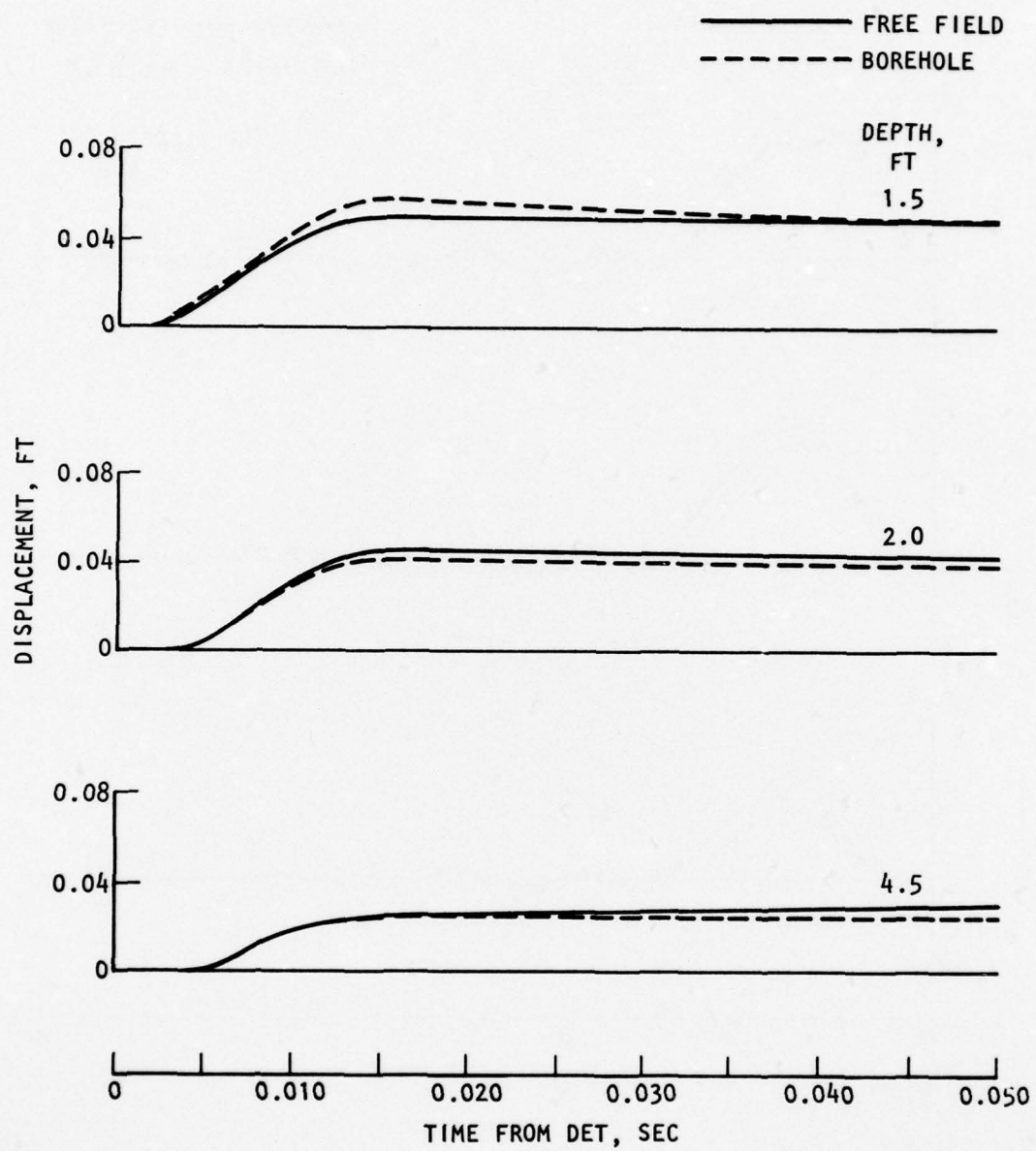


FIGURE 6-11. DISPLACEMENTS IN TEST CBMI-13

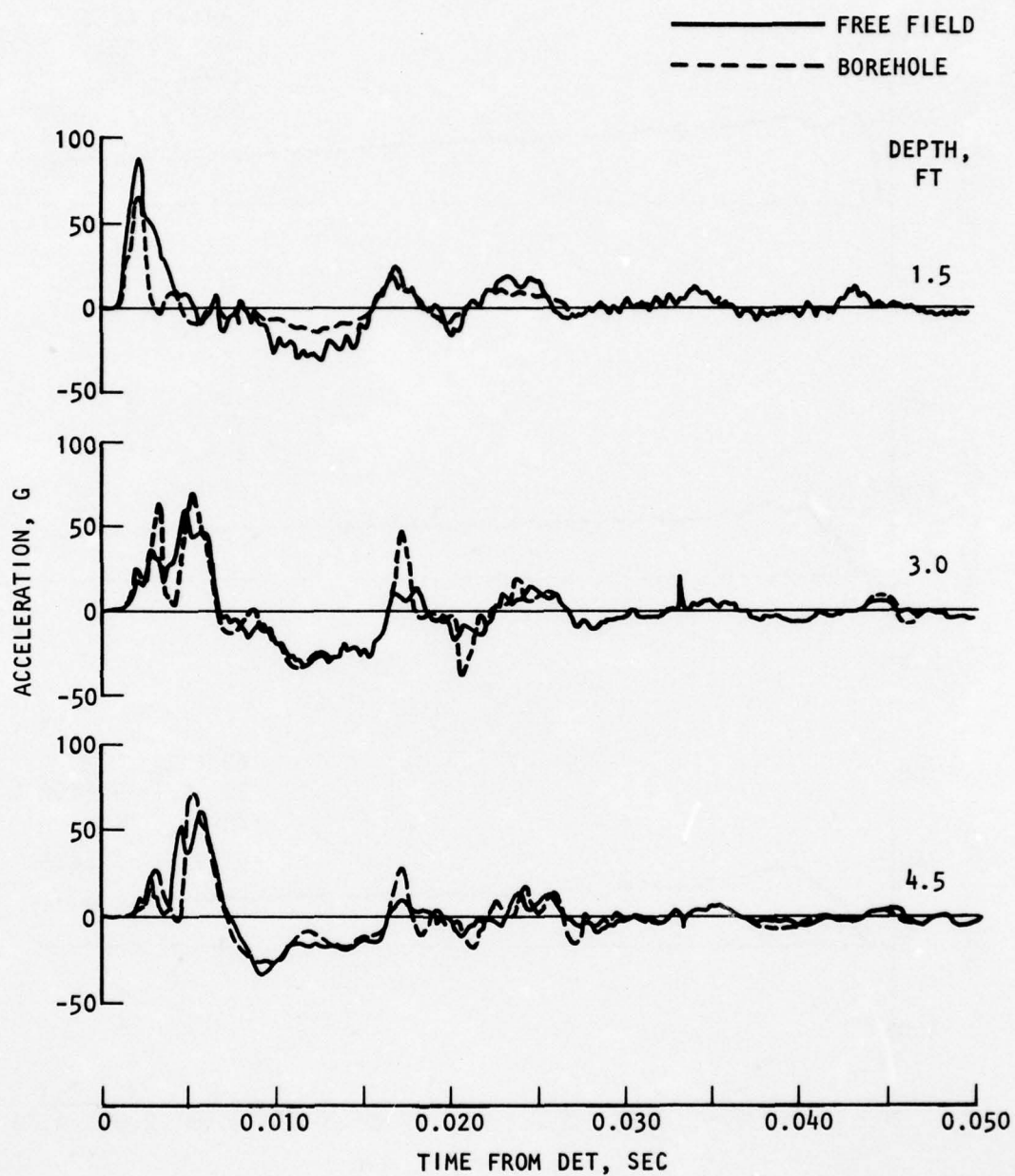


FIGURE 6-12. ACCELERATIONS IN TEST CBMI-13

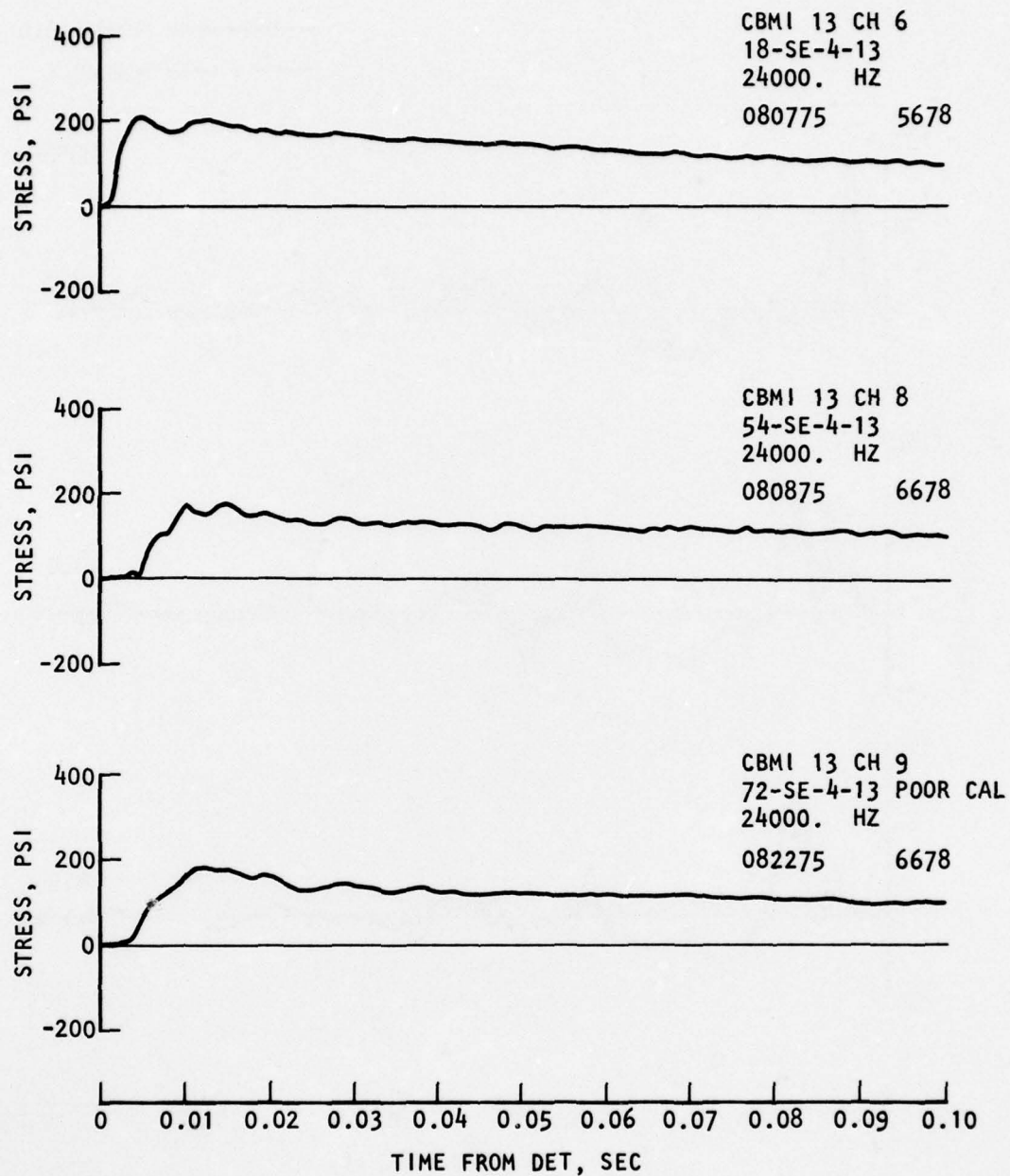


FIGURE 6-13. FREE-FIELD STRESSES IN TEST CBMI-13

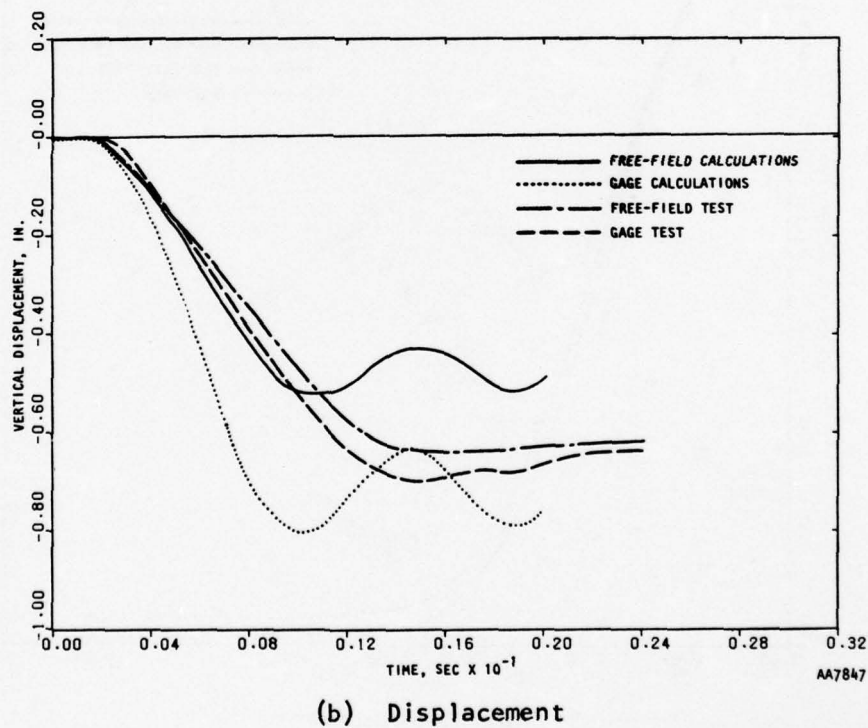
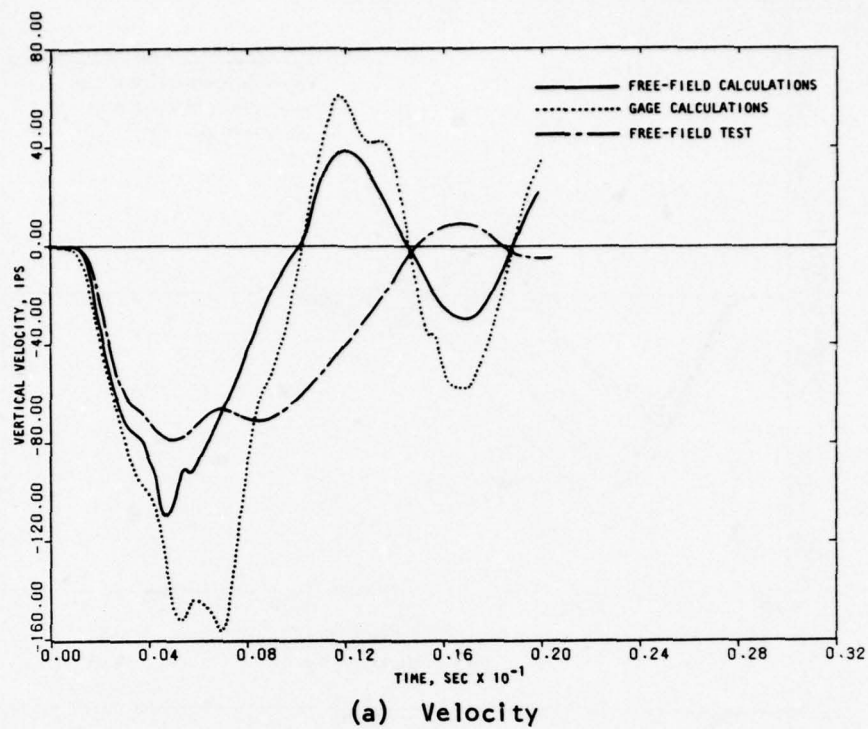
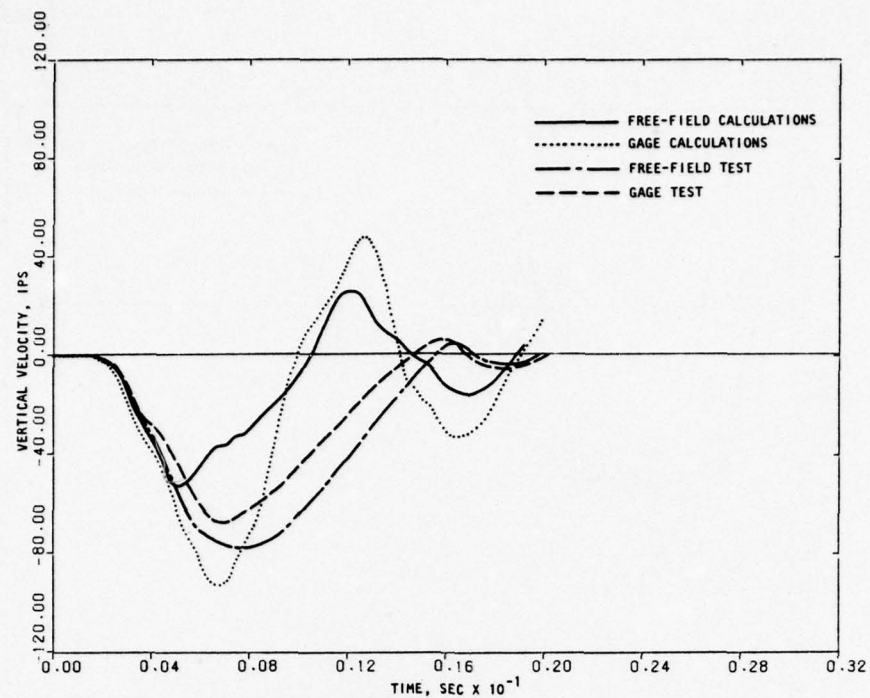
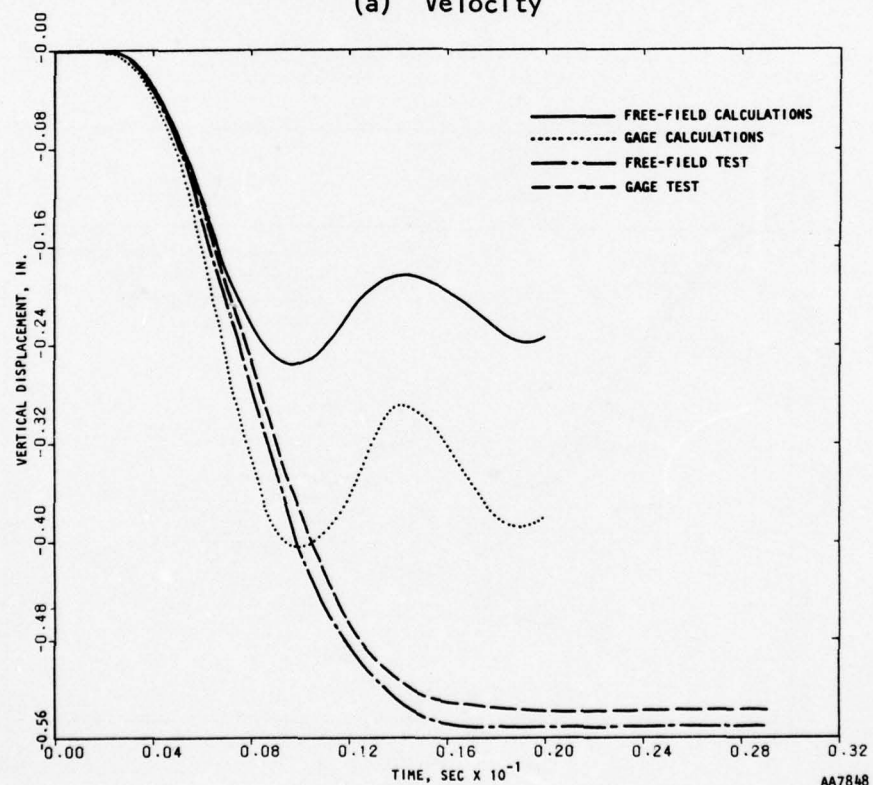


FIGURE 6-14. COMPARISON OF CBMI-13 CALCULATIONS AND TEST AT 18-IN. DEPTH

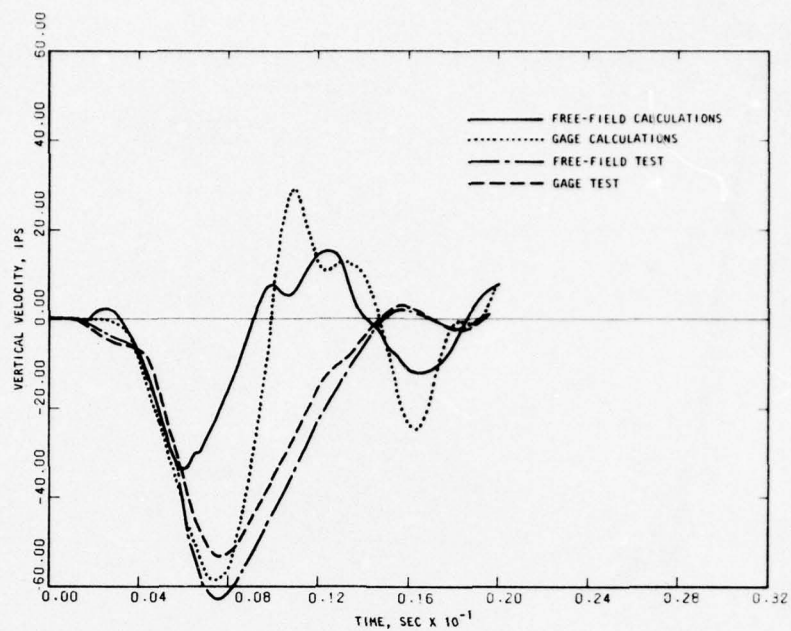


(a) Velocity

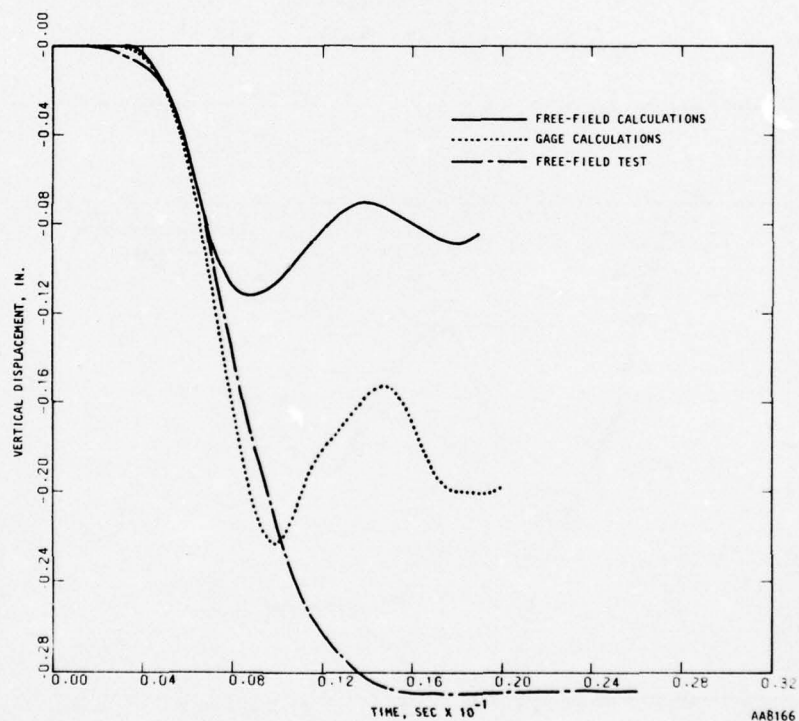


(b) Displacement

FIGURE 6-15. COMPARISON OF CBMI-13 CALCULATION WITH TEST AT 36-IN. DEPTH

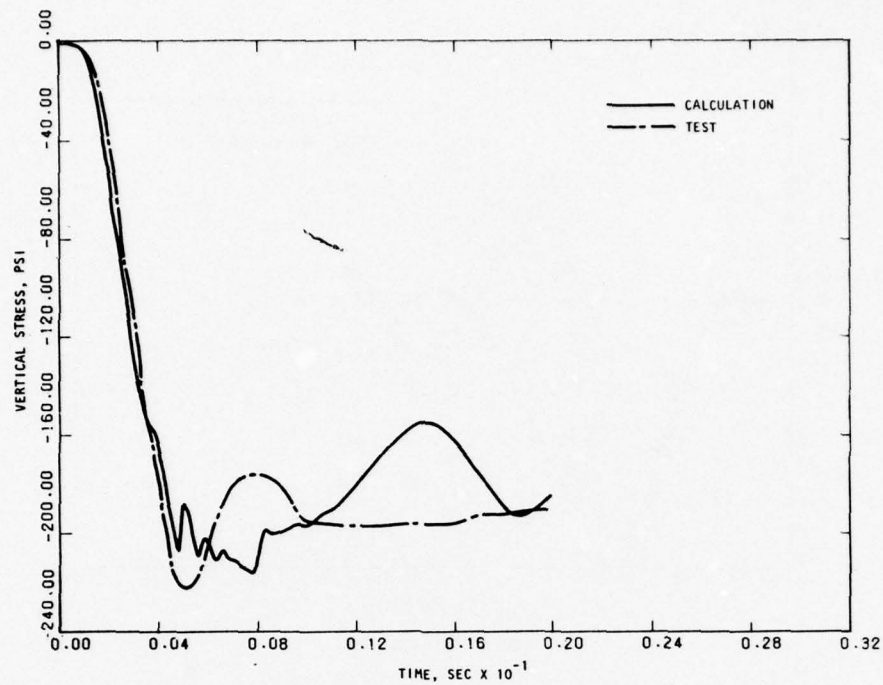


(a) Velocity

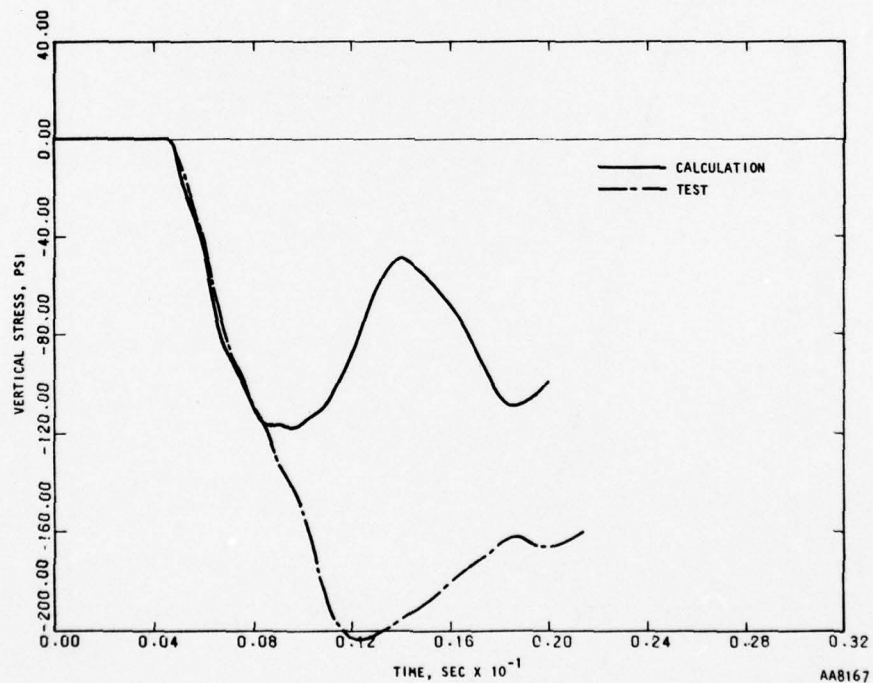


(b) Displacement

FIGURE 6-16. COMPARISON OF CBMI-13 CALCULATIONS AND TEST AT 54-IN. DEPTH



(a) Stress at 18-in. depth



(b) Stress at 72-in. depth

FIGURE 6-17. COMPARISON OF CBMI-13 CALCULATIONS WITH TEST, STRESSES

A cursory examination of these plots shows that the correlation between the calculations and test data is poor. More disturbingly, the agreement between the gage and free-field outputs within the calculations themselves is considerably less satisfactory than that among the test data.

The following deficiencies may be noted among the results of the calculation.

- a. Peak values of calculated velocities show much greater attenuation with depth than that observed in the test.
- b. Calculated velocities return to zero much sooner than in the test.
- c. Positive (upward) velocity peaks are higher in the calculations.
- d. Gage velocities in the calculations depart significantly from the free-field velocities, their peak values being almost twice as large.
- e. Calculated maximum displacements are less than the maximum displacements in the test. The disagreement between the two increases with depth, the observed free-field displacements being almost three times the calculated value at the 54-in. depth.
- f. Calculated displacements in the gages are consistently larger than those in the free field, differing by up to a factor of two.
- g. Calculated displacements show an upward "bounce back" absent from the data.
- h. The calculated stress in the bottom layer of the free field shows an upward bulge, whereas the test stress-time history shows a smooth movement towards its peak value.

An interpretation of the results follows in the next subsection and provides explanations to the above inconsistencies.

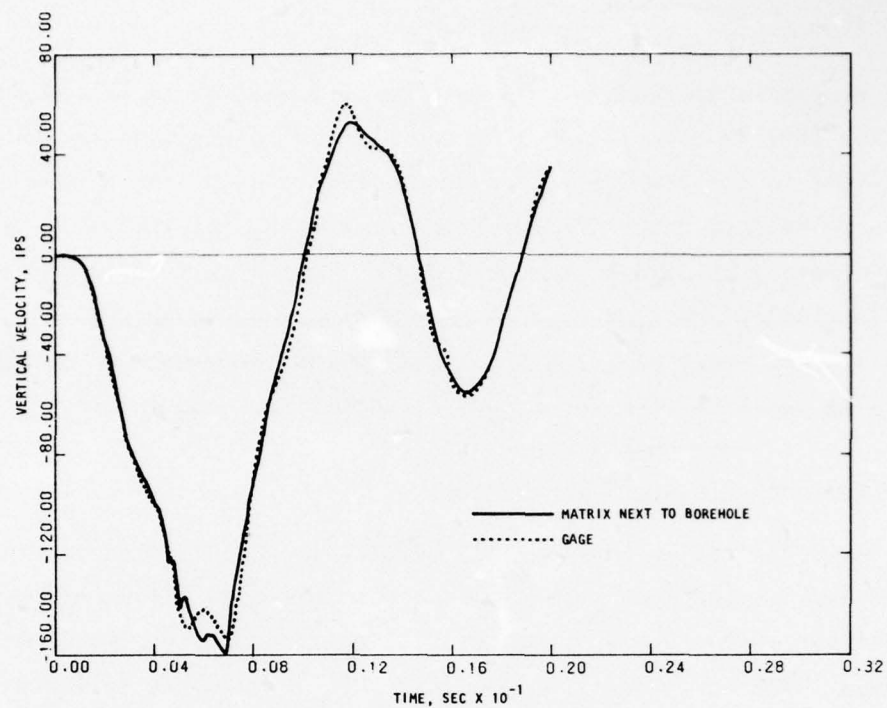
6.6 INTERPRETATION OF THE RESULTS

The results presented in Section 6.5 are interpreted in this subsection, and the underlying reasons for the unsatisfactory results of the calculation are identified.

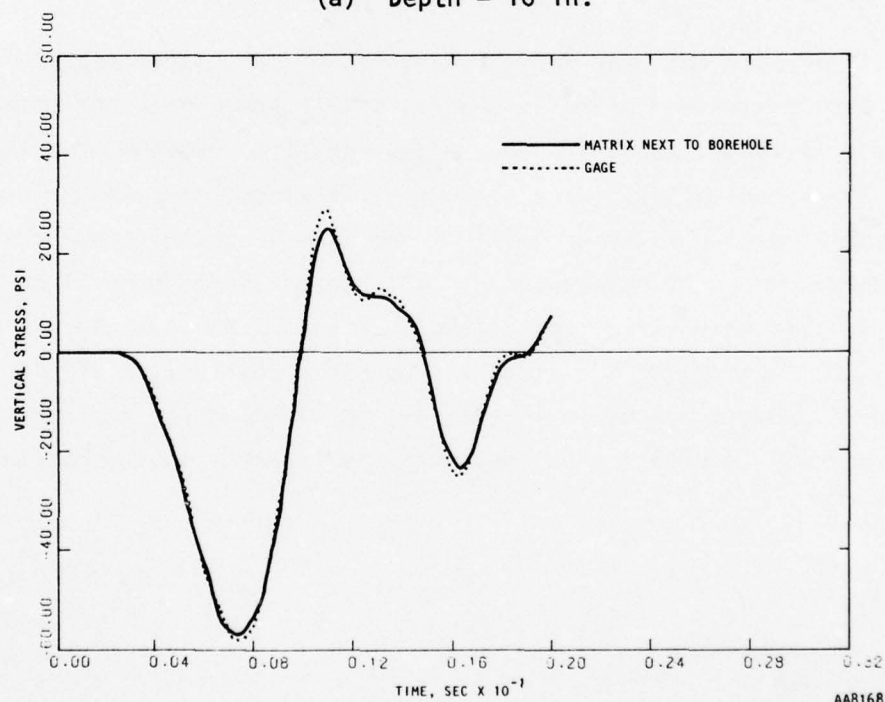
6.6.1 INTERPRETATION

The considerable attenuation observed in the calculations suggests that dissipation may have been excessive. Furthermore, studies with the slip model described in Section 4 indicated that a relatively rapid return of the velocities to zero is associated with higher frictional resistance at the boundary. From these two considerations, therefore, it appears that the frictional resistance assumed at the SBLG wall in the CBMI-13 calculations was too high.

Further support of the above interpretation may be found by analyzing the discrepancy between the gage and free-field motion (Items *d* and *f* of the list in Section 6.5). With significant frictional resistance at the SBLG wall, the motion of the specimen may be expected to be truly two-dimensional with displacements and velocities at the center being significantly larger than those closer to the SBLG wall. Confirmation of this is to be found in the plots in Figure 6-18, which show the velocity at the gage and in the matrix in the immediate neighborhood. The overlaid time histories are almost indistinguishable, showing that the "gage" locations of the finite element mesh did indeed faithfully follow the motion of the matrix in their vicinity. The discrepancy between the calculated motions of the gage and free field noted in Figures 6-15 through 6-17 is thus shown to be a two-dimensional effect caused by the frictional resistance at the SBLG wall. Incidentally, the excellent correlation in Figure 6-18 establishes that the properties used for the interface between the canister locking grout and the matrix did, in fact, achieve the objective of "locking."



(a) Depth = 18 in.



(b) Depth = 54 in.

FIGURE 6-18. COMPARISON OF VELOCITY IN THE GAGE AND NEIGHBORING MATRIX, CBMI-13 CALCULATIONS

AD-A037 098

AGBABIAN ASSOCIATES EL SEGUNDO CALIF

F/G 19/4

GROUT/SOIL INTERACTION AND VELOCITY GAGE EMPLACEMENT FOR GROUND--ETC(U)

AUG 76 M B BALACHANDRA, J A MALTHAN

DNA001-74-C-0100

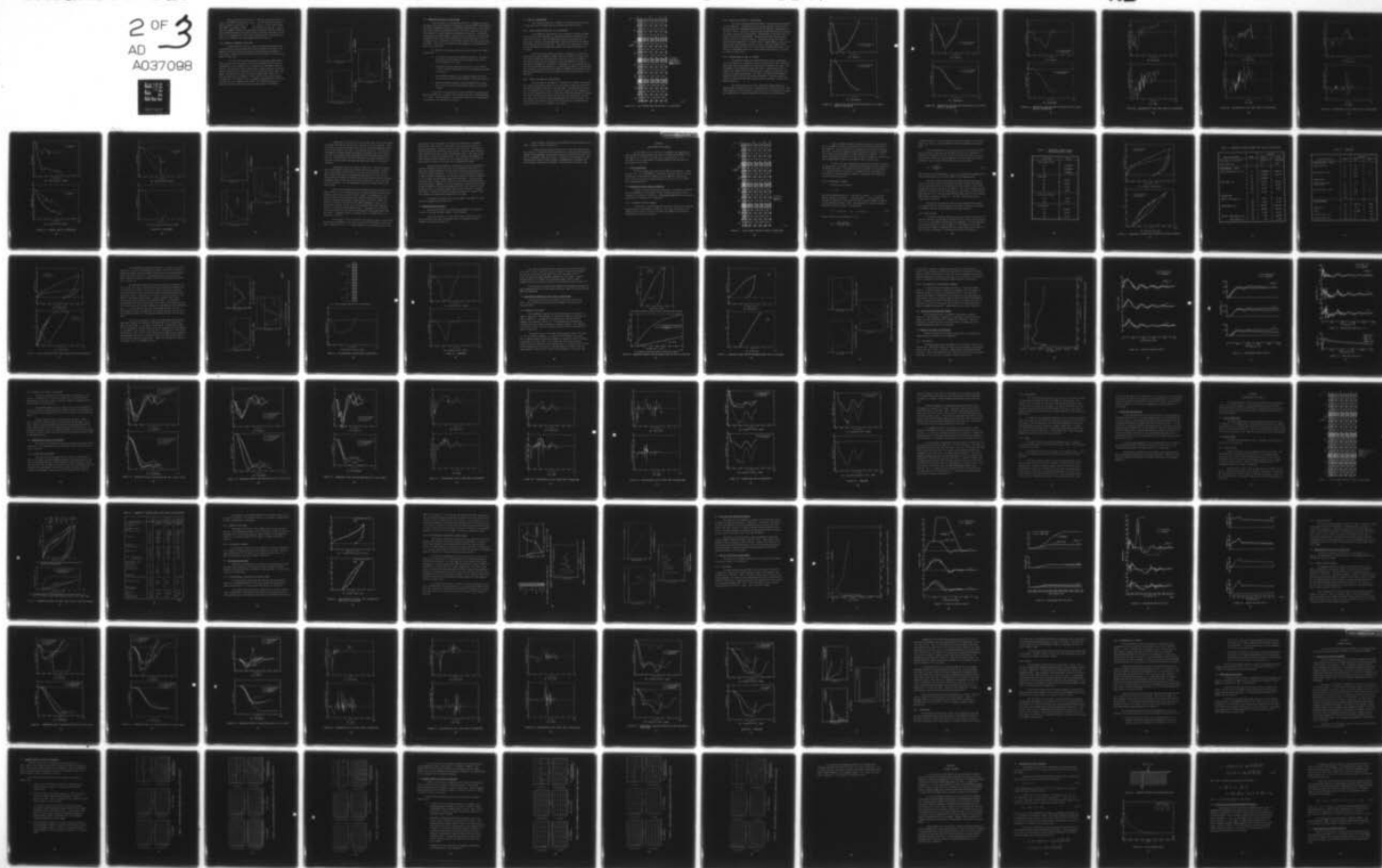
UNCLASSIFIED

AA-R-7364-7-4265

DNA-4089F

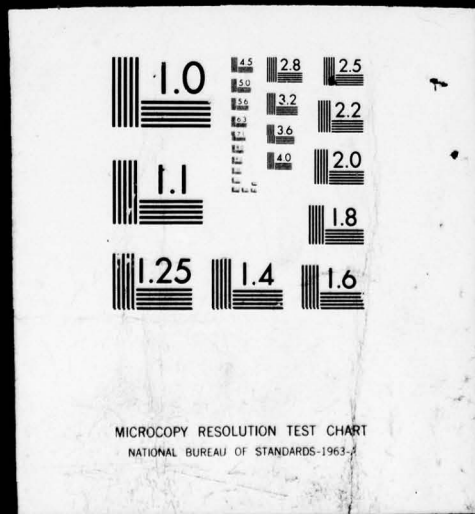
NL

2 OF 3
AD
A037098



2 OF 3
AD

A037098

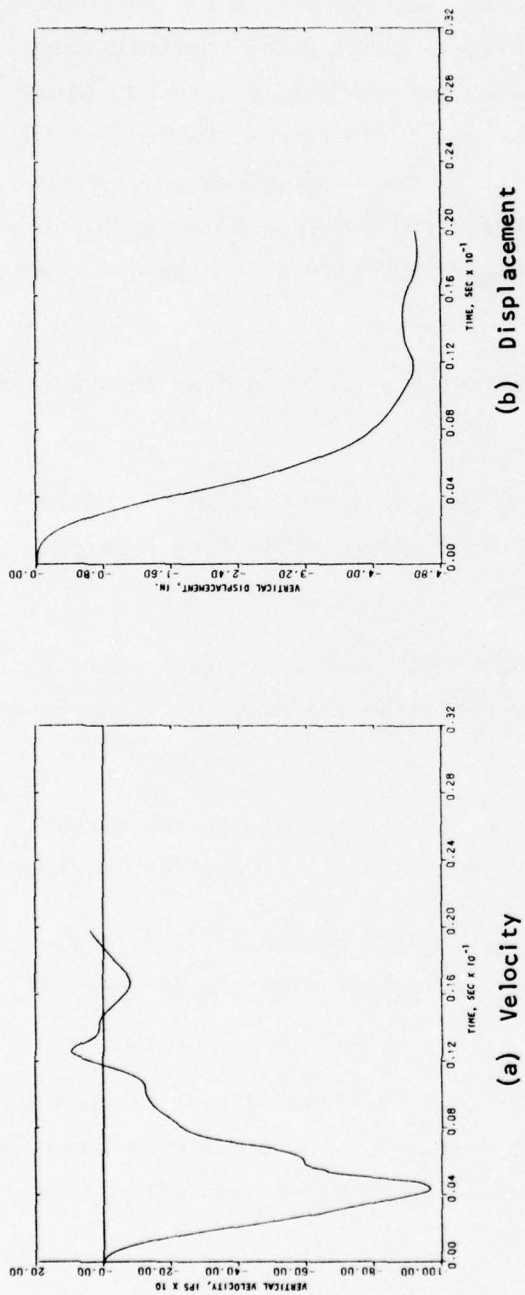


Having identified friction at the SBLG wall as the chief source of error in the CBMI-13 calculations, we can proceed to explain the inconsistencies listed in Section 6.5, one by one. Points *a*, *b*, and *d* have already been shown to be caused by high frictional resistance at the wall. Items *c* and *h* are probably related to the observation that high friction at the wall masks reflection effects and produces spurious unloading pulses (Sec. 4.4.2). Item *e* is a consequence of *a* and *b* while *f* follows from *d*. The bounce back noted in *g* is caused by the large upward velocities noted in *c*.

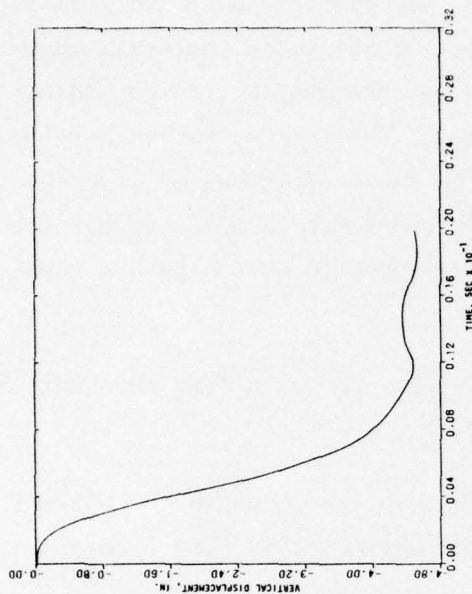
6.6.2 BEHAVIOR OF BOREHOLE FILLER GROUT

As described in Section 5.3, numerical problems were experienced in preliminary calculations made with the soft borehole filler grout. The behavior of the soft grout was, therefore, monitored during the CBMI-13 calculations. The results at the top level of the borehole filler grout are shown in Figure 6-19.

It is seen that the velocity attains a much higher peak (close to 1000 ips) than any of the peaks in Figures 6-14 through 6-16 and that the displacement is large, about 4.8 in., attesting to a "punchdown" effect at the top. The stress plot shows a spike that is almost certainly a numerical effect associated with a corner point of the stress/strain curve (Sec. 5.3). However, these numerical spikes are quickly brought under control and, as seen from Figures 6-14 through 6-17, their effect on the overall response is negligible. The reason for this is probably a combination of (1) the low total mass of grout compared to the matrix, (2) locking the canister in position, and (3) interface shear causing load transfer to the matrix.



(b) Displacement



(c) Stress

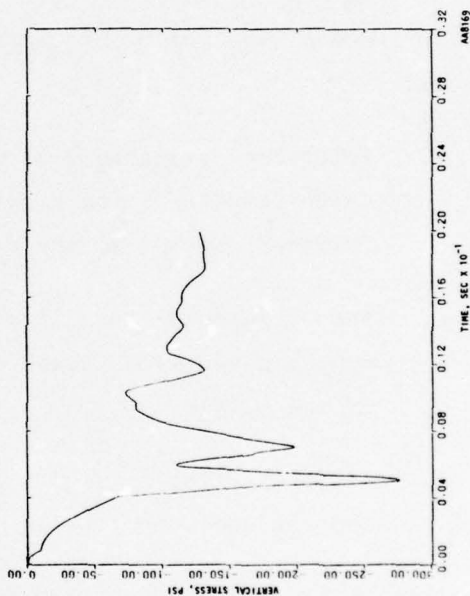


FIGURE 6-19. CALCULATED RESPONSE OF BOREHOLE FILLER GROUT AT TOP
(2-IN. DEPTH)

6.7 CONCLUSIONS FROM CBMI-13 CALCULATIONS

From the analysis of the previous section it is apparent that the frictional resistance assumed at the SBLG wall during the CBMI-13 calculations was grossly exaggerated leading to a distorted representation of the response. This implies that the differences noted in Section 5.1 among the tests must arise primarily from the progressive hardening of the matrix. Large radial stresses may have been present in the interior of the matrix, but either they decreased to small values near the SBLG wall or the coefficient of friction at the wall was so low that very little shear transfer took place across the interface. In any case, the residual stresses appear to have played a negligible role in the tests.

In summary, the following conclusions may be drawn from the CBMI-13 calculations:

- a. Frictional resistance at the SBLG wall assumed in the CBMI-13 calculations was too high; there was probably very little friction present in the test.
- b. The differences among the observed results of Tests CBMI-12, -13, and -14 were caused primarily by the progressive hardening of the matrix.
- c. The properties assumed for the interface between the matrix and the canister locking grout adequately simulated "locking."
- d. Numerical problems caused by the soft borehole filler grout were strictly local and had negligible effect on the overall response.

At this point it was decided to repeat the CBMI-13 calculations by deleting the SBLG wall altogether from the mesh and using a roller boundary in its place. This calculation is designated as CBMI-13-1 for reference and is described in the remainder of Section 6.

6.8 CBMI-13-1 CALCULATIONS

This subsection describes the CBMI-13-1 calculations and discusses the improved results stemming from the elimination of wall friction.

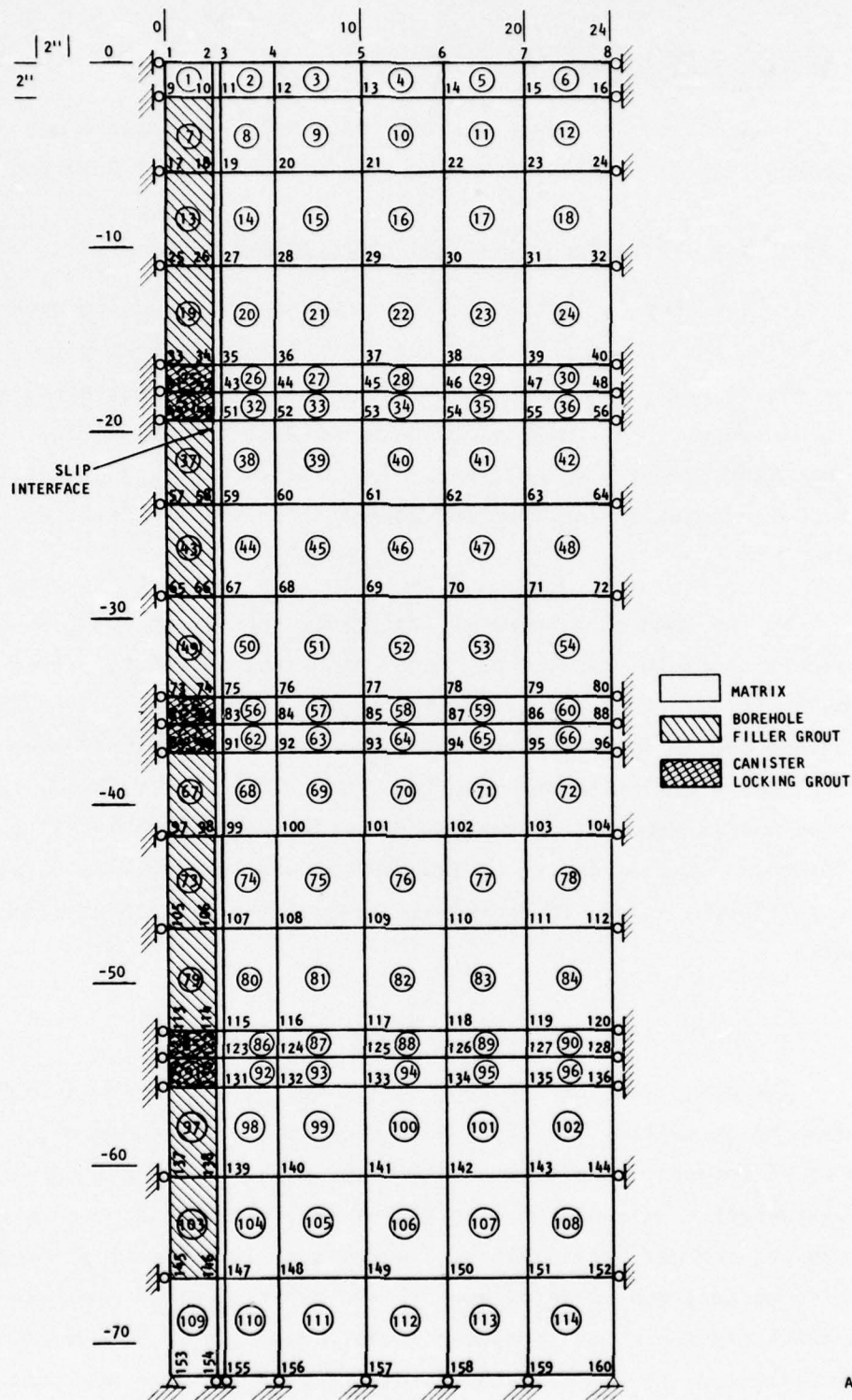
6.8.1 RESULTS EXPECTED FROM CBMI-13-1 CALCULATIONS

In the CBMI-13-1 calculations it was decided to eliminate the SBLG wall and use a rolled boundary to represent the extreme condition of zero friction at the wall. This was expected to result in an essentially one-dimensional response giving good agreement between the velocities calculated at the gage and free-field locations. The time for the velocities to return to zero was expected to lengthen and approach the values exhibited by the test data.

At the same time, however, reference to Section 6.3.1 shows that peak velocities would probably be higher than test values by a factor of two. This would indicate that the properties of the matrix used in the CBMI-13 calculations led to too soft a material and did not adequately account for the extent of hardening in the material. Nevertheless, it was decided not to modify the matrix material properties in performing the CBMI-13-1 calculations. The differences in the results of the CBMI-13 and CBMI-13-1 calculations could then be attributed solely to the elimination of the frictional effects at the SBLG wall.

6.8.2 INPUT TO THE CBMI-13-1 CALCULATIONS

The mesh used for the CBMI-13-1 calculations is shown in Figure 6-20. It is seen to be exactly identical to the one shown in Figure 6-1 except for the modified boundary condition at the outer edge. The input pulse and schedule of integration were as shown in Figure 6-9, except that the integration time step was changed from 0.025 to 0.05 msec at 10.0 msec instead of 12.5 msec. The entire calculation covering a real-time duration of 20 msec was carried out in 602 steps taking an average computational time of 8.16 sec/step. All the materials and interfaces used in this calculation were assigned exactly the same properties as in the CBMI-13 calculation.



AA 7805

FIGURE 6-20. FINITE ELEMENT MESH USED FOR CBMI-13-1 CALCULATION

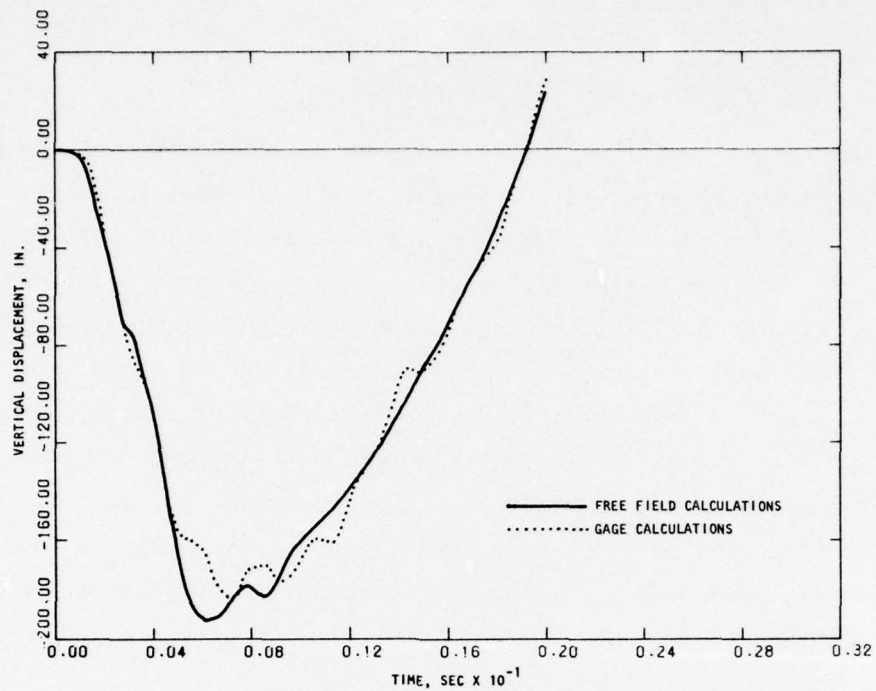
6.8.3 RESULTS OF THE CBMI-13-1 CALCULATIONS

The results obtained during the CBMI-13-1 calculations are presented in this subsection. Interpretation of the results follows in Section 6.8.4. The velocities and displacements obtained from the CBMI-13-1 calculations at the 18-in., 36-in., and 54-in. depths at both the gage and free-field locations are shown in Figures 6-21 through 6-23. Accelerations at the same levels are shown in Figures 6-24 through 6-26. The acceleration plots have not been overlaid so as not to lose the details. Calculated stresses are shown in Figures 6-27a through 6-27d. The first three of these compare stresses at the gage and free-field locations at 18-in., 36-in., and 54-in. depths, while Figure 6-27d shows the stress in the free field at the SBLG base level. The velocity, displacement and stress in the borehole filler grout at two levels are shown in Figure 6-28.

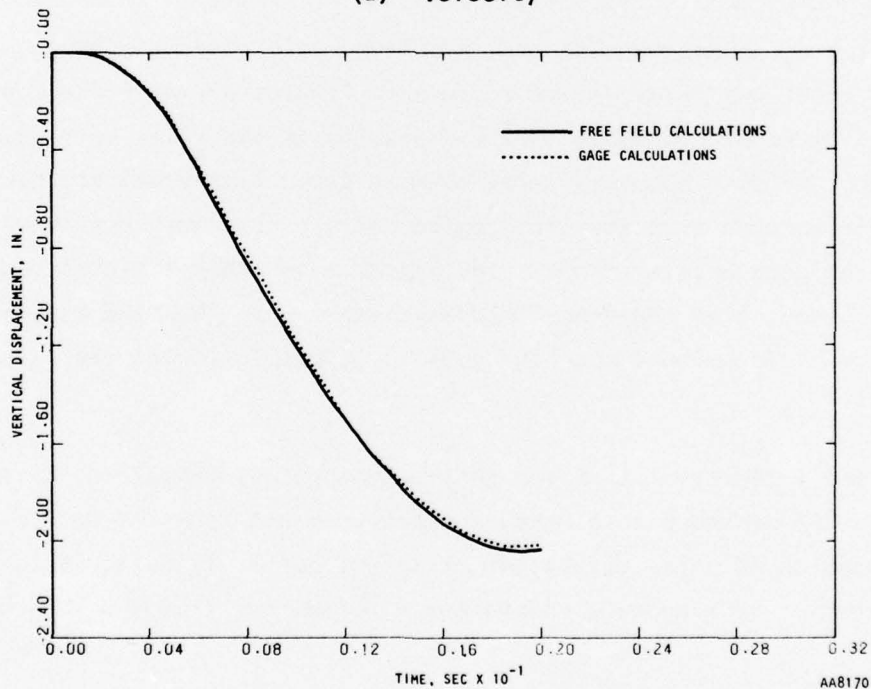
6.8.4 INTERPRETATION OF CBMI-13-1 RESULTS

The agreement between the calculated velocities at the gage and free-field locations is excellent as seen in Figures 6-21a, 6-22a, and 6-23a. Peak values agree within about 10%, and phasing is generally very good. As a consequence, the displacements agree even better. Accelerations shown in Figures 6-24 through 6-26 correlate quite well, except for occasional large spikes in the gage accelerations. The latter also exhibit high-frequency components absent from the free-field accelerations. Thus the response is seen to be one-dimensional with the gage locations following the free-field motion faithfully.

The velocity plot at the 54-in. depth (Fig. 6-23a) exhibits an upward bulge at around 6 to 8 msec, a feature absent from the test data. The true explanation of this feature is not known, but it is believed to be caused by a combination of a modulus change and a reflection from the SBLG base.



(a) Velocity



(b) Displacement

FIGURE 6-21. COMPARISON OF GAGE AND FREE-FIELD MOTION AT 18-IN. DEPTH, CBMI-13-1 CALCULATION

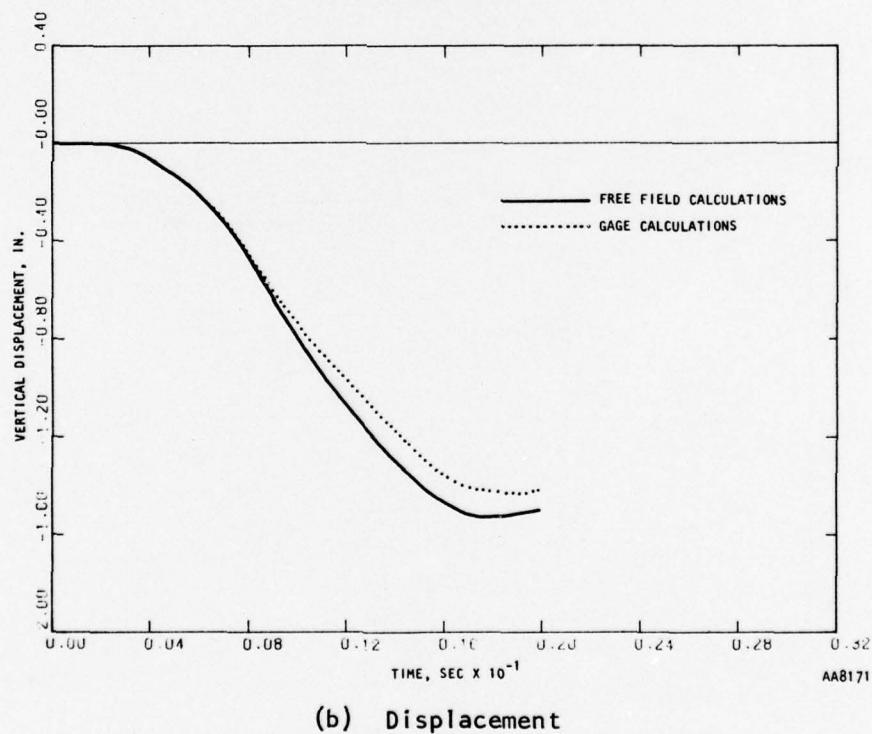
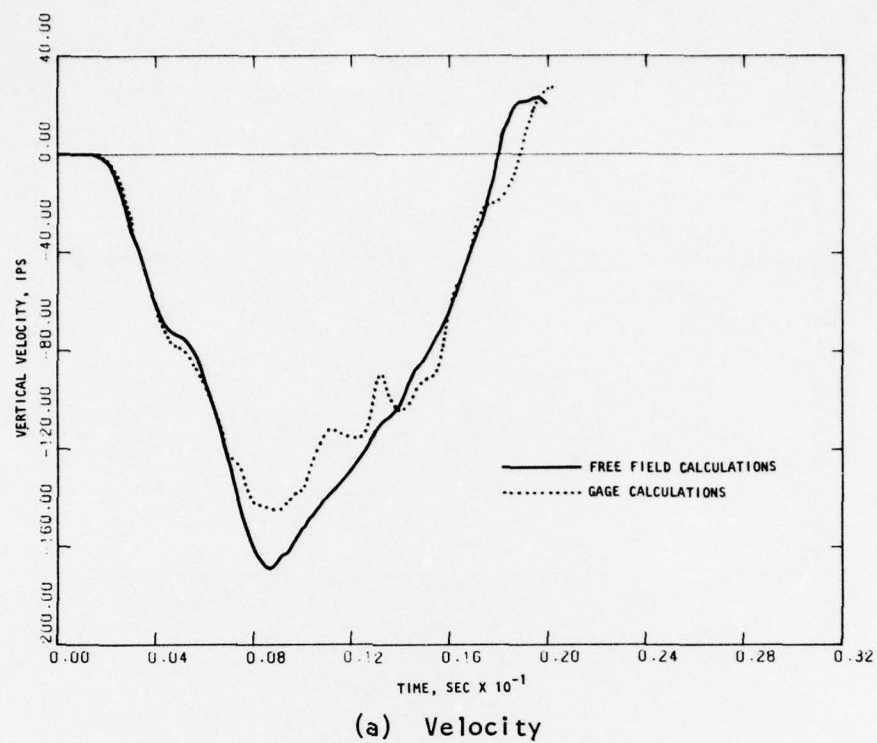
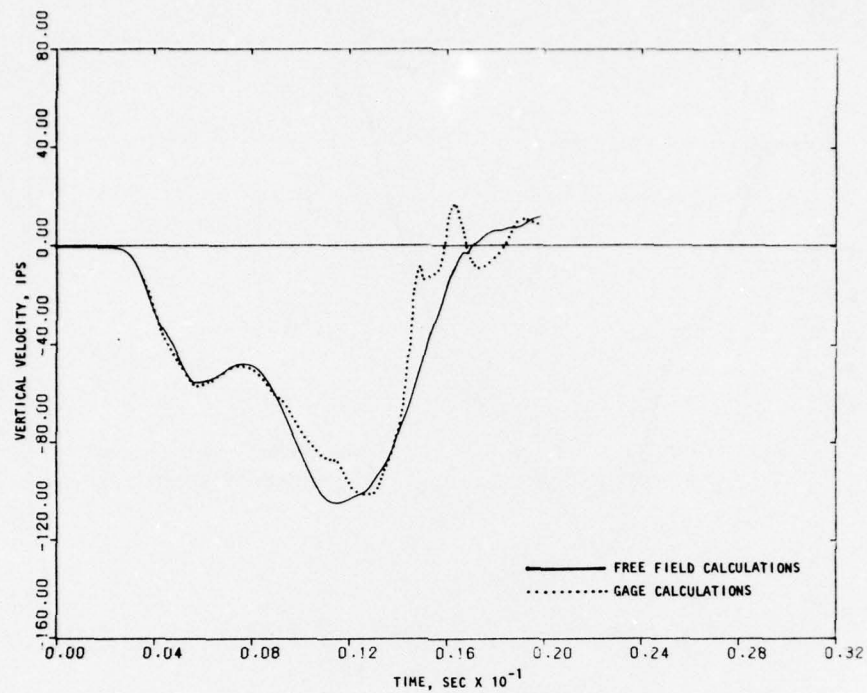
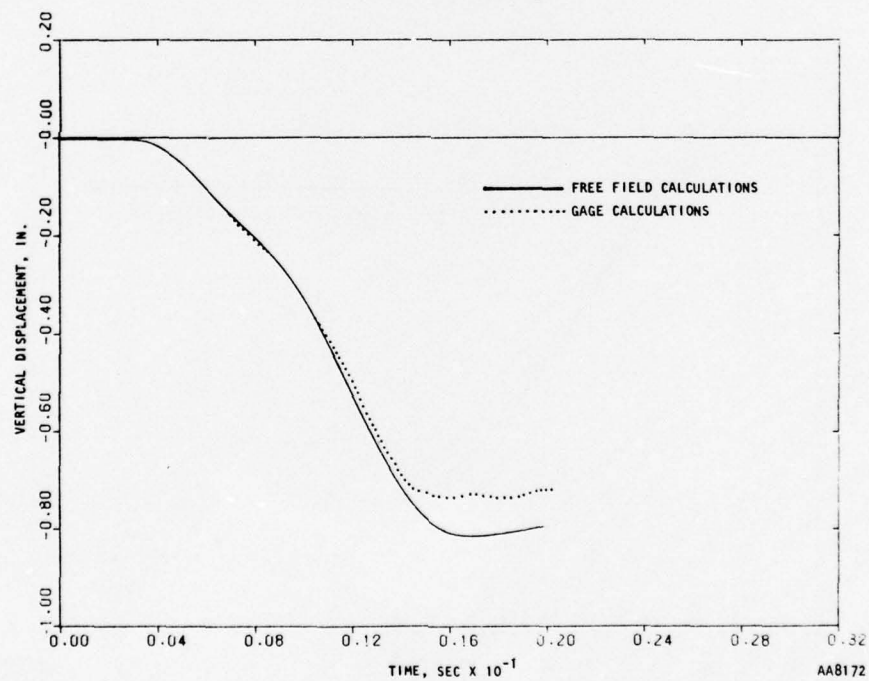


FIGURE 6-22. COMPARISON OF GAGE AND FREE-FIELD MOTION AT 36-IN. DEPTH, CBMI-13-1 CALCULATIONS

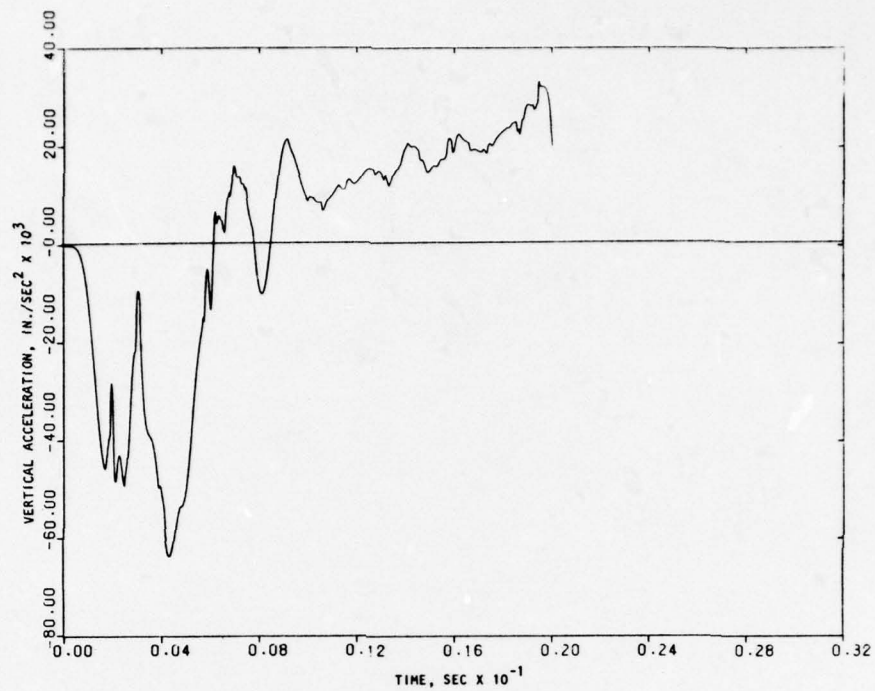


(a) Velocity

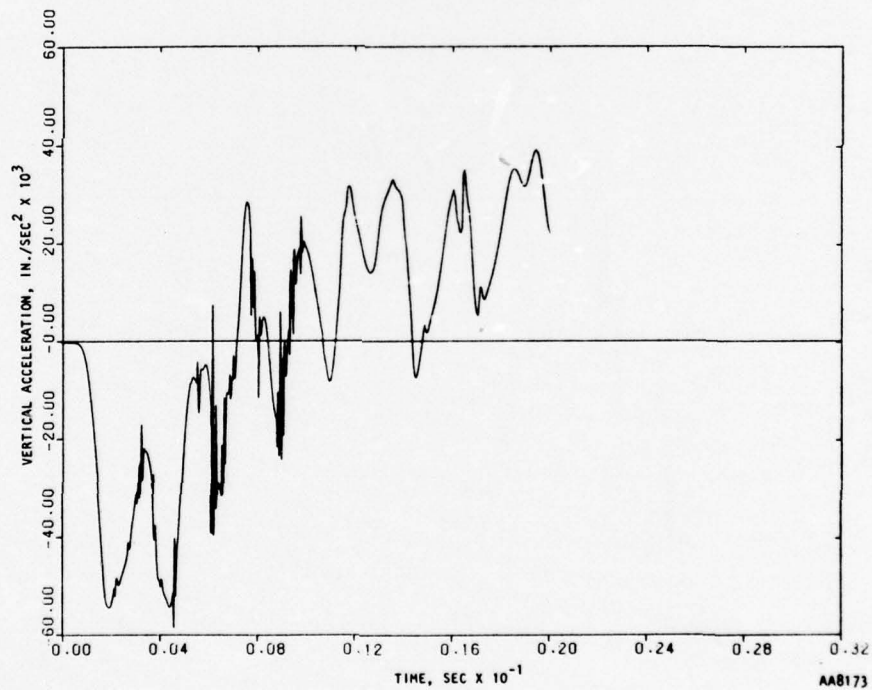


(b) Displacement

FIGURE 6-23. COMPARISON OF GAGE AND FREE-FIELD MOTION AT 54-IN. DEPTH, CBMI-13-1 CALCULATIONS

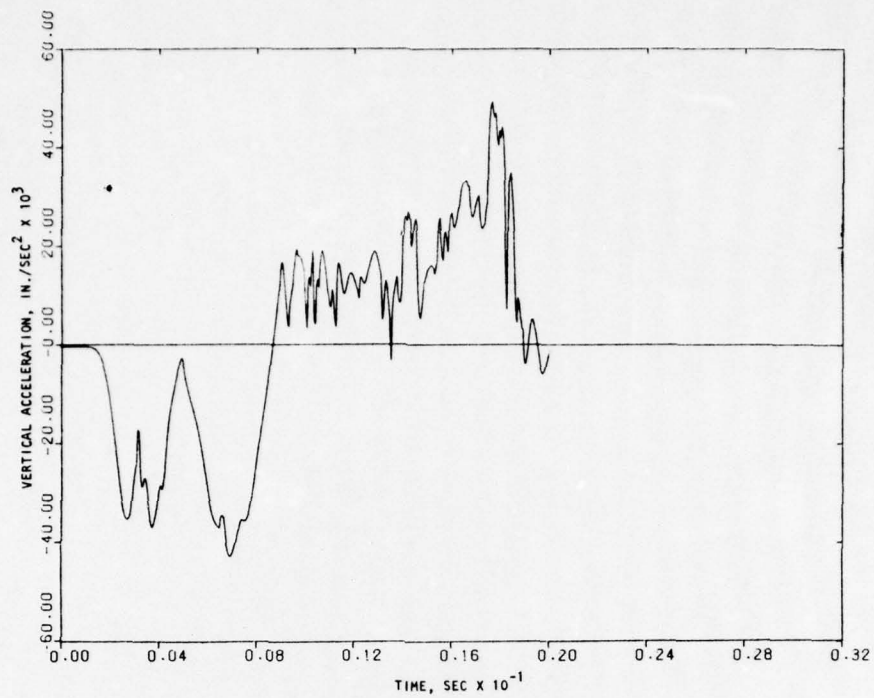


(a) Free field

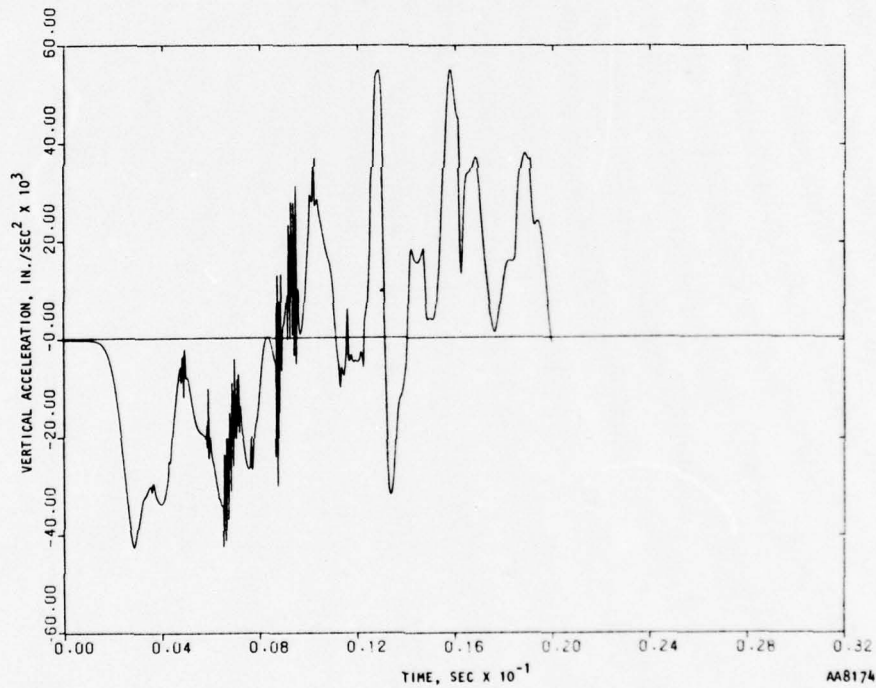


(b) Gage

FIGURE 6-24. ACCELERATION AT 18-IN. DEPTH, CBMI-13-1 CALCULATIONS

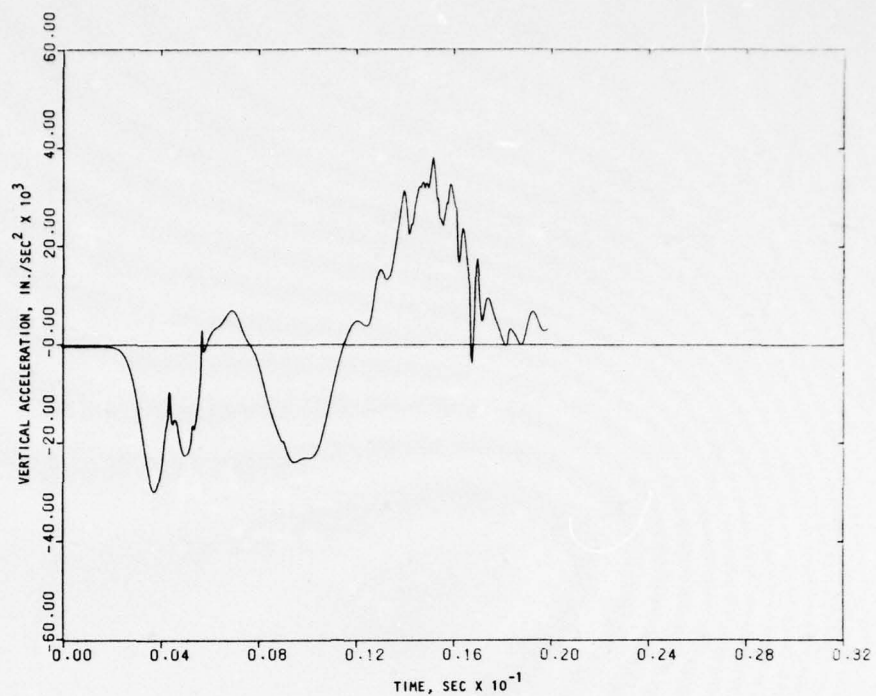


(a) Free field

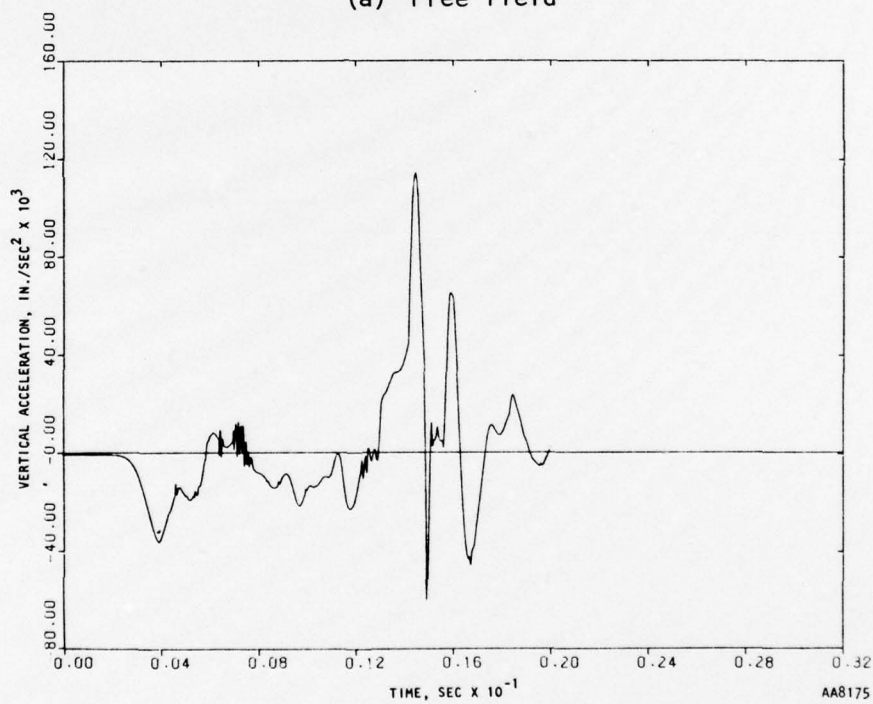


(b) Gage

FIGURE 6-25. ACCELERATION AT 36-IN. DEPTH, CBMI-13-1 CALCULATIONS

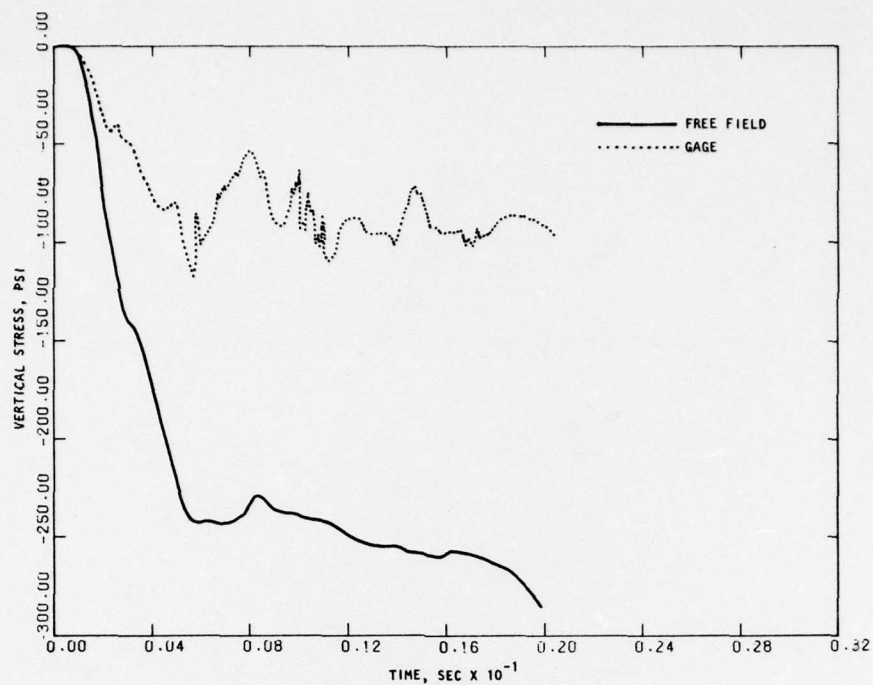


(a) Free field

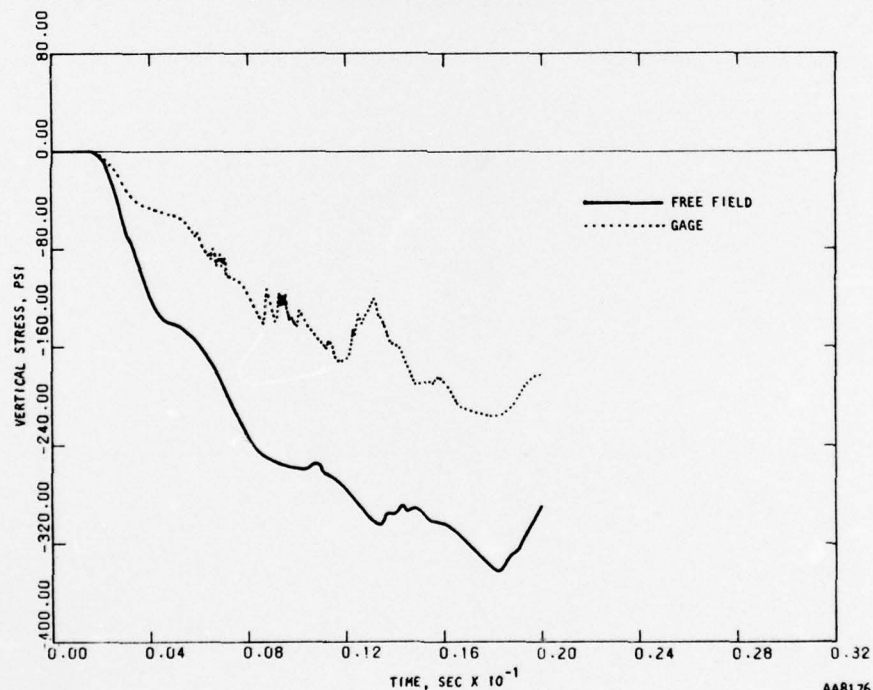


(b) Gage

FIGURE 6-26. ACCELERATION AT 54-IN. DEPTH, CBMI-13-1 CALCULATIONS

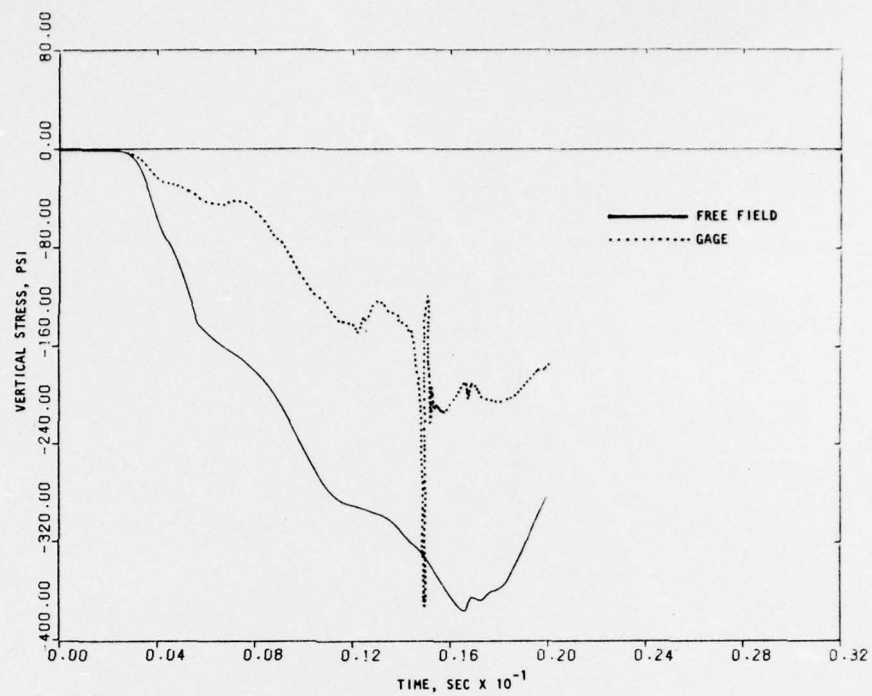


(a) Stress at 18-in. depth

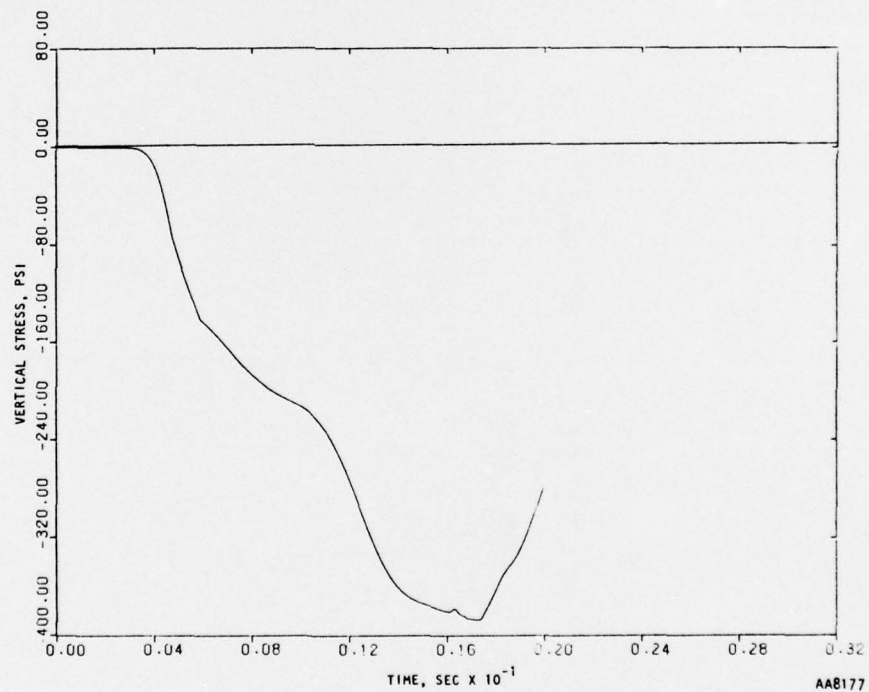


(b) Stress at 36-in. depth

FIGURE 6-27. STRESSES, CBMI-13-1 CALCULATIONS

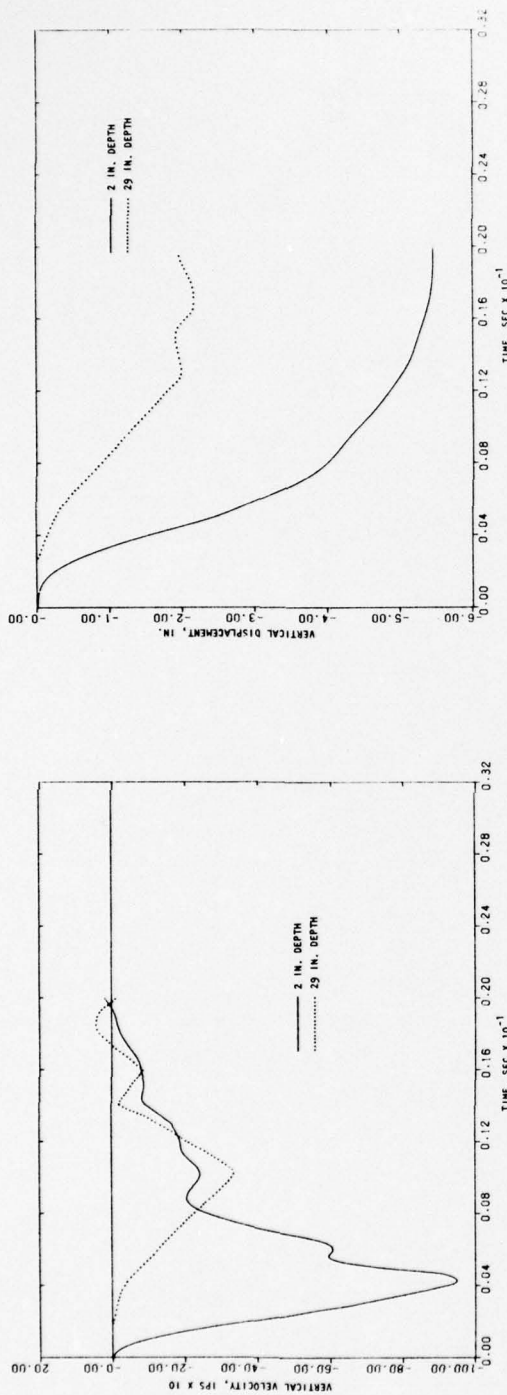


(c) Stress at 54-in. depth

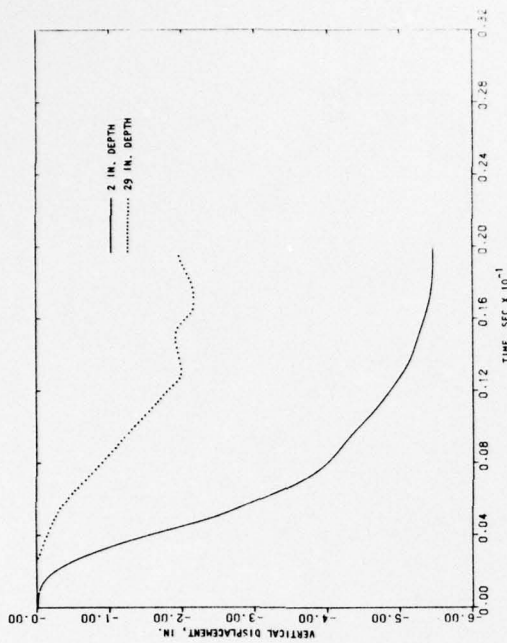


(d) Free field stress at 72-in. depth

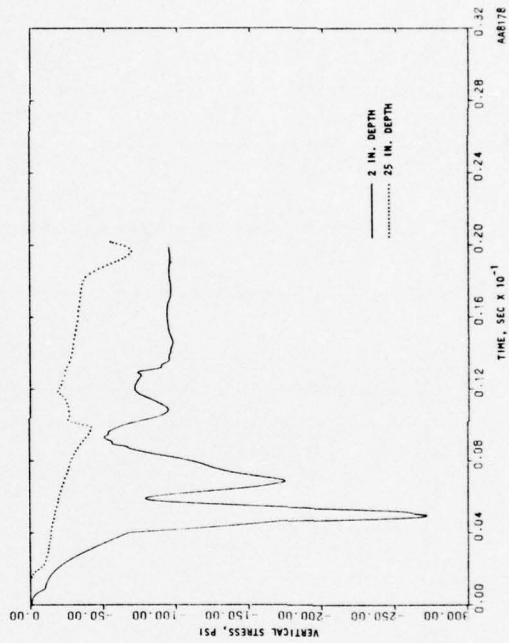
FIGURE 6-27. (CONCLUDED)



(a) Velocity



(b) Displacement



(c) Stress

FIGURE 6-28. RESPONSE OF BOREHOLE FILLER GROUT, CBMI-13-1 CALCULATIONS

Comparison of these results with test data shows that the peak values are higher than those of the test by a factor of 2 to 2.5 as expected. Calculated peaks are attained somewhat later, and the calculated velocities return to zero significantly later than in the measured velocities. All these factors combine to produce maximum calculated displacements that are as much as 3.3 times the maximum measured displacements and are attained later than in the test. Accelerations in the free field show first peaks comparable with test data but show larger excursions and higher peak values in the upward direction.

15 Calculated stresses are shown in Figure 6-27. Free-field stresses show clear evidence of stress wave reflections from the bottom of the SBLG. This is consistent with the results of the slip model study (Sec. 4-4.2), which showed reflections to be conspicuous when the wall friction was low. Peak stresses are boosted by reflection at the lower levels, and the reflected compression wave is just seen to be arriving at the 18-in. level at the end of the calculations. The calculated peak stresses are larger than the test peak stresses.

Figures 6-27a through 6-27c also show the stresses calculated at the gage locations. These are generally seen to be about one-half the free field stresses, except for a spike at the 54-in. depth. An explanation for the lower stresses at these locations may be offered along the following lines. The hard, canister-locking grout, being locked to the matrix, follows the motion of the matrix and has nearly the same displacement, velocity, and acceleration; however, because of the soft borehole filler grout above and below it, it experiences much smaller strains. Consequently, the stresses are smaller despite the fact that the hard grout has much larger moduli than the matrix. A somewhat different situation exists in the CBMI-14 test as described in Section 7.

The response of the soft borehole filler grout is shown in Figure 6-28. The velocity, displacement, and stress at the top of the borehole filler grout and at a depth of 24 in., i.e., midway between the two top gage locations, have

been plotted. The displacement plot shows clear evidence of a punchdown effect at the top, but this is restrained so that at the lower level the maximum displacement is barely one-third of that at the top. The velocity and stress plots both show large initial spikes. The actual peak values are almost certainly spurious, arising from numerical causes. The stress at the lower level is seen to be extremely small. This indicates that because of shear transfer at the interface, most of the applied load is carried by the matrix and the stresses in the grout are correspondingly reduced.

The results of the CBMI-13-1 calculations are thus qualitatively in excellent agreement with the test data. The discrepancies that exist in a quantitative comparison appear to stem from an inaccurate representation of the matrix material properties. At this point, it would have been possible to make yet another calculation, with the matrix material properties modified so as to account for the hardened condition of the matrix. Such a calculation would seek to obtain results close to the test data, both qualitatively and quantitatively. However, it was felt unnecessary to make this calculation because the CBMI-13-1 calculations adequately portray the trends of the test and provide all the information sought from the test conditions. Moreover, the subject of prediction accuracy introduces a separate, but equally important, question not specifically addressed in this study.

The general conclusions drawn from the CBMI-13 and CBMI-13-1 calculations are summarized in Section 6.9.

6.9 CONCLUSIONS AND DISCUSSION

The basic conclusion from the CBMI-13 and CBMI-13-1 calculations relative to the gage placement problem is the following:

Locking the canisters in place forces them to follow free-field motion faithfully even when the borehole filler is extremely soft when compared to the free-field material.

Other secondary conclusions that emerged from these calculations are Items *b* through *d* listed in Section 6.7.

An additional point worth noting has to do with the comparison of the stresses at the gage and free-field locations. These show that conditions leading to good agreement between borehole and free-field motion are not conducive to agreement among the stresses. Therefore, if stress gages are under consideration instead of velocity gages, recommendations on placement procedure would be substantially different. This matter merits further study.

SECTION 7

CALCULATION OF TEST CBMI-14

As described briefly in Section 5, the CBMI-14 test employed the same specimen that had previously been used in the CBMI-12 and CBMI-13 tests. The borehole was filled for this test with a very hard grout. As in Test CBMI-13 a 2-in. deep layer of the matrix material was used on top of the borehole filler grout.

7.1 FINITE ELEMENT MESH

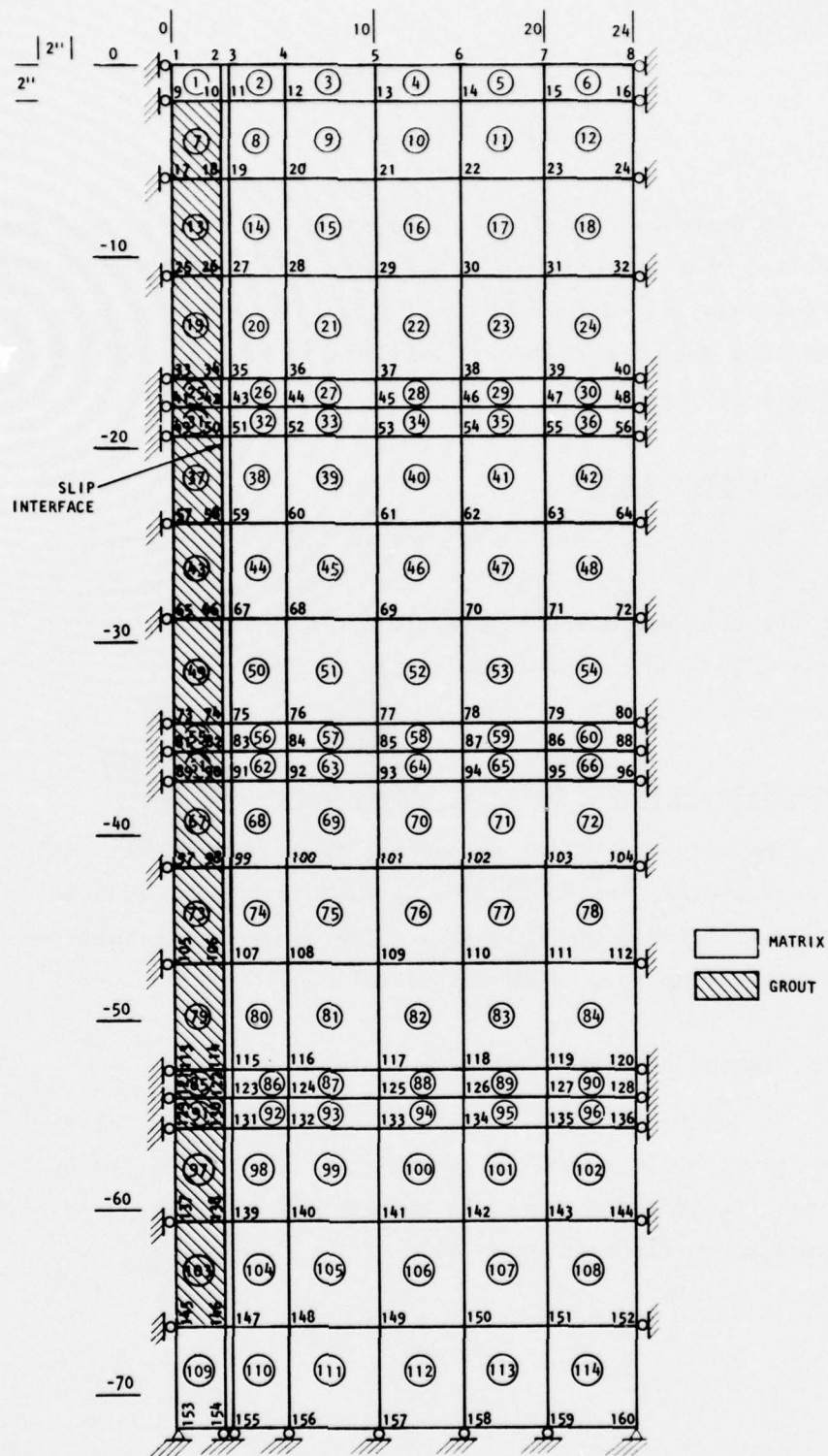
The finite element mesh used for the CBMI-14 calculations is shown in Figure 7-1. As in the CBMI-13-1 calculations, the outer edge is rolled. The mesh has the same overall geometry as in the CBMI-13-1 calculations, but in this case the entire borehole (except for the top 2 in.) is filled with a homogeneous grout.

7.2 GENERATION OF MATRIX MATERIAL PROPERTIES

The matrix material properties to be used in the CBMI-14 calculations had to be generated, in the absence of data, by making allowances for the progressive stiffening of the matrix. The procedure adopted and the resulting properties are discussed in this subsection.

7.2.1 STIFFENING OF MATRIX MATERIAL

In Section 6 it was concluded that the matrix material had stiffened progressively from Test CBMI-12 to CBMI-14. The results of Section 6 also showed that the properties used in the CBMI-13 and CBMI-13-1 calculations represented an overly soft material.



AA 7805

FIGURE 7-1. FINITE ELEMENT MESH USED IN CBMI-14 CALCULATIONS

It was, therefore, decided to generate new material properties for use in the CBMI-14 calculations accounting for the stiffening the material had undergone. This was done mainly by comparing the peak velocities among the tests. The material properties were generated in two steps to represent the stiffening from Test CBMI-12 to CBMI-13 and then to CBMI-14. In the sequel, the materials obtained at the end of these two steps are referred to as the stiffened CBMI-13 matrix and the CBMI-14 matrix, respectively.

In view of the many uncertainties surrounding the actual properties of the materials in the tests, complicated manipulation of material properties was deemed inadvisable. The properties used in the CBMI-13-1 calculations, i.e., those of the Layer 2 material in the CBMI-12 test, were chosen as a starting point, mainly because the CBMI-13-1 calculations represented the trends of the test quite well.

7.2.2 STIFFENED CBMI-13 MATRIX

Consider the relationship

$$\sigma = \rho c v \quad (7-1)$$

that exists between the stress σ and particle velocity v in a linear, elastic material with density ρ and wave speed c . It was decided to estimate the degree of stiffening of the matrix from Test CBMI-12 to CBMI-13 by using the above relation. Thus, using subscripts 12 and 13 to indicate quantities from the two tests, it follows that

$$\sigma_{13} = \rho_{13} c_{13} v_{13} \quad \sigma_{12} = \rho_{12} c_{12} v_{12} \quad (7-2)$$

The two relations can be combined to yield

$$c_{13} = \left(\frac{\sigma_{13} \rho_{12} v_{12}}{\sigma_{12} \rho_{13} v_{13}} \right) c_{12} \quad (7-3)$$

If the peak values of stress and velocity are used in Equation 7-3, the wave speeds c_{12} and c_{13} may be regarded as those corresponding to the secant moduli.

The stiffened CBMI-13 matrix was constructed by increasing the bulk moduli from their values used for the CBMI-13 calculations, keeping the transition of the moduli from one value to the next at the same stress level. Since the bulk modulus varies as the square of the wave speed, each value of the modulus K_{13} for the stiffened CBMI-13 matrix was taken as

$$K_{13} = \left(\frac{c_{13}}{c_{12}} \right)^2 K_{12} \quad (7-4)$$

where the ratio of the wave speeds, c_{13}/c_{12} was calculated from Equation 7-3, using the peak values of stress and velocity in the measured data.

The finite element code updates the moduli based on the values of strain rather than stress, and therefore the strains at which these changes occur were calculated using the new values of the bulk moduli. The failure envelope and Poisson's ratio were not modified. Thus, this procedure requires alteration of coefficients B_1 through B_9 , B_{11} , B_{16} , and B_{17} of the material model (see Sec. 3.2). The new values of these coefficients for the stiffened CBMI-13 matrix are shown in Table 7-1. The other coefficients have the values shown in Table 6-1.

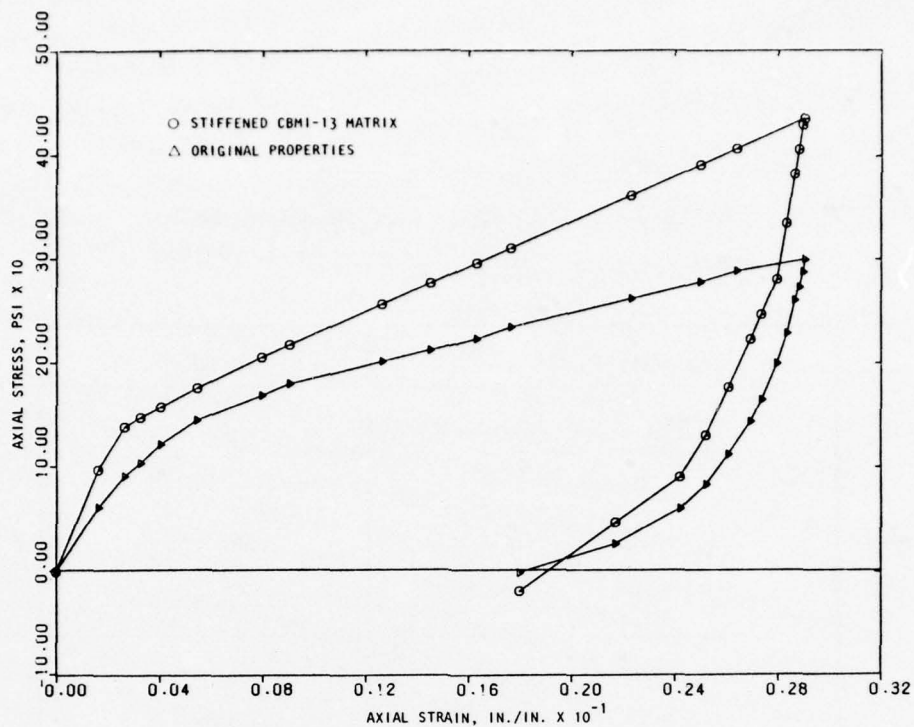
The uniaxial stress/strain and stress path behavior of the model are compared with the original properties in Figure 7-2 to assess the degree of stiffening that has been introduced by the above procedure.

7.2.3 CBMI-14 MATRIX

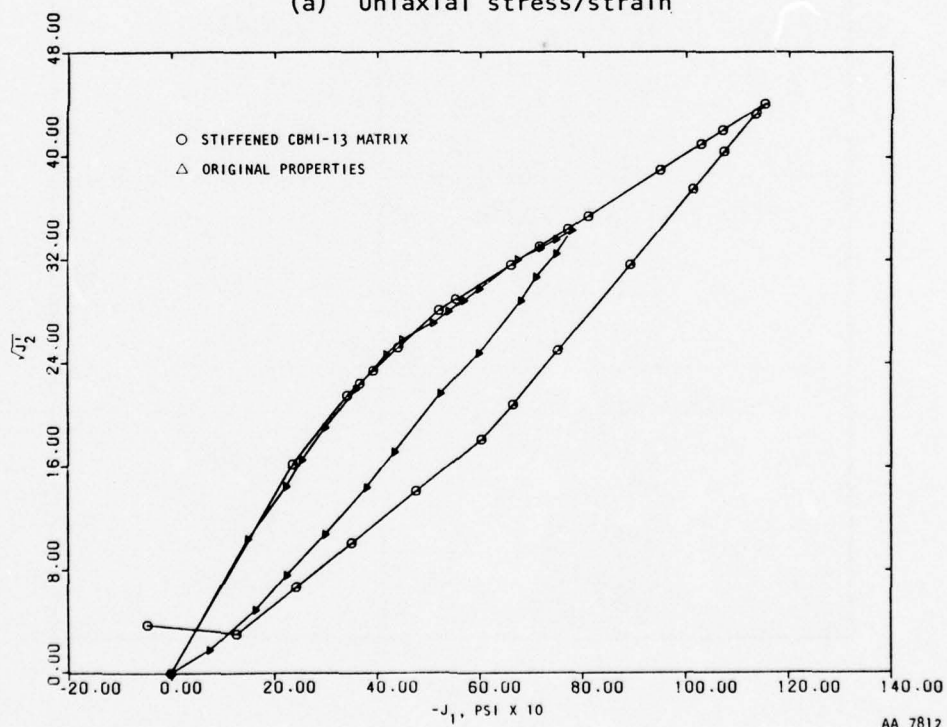
Following a procedure identical to the one outlined in Section 7.2.2 and using the data from the CBMI-13 and CBMI-14 tests, matrix material properties for use in the CBMI-14 calculations were generated. The final parameters of the material model are shown in Table 7-2. The behavior of the model under uniaxial loading is compared with the original properties in Figure 7-3 and illustrates the degree of stiffening the material has undergone.

TABLE 7-1. PARAMETERS OF MATERIAL MODEL
FOR STIFFENED CBMI-13 MATRIX

Coefficient	Value
Strain Break Points	
B_1	-0.0010288
B_2	-0.0026593
B_3	-0.0063995
Load Moduli	
B_4	56,465
B_5	34,823
B_6	11,453
B_7	9,982
Control Line Slopes	
B_{11}	9,178
B_{12}	3,645
Unload Moduli	
B_8	129,658
B_{16}	49,034
B_{17}	15,513



(a) Uniaxial stress/strain



(b) Uniaxial stress path

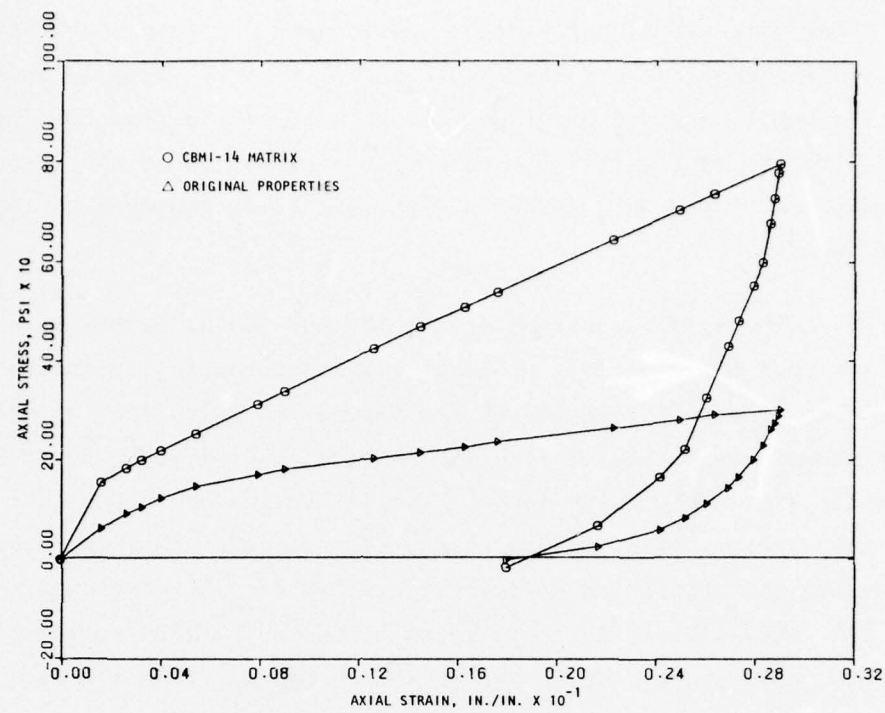
FIGURE 7-2. COMPARISON OF STIFFENED CBMI-13 MATRIX WITH ORIGINAL PROPERTIES

TABLE 7-2. PARAMETERS OF MATERIAL MODELS USED IN CBMI-14 CALCULATIONS

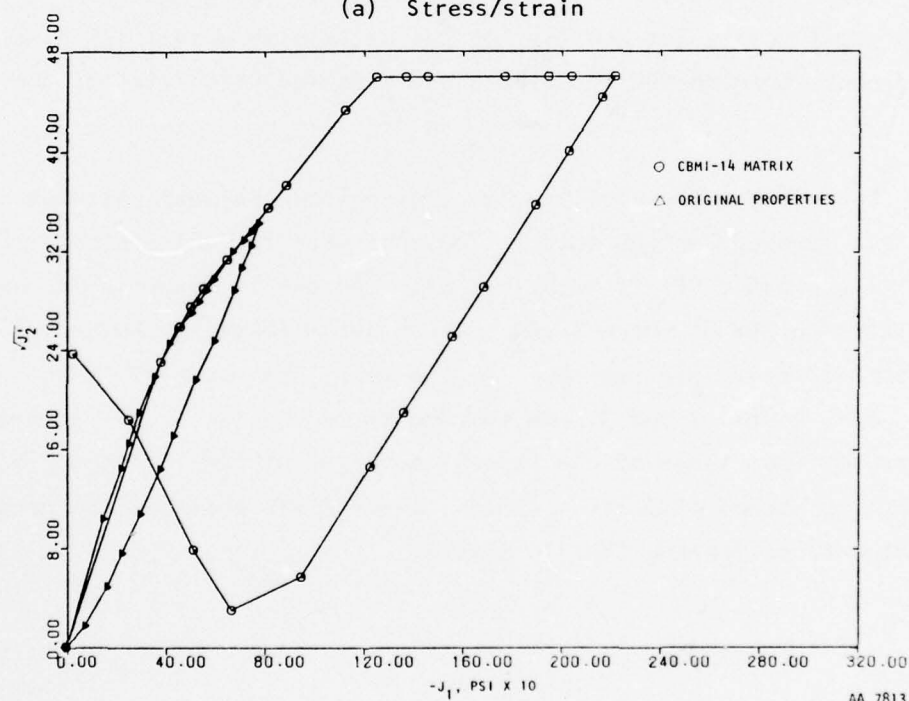
Quantity and Units	Symbol	Material	
		Matrix	Grout
Mass density, lb-sec ² /in. ⁴	ρ	0.00013105	0.00017897
Unit weight, pcf	γ	87.5	119.5
<u>Bulk Modulus:</u> Loading			
Strain break points, in./in.	B ₁	-0.00046343	-0.001125
	B ₂	-0.0011979	-0.00155
	B ₃	-0.0028827	--
Load moduli, psi	B ₄	125,352	155,556
	B ₅	77,307	97,391
	B ₆	25,426	59,829
	B ₇	22,160	--
Unload/reload			
Control line slopes, psi	B ₁₁	10,375	72,593
	B ₁₂	8,092	34,741
Unload moduli, psi	B ₈	287,841	1,555,556
	B ₁₆	108,856	389,926
	B ₁₇	34,439	157,193
Tension: Bulk modulus, psi	B ₁₀	3,500	100,000
Shear modulus, psi	G ₁₀	300	21,429

TABLE 7-2. (CONCLUDED)

Quantity and Units	Symbol	Material	
		Matrix	Grout
<u>Poisson's Ratio:</u> Loading			
Break points, psi	G ₆	-94	--
	G ₇	-173	--
Load Poisson's ratio	G ₁	0.416	0.4
	G ₁₁	0.453	--
Unload/reload			
Control line slopes, dimensionless	G ₈	-0.03	--
	G ₉	--	--
Unload Poisson's ratio	G ₂	0.44	0.4
	G ₁₃	0.46	--
	G ₁₄	--	--
<u>Yield Parameters</u>			
	Y ₁₀	-162.175	-1,852
Cohesion, psi	Y ₁₁	19.4	289
Slope	Y ₁₂	-0.16402	-0.156
von Mises limit, psi	Y ₁₆	46	578
Tension cutoff, psi	Y ₂₅	61	150



(a) Stress/strain



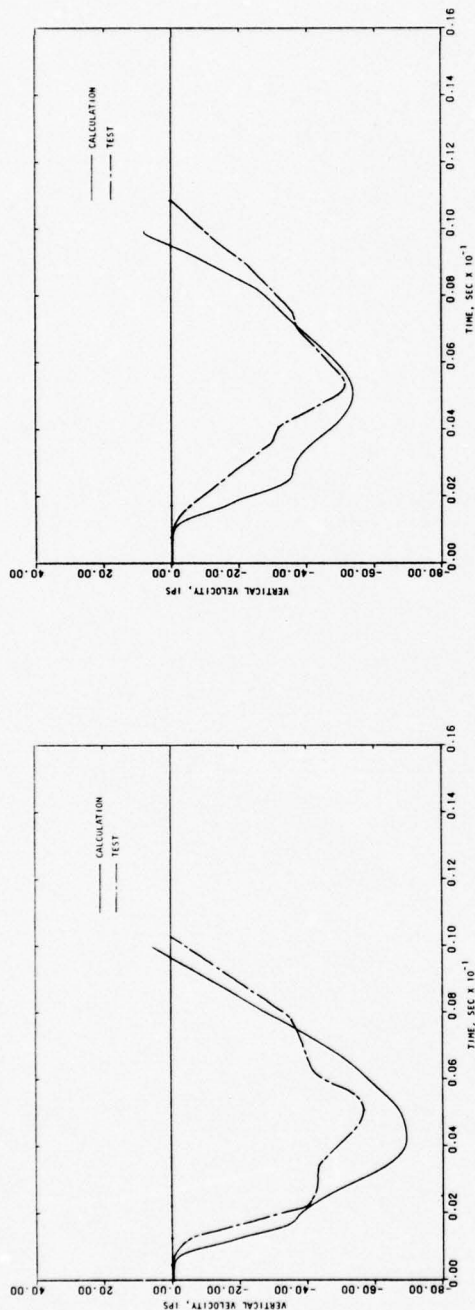
(b) Stress path

FIGURE 7-3. UNIAXIAL BEHAVIOR OF CBMI-14 MATRIX COMPARED WITH ORIGINAL PROPERTIES

A one-dimensional calculation was made on a column with the above properties, using the finite-element mesh shown in Figure 6-7a in order to compare the dynamic response obtained from the use of the generated material properties with the test data. The calculated velocities at the 18-in., 36-in., and 54-in. depths are compared with velocities measured during the test in Figure 7-4.

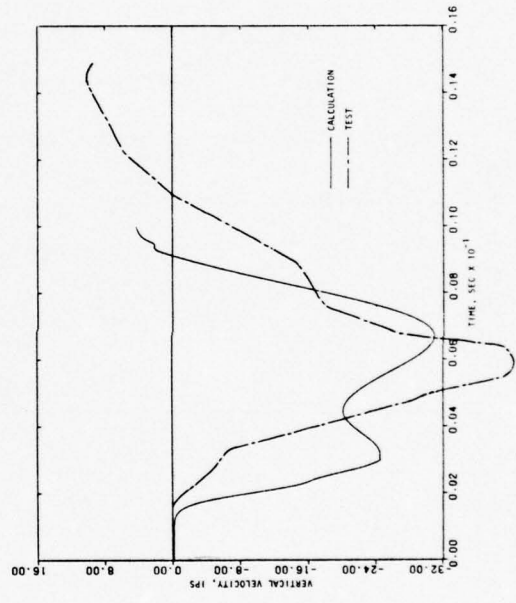
The calculated velocities at the 18- and 36-in. depths agree very well with the test data in terms of peak values and phasing, although there are differences in detail. At the 54-in. depth, the calculated velocity rises more steeply in the initial region and then exhibits an upward bulge starting at 3 msec. This bulge is very similar to the one observed in the CBMI-13-1 calculations (Fig. 6-23a). It begins somewhat earlier here, consistent with the stiffening of the material model. As mentioned in Section 6.8.4, this feature is believed to be caused by the combined action of a reflected wave and a modulus change at a break point in the stress/strain curve. It is also possible that some layering may have been present in the actual soil matrix not modeled for the calculations that may have led to the differences between the calculated and measured velocities at the 54-in. depth.

To test this possibility, another one-dimensional calculation was made using a layered configuration. The mesh used for this calculation is shown in Figure 7-5a. It is identical with the one in Figure 6-7a, except for the introduction of three layers, which are arranged to be as recommended for the CBMI-12 test (see Sec. 5.2, Fig. 5-2a). The material in the top and bottom layers, Layers 1 and 3, was assumed to be the same, and its properties were generated from those of the Layer 1 material of CBMI-12 (described in Sec. 8) by the method of Section 7.2.1. Layer 2 was assigned the properties calculated earlier for the CBMI-14 matrix.



(a) Velocity at 18-in. depth

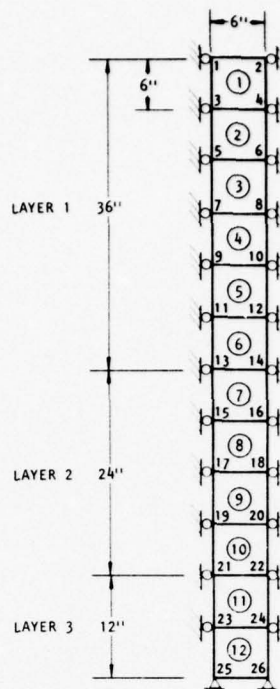
(b) Velocity at 36-in. depth



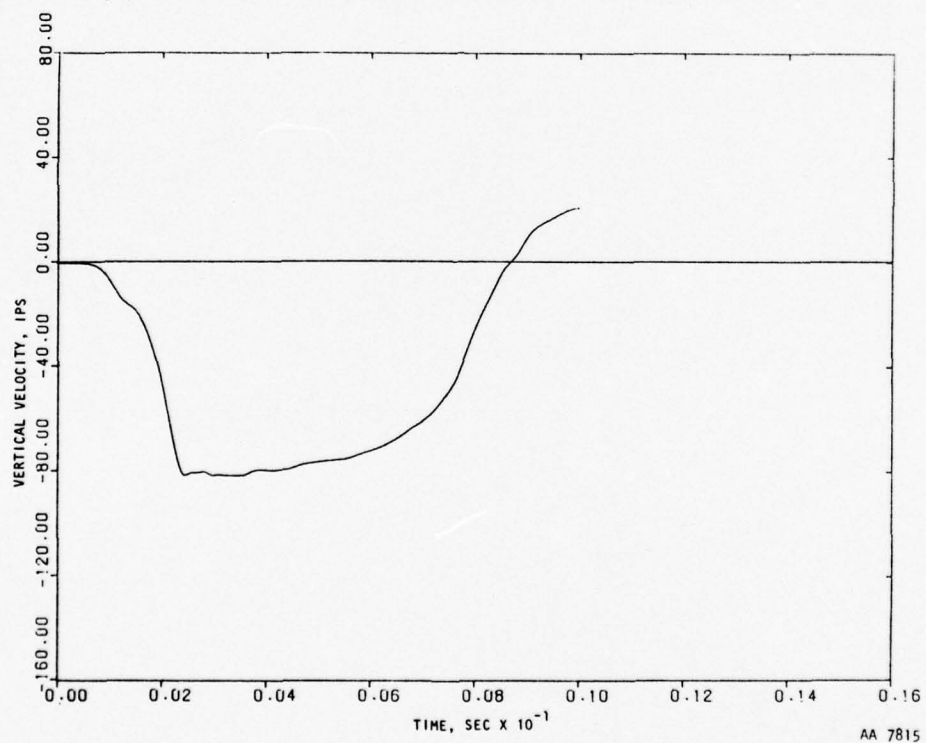
(c) Velocity at 54-in. depth

FIGURE 7-4. COMPARISON OF 1-D CALCULATION ON MATRIX COLUMN WITH CBMI-14 TEST DATA

AA 7817

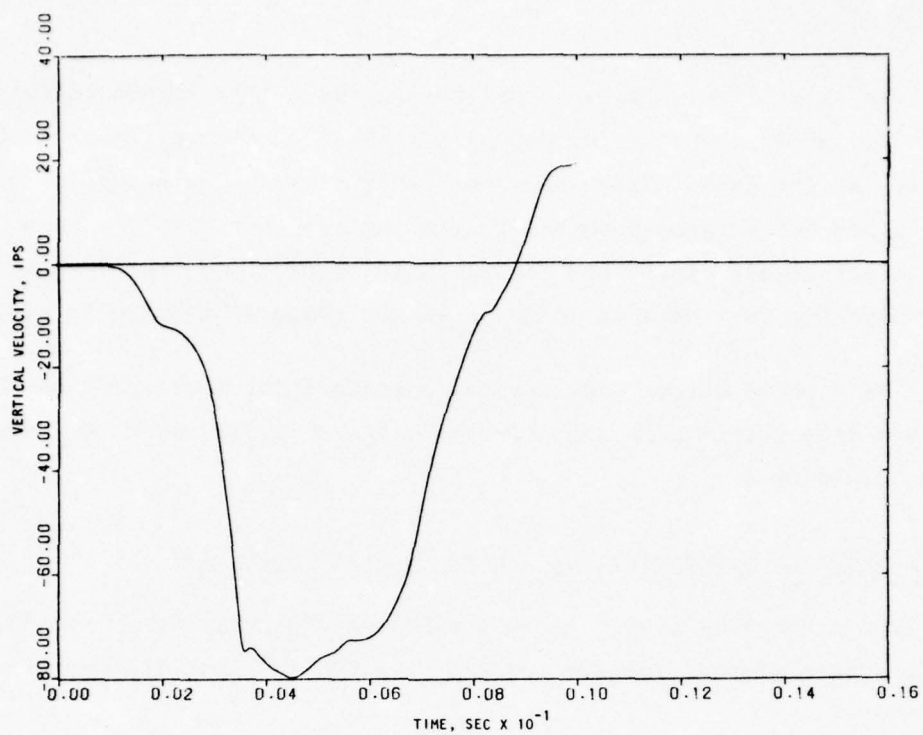


(a) Finite element mesh used in the calculation

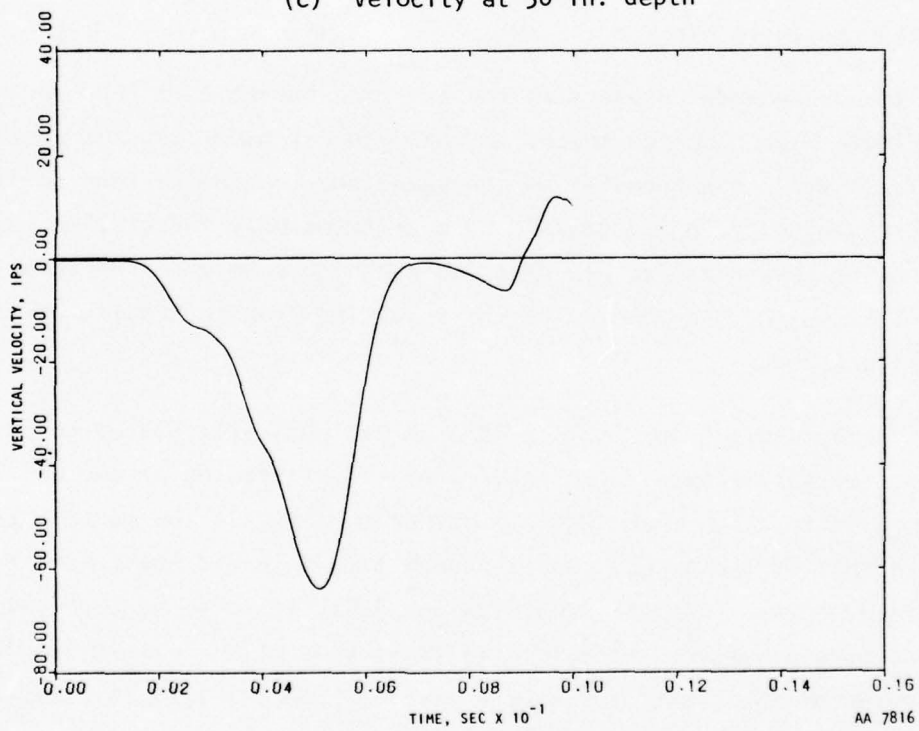


(b) Velocity at 18-in. depth

FIGURE 7-5. ONE-DIMENSIONAL CALCULATION WITH LAYERED MATRIX



(c) Velocity at 36-in. depth



(d) Velocity at 54-in. depth

FIGURE 7-5. (CONCLUDED)

The velocities obtained from the layered matrix column calculations at the 18-in., 36-in., and 54-in. depths are shown in Figures 7-5b through d. The velocity at the 54-in. depth does not exhibit the bulge noted in Figure 7-4c and has a shape somewhat resembling the test result. However, the peak values at all depths are considerably higher, and the overall agreement with the test data is inferior to the comparison shown in Figure 7-4.

The layered matrix geometry was abandoned for subsequent calculations, and a homogeneous matrix with the properties shown in Table 7-2 was used for the CBMI-14 calculations.

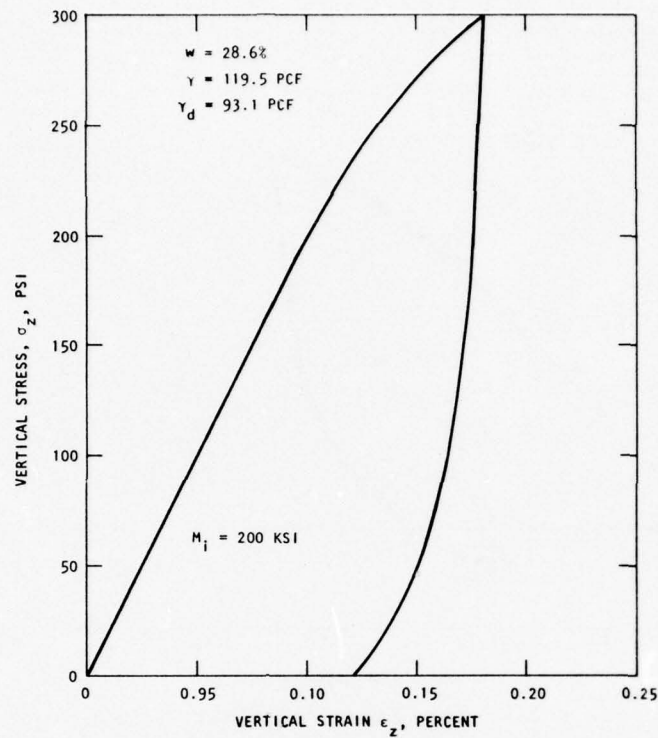
7.3 OTHER MATERIAL PROPERTIES USED IN CBMI-14 CALCULATIONS

The properties used for the borehole filler grout and the slip model at the matrix/grout interface during the CBMI-14 calculations are described herein.

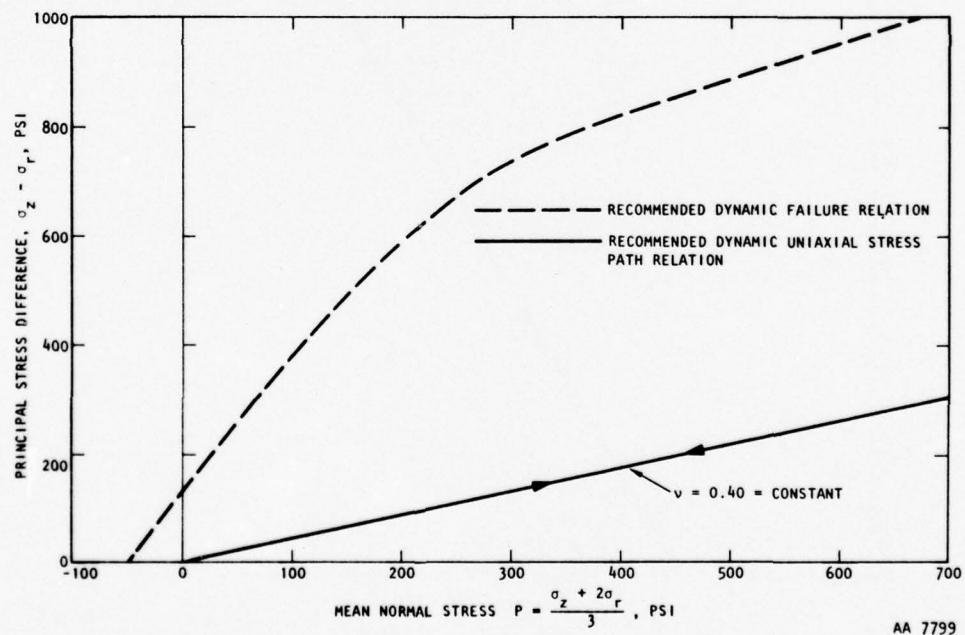
7.3.1 BOREHOLE FILLER GROUT

The recommended properties for the hard borehole filler grout are shown in Figure 7-6. The parameters of the material model for the grout are shown in Table 7-2. The behavior of the model under uniaxial loading is compared with the data in Figure 7-7. A one-dimensional calculation was performed using this model to evaluate its dynamic response. The velocities at the 18-in., 36-in., and 54-in. depths resulting from this calculation are shown in Figure 7-8.

The borehole grout in Test CBMI-14 was nominally slated to be twice as stiff as the matrix material. In view of the stiffening of the matrix due to repeated loading, there was a tendency to increase the matrix stiffness to approach that of the grout. As it turned out, this did not create a problem since, by examining Figures 7-3a and 7-6a, it is found that the initial constrained modulus of the grout is 1.29 times that of the matrix, and the secant modulus of the grout at a stress level of 300 psi is 4.16 times that

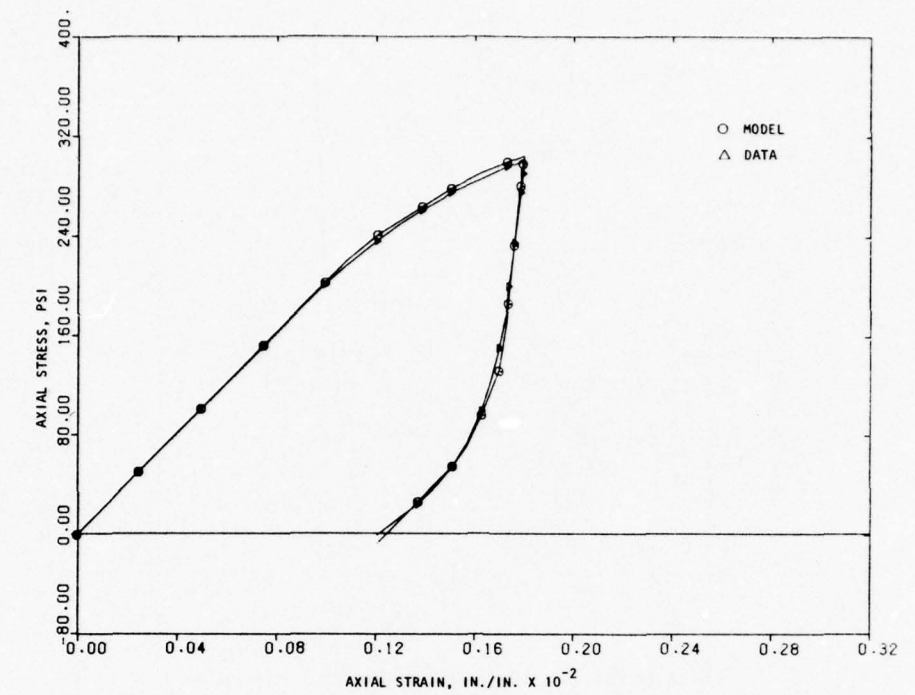


(a) Dynamic uniaxial vertical stress vs vertical strain relation

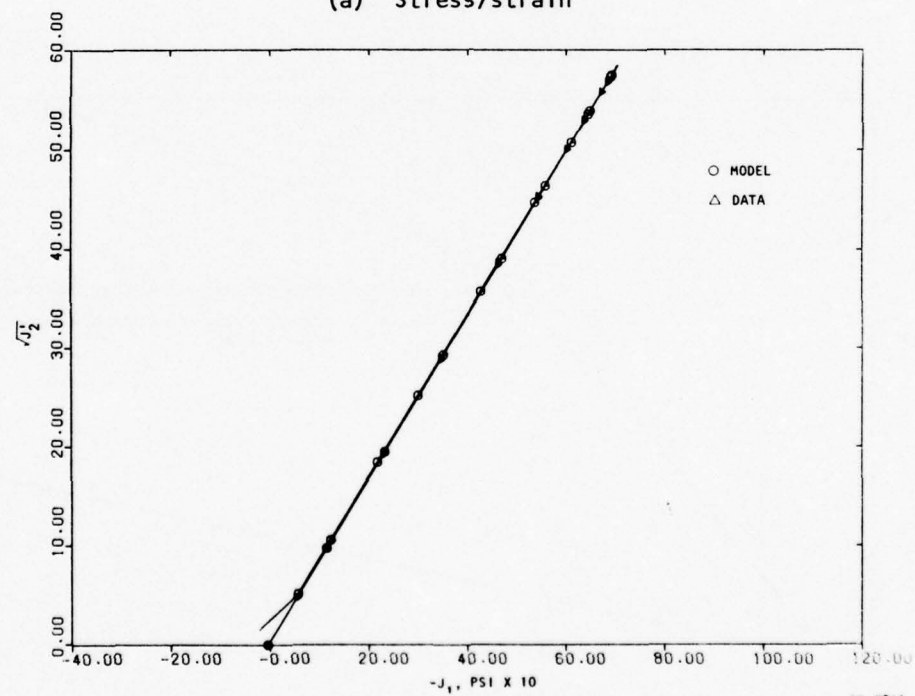


(b) Dynamic failure and uniaxial stress path relations

FIGURE 7-6. RECOMMENDED PROPERTIES FOR HARD BOREHOLE GROUT FOR CBMI-14 CALCULATIONS



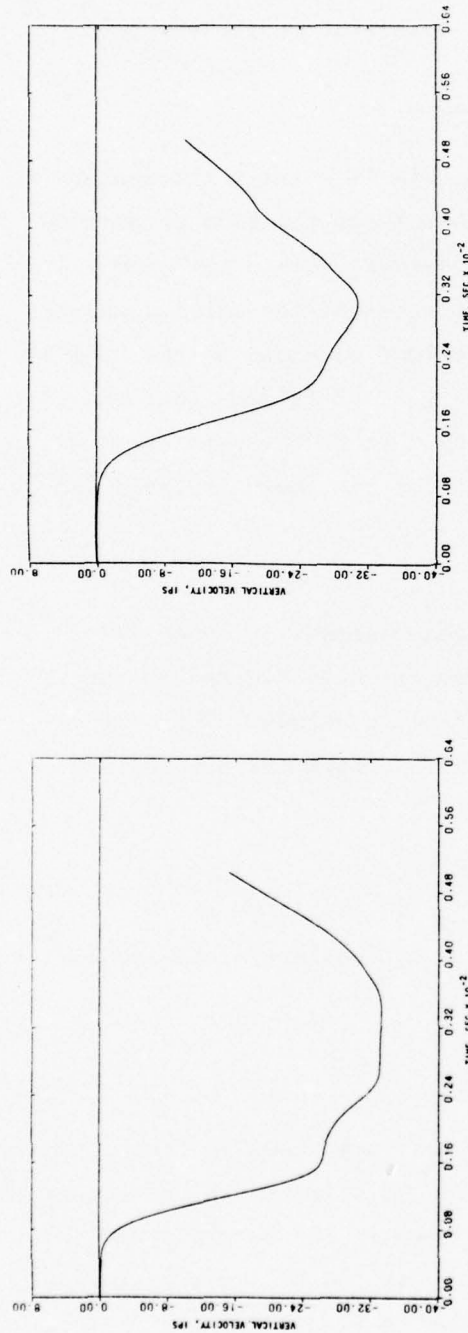
(a) Stress/strain



(b) Stress path

AA 7814

FIGURE 7-7. COMPARISON OF MODEL AND DATA FOR BOREHOLE GROUT--CBMI-14 CALCULATIONS



(b) Velocity at 36-in. depth

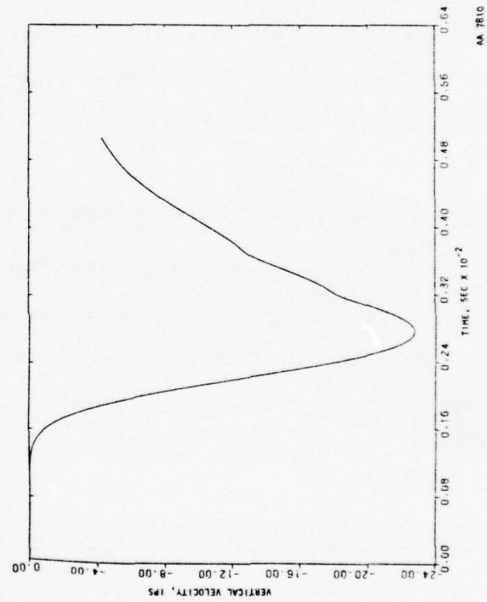


FIGURE 7-8. ONE-DIMENSIONAL CALCULATION WITH CBMI-14 BOREHOLE GROUT

of the matrix. Moreover, a comparison of the velocity-time histories of Figures 7-4 and 7-8 shows the peaks of Figure 7-8 to be smaller and attained earlier, indicating the greater stiffness of the grout compared to the matrix. Therefore, despite the stiffening of the matrix, the stiffness of the borehole grout is considered to be significantly higher than that of the matrix.

7.3.2 SLIP PROPERTIES AT MATRIX/GROUT INTERFACE

At the matrix/grout interface, the matrix is clearly the weaker material. In order to ensure a strong bond, therefore, the slip properties should be based on the failure envelope of the matrix. Since the same criterion was adopted in choosing the slip properties at the matrix/canister locking grout interface in Section 6 and the failure envelope of the CBMI-14 matrix is identical with that of the CBMI-13 matrix, it follows that the slip properties to be used in the present calculations must be the same as those used in the CBMI-13 calculations. These properties are shown in Table 6-2.

7.4 INPUT PULSE AND INTEGRATION SCHEDULE

The input pulse used in the CBMI-14 calculations is shown in Figure 7-9. The schedule of integration is also shown in Figure 7-9 and is exactly the same as the one used in the CBMI-13 calculations. The entire calculation, covering 20 msec of real-time duration, took 602 steps at an average computational time of 7.35 sec/step.

7.5 RESULTS OF THE CBMI-14 CALCULATIONS

Results obtained from the CBMI-14 calculations are presented and compared with the test data in this subsection.

7.5.1 TEST RESULTS

The data measured during the CBMI-14 test are shown in Figures 7-10 through 7-13. Motion data include the velocities, displacements, and accelerations at the 18-in., 36-in., and 54-in. depths both in the borehole and the free field. The stress gage at the 18-in. depth was the only one that remained functional for this test, and its output is shown in Figure 7-13.

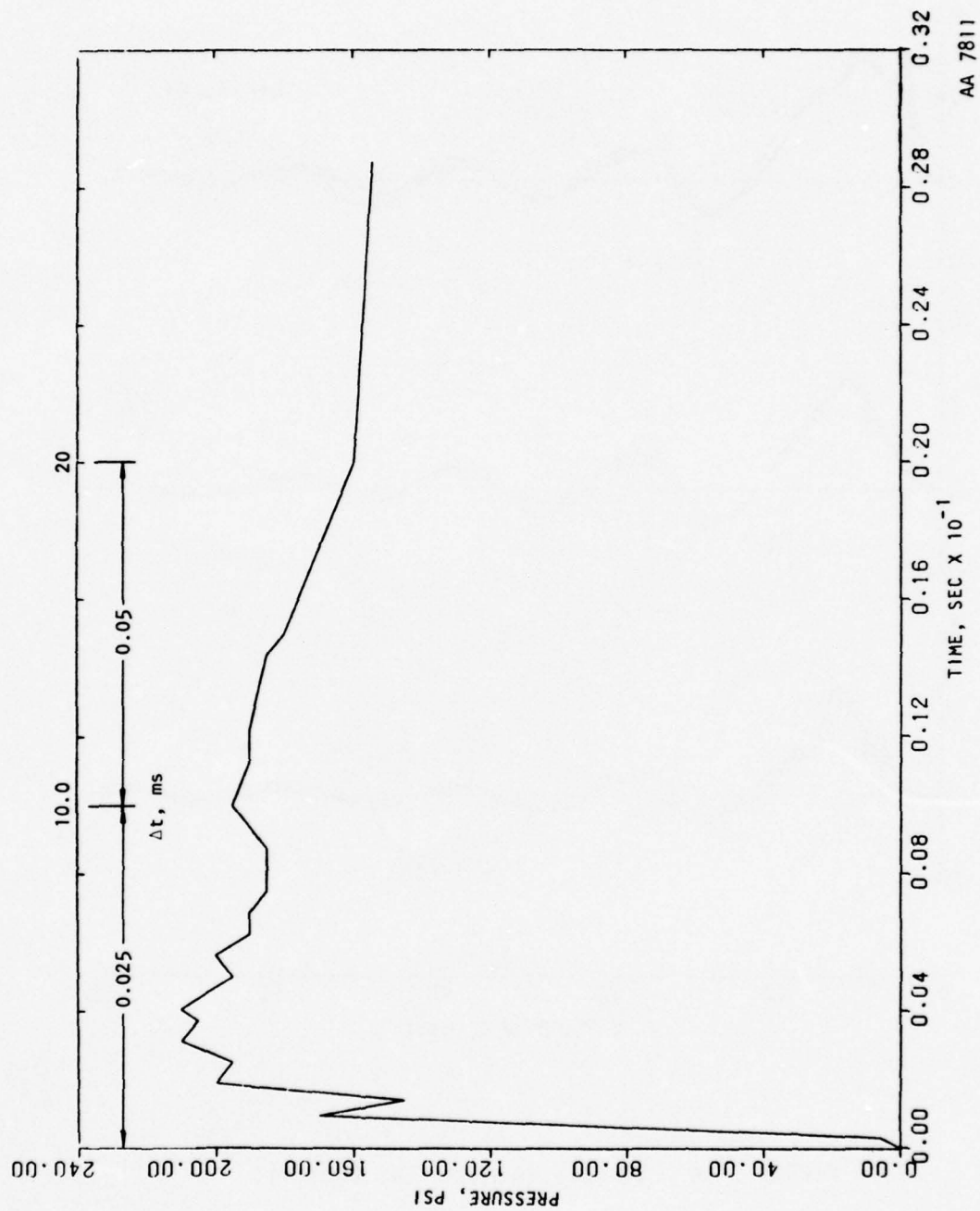


FIGURE 7-9. INPUT PULSE AND INTEGRATION SCHEDULE USED IN CBMI-14 CALCULATIONS

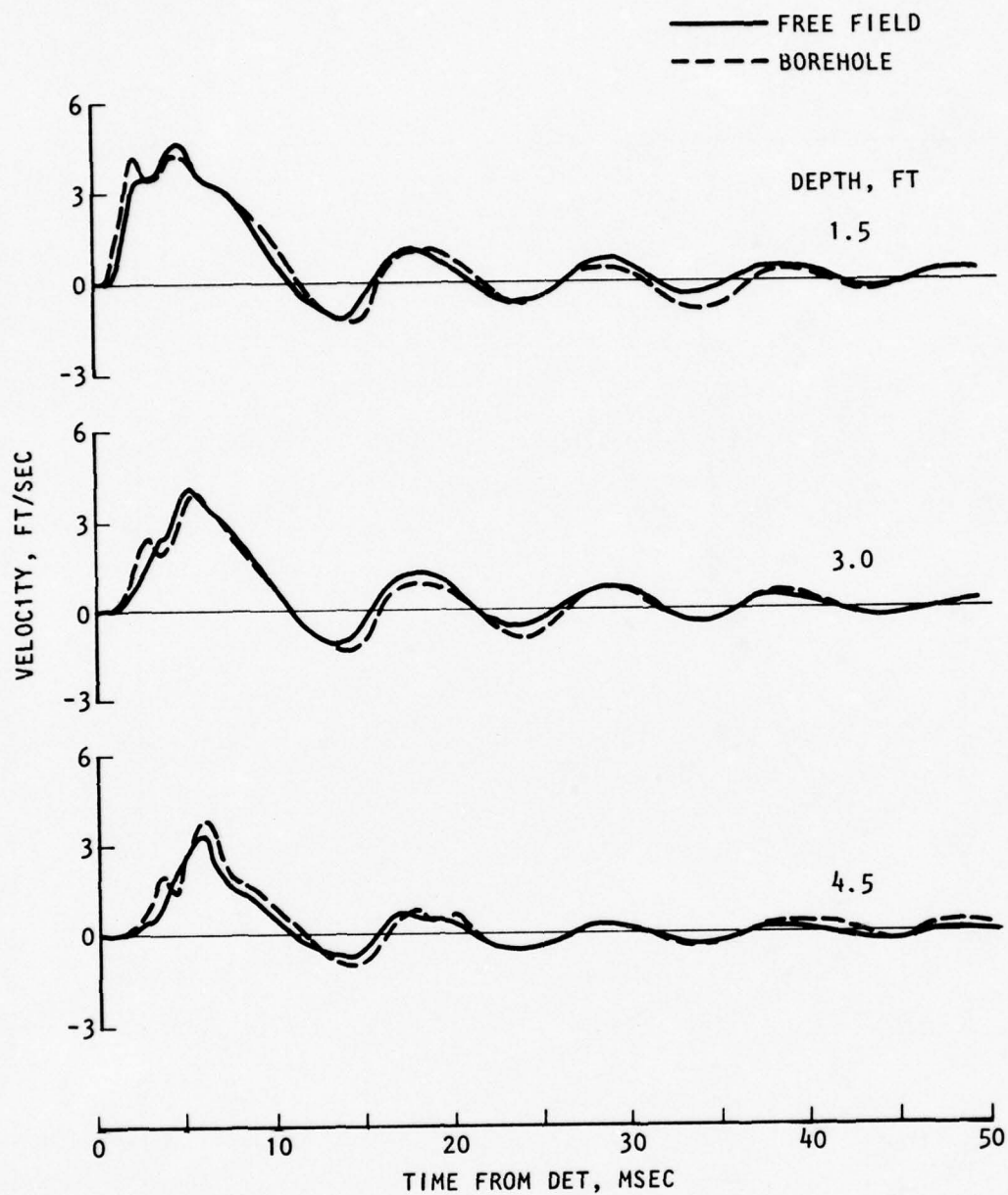


FIGURE 7-10. VELOCITIES FROM TEST CBMI-14

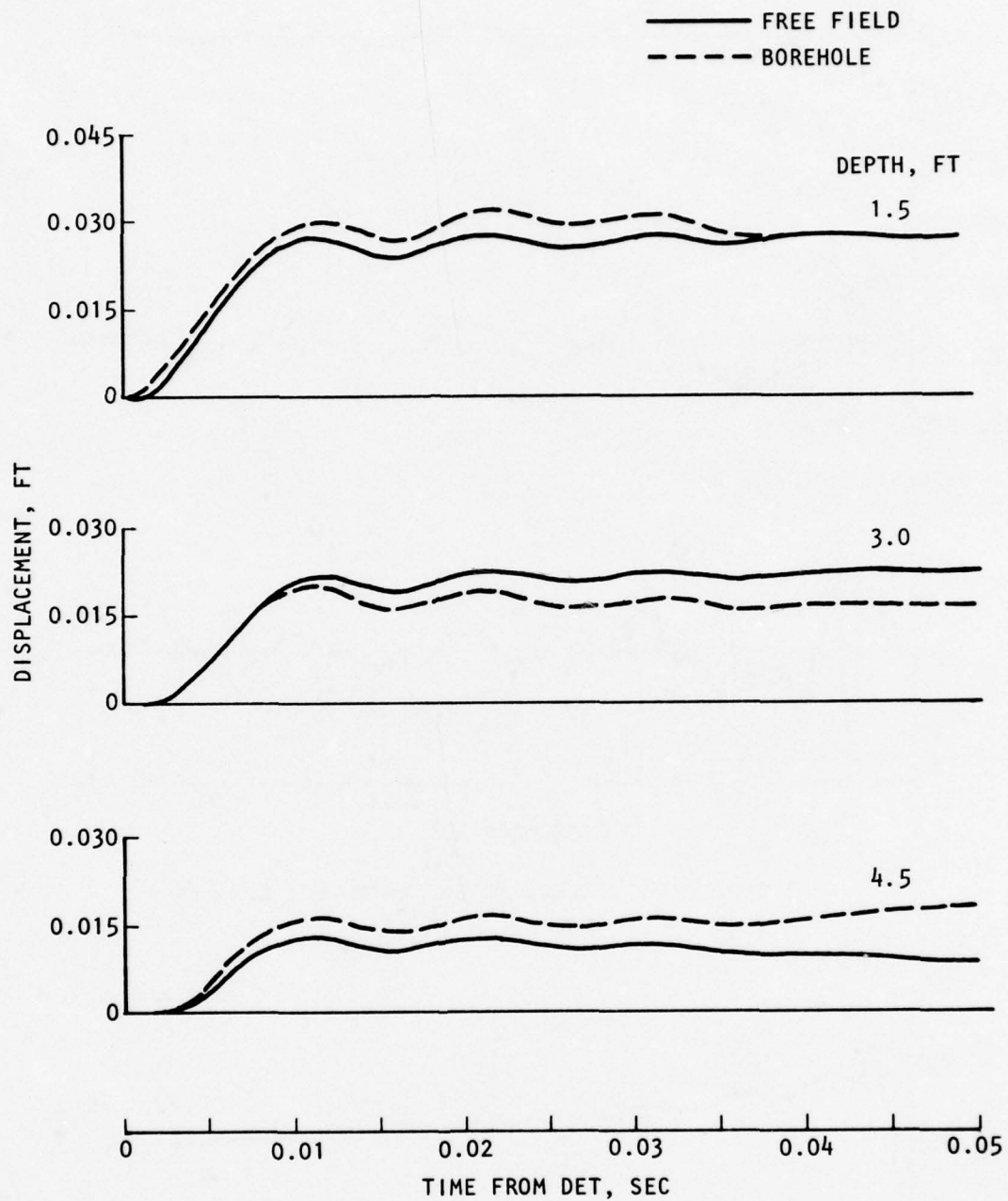


FIGURE 7-11. DISPLACEMENTS FROM TEST CBMI-14

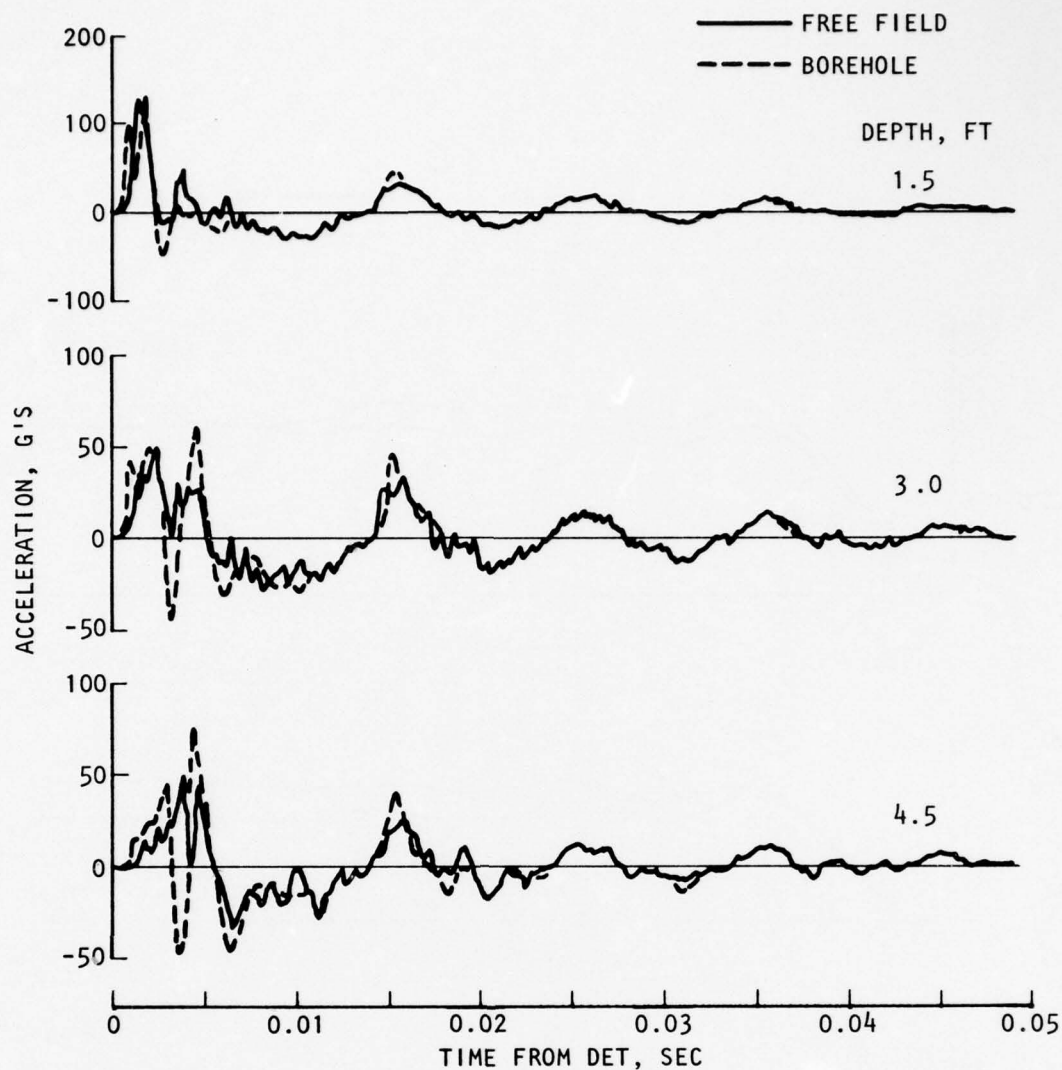


FIGURE 7-12. ACCELERATIONS FROM TEST CBMI-14

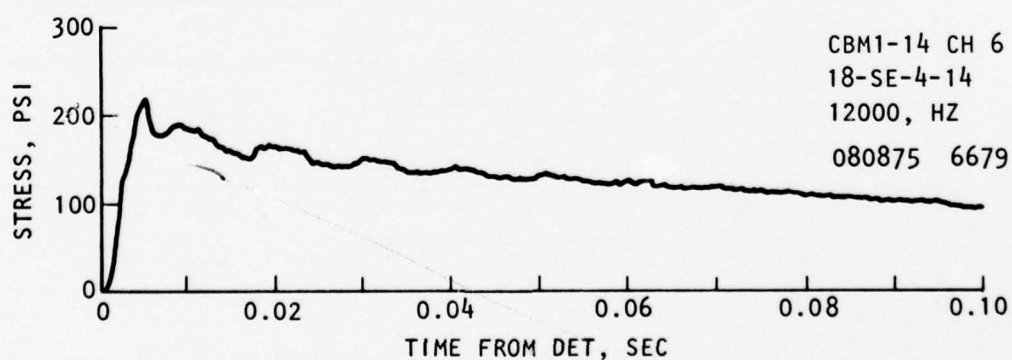


FIGURE 7-13. STRESS FROM TEST CBMI-14

7.5.2 RESULTS OF THE CBMI-14 CALCULATIONS

The results obtained from the calculations are presented in this section. Interpretations are given in Section 7.6. The velocities and displacements at the 18-in., 36-in., and 54-in. depths are compared with test data in Figures 7-14 through 7-16.

Accelerations obtained from the calculations at the same depths at both the free-field and gage locations are shown in Figures 7-17 through 7-19. As in Section 6, the acceleration plots are not overlaid in order to preserve detail.

Stresses obtained from the calculations at the 18-in., 36-in., 54-in., and 72-in. depths are shown in Figure 7-20a through 7-20d. At the 18-in. depth, stresses calculated at the free-field and gage locations are shown, along with the only stress measurement available from the test. At the 36-in. and 54-in. levels, the stresses computed at the free-field and gage locations are shown, while Figure 7-20d shows the calculated free-field stress at the SBLG base level.

7.6 INTERPRETATION OF CBMI-14 CALCULATIONS

The results of the CBMI-14 calculations presented in Section 7.5 are interpreted in this subsection and the correlation of test data and calculations is analyzed.

7.6.1 VELOCITY AND DISPLACEMENT

The velocity and displacement plots in Figures 7-14 through 7-16 show, on the whole, excellent agreement between the calculated motion at the free-field and gage locations. Peak velocities at 18-in. and 36-in. depths agree within 5%, and the phasing is so similar that the displacement plots are virtually indistinguishable. At the 54-in. depth, the velocity plots are somewhat more divergent, differing up to 20% in the peak value, and this

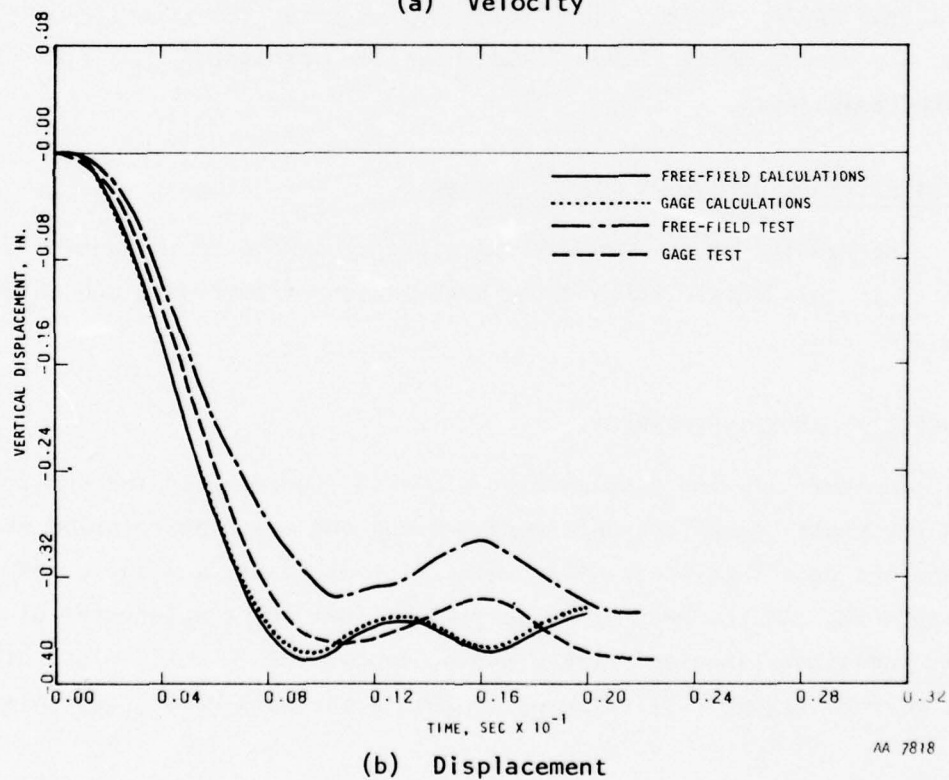
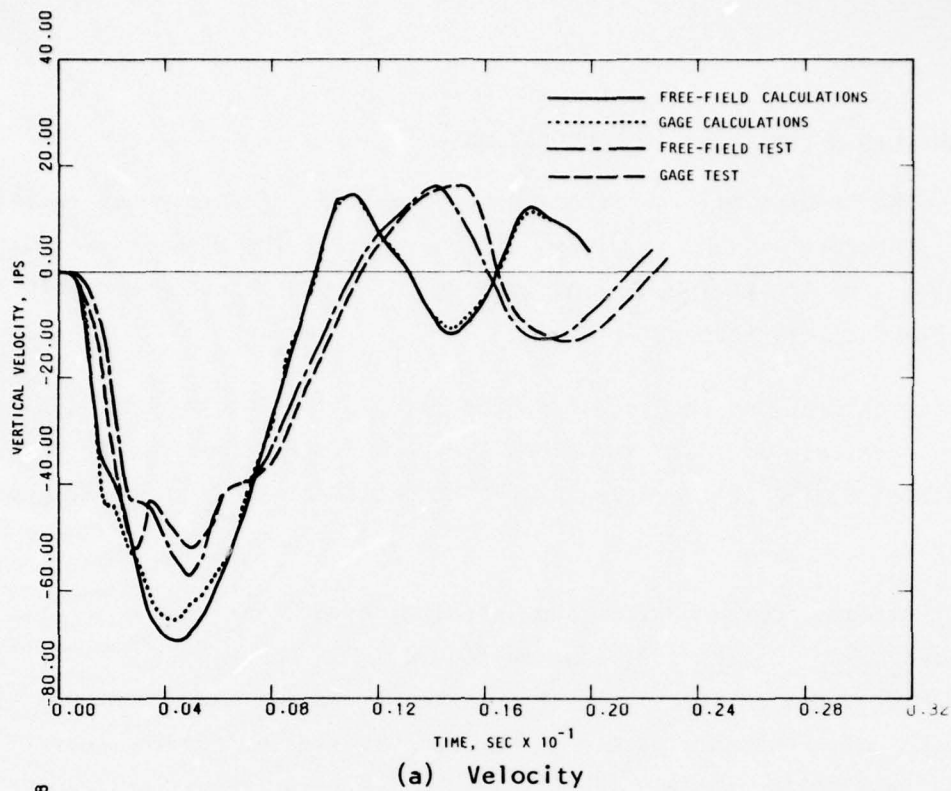
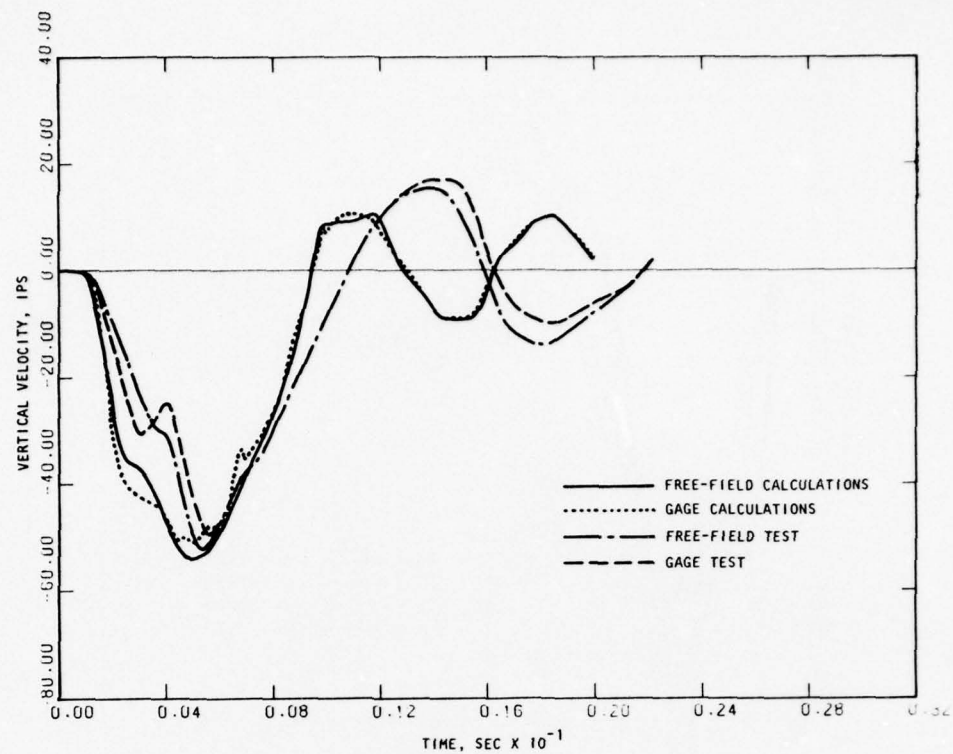
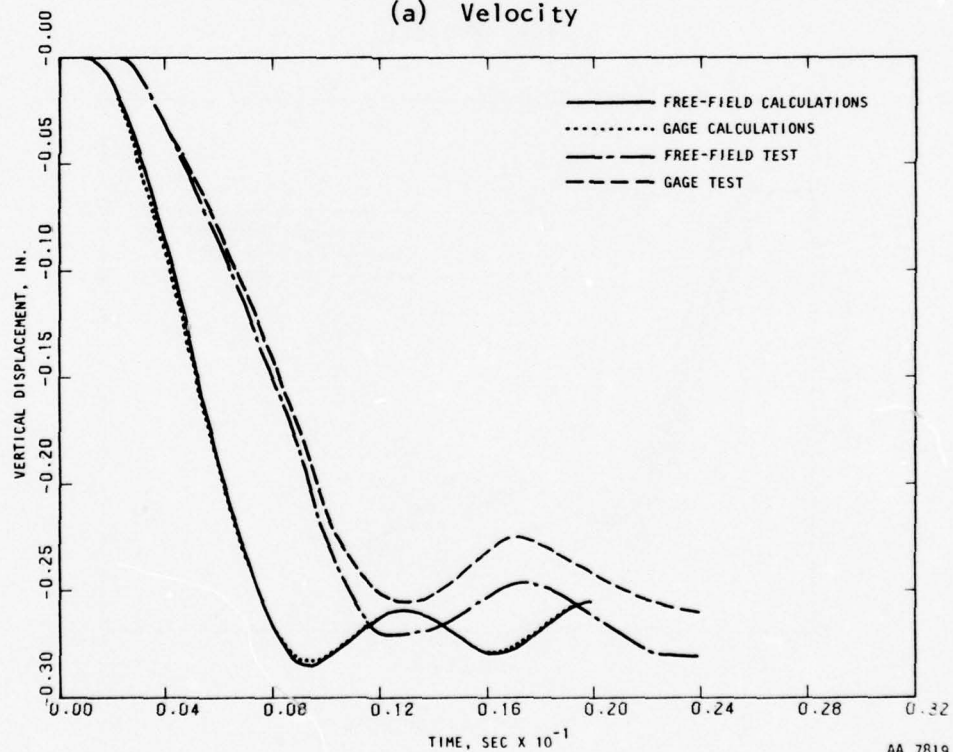


FIGURE 7-14. COMPARISON OF CBMI-14 CALCULATIONS AND TEST AT 18-IN. DEPTH



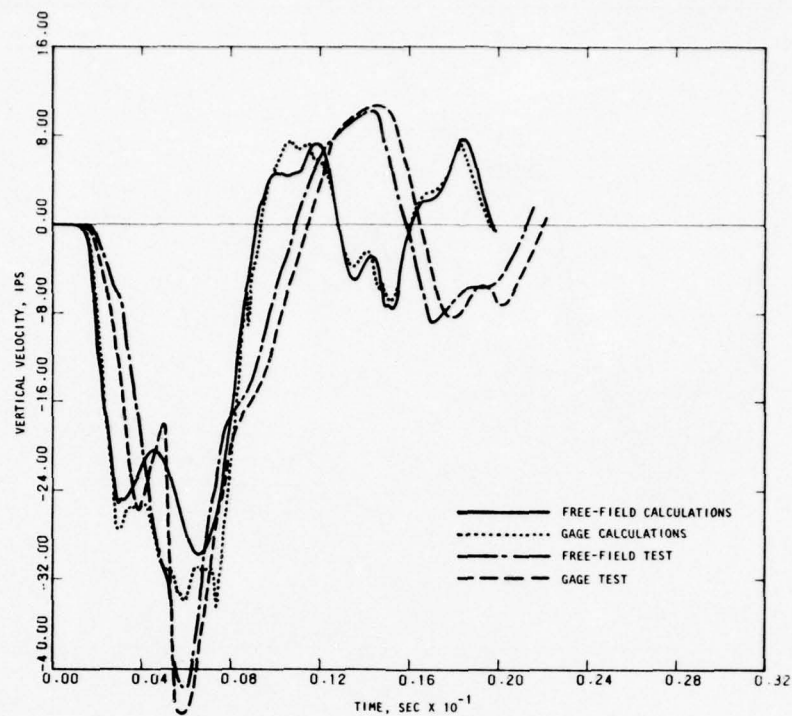
(a) Velocity



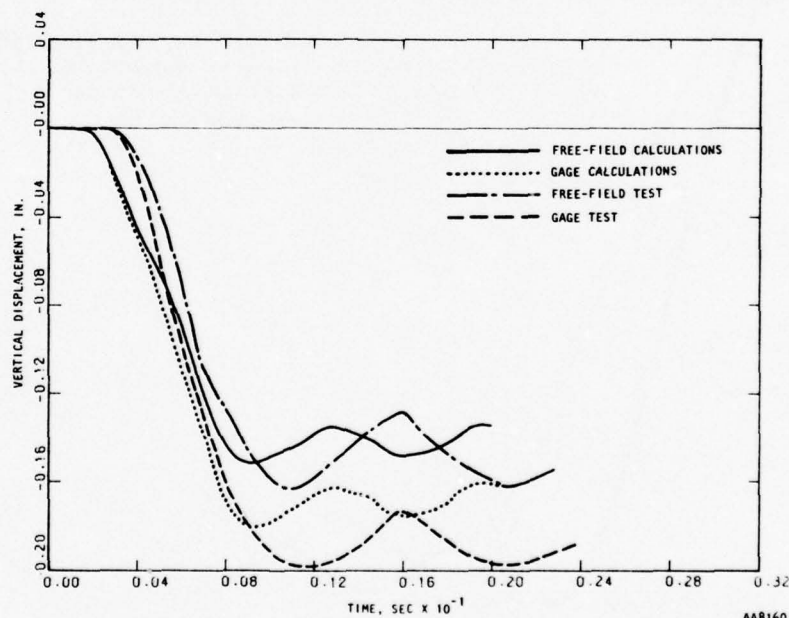
AA 7819

(b) Displacement

FIGURE 7-15. COMPARISON OF CBMI-14 CALCULATIONS AND TEST AT 36-IN. DEPTH

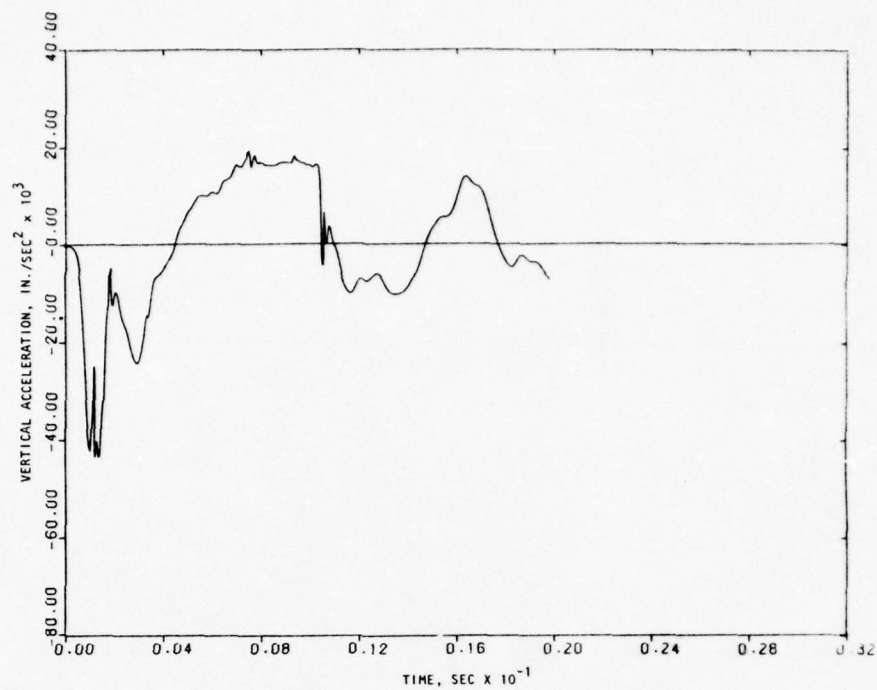


(a) Velocity

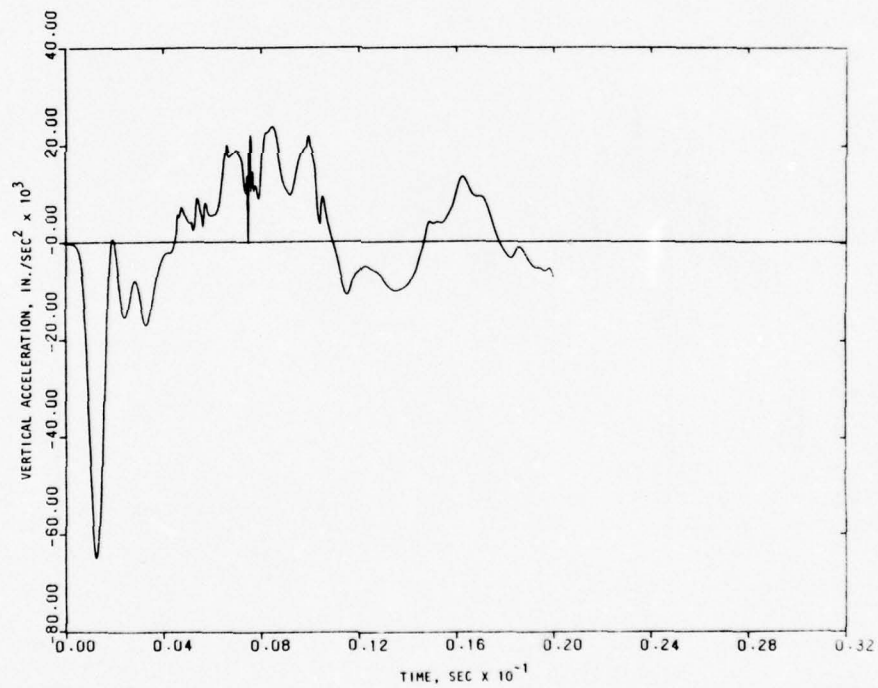


(b) Displacement

FIGURE 7-16. COMPARISON OF CBMI-14 CALCULATIONS AND TEST AT 54-IN. DEPTH



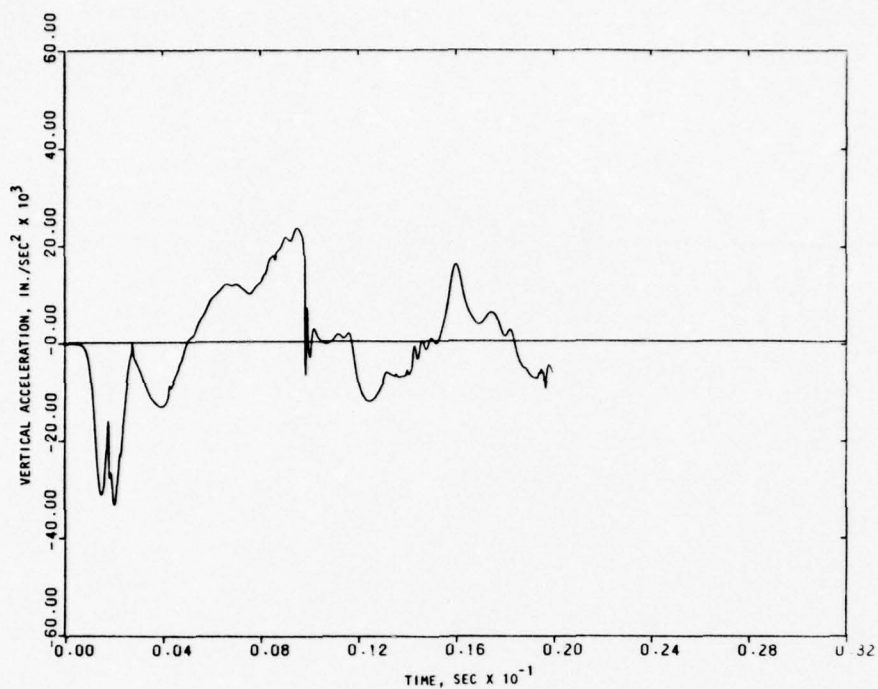
(a) Free field



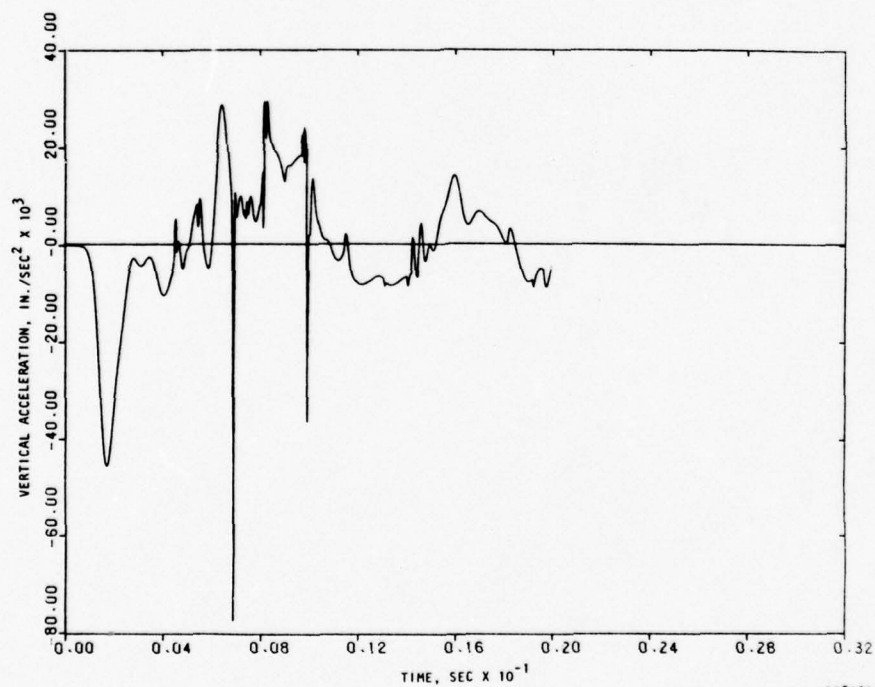
(b) Gage

AA8161

FIGURE 7-17. ACCELERATIONS AT 18-IN. DEPTH CBMI-14 CALCULATIONS



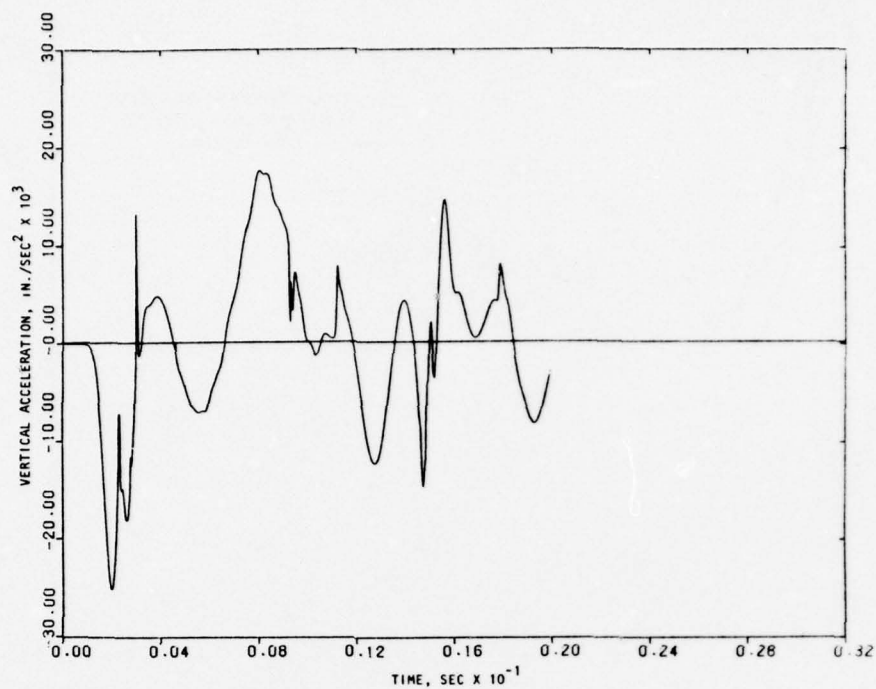
(a) Free field



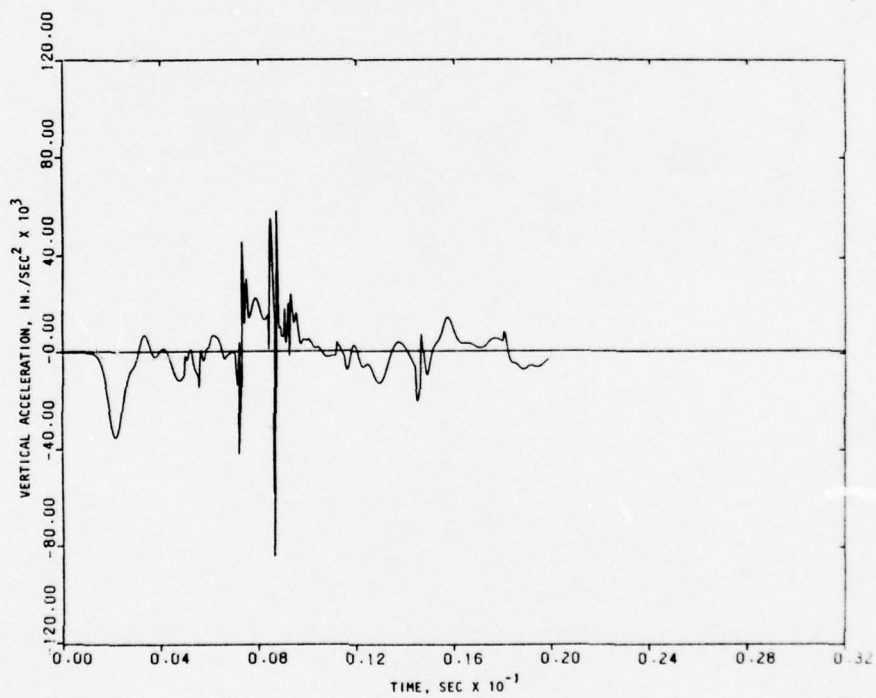
(b) Gage

AA8162

FIGURE 7-18. ACCELERATIONS AT 36-IN. DEPTH CBMI-14 CALCULATIONS



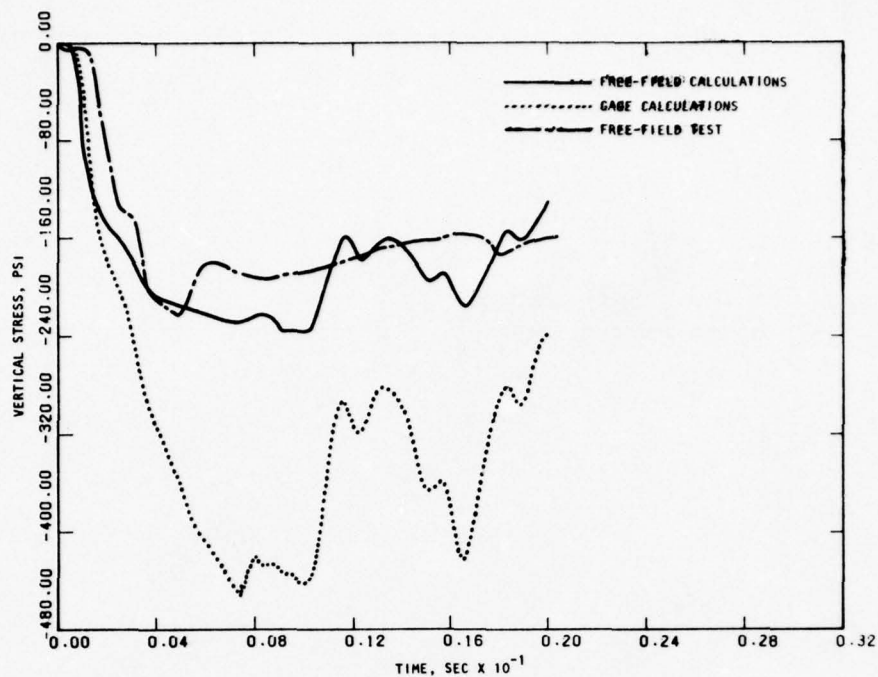
(a) Free field



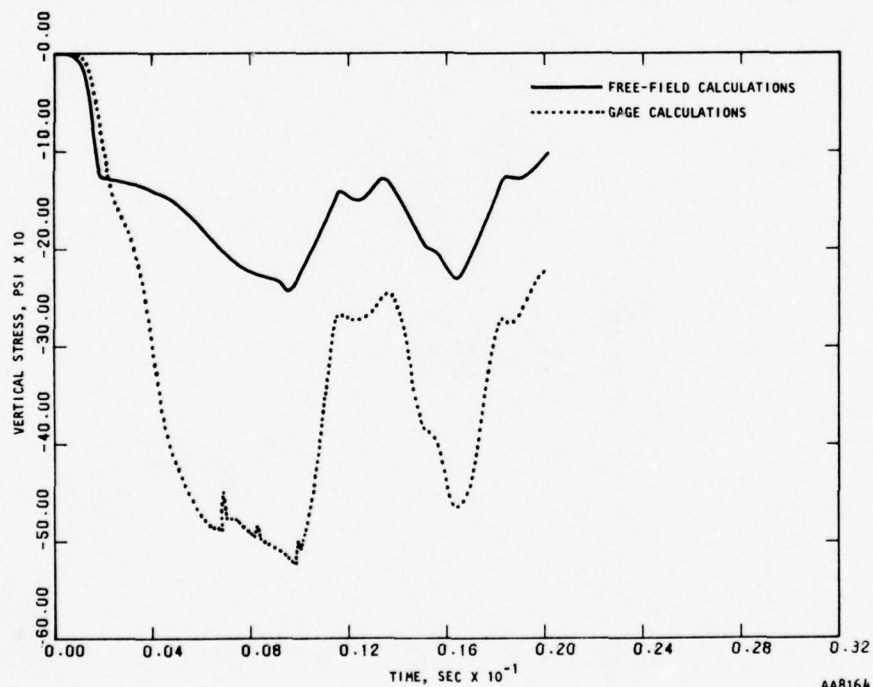
(b) Gage

AAB163

FIGURE 7-19. ACCELERATIONS AT 54-IN. DEPTH--CBMI-14 CALCULATIONS



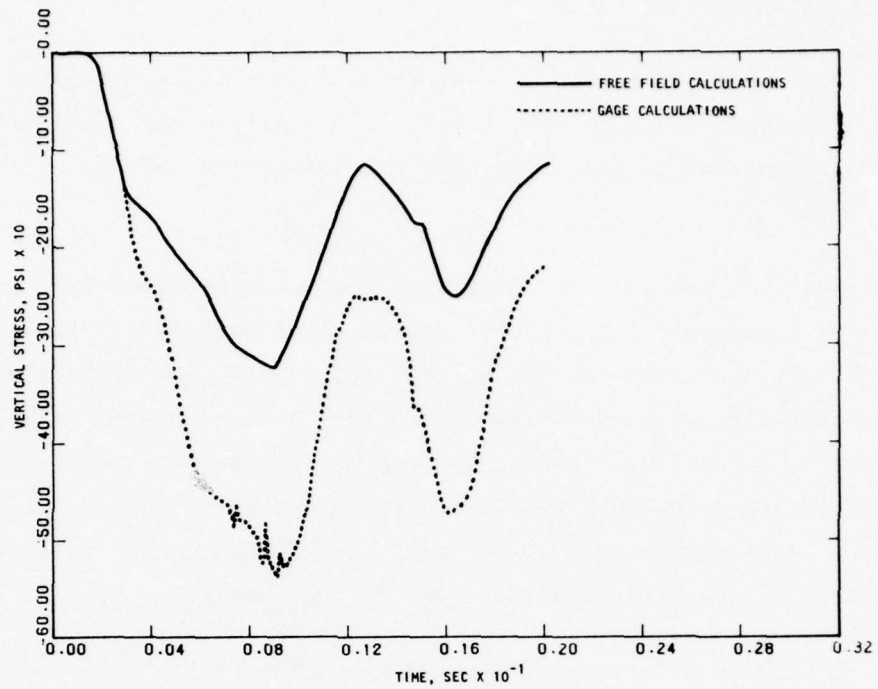
(a) Stresses at 18-in. depth



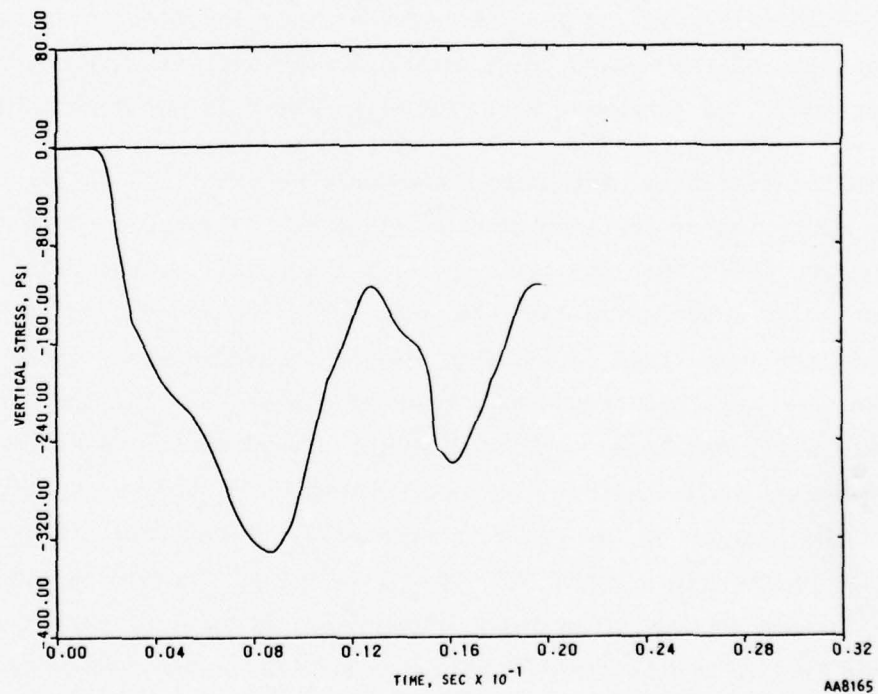
(b) Stresses at 36-in. depth

AA8164

FIGURE 7-20. STRESSES FROM CBMI-14 CALCULATIONS



(c) Stresses at 54-in. depth



(d) Free field stresses at 72-in. depth

FIGURE 7-20. (CONCLUDED)

results in about the same degree of difference in the maximum displacements. The agreement between the gage and free-field velocities and displacements is better at all depths in the calculated time histories than in the test data.

Comparison between the calculated and measured velocities and displacements is generally very good. Agreement of peak values is within about 20%, except at the 54-in. depth. The calculated peak velocities are larger and occur earlier than in the test data. The calculated velocities also return to zero earlier. Once again the calculated peak velocities show greater attenuation with depth than measured velocities. Both calculated and measured data show substantial "bounce back" of the specimen. This feature is consistent with the stiffened condition of the matrix.

The anomalous feature of the velocity plot at the 54-in. depth observed in the CBMI-13-1 and the one-dimensional calculations persists, as expected. It is felt that the peak velocity at this location is substantially decreased because of the upward bulge around 4 msec and does not represent true attenuation. The agreement with the test result is worsened as a result.

In the test data, the borehole velocities exhibit a double peak, the second peak occurring at the same time as the free-field peak. This could be explained on the basis that the first peak is the result of the pulse traveling faster through the grout while the second is attained when the pulse has propagated in the free field to the depth under consideration. The overall agreement between gage and free-field measurements in the test indicates very good bonding, which may have resulted from the use of expansive cement. But the above analysis suggests that the bond, though very good, was not perfect and allowed some motion of the grout independently of the free field. In the calculations, on the other hand, the above double-peak feature is not observed. This is thought to be a consequence of the use of nearly perfect interface bonding in the calculations, i.e., assuming a stronger bond than what probably prevailed during the test.

7.6.2 ACCELERATION

The calculated acceleration plots of Figures 7-17 through 7-19 have the same general features observed in the CBMI-13-1 calculations. The accelerations at the gage and free-field locations agree quite well except for occasional large spikes at the gages. The gage accelerations have somewhat higher peaks and show more high-frequency oscillations. The maximum downward acceleration in the free field is about 120g at the 18-in. depth and 60g at 54 in.

On comparing the calculated accelerations with the measured accelerations, it is seen that the free-field accelerations agree quite well in their peak values. The test data (Fig. 7-12) show maximum downward accelerations of 130g and 50g at the 18-in. and 54-in. depths, respectively, as against the calculated values quoted above. The borehole accelerations show larger peak values in the test data just as in the calculations. Phasing agreement between calculations and test is less satisfactory.

7.6.3 STRESS

In Figure 7-20a the only available measured stress is compared with the calculated stress in the free field at 18-in. depth. The correlation is seen to be very good.

The calculated stresses in the free field at depths of 36 in., 54 in., and 72 in. show progressively clearer indications of reflection from the SBLG base.

Calculated stresses in the free field are compared with those at gage locations at the 18-in., 36-in., and 54-in. depths in Figures 7-20a through 7-20c. The gage stresses are about twice the free-field stresses. An explanation of this is to be found in the fact that the borehole grout moves with the free field. Since the entire borehole is filled with one uniform material, this implies that the strain in the grout matches that in the free field. Therefore, the stresses in the grout and the free field

are in the proportion of their stiffnesses. This situation is to be contrasted with that in the CBMI-13-1 calculations, where compatibility of motion between gage and free-field locations did not imply that of strains. These considerations are important in formulating recommendations for the placement of stress gages.

7.7 CONCLUSIONS AND DISCUSSION

It has been shown that velocity-time histories at the borehole and free-field locations are in very good agreement both in the calculations and in the test data. A factor contributing to this agreement may have been the interface bond between the borehole grout and the free-field matrix. In the calculations, near perfect bonding was assumed, while in the test, use of the expansive cement probably led to a very good bond. Moreover, while there are differences between the calculated and measured waveforms, the similarities between the measured velocities in the free field and borehole and the corresponding similarity in the calculations forms a basis on which a general observation is made.

A velocity gage embedded in a grout substantially stiffer than the matrix material faithfully follows the motion of the free field, if good interface bonding between the borehole and matrix is maintained.

Additionally, the above conditions lead to strain matching rather than stress matching between the borehole and free field. Therefore, guidelines for installing stress gages will demand a different set of placement conditions.

SECTION 8

CALCULATION OF TEST CBMI-12

As described briefly in Section 5, the CBMI-12 test was conducted with a virgin matrix specimen. The borehole grout, which was nominally concocted to have a stiffness one-half that of the matrix material, turned out to be extremely soft, and this resulted in difficulties in both the test and the calculations.

8.1 FINITE ELEMENT MESH

The finite element mesh used in the CBMI-12 calculations is shown in Figure 8-1. The configuration is identical with that used for the CBMI-14 calculations (Fig. 7-1) except that the matrix in this case has three distinct layers as described in Section 8.3. Also, unlike the CBMI-13 and CBMI-14 tests, this test did not employ a 2-in. deep layer of soil at the top of the borehole.

8.2 MATERIAL MODELS

The material model parameters used in the CBMI-12 calculations are discussed in this subsection.

8.2.1 MATRIX MATERIAL

Based on laboratory tests on specimens taken from the matrix, WES recommended use of three distinct layers (Ref. 8). The top and bottom layers were found to have identical properties, with an initial stiffness considerably less than that of the intermediate layer, but with a tendency to harden at larger strains in contrast to the intermediate layer. The recommended properties are shown in Figure 8-2.

The properties of Layer 2 were the ones used in the CBMI-13 calculations. The model constructed for this material is described in Section 6.2, and its parameters are shown in Table 6-1 and they are repeated in Table 8-1. The uniaxial behavior of the model is compared with the WES recommendation in Figure 6-3.

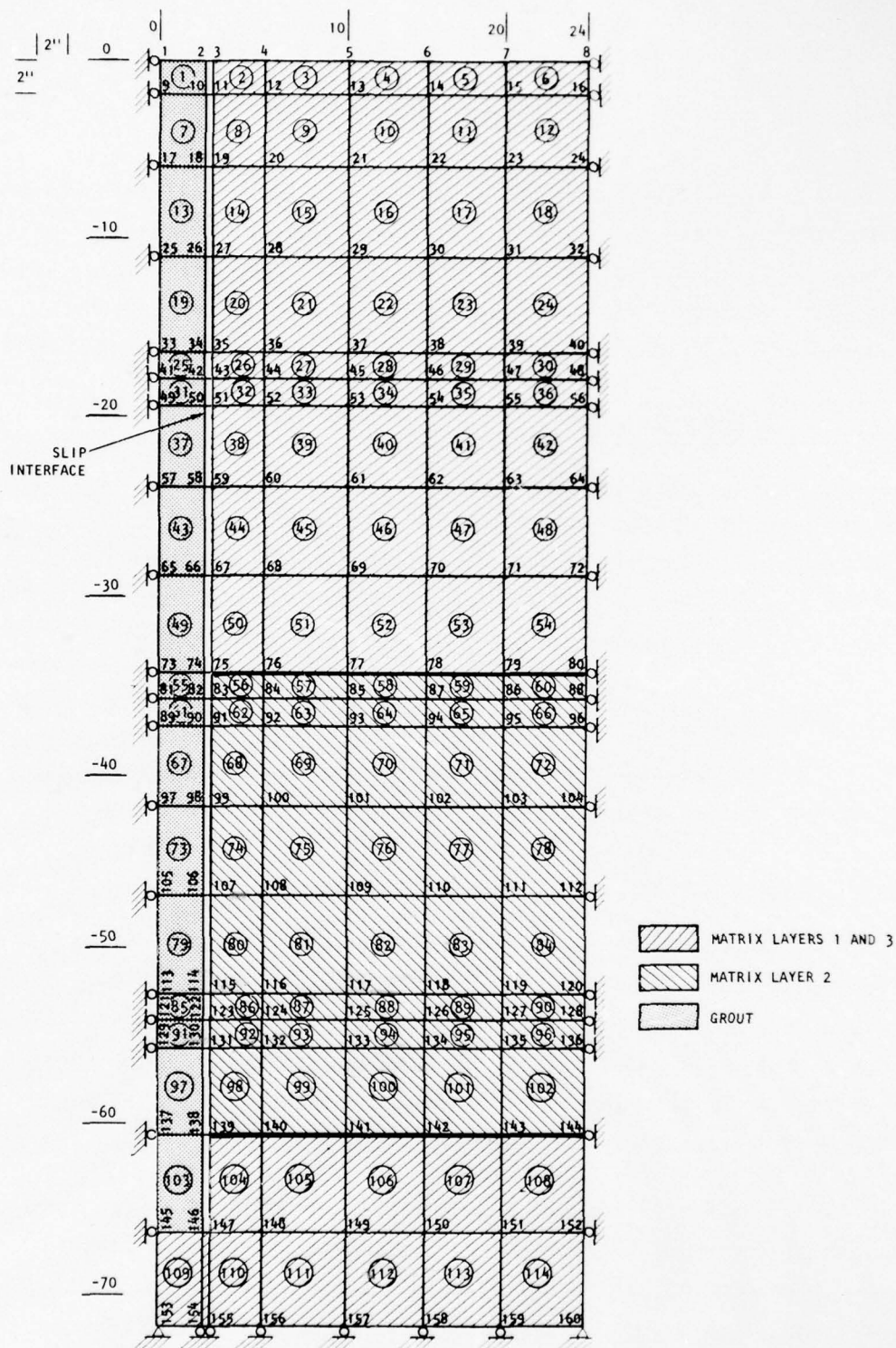
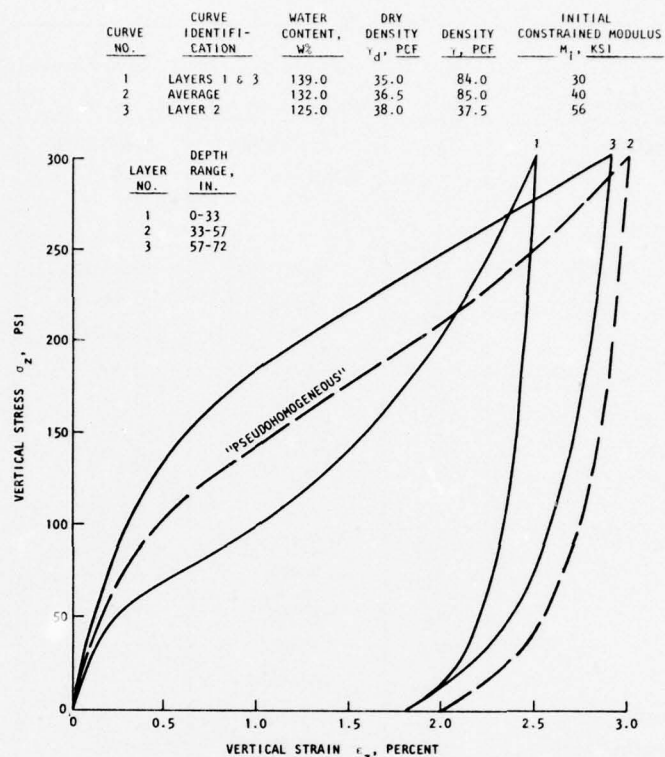
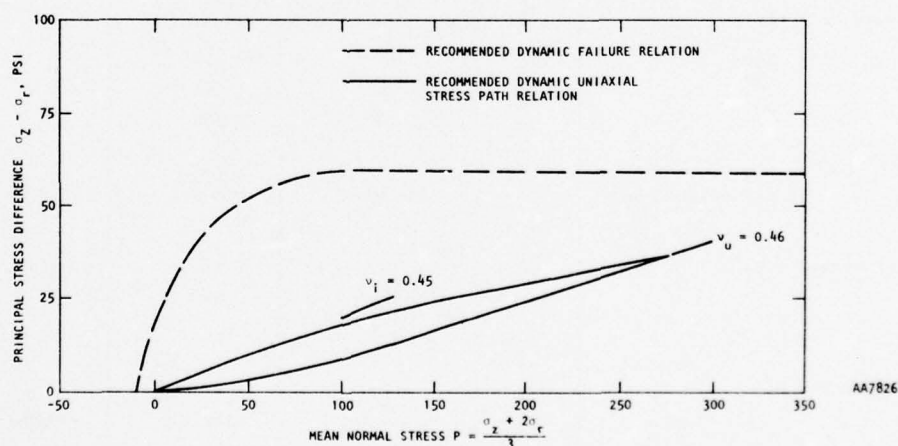


FIGURE 8-1. FINITE ELEMENT MESH USED IN CBMI-12 CALCULATIONS



(a) Recommended dynamic uniaxial strain vertical stress vs vertical strain relations



(b) Recommended dynamic failure and uniaxial stress path relations for Layer 1 (0 to 30-in. depth range) and Layer 3 (57 to 72-in. depth range)

FIGURE 8-2. RECOMMENDED PROPERTIES FOR LAYERS 1 AND 3 OF CBMI-12 FREE-FIELD MATERIAL

TABLE 8-1. PARAMETERS OF MATERIAL MODELS USED IN CBMI-12 CALCULATIONS

Quantity and Units	Symbol	Material		
		Matrix Layer 1/3	Matrix Layer 2	Borehole Filler Grout
Mass Density, lb-sec ² /in. ⁴	ρ	0.0001258	0.00013105	0.00006545
Unit Weight, pcf	γ	84	87.5	43.7
<u>Bulk Modulus: Loading</u>				
Strain break points, in./in.	B ₁	-0.002109	-0.001875	-0.0046875
	B ₂	-0.01219	-0.004843	-0.3781
	B ₃	-0.02031	-0.009844	-0.4594
Load moduli, psi	B ₄	21,466	30,982	1,552
	B ₅	5,998	19,107	124
	B ₆	10,302	6,284	905
	B ₇	18,848	5,477	5,022
<u>Unload/reload:</u>				
Control line slopes, psi	B ₁₁	4,950	5,036	122.80
	B ₁₂	2,400	2,000	59.45
Unload moduli, psi	B ₈	124,133	71,143	32,945
	B ₁₆	43,446	26,905	944
	B ₁₇	13,291	8,112	528
Tension: Bulk modulus, psi	B ₁₀	5,000	3,500	1,000
Shear modulus, psi	G ₁₀	200	300	100
<u>Poisson's Ratio: Loading</u>				
Break points, psi	G ₆	-79	-94	-- --
Load Poisson's ratio	G ₇	-175	-173	-- --
Load Poisson's ratio	G ₁	0.45	0.416	0.4
	G ₁₁	0.47	0.453	-- --
	G ₁₂	0.4765	0.468	--
<u>Unload/reload</u>				
Control line slope, dimensionless	G ₈	-0.0146	-0.03	-0.014838
	G ₉	--	--	--
Unload Poisson's ratio	G ₂	0.46	0.44	0.466
	G ₁₃	0.481	0.46	0.48
	G ₁₄	--	--	--
<u>Yield Parameters</u>				
Cohesion, psi	Y ₁₀	-204.176	-162.175	-10,000
	Y ₁₁	9.5	19.4	5.4
Slope	Y ₁₂	-0.12979	-0.16402	-0.01875
von Mises limit, psi	Y ₁₆	36	46	185
Tension cutoff, psi	Y ₂₅	29	61	14

AA8193

The parameters of the model constructed to represent Layers 1 and 3 are shown in Table 8-1. The uniaxial behavior of this model is compared with the WES recommendations in Figure 8-3.

8.2.2 BOREHOLE FILLER GROUT

The borehole filler used in Tests CBMI-12 and -13 were the same material. The recommended properties of this material are shown in Figure 5-2. The parameters of the material model are shown in Table 6-1 and repeated in Table 8-1. The uniaxial behavior of the model is compared with data in Figure 6-4.

8.2.3 MATRIX/GROUT INTERFACE

As discussed in Section 6.3, the properties of the slip elements at this interface are governed by the failure envelope of the grout. The properties selected for the slip model are the same as the ones used in the CBMI-13 calculations, and they are shown in Table 6-2.

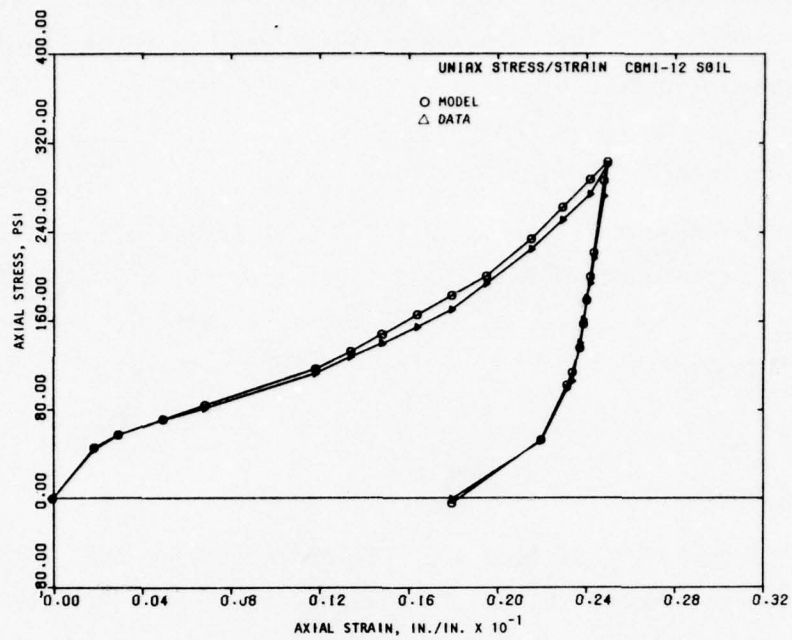
8.3 PRELIMINARY CALCULATIONS

Preliminary, one-dimensional calculations were performed with both the matrix and the borehole filler grout in order to assess the dynamic behavior of the material models prepared for these materials. These calculations are discussed below.

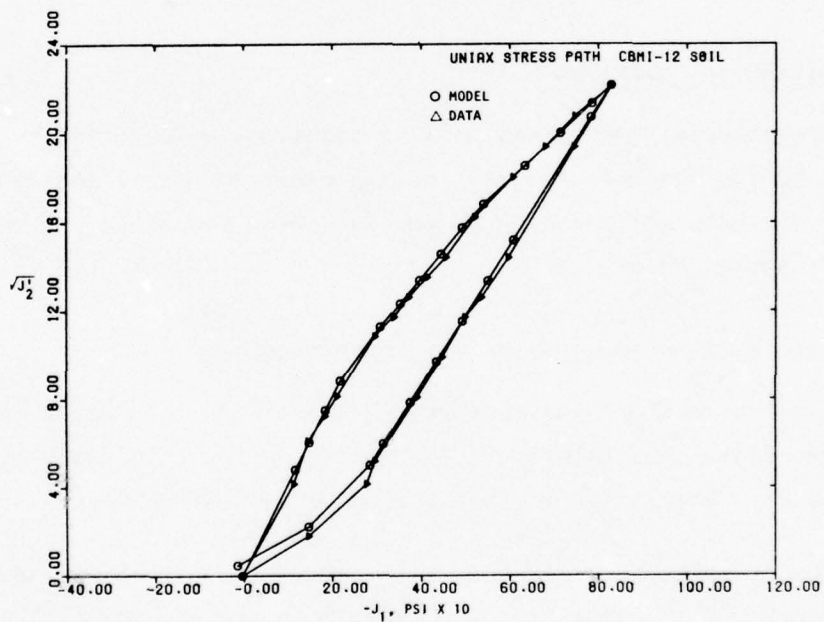
8.3.1 ONE-DIMENSIONAL CALCULATION WITH MATRIX COLUMN

A one-dimensional calculation was made with the matrix material assuming the recommended layering. The mesh used for this calculation is shown in Figure 8-4a; it is the same one shown earlier in Figure 7-5a.

The velocity obtained from this calculation at the 18-in. depth is shown in Figure 8-4b. Also shown in Figure 8-4b are the velocities at the same depth obtained in a one-dimensional calculation performed by WES and the



(a) Uniaxial stress/strain relation



(b) Uniaxial stress path

FIGURE 8-3. MATERIAL MODEL FOR LAYERS 1 AND 3 COMPARED WITH DATA--CBMI-12 CALCULATIONS

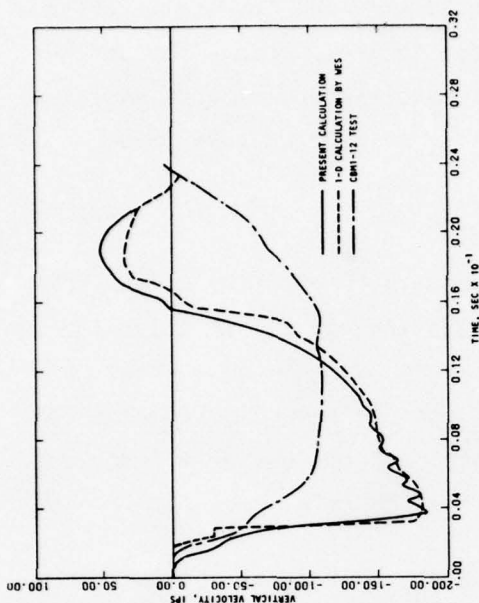
CBMI-12 test results. It is seen that the two one-dimensional calculations are in complete agreement and both show an earlier, more rapid return of the velocity to zero in comparison with the test data. This suggests that some differences probably exist between the recommended material properties of the matrix shown in Figure 8-2 and the properties that actually prevailed during the test. These results also indicate the kind of differences to be expected between the results of the final CBMI-12 calculations and the test data.

8.3.2 ONE-DIMENSIONAL CALCULATION ON GROUT COLUMN

The numerical difficulties expected from the properties of the soft borehole grout have been discussed in Sections 5.3 and 6.6.2. In order to assess these problems, a one-dimensional calculation was made on a grout column. The mesh used for this calculation was the one shown in Figure 6-7a, i.e., similar to that shown in Figure 8-4a, except for the use of a homogeneous material instead of the layered configuration shown therein.

The velocity, displacement, and stress at the top, as well as the velocity at a depth of 18 in., obtained from this calculation are shown in Figure 8-5a through 8-5d. All these quantities show unrealistically large peak values: a stress peak of almost 800 psi and velocity peaks of 2000 ips and 1600 ips at the top and 18-in. depth, respectively. The velocity and stress at the top show large amplitude oscillations caused by the numerical problems associated with corner points of the stress/strain curve (Sec. 5.3). A comparison of the arrival times of the peak at 18-in. depth in Figures 8-4b and 8-5b illustrates the considerable difference between the wave speeds of the matrix and the grout.

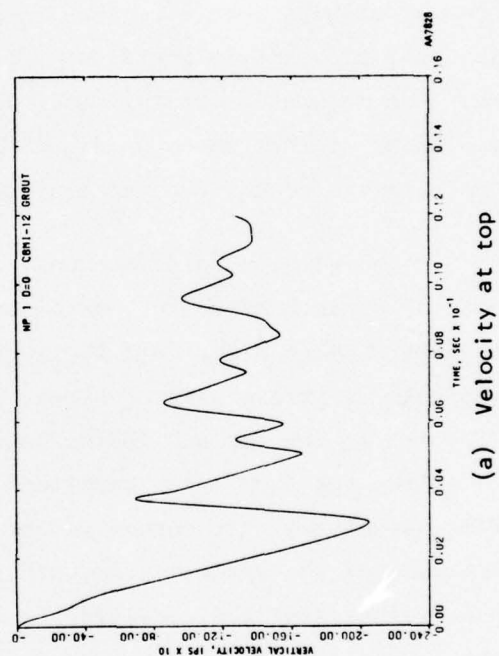
The response of the grout was found to be quite influential on the final two-dimensional CBMI-12 calculations, but the numerical anomalies noted above were considerably toned down by the beneficial influences of the interface shear transfer and the much larger mass of the soil matrix compared to the grout.



(a) Finite element mesh used in the calculation

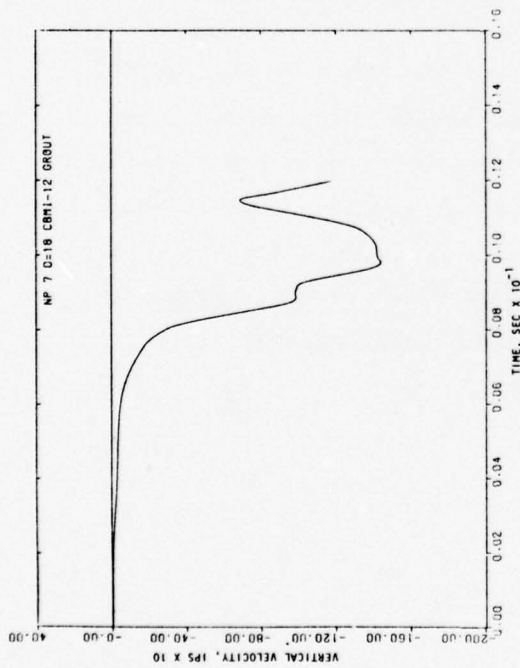
(b) Velocity at 18-in. depth

FIGURE 8-4. ONE-DIMENSIONAL CALCULATION ON CBM1-12 MATRIX COLUMN

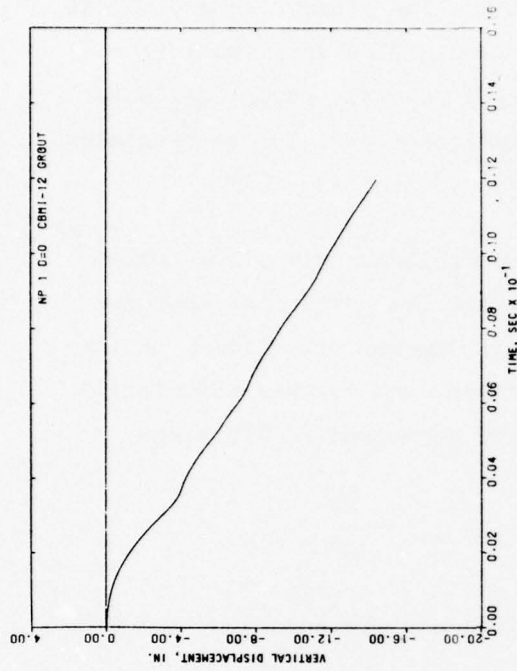


(a) Velocity at top

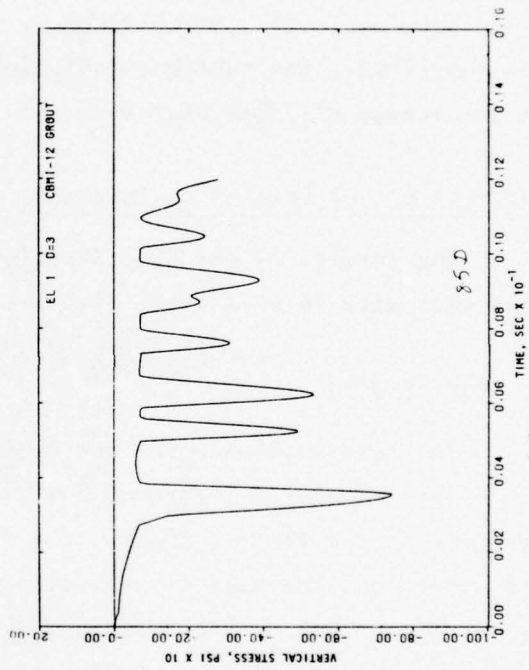
FIGURE 8-5. ONE-DIMENSIONAL CALCULATION ON GROUT COLUMN



(b) Velocity at 18-in. depth



(c) Displacement at top



(d) Stress at top

FIGURE 8-5. (CONCLUDED)

8.4 INPUT PULSE AND INTEGRATION SCHEDULE

The input pulse and schedule of variation of the time step used in the CBMI-12 calculations are shown in Figure 8-6. The steep rise and unload in the initial portion of the pulse prompted the use of a very small time step of 0.01 msec, initially, in order to control possible numerical instability. Uncertainties about the behavior of the grout also led to retaining the time step at 0.025 msec up to a real time of 18 msec.

On account of the softer matrix and correspondingly slower wave speeds in CBMI-12 compared to CBMI-12 and -14, the test data show that the velocities had not returned to zero at 20 msec. However, the trends of the pulse had been definitely established by this time, and further calculation was not justified. The entire calculations were performed in 820 steps, taking an average of 7.354 sec/step.

8.5 RESULTS OF THE CBMI-12 CALCULATIONS

The results of the CBMI-12 calculations are presented and compared with the test data in this subsection.

8.5.1 TEST RESULTS

The data obtained from the CBMI-12 test are shown in Figures 8-7 through 8-10. Figures 8-7 through 8-9 depict velocity, displacement, and acceleration at the 18-in., 36-in., and 54-in. depths both in the free field and the borehole. The velocity and displacement at the 18-in. depth show the effect of the venting of explosive gases into the borehole after the rupturing of the loading diaphragm (Sec. 5.3). Figure 8-10 shows stresses measured during the test at the 18-in., 36-in., 54-in. and 72-in. depths.

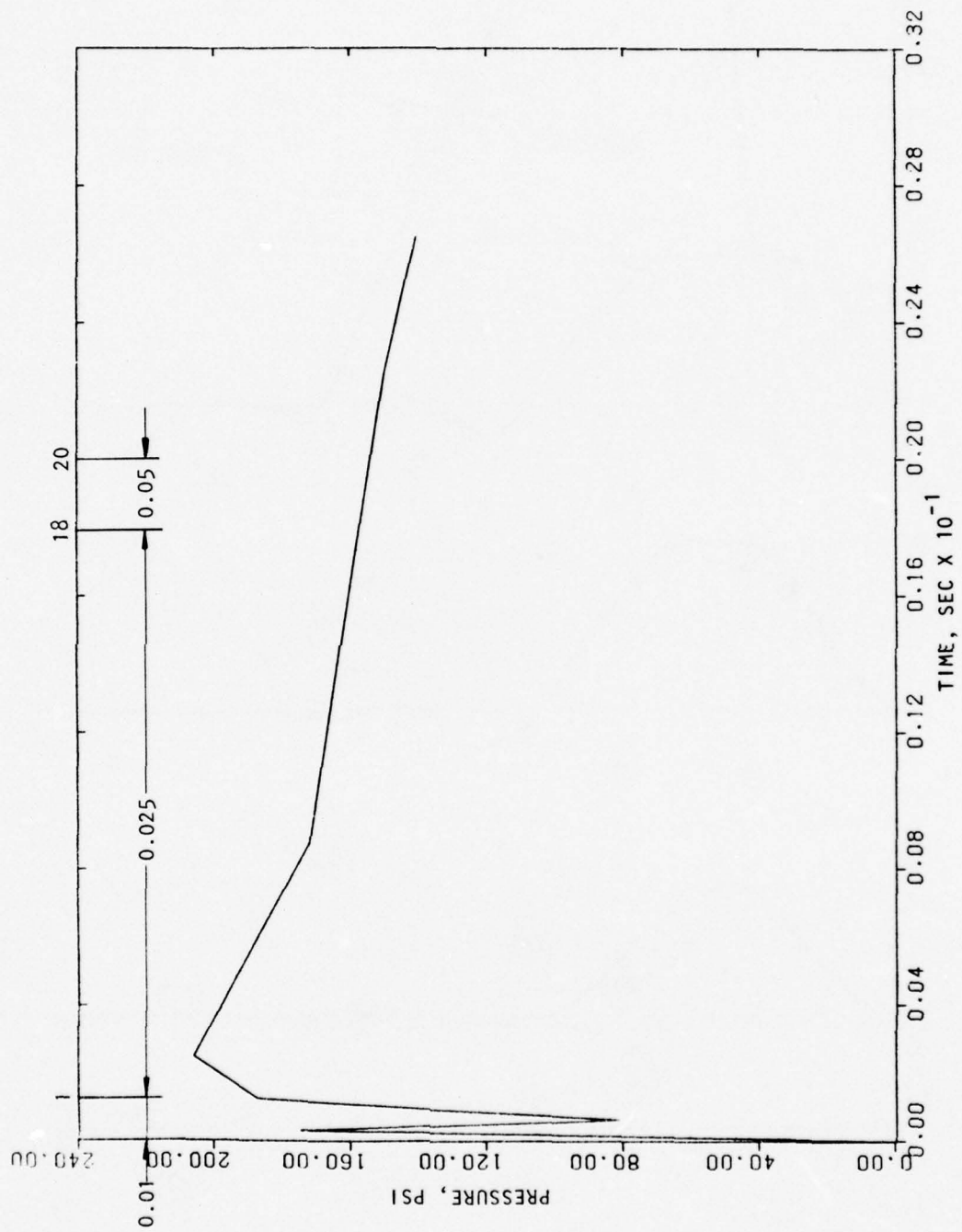


FIGURE 8-6. INPUT PULSE AND SCHEDULE OF INTEGRATION USED IN CBMI-12 CALCULATIONS

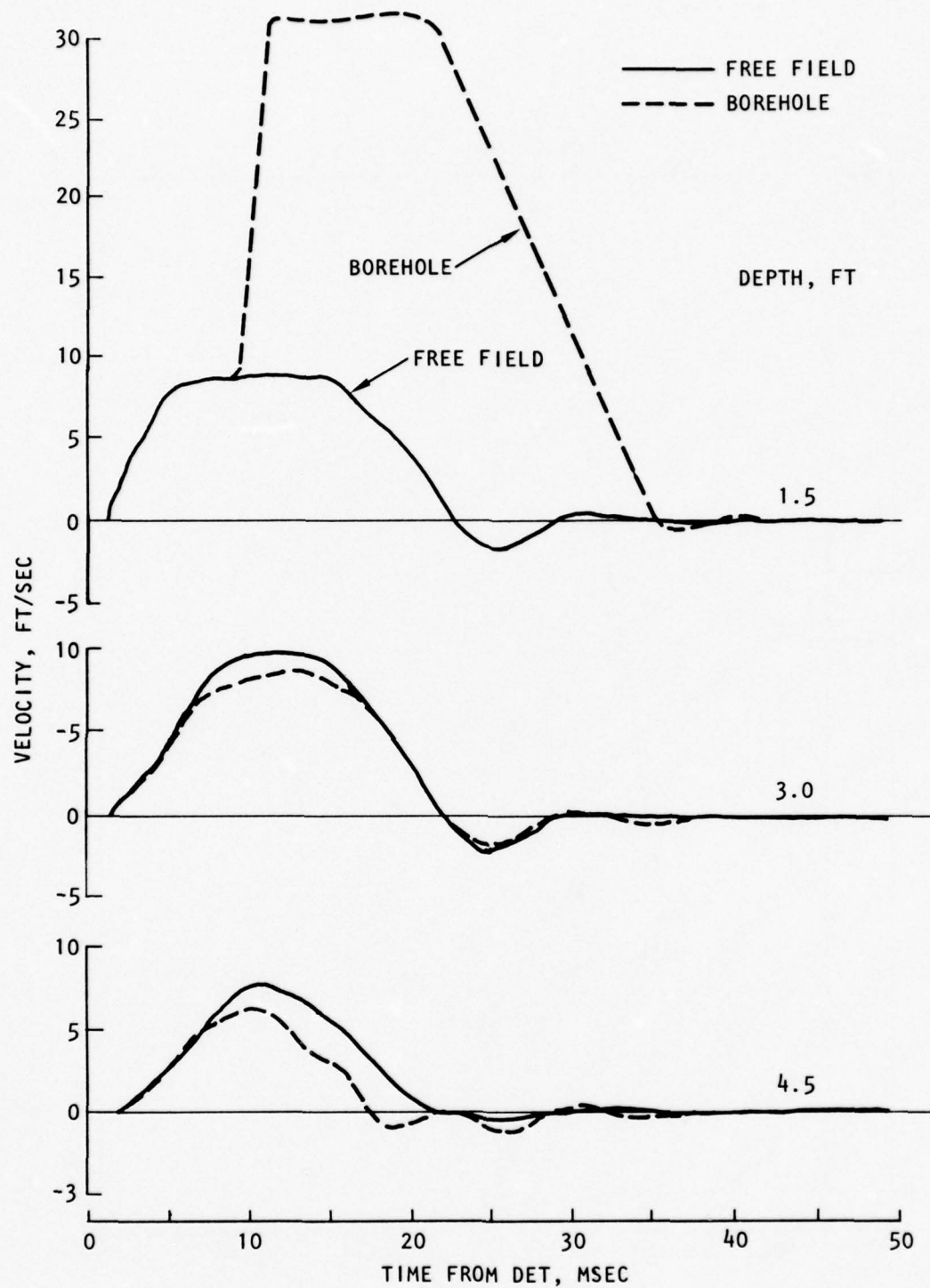


FIGURE 8-7. VELOCITIES FROM TEST CBMI-12

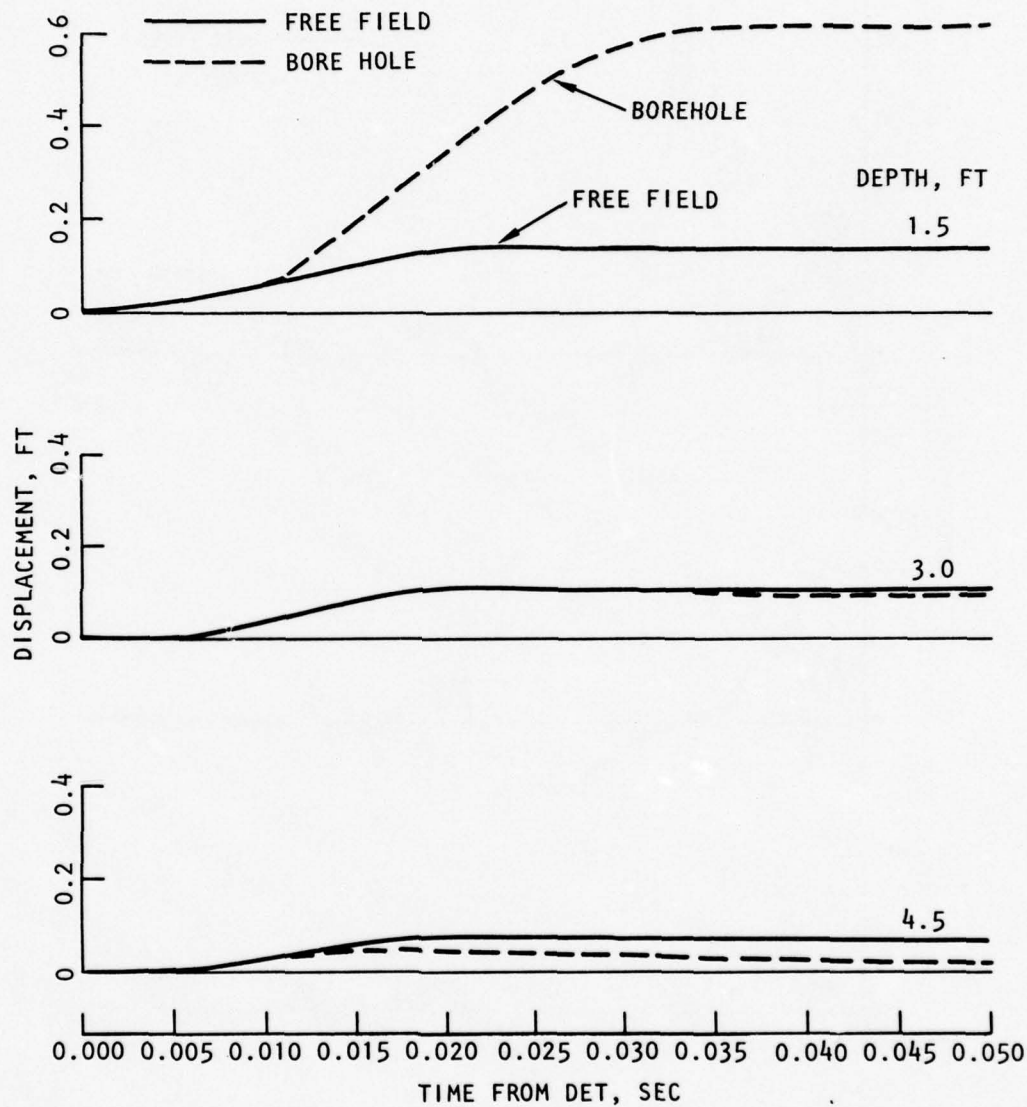


FIGURE 8-8. DISPLACEMENTS FROM TEST CBMI-12

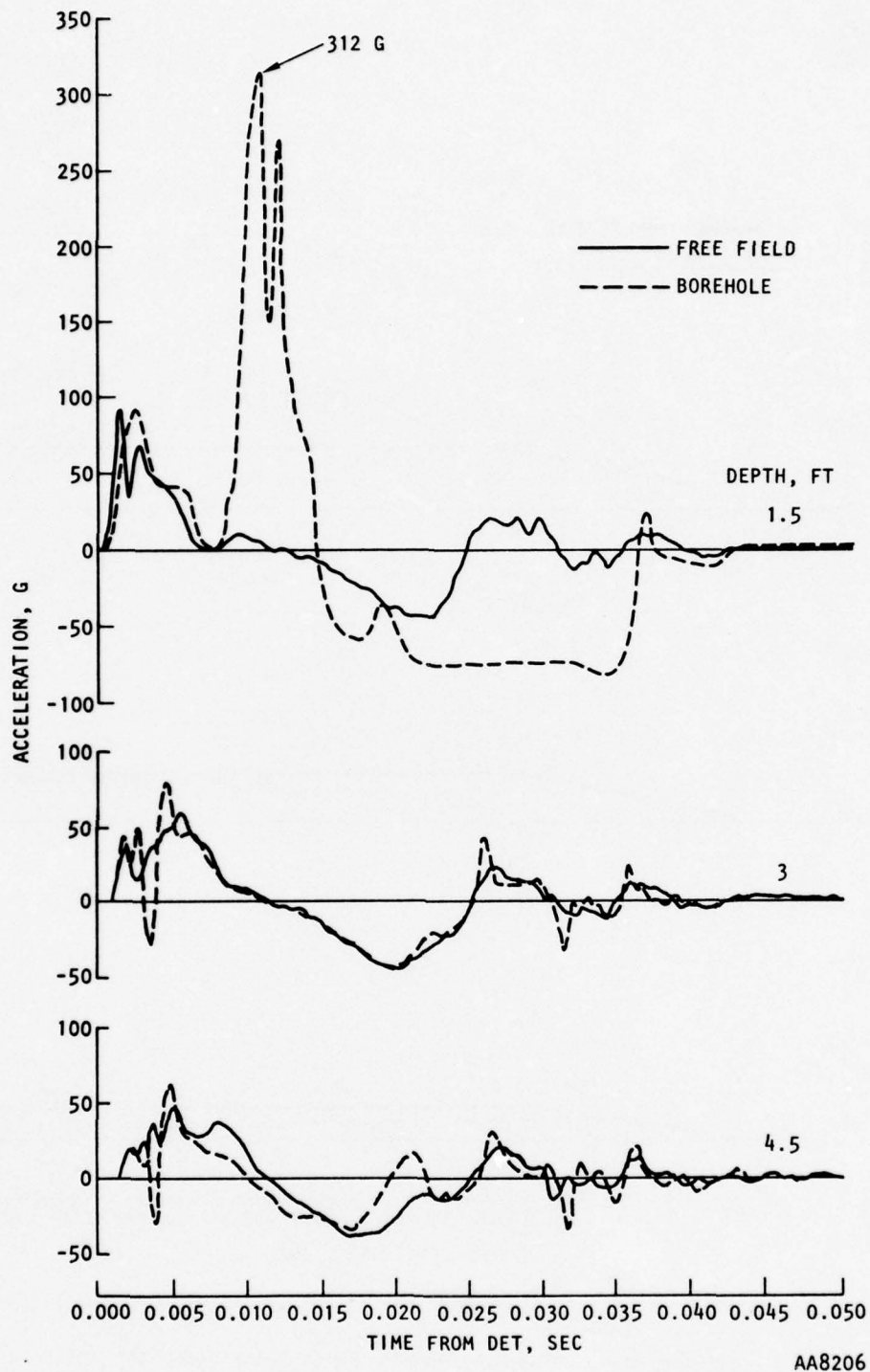
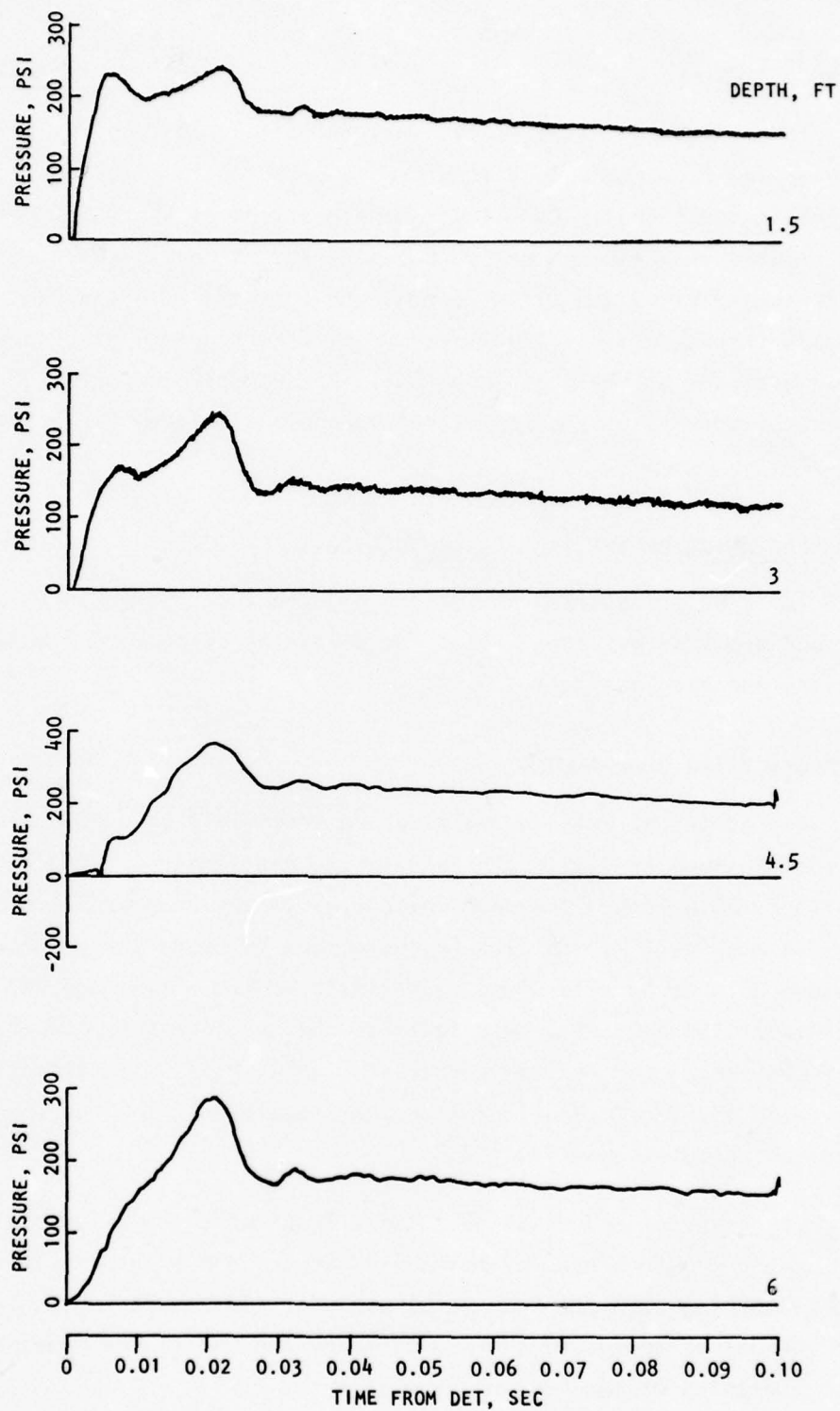


FIGURE 8-9. ACCELERATIONS FROM TEST CBMI-12



AA7830

FIGURE 8-10. STRESSES FROM TEST CBMI-12

8.5.2 CALCULATED RESULTS

Velocities and displacements at the 18-in., 36-in., and 54-in. depths at both gage and free field locations are compared against test data in Figures 8-11 through 8-13. Calculated accelerations at the same depths are shown in Figures 8-14 through 8-16. Calculated stresses in the free field at 18-in., 36-in., 54-in., and 73-in. depths are compared with test data in Figure 8-17a through 8-17d. The first three of these plots also show the calculated stresses at the gage locations. Figure 8-18 compares the velocity, displacement, and slip at the top of the borehole with the same quantities at 18-in. depth.

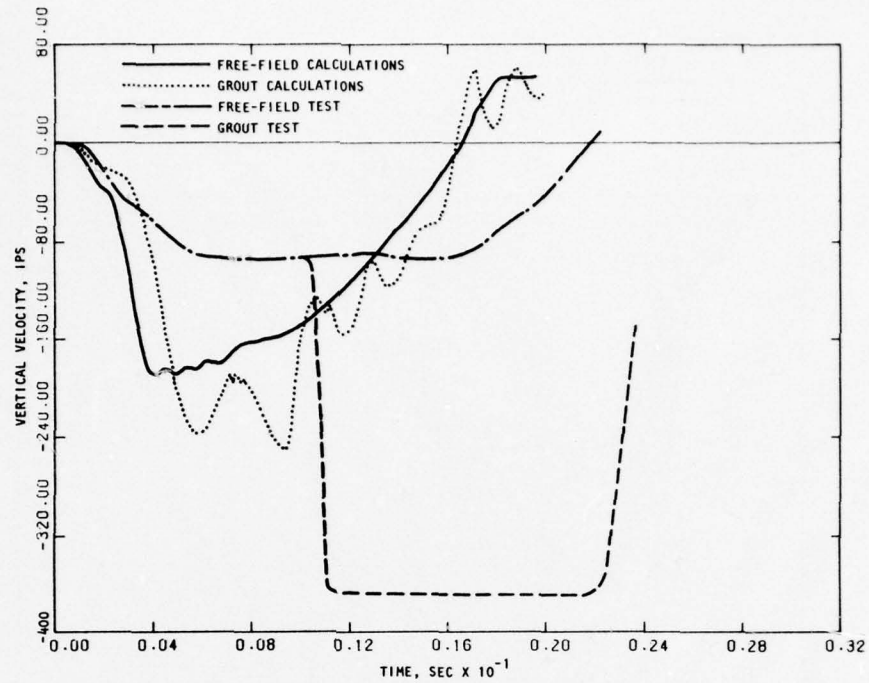
8.6 INTERPRETATION OF THE CBMI-12 CALCULATIONS

The results reported in Section 8.5 are interpreted in this section, and explanations are offered for points of disagreement between the calculations and the test data.

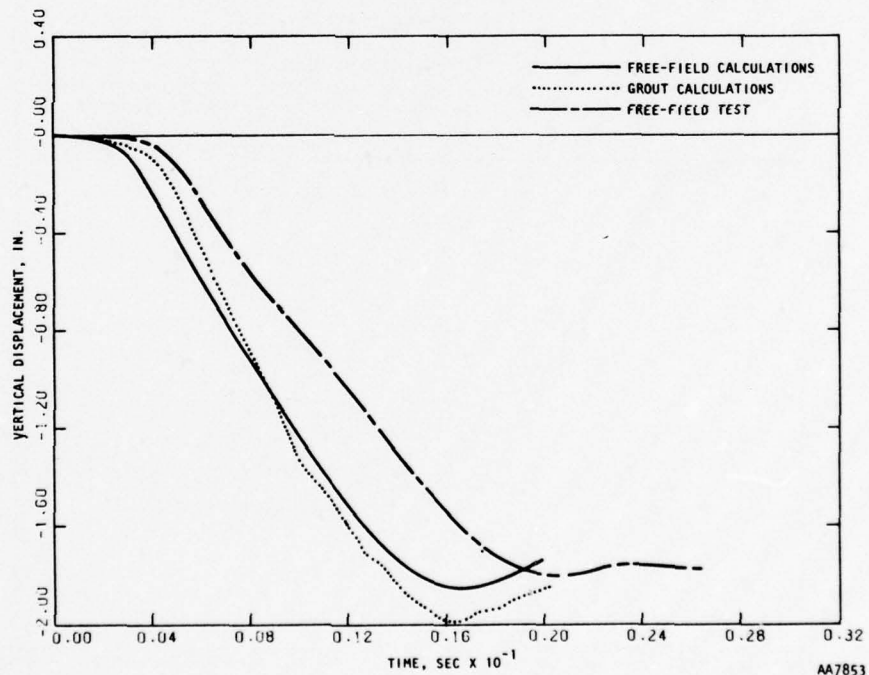
8.6.1 VELOCITY AND DISPLACEMENT

The agreement between the gage and free-field velocities in the CBMI-12 calculations is distinctly inferior to that found in the CBMI-13-1 and CBMI-14 calculations. The peak velocities in the downward direction differ by as much as 25%. The phasing agreement is poor--the grout exhibiting oscillations with large excursions, especially at the 36-in. and 54-in. depths. This oscillatory behavior may be related to the grout response observed in the one-dimensional grout column calculation (Fig. 8-5). The velocity in the free field is almost identical with that obtained in the one-dimensional matrix column calculation (Fig. 8-4b).

The displacement plots show the effects of the oscillatory velocity response in the grout. Thus, at the 36-in. depth, the grout displacement shows some bouncing with the peak value about 15% less than in the free field, while at the 54-in. depth, there is a distinct rebound in the grout that amounts to almost one-third of the maximum displacement.

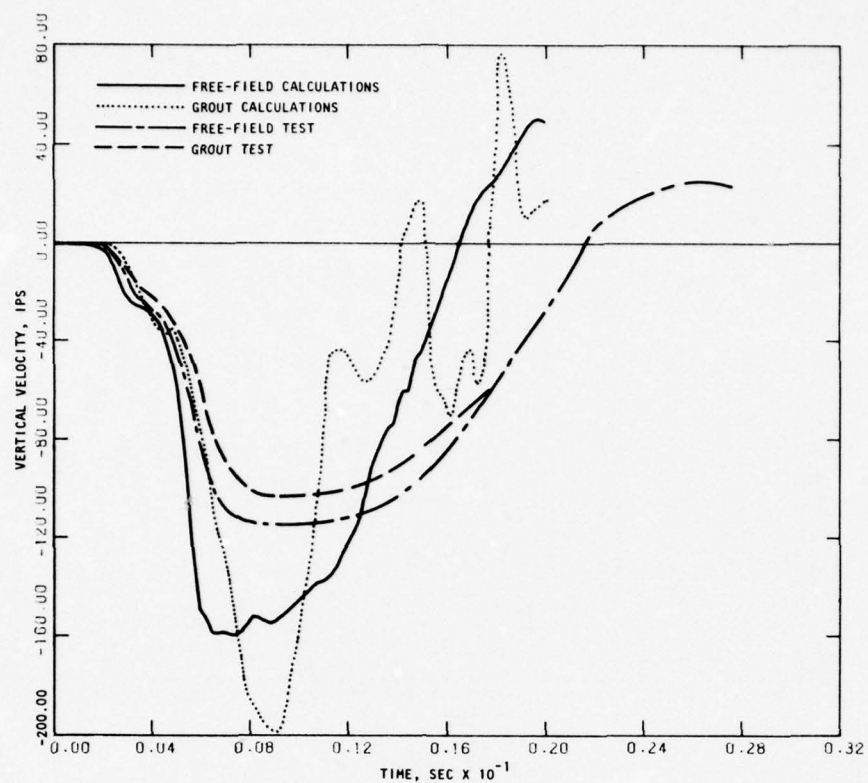


(a) Velocity

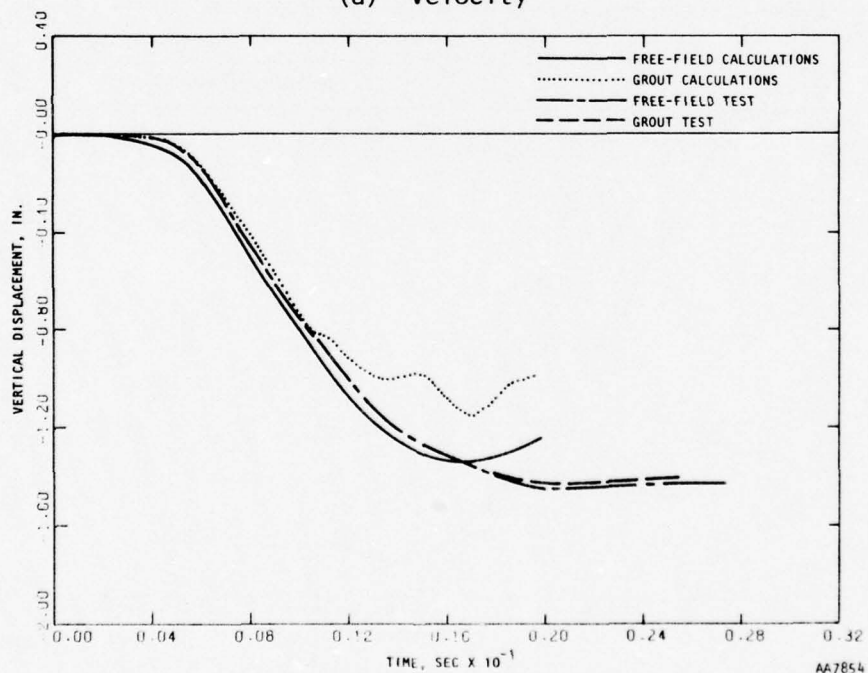


(b) Displacement

FIGURE 8-11. COMPARISON OF CBMI-12 CALCULATIONS AND TEST AT 18-IN. DEPTH

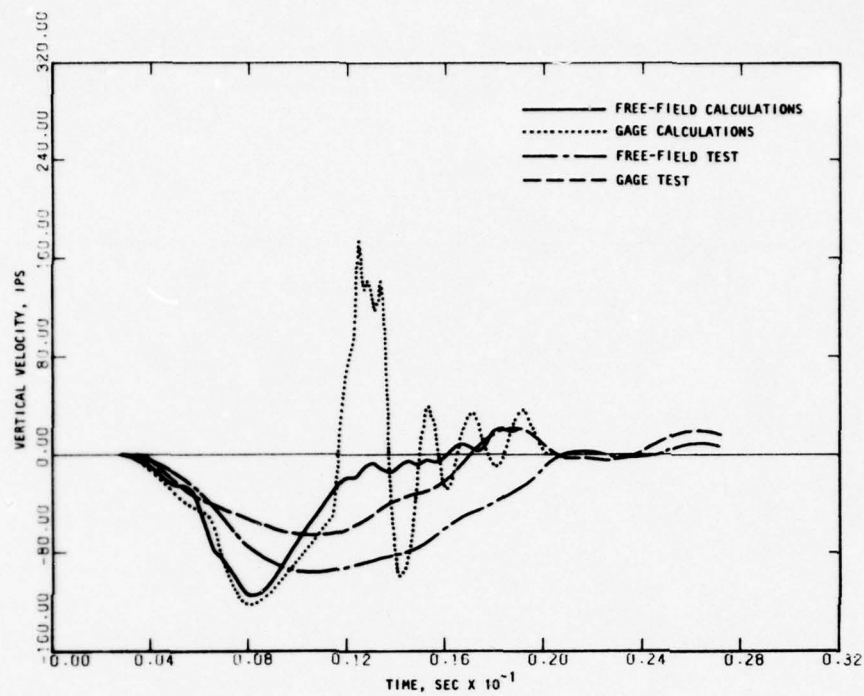


(a) Velocity

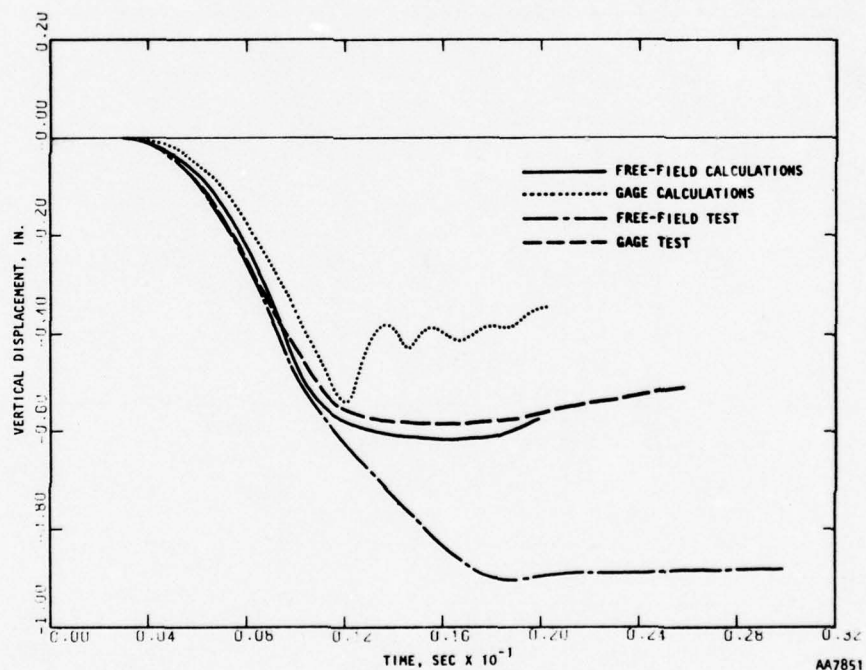


(b) Displacement

FIGURE 8-12. COMPARISON OF CBMI-12 CALCULATIONS AND TEST AT 36-IN. DEPTH

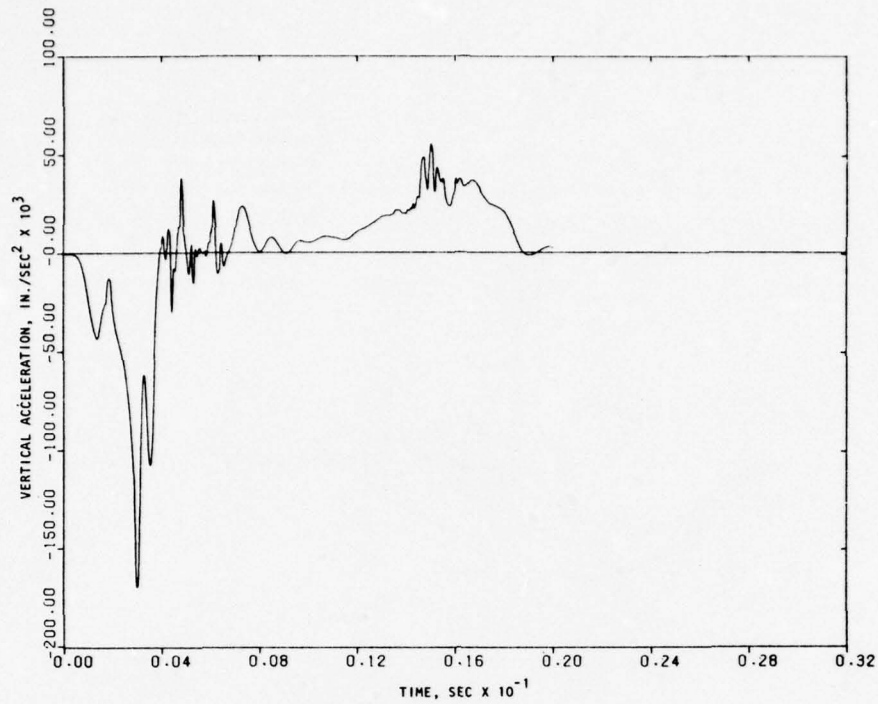


(a) Velocity

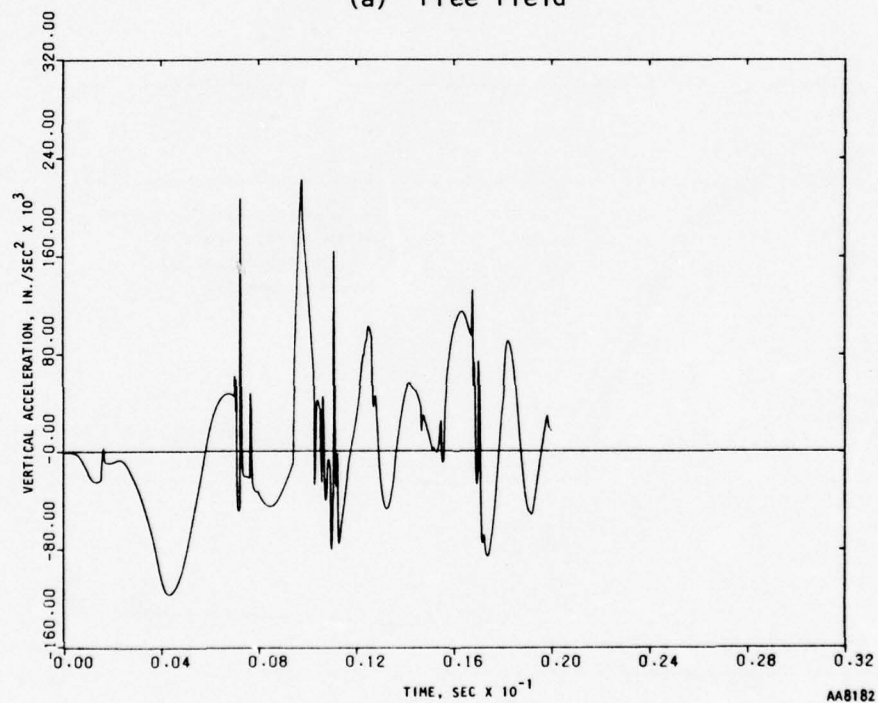


(b) Displacement

FIGURE 8-13. COMPARISON OF CBMI-12 CALCULATION AND TEST AT 54-IN. DEPTH

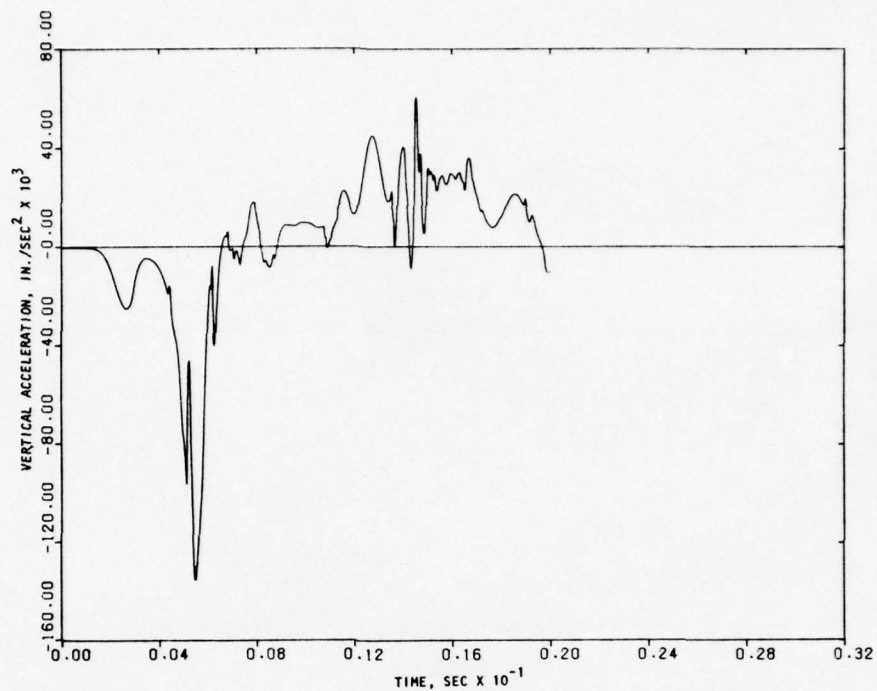


(a) Free field

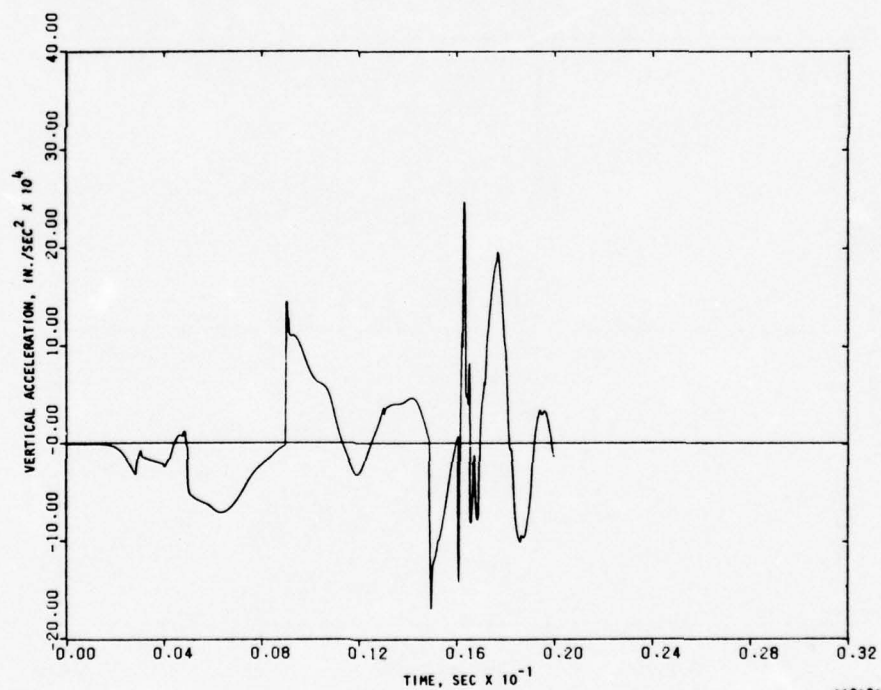


(b) Grout

FIGURE 8-14. ACCELERATION AT 18-IN. DEPTH--CBMI-12 CALCULATIONS



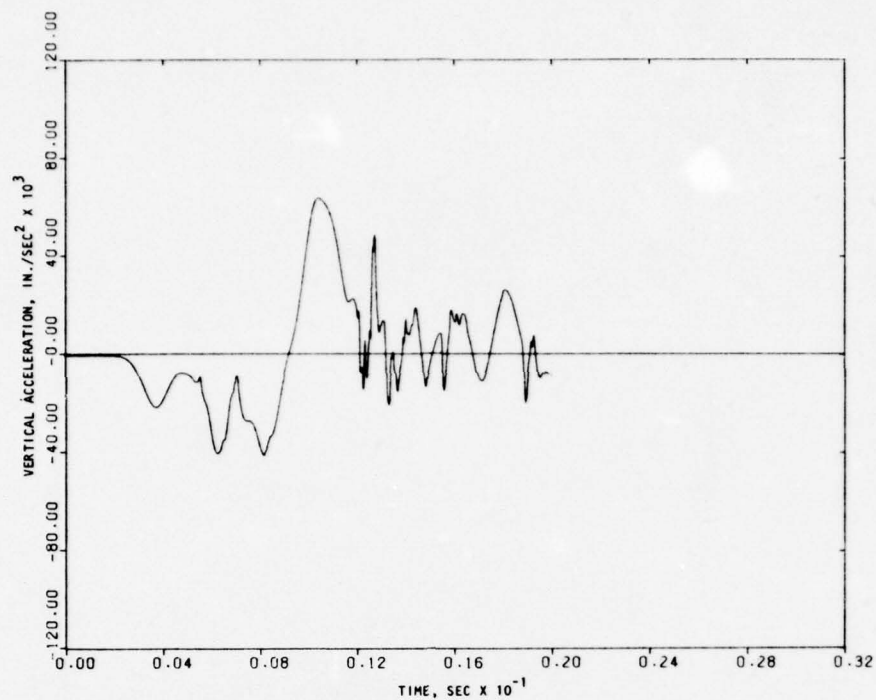
(a) Free field



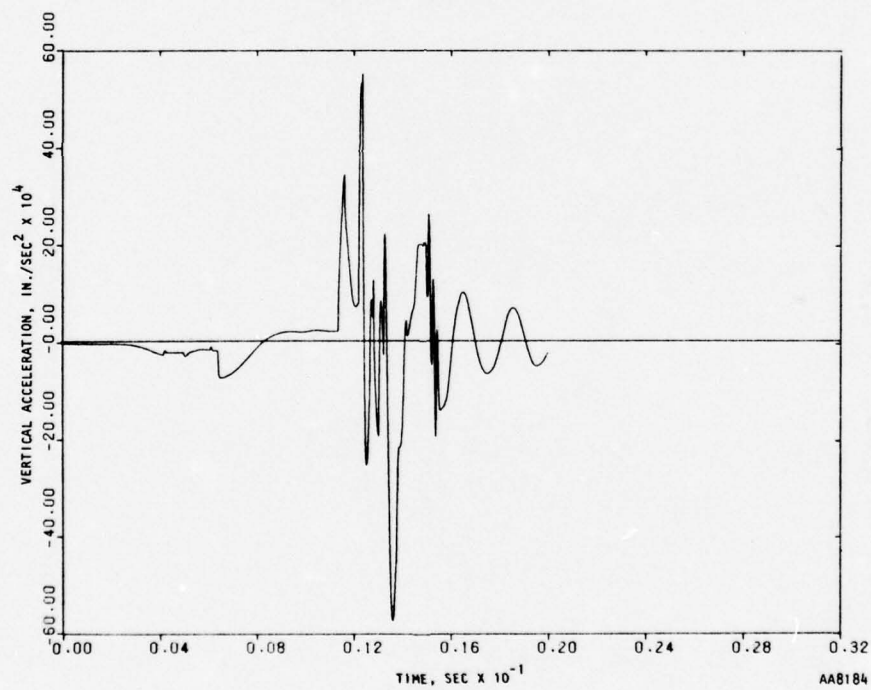
(b) Grout

AA8183

FIGURE 8-15. ACCELERATION AT 36-IN. DEPTH--CBMI-12 CALCULATIONS

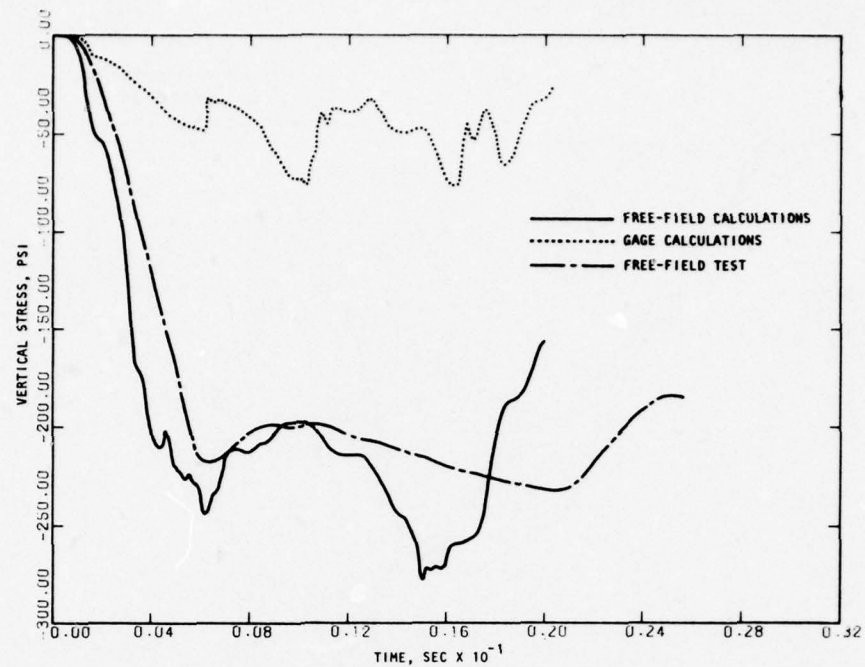


(a) Free field

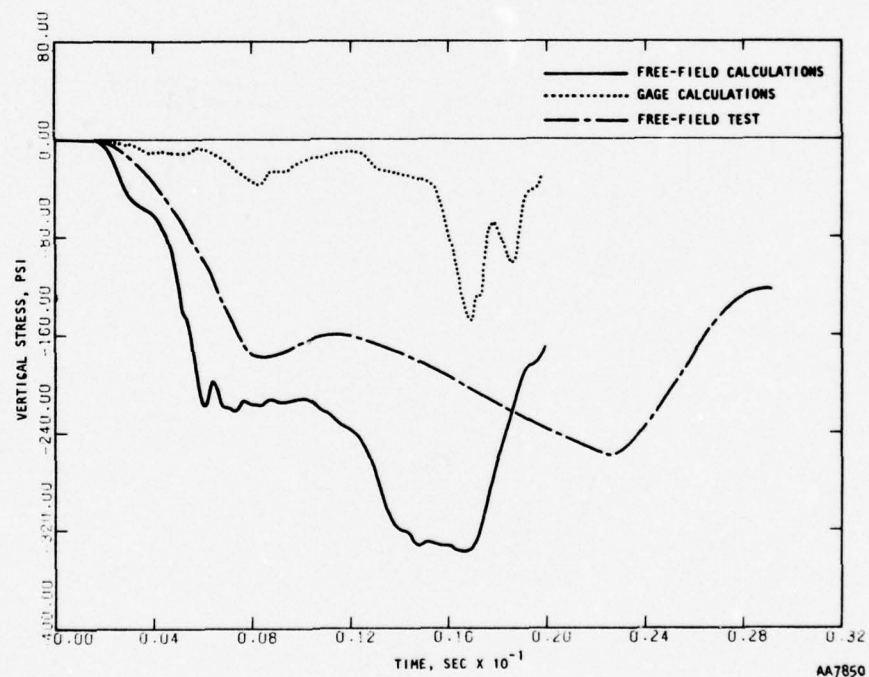


(b) Grout

FIGURE 8-16. ACCELERATION AT 54-IN. DEPTH--CBMI-12 CALCULATIONS

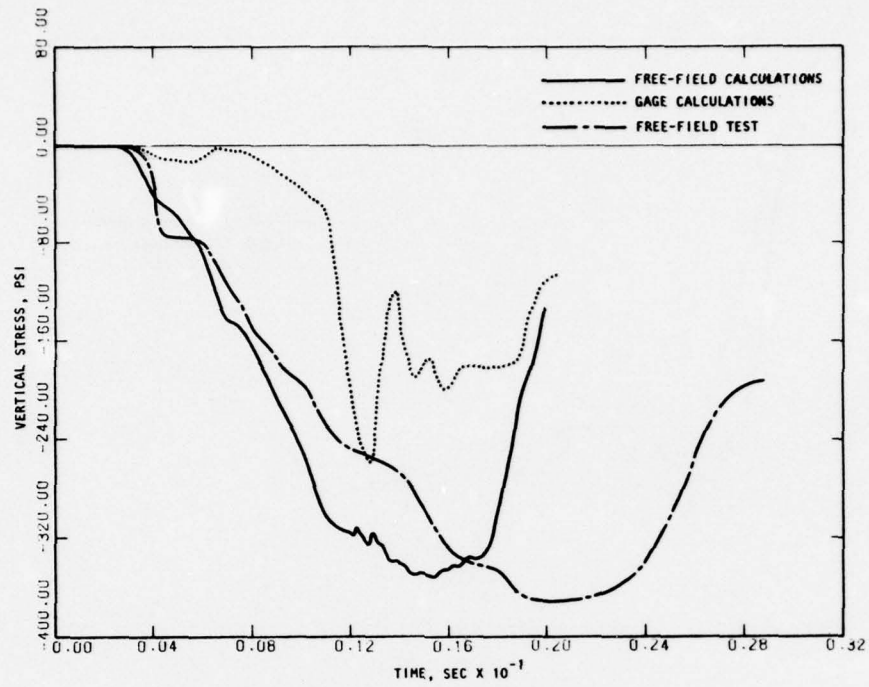


(a) Stresses at 18-in. depth

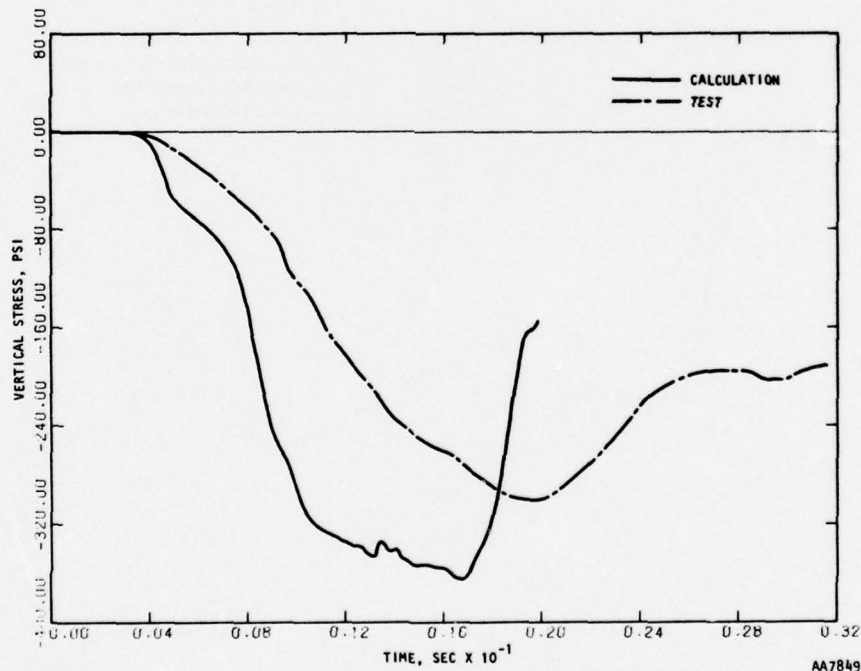


(b) Stresses at 36-in. depth

FIGURE 8-17. COMPARISON OF CALCULATED STRESSES WITH TEST DATA--CBMI-12 CALCULATIONS



(c) Stresses at 54-in. depth



(d) Stresses at 72-in. depth

FIGURE 8-17. (CONCLUDED)

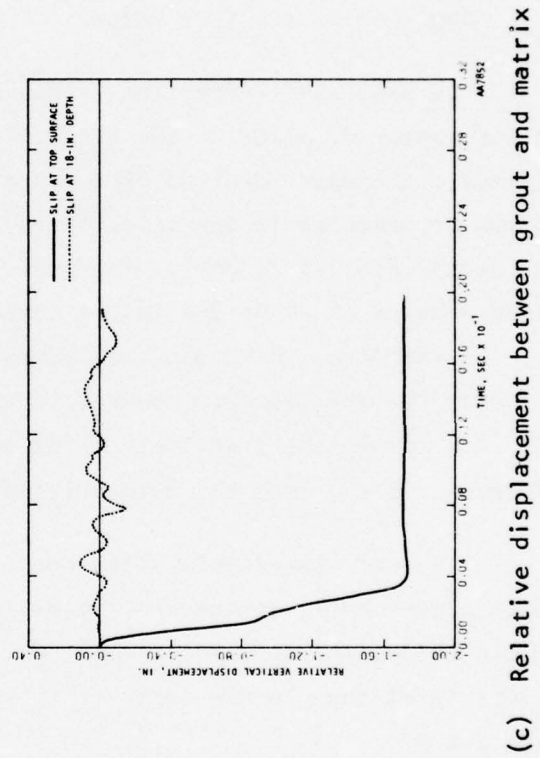
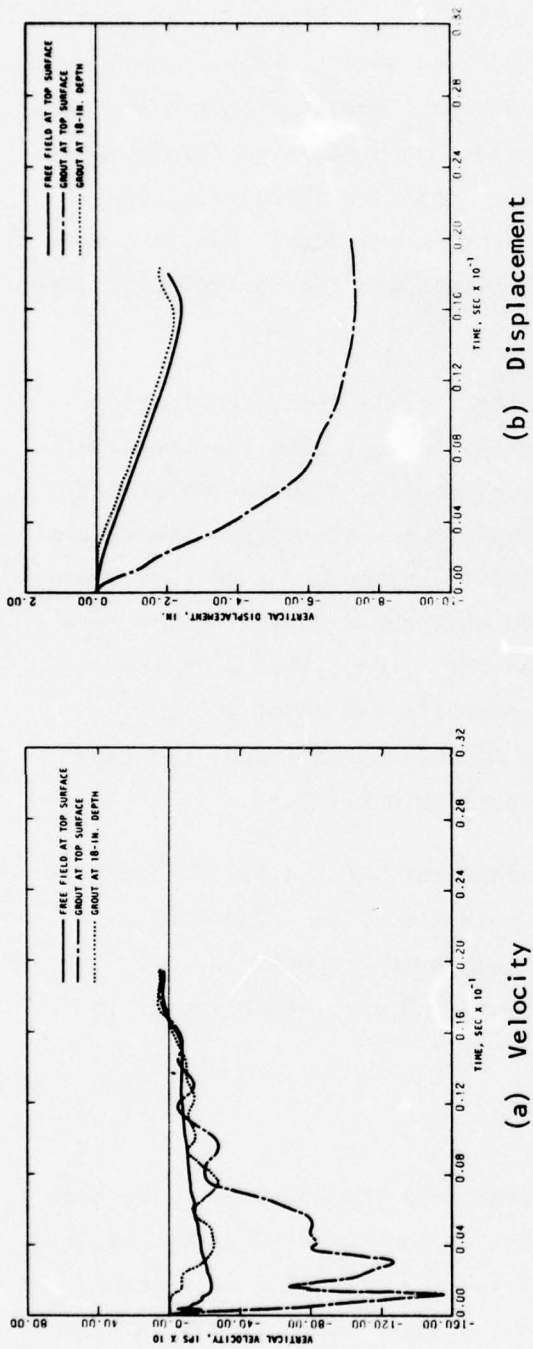


FIGURE 8-18. PUNCH DOWN OF BOREHOLE GROUT IN CBMI-12 CALCULATIONS

Comparison of the free-field calculated velocities with the test data shows discrepancies that were expected from the one-dimensional calculation (Sec. 8.4.1). Thus, the calculated velocities have higher peaks that are attained earlier and return to zero earlier and more steeply. The larger peaks and earlier return to zero in the calculated velocities compensate each other to some extent, and therefore the calculated and observed displacements at the 18-in. and 36-in. depths are much closer than the velocities, the maximum values agreeing within about 5%. At the 54-in. depth, however, the calculated velocity shows considerable attenuation, and the maximum displacement is about 65% of the test value.

As mentioned in Section 5, during the CBMI-12 test, the loading diaphragm ruptured, allowing the explosive gases to vent into the borehole. As a result, the upper regions of the grout experienced a punchdown effect, which may be observed in the velocity and displacement plots from the test at 18-in. depth (Figs. 8-7, 8-8). The peak velocity in the grout at this depth attained a value of about 360 ips as compared with about 80 ips in the free field. Furthermore, this value was sustained for a long time, with the result that the maximum displacement in the borehole was about 7.2 in. as against 1.8 in. in the free field. (Because of this large value, the gage displacement in the test has been omitted from Figure 8.11b.)

The calculated velocities and displacements at the 18-in. depth, as shown in Figure 8-11, do not show nearly as much disparity. There is a punchdown effect in the calculations, but it seems to be confined to a shallower level than in the test. This is discussed in greater detail in Section 8.6.4.

8.6.2 ACCELERATION

The calculated accelerations, Figures 8-14 through 8-16, show that the free-field accelerations have larger peaks in the downward direction at the 18-in. and 36-in. depths, but that at 54 in. the situation is reversed. The grout accelerations have larger peaks in the upward direction at all depths.

This may be due to the numerical difficulties associated with a wide disparity in the loading and unloading moduli as found in the grout. Peak values of acceleration are in the neighborhood of 400g with occasional spikes in the grout reaching 1500g.

The test data of Figure 8-9 show that the grout attains higher peaks at all depths. The peak values in the test are under 100g except for a value of 312g in the borehole at the 18-in. depth.

8.6.3 STRESS

The calculated free-field stresses at the 18-in., 36-in., 54-in., and 72 in. depths show reasonably good correlation with the measured stresses as seen in Figure 8-17. The arrival times of the calculated stresses are somewhat shorter. Wave reflection from the SBLG base is marked in the calculated stress plots and discernible in the test stress plots. Initial peak values agree within 25% at the two upper locations, but the more predominant reflection in the calculations widens the margin on the second peaks. At the lower stations, initial peaks are smeared and later peaks agree almost exactly at 54 in. and within 25% at the SBLG base.

Figure 8-17a through 8-17c also show the computed stresses at the gage locations at these depths. These stresses are considerably smaller than the free-field stresses except for a spike at the 54-in. depth.

The low values of the stresses in the grout are easily explained following the same argument as in Section 7.6.3. In this calculation also, the borehole is filled with a uniform grout, and the assumed interface properties ensure motion compatibility between the borehole and the matrix. This, in turn, leads to strain compatibility and implies that stresses are in the ratio of the stiffnesses. The grout being much less stiff than the matrix, the stresses in the grout are considerably smaller in contrast to the situation in the CBMI-14 calculations.

8.6.4 PUNCHDOWN EFFECT IN GROUT

The calculations do exhibit a punchdown in the borehole grout, although this is not evident in the motion plots at the 18-in. depth and deeper. In order to illustrate this punchdown, motion of the grout at the top surface is compared with that at the 18-in. depth in Figure 8-18. Figures 8-18a and 8-18b show the velocity and displacement, respectively, while Figure 8-18c shows the relative or slip displacement between the grout and the matrix at these two depths. The free-field velocity and displacement at the top surface are also included in Figures 8-18a and 8-18b for comparison.

These figures show that the grout at the top surface has a peak velocity of 1600 ips and maximum displacement of over 7 in. as against a peak velocity of 200 ips and maximum displacement of 2 in. in the free field. On the other hand, at a depth of 18 in., the grout shows a peak velocity of 240 ips and a maximum displacement of 2 in. The peak velocity of 1600 ips is probably spurious, but the displacement comparisons show that the upper portions of the grout displace considerably more than the matrix at the same level. This is further borne out by the slip displacement plot of Figure 8-18c, which shows a relative displacement of about 1.75 in. at the top compared with about 0.25 in. at the 18-in. depth.

These plots show that the grout does experience a punchdown but that it is confined to the very top of the borehole. At the 18-in. depth, the grout compacts no more than the surrounding matrix and follows the motion of the free field. A similar effect may be deduced from the test data, but the punchdown in the test is greater at the top and extends further down, the grout continuing to compact between 18 in. and 36 in.

The difference between the extent of the punchdown in the grout observed in the calculations and the test data probably stems from two sources:

- a. The grout used in the test is an air-entrained grout. It is possible that during the process of preparation of the test specimen, there was a tendency for air bubbles to rise to the

top with the result that the grout properties varied through the depth, with the upper regions being softer than assumed in the calculations. This would account for a greater punchdown in the test at the upper levels.

- b. The action of the gases in venting down into the borehole after the rupture of the loading diaphragm may have led to loading conditions that strained the grout more than the uniform loading over the top surface assumed in the calculations.

Some of the discrepancy could be assigned to the undefined coupling between the soil and the grout in the test. Such cases are difficult to reliably investigate using numerical calculations.

8.7 CONCLUSIONS AND DISCUSSION

As recognized from the outset, the CBMI-12 test was an anomalous one. However, it sheds some valuable light on the problem of placement of motion gages, representing as it does, an extreme case.

It may be concluded that even with the use of an extremely soft grout, as in this test, the borehole follows the motion of the free field except near the surface when there is a reasonably strong interface bond between the grout and soil.

It may also be concluded that motion continuity at the interface, in the presence of a homogeneous borehole filler, leads to strain continuity. Therefore, it is likely that stress discontinuities would occur at the interface reflecting the impedance differences of the soil and grout. Accordingly, stress gages will not likely measure free-field stress states using the grouting procedures discussed above.

SECTION 9

FREQUENCY ANALYSIS

This Section describes analyses performed in the frequency domain and identifies frequency bands of interest in the calculated response.

9.1 DESCRIPTION OF ANALYSES PERFORMED

The calculated responses from Tests CBMI-12 through 14 have demonstrated that the similarity of borehole motion and free-field motion depends on the parameter being compared. Thus, displacement and velocity show better agreement than acceleration. This observation suggests that certain frequency components correlate better than others. Hence, the degree of ground-motion measurement accuracy apparently is a function of frequency and, since frequency analyses are relatively easy to perform, it is beneficial to establish the frequency bands in which acceptable measurement accuracy can be expected.

The results of the CBMI-14 and CBMI-12 calculations were selected for frequency analysis. In each case, the frequency spectra of the calculated velocity responses at the 18-in., 36-in., and 54-in. depths at both free-field and borehole locations were computed via the fast Fourier transform (FFT) and presented in the form of PSD's. In addition, "transfer functions" were computed between the borehole and free-field responses in order to evaluate the accuracy of the records at different frequencies. The term transfer function is construed to be the frequency domain division of the borehole response by the free-field response. Unity gain at any frequency implies perfect correlation at the frequency even though the response in the free field and borehole were obtained via nonlinear finite element calculations. The results were also expected to reveal the overall frequency range of the velocity response and indirectly verify that the refinement of the finite element mesh used in the calculation was adequate for the frequency ranges of interest.

The results of the frequency analyses of the calculated velocities for the two tests are discussed below.

9.2 FREQUENCY ANALYSIS OF CBMI-14 CALCULATION

The PSD's of the velocity response and the RMS velocities at 18-in. depth at the borehole and free-field locations are shown in Figure 9-1a and b. The transfer function between the two responses is shown in Figure 9-1c. Similar frequency domain comparisons of the velocity responses at 36-in. and 54-in. depths are shown in Figures 9-2 and 9-3.

The following conclusions emerge from a study of the frequency domain plots:

- a. Virtually all of the velocity response is contained in the frequency range 0 to 200 Hz as can be seen from the RMS velocity plots.
- b. Within this range, the borehole response is within 15% of the free-field response and the borehole response is smaller, except at the 54-in. depth as evidenced by the transfer functions. Phase agreement is also very good.
- c. It is further noted from the transfer functions that good correlation extends beyond the frequency range in Item a above to 350 Hz at 18 in. and 275 Hz at 36 in. These results imply that a limited frequency range of acceleration fidelity is achieved under the same circumstances for the emplacement techniques adopted for velocity gages.
- d. Sharp resonances are observed at higher frequencies with the borehole response tending to lag behind the free-field response at the two upper locations. However, the energy content at these frequencies, from the viewpoint of velocity, is extremely small.

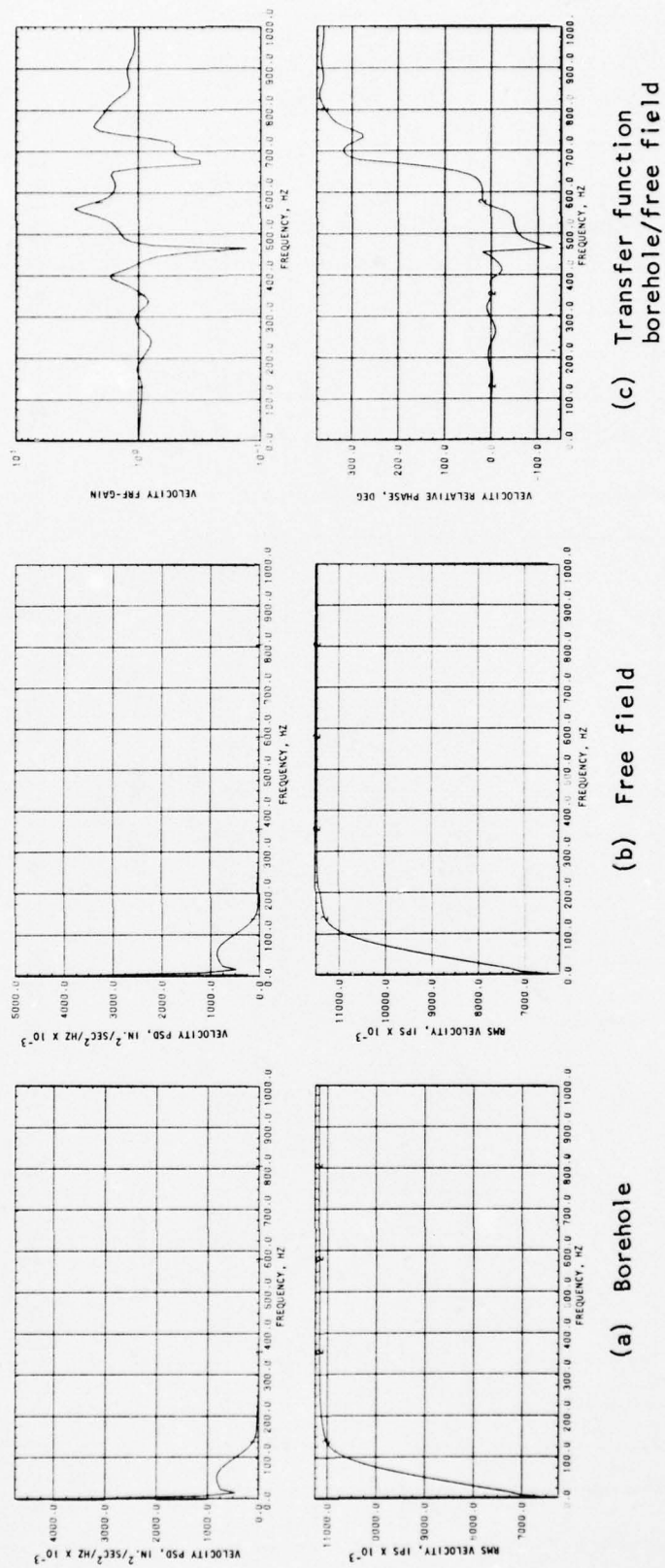
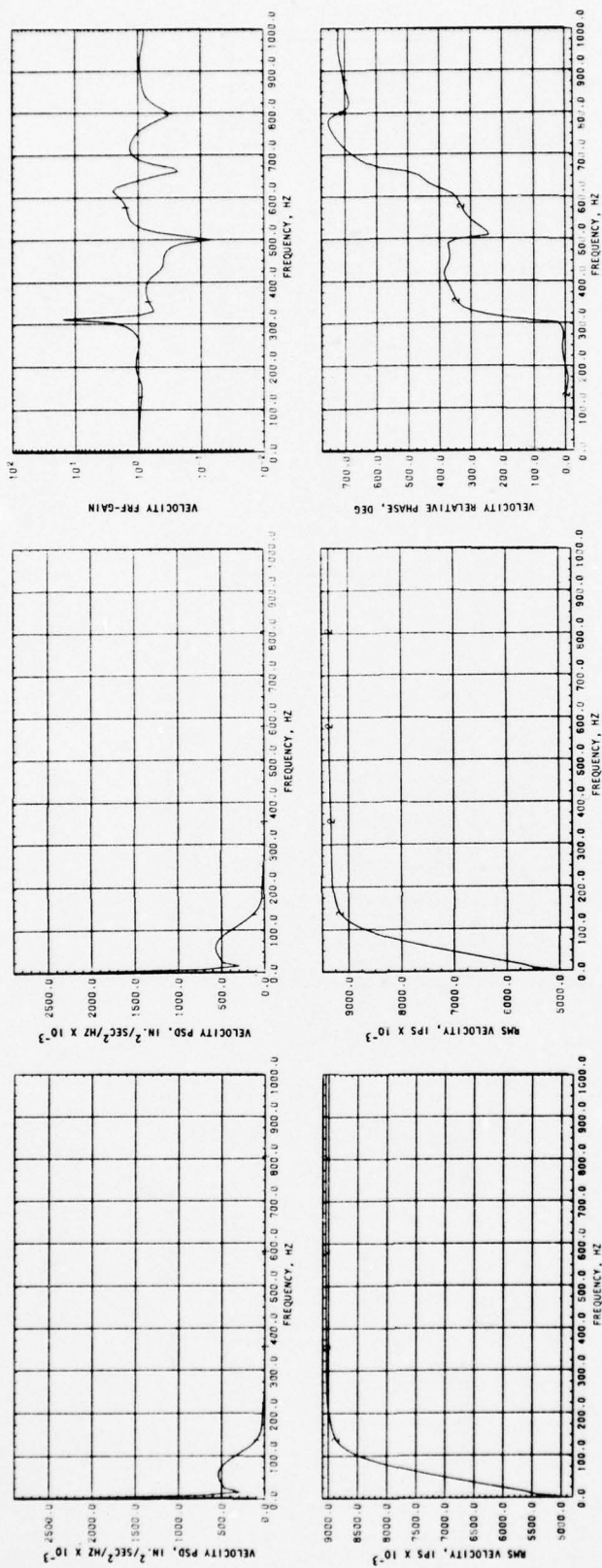


FIGURE 9-1. VELOCITY RESPONSE IN FREQUENCY DOMAIN--18-IN., CBMI-14 CALCULATION



(a) Borehole

(b) Free field

(c) Transfer function
borehole/free field

FIGURE 9-2. VELOCITY RESPONSE IN FREQUENCY DOMAIN--36-IN. DEPTH, CBMI-14 CALCULATION

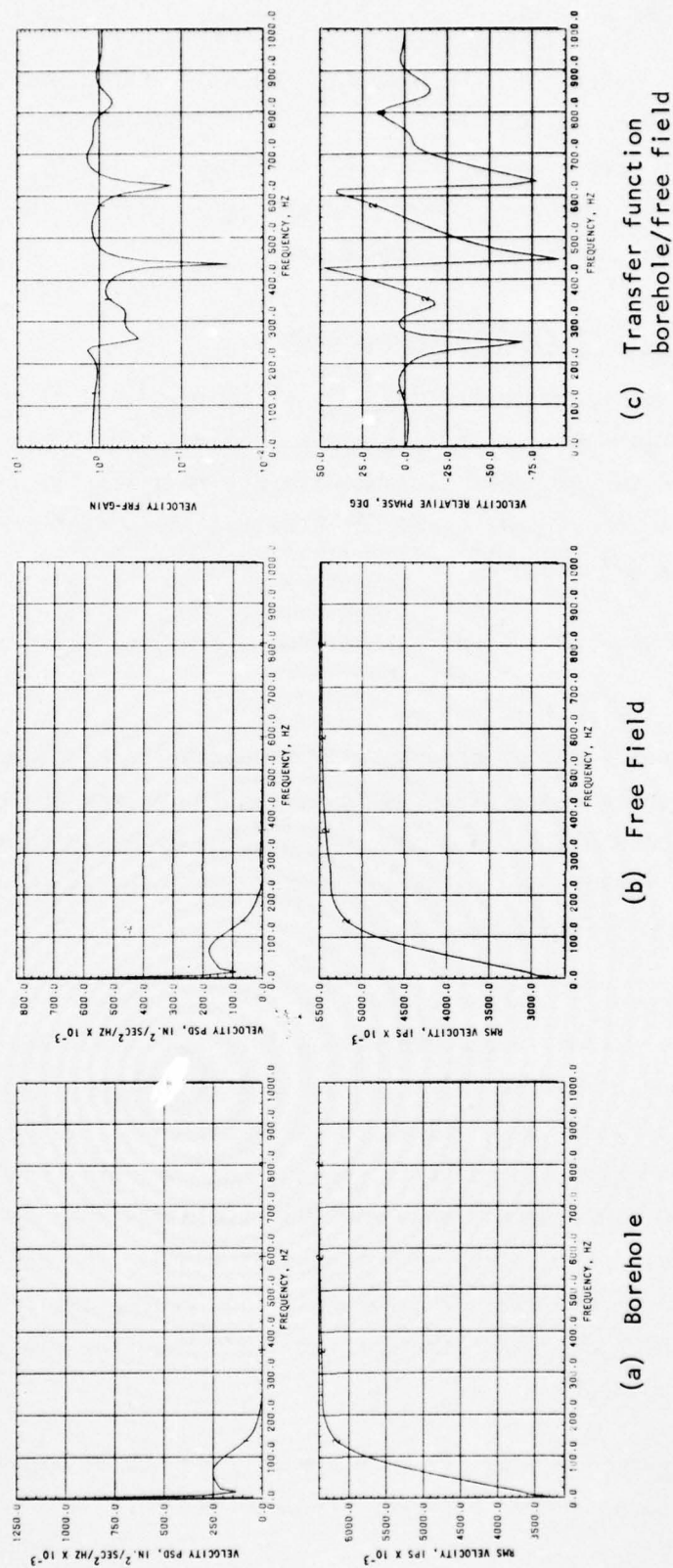


FIGURE 9-3. VELOCITY RESPONSE IN FREQUENCY DOMAIN--54-IN. DEPTH, CBMI-14 CALCULATION

It is also noted that the Nyquist frequency of the mesh, assuming a wave propagation speed of 1000 ft/sec in the medium is 1000 Hz. The observation that the frequency range of the calculated velocity response extends only to 200 Hz therefore shows that the refinement of the calculational mesh is adequate from the frequency standpoint.

9.3 FREQUENCY ANALYSIS OF CBMI-12 CALCULATION

The PSD's of the velocity response at 18-in. depth at the borehole and free-field locations are shown in Figures 9-4a and b. The transfer function between the two responses is shown in Figure 9-4c. Similar frequency domain comparisons of the velocity responses at the 36-in. and 54-in. depths are shown in Figures 9-5 and 9-6.

The following conclusions emerge from a study of the frequency domain plots:

- a. Virtually all of the velocity response is contained in the frequency range 0 to 200 Hz at the 18-in. and 36-in. depths. The borehole shows a somewhat greater velocity range than the free field. At the 54-in. depth, the velocity range in the borehole extends to 500 Hz.
- b. Agreement of borehole and free-field response is less satisfactory than in the CBMI-14 calculation at all depths. The responses differ within a factor of two at the upper location, and a factor of 1-1/2 at the midlocation in the frequency band to 200 Hz. At the 54-in. depth, the borehole response is up to 40 times larger than the free-field response at 500 Hz. Assuming a more realistic range of 200 Hz, the latter factor reduces to 3-1/2. The borehole lags behind the free field at the two upper locations and leads the free field at the 54-in. depth.
- c. Resonances are easily observed at frequencies above 400 Hz and perhaps even at lower frequencies.

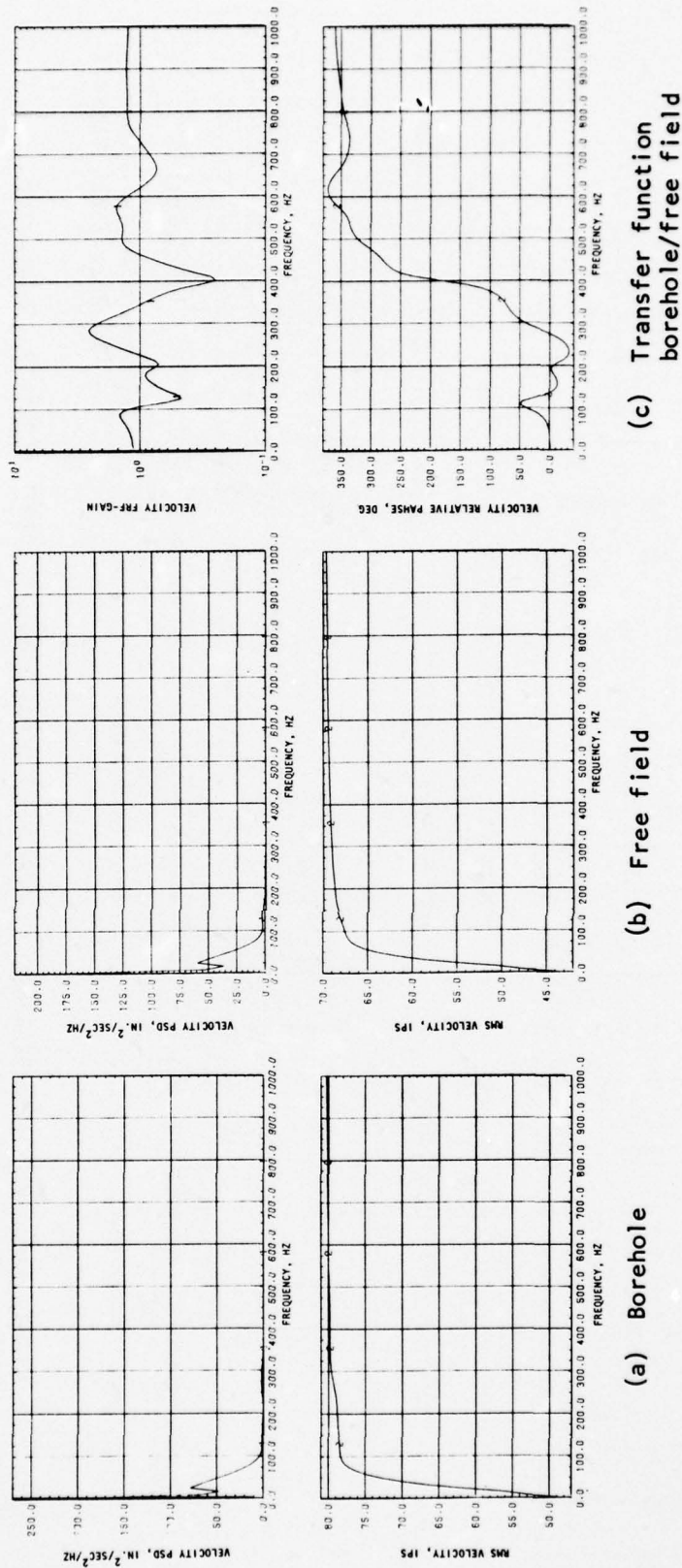


FIGURE 9-4. VELOCITY RESPONSE IN FREQUENCY DOMAIN--18-IN. DEPTH, CBMI-12 CALCULATION

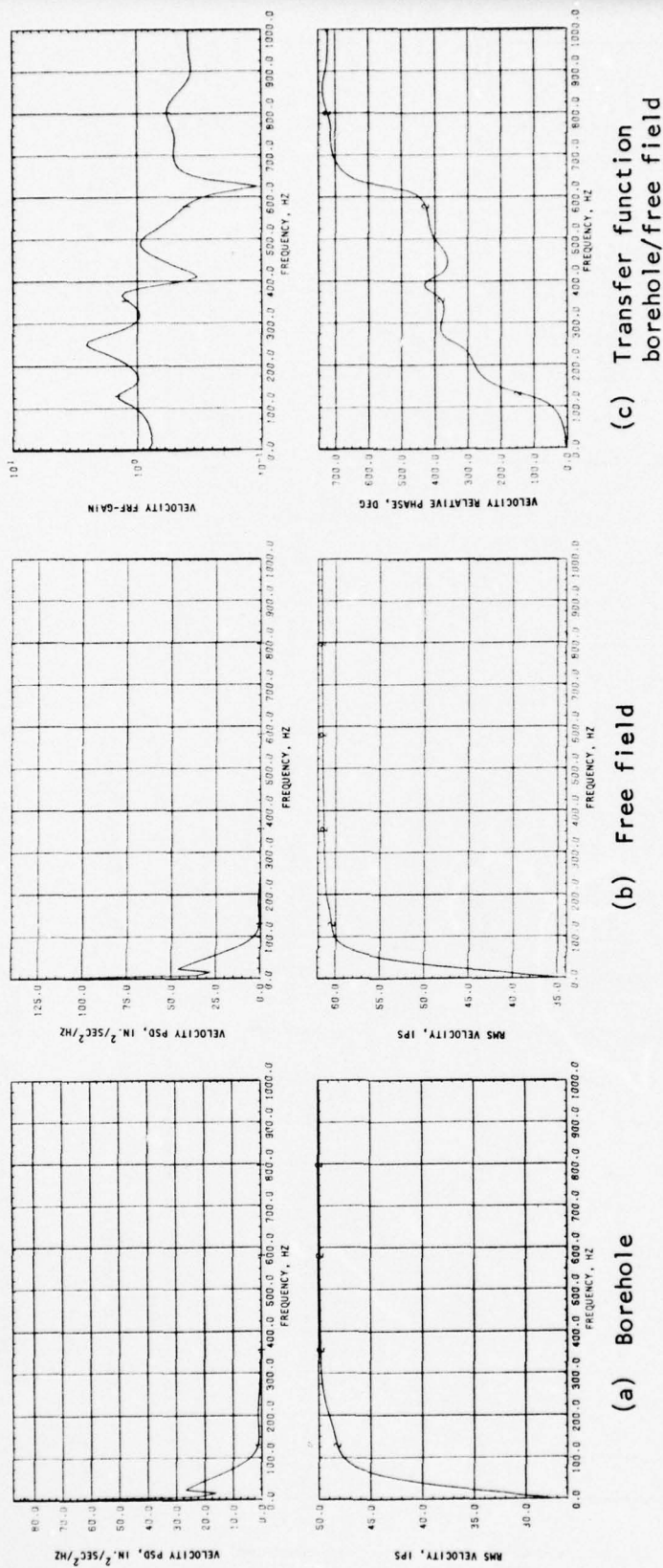


FIGURE 9-5. VELOCITY RESPONSE IN FREQUENCY DOMAIN--36-IN. DEPTH, CBMI-12 CALCULATION

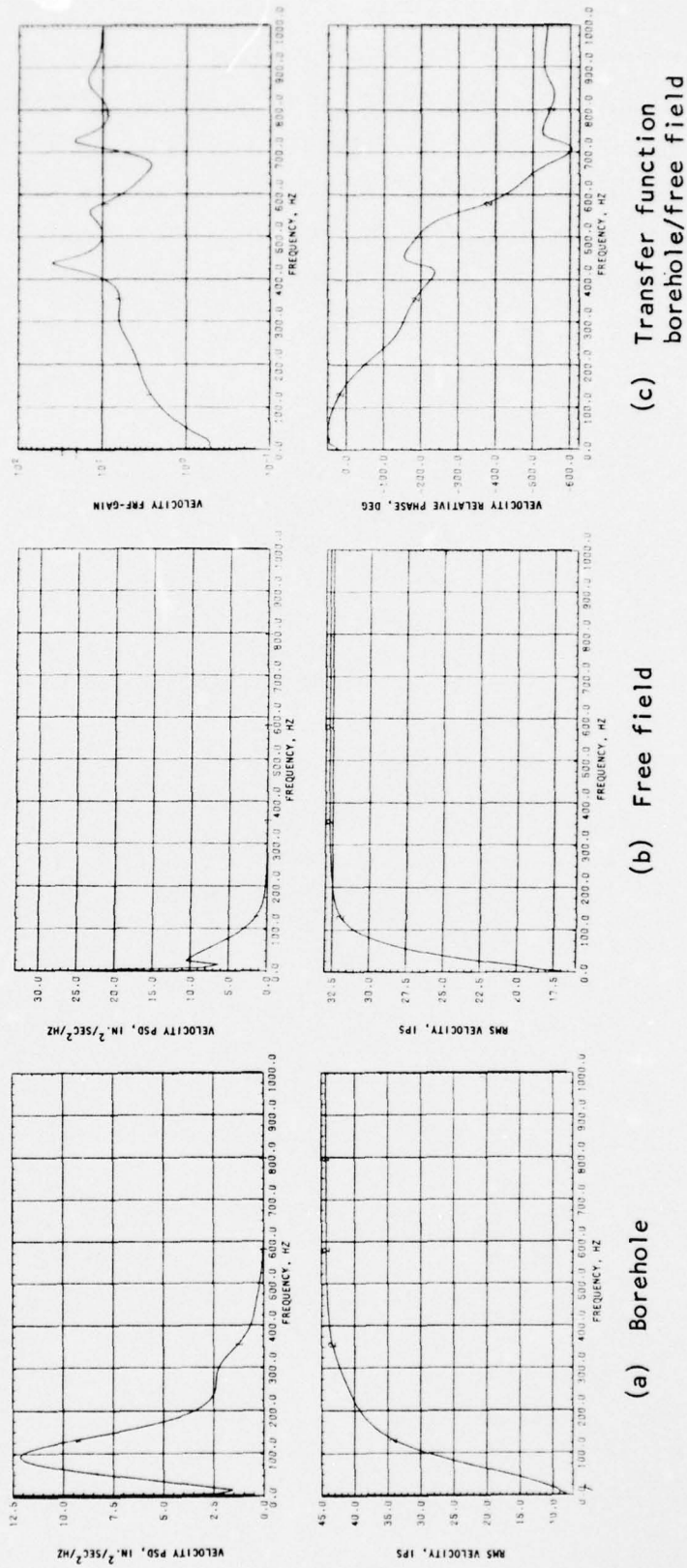


FIGURE 9-6. VELOCITY RESPONSE IN FREQUENCY DOMAIN--54-IN. DEPTH, CBMI-12 CALCULATION

In the light of the anomalous behavior of the borehole and consequent *numerical difficulties* (see Sec. 5.3, 6.2.2, and 8.3.2), it is not surprising that the velocity response in the CBMI-12 calculation shows a more radical behavior in the frequency domain. It is likely that this erratic response is, in large part, of numerical origin.

SECTION 10

OBLIQUE INCIDENCE

In all the tests of the CBMI series, the borehole was aligned with the direction of the applied pulse, resulting in a more or less one-dimensional stress wave propagation. This simulates with reasonable accuracy ground shock induced by highly superseismic air blast. In some field situations, i.e., trans- and subseismic air blast, two-dimensional propagation is likely to prevail and it is, therefore, of interest to investigate whether a velocity gage would faithfully record free-field motion when it is transmitted to the gage along a direction inclined to the borehole.

A truly representative analysis of the response of the borehole column under oblique incidence would require a three-dimensional analysis. This is because an axisymmetric formulation of the type used in the CBMI calculations would be incapable of simulating a wave propagating across the ground, while a plane stress or plane strain formulation would misrepresent the geometry of the borehole configuration. An elaborate analysis was not deemed justifiable in the present context because, on intuitive grounds, it was felt that any component of the shock wave transverse to the borehole would be recorded faithfully by the gage. However, there is another contingency that might arise and this was considered in the analysis discussed below.

There appears to be a possibility, under some loading conditions, that the borehole filler grout may extrude out of the instrumentation borehole. It was postulated that such extrusion would not occur if the stress state in the grout was contained within the failure envelope of the grout thereby precluding yielding of the grout. The following analysis describes the procedure used to develop a "minimal" strength envelope as an aid to specifying grout properties.

10.1 DEVELOPMENT OF ELASTIC ANALYSIS

The analysis uses as a point of departure, the results obtained by Cole and Huth (Ref. 12) for the case of a moving point load on an elastic half-space.

Reference 12 considered a moving point load as shown in Figure 10-1. The position of the load was expressed by the equation

$$\bar{x}_p + U\bar{t} = 0 \quad (10-1)$$

in the fixed coordinate system $(\bar{x}, \bar{y}, \bar{z}, \bar{t})$. The region $\bar{z} > 0$ was considered and plane strain was assumed.

Three cases were distinguished: (1) subseismic, $M_L < M_T < 1$, (2) transseismic, $M_L < 1 < M_T$, and (3) superseismic, $1 < M_L < M_T$. Here M_L and M_T represent the Mach number of the moving load with respect to the longitudinal and shear waves, respectively, and are given by

$$M_L = U/C_L, \quad M_T = U/C_T \quad (10-2)$$

where C_L, C_T are the longitudinal and shear wave speeds in the medium and U is the shock wave propagation speed. The present treatment considers only the superseismic case since this is the stress regime in which soil failures are most likely to occur (due to combinations of applied pressure intensities and degrees of obliqueness of the ground shock).

The results of Reference 12 were first generalized for the case of a distributed pressure pulse moving across the surface. A typical pressure pulse $p(t)$ of the type shown in Figure 10-2 was considered. The stress components under these conditions are given by:

$$\begin{aligned} \sigma_x = & K_5 \left(2 + \frac{\lambda}{\mu} M_L^2 \right) H \left(\bar{x} - U\bar{t} - m_L \bar{z} \right) p \left(\frac{\bar{x} + U\bar{t} - m_L \bar{z}}{U} \right) \\ & + 2 K_6 m_T H \left(\bar{x} + U\bar{t} - m_T \bar{z} \right) p \left(\frac{\bar{x} + U\bar{t} - m_L \bar{z}}{U} \right) \end{aligned}$$

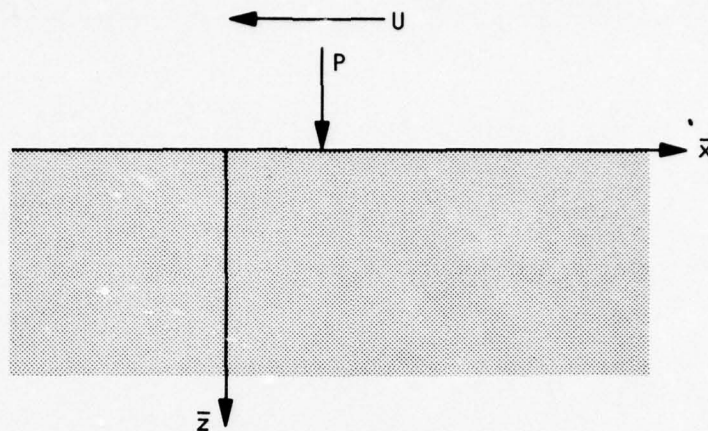


FIGURE 10-1. GEOMETRY OF MOVING POINT LOAD ON HALF PLANE

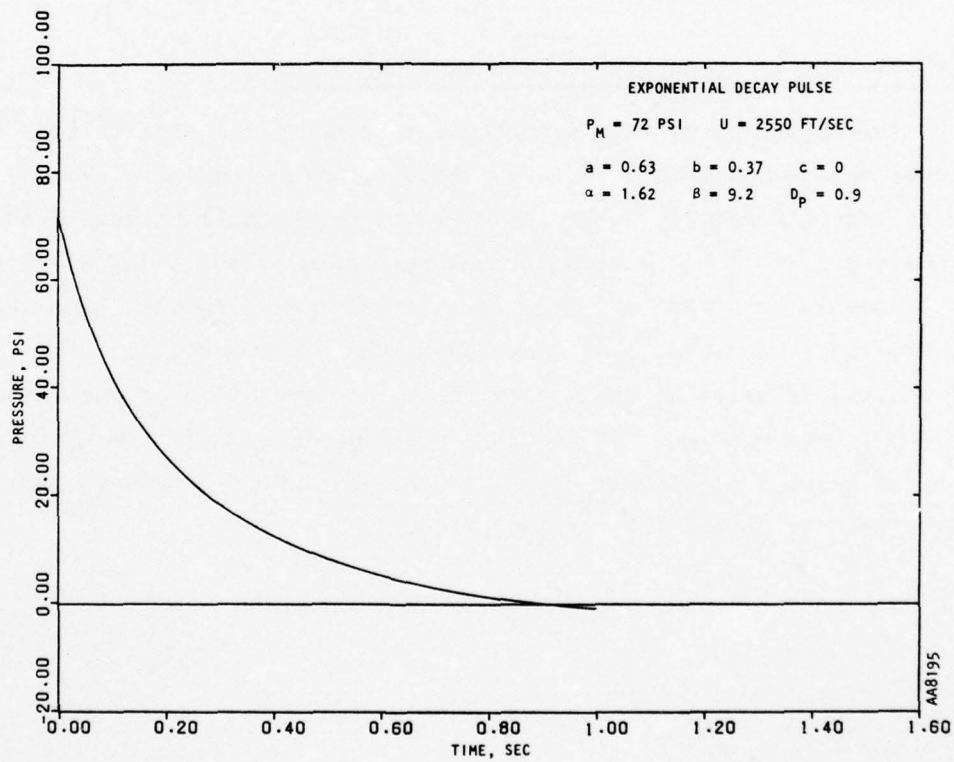


FIGURE 10-2. TYPICAL PRESSURE PULSE

$$\begin{aligned}\sigma_z = & - \left(2 - M_T^2\right) K_5 H \left(\bar{x} + U\bar{t} - m_L \bar{z} \right) \rho \left(\frac{\bar{x} + U\bar{t} - m_L \bar{z}}{U} \right) \\ & - 2m_T K_6 H \left(\bar{x} + U\bar{t} - m_T \bar{z} \right) \rho \left(\frac{\bar{x} + U\bar{t} - m_T \bar{z}}{U} \right)\end{aligned}\quad (10-3)$$

where $H(x)$ represents the Heaviside step function,

$$m_L = \left(M_L^2 - 1\right)^{\frac{1}{2}}, \quad m_T = \left(M_T^2 - 1\right)^{\frac{1}{2}}$$

$$K_5 = \frac{1}{D} \left(2 - M_T^2\right), \quad K_6 = 2m_L/D, \quad D = \left(2 - M_T^2\right)^2 + 4 m_T m_L$$

and λ, μ are the Lamé constants of the medium.

10.2 DESCRIPTION OF CALCULATIONS PERFORMED AND RESULTS

The objective of this effort was to compute the stress state in a homogeneous medium based on the above analysis, using realistic shock parameters and determine if a minimum yield strength could be specified for the borehole grout. Thus, a computer program was written to calculate the stress components σ_x and σ_z from Equation 10-3 and then evaluate the stress invariants J_1 and $\sqrt{J_2'}$. By repeating this computation with several choices of material shock parameters, the variation of the maximum values $\sqrt{J_2'}$ was studied. It was then possible to specify the minimum strength the grout must have in order not to yield and presumably, this would preclude the possibility of extrusion.

The computer program was designed to accept different choices of material and shock pulse parameters. The dilatational wave speed in the material was held constant at 1500 ft/sec and the shock propagation speed was varied from 1650 ft/sec to 3000 ft/sec, providing longitudinal Mach numbers varying from 1.1 to 2.0. The stress state at a point 1.5 ft beneath the surface was monitored.

In order that the input pulse may realistically simulate the shock wave from a nuclear explosion, a pulse shape of the type shown in Figure 10-2 was employed. The peak overpressures corresponding to the propagation speeds were taken from Brode (Ref. 13) and are shown in Table 10-1. The pulse shown in Figure 10-2 exhibits zero rise time and an exponential decay as represented by the equation:

$$p(t) = p_M (1 - \tau) (ae^{-\alpha\tau} + be^{-\beta\tau} + ce^{-\gamma\tau}), \tau = t/D_p \quad (10-4)$$

where a , b , c , α , β , γ and D_p are empirical constants depending on the peak overpressure p_M and are given in Reference 13. The pulse shown in Figure 10-2 is a representative pulse and corresponds to the case $p_M = 72$ psi ($U = 2550$ ft/sec). The other constants are shown on the figure.

For each pulse, the maximum value of $\sqrt{J_2^I}$ was computed. The maximum values of $\sqrt{J_2^I}$ are shown plotted against the peak overpressure p_M in Figure 10-3 for two values of Poisson's ratio, $\nu = 0.4$ and $\nu = 0.2$.

10.3 CONCLUSIONS AND LIMITATIONS OF ANALYSIS

Plots of the type shown in Figure 10-3 may be used to estimate the expected maximum values of J_2^I for a given range of peak overpressure. A grout with a higher yield strength (specified in terms of J_1 and $\sqrt{J_2^I}$) would then, presumably, not yield under the action of the applied shock pulse.

AD-A037 098

AGBABIAN ASSOCIATES EL SEGUNDO CALIF

F/G 19/4

GROUT/SOIL INTERACTION AND VELOCITY GAGE EMPLACEMENT FOR GROUND--ETC(U)

AUG 76 M B BALACHANDRA, J A MALTHAN

DNA001-74-C-0100

UNCLASSIFIED

AA-R-7364-7-4265

DNA-4089F

NL

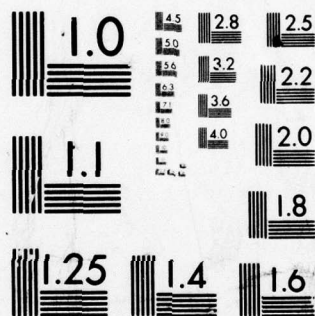
3 OF 3

AD
A037098



END

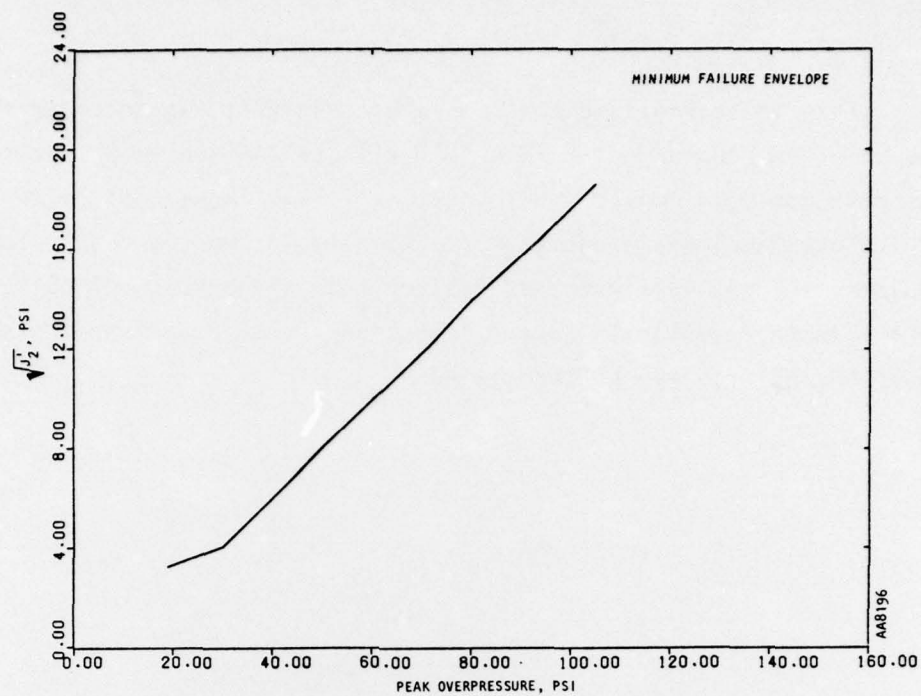
DATE
FILMED
4-77



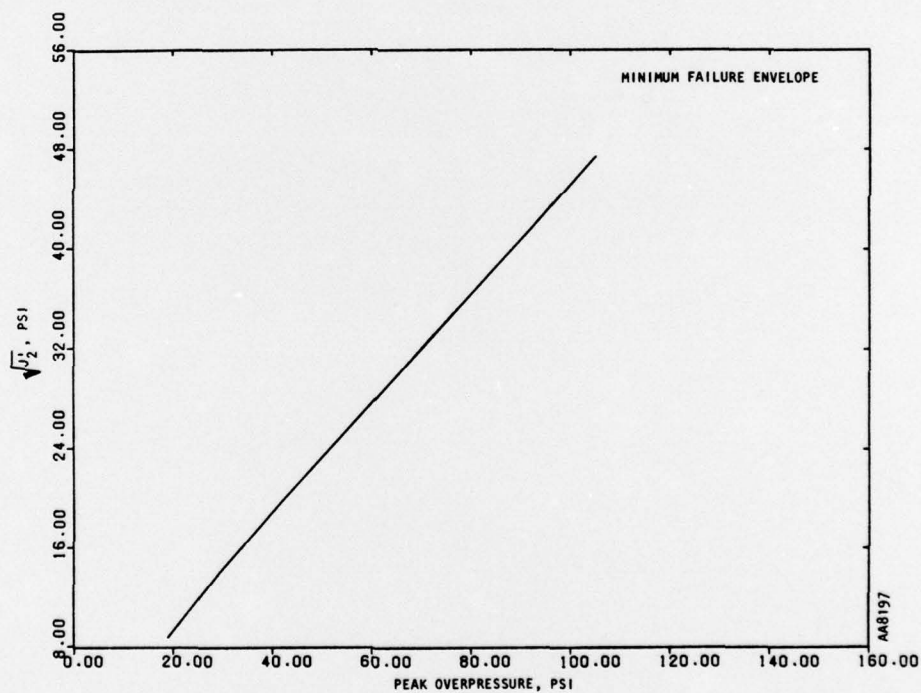
MICROCOPY RESOLUTION TEST CHART
NATIONAL BUREAU OF STANDARDS-1963-A

TABLE 10-1. PEAK OVERPRESSURES AND SHOCK PROPAGATION SPEEDS
CONSIDERED (Ref. 13)

Longitudinal Mach Number $M_L = \frac{U}{C_L}$	Peak Overpressure	Shock Speed U, fps
1.0	13	1500
1.1	19	1650
1.25	30	1875
1.4	43	2100
1.5	50	2250
1.6	60	2400
1.7	72	2550
1.8	80	2700
1.9	92	2850
2.0	105	3000



(a) Poisson's ratio, $\nu = 0.4$



(b) $\nu = 0.2$

FIGURE 10-3. PLOT OF MAXIMUM $\sqrt{J_2}$ VS PEAK OVERPRESSURE

It is to be realized that the above analysis was intended for guidance only. Borehole/medium interface effects and nonlinear material behavior have not been considered in the analysis. These could alter the results obtained herein and may have some impact on the conclusions. Nevertheless, the analysis provides insight into the problem of oblique incidence effects on velocity gage response and forms a basis on which more advanced analyses may be formulated.

SECTION 11

CONCLUSIONS AND GAGE EMPLACEMENT RECOMMENDATIONS

This section summarizes the conclusions arising from the analytical studies performed under this project and sets forth recommended field practices to be followed in the emplacement of velocity gages.

11.1 GROUT AND MATRIX STIFFNESS CONSIDERATIONS

Reference has been made in Section 2.2 to the ambiguity in referring to the "stiffness" of nonlinear materials. While referring to the relative stiffnesses of grout and medium, it is possible to avoid ambiguity by identifying a particular modulus such as the tangent modulus or secant modulus at a specified stress level. In the present report, the term "stiffness" has been used in a very loose context. Given the uncertainties surrounding the actual properties of earth materials under in situ conditions and the wide ranges over which the properties of artificial mixes vary even under controlled conditions of preparation, precise definitions of stiffness ratios appear to be unwarranted. Nevertheless, in order to provide some guidance in the preparation of grouts, comparisons of the properties of grout and matrix materials properties used in the CBMI test series are presented in the next subsection.

11.2 GROUT/MATRIX STIFFNESS COMPARISONS IN CBMI TEST SERIES

In attempting to define the relative stiffnesses of borehole and free-field materials, it is convenient to refer to the constrained modulus since this is readily determined from a uniaxial stress/strain curve. Hereinafter, the term modulus is construed to mean constrained modulus.

As noted previously, the use of the initial tangent modulus or the secant modulus at the maximum expected stress level σ avoids ambiguity. It may also be desirable to compare tangent moduli at some intermediate stress level, say 0.5σ , in order to have an idea of the shape of the stress/strain

curves. Based on such considerations, it was somewhat arbitrarily decided that the ratio R between the borehole and the free-field matrix stiffnesses be interpreted as the ratio of the secant moduli at 1.2σ with the additional restriction that the ratio of the tangent moduli at σ should lie between 1 and R (Ref. 14).

In order to put the results of the CBMI test series in perspective, the ratios of tangent and secant moduli of the borehole and matrix materials at various stress levels in the CBMI-12 and CBMI-14 tests are shown in Table 11-1. In the CBMI-12 test, the matrix was layered and the property comparisons of the free field and borehole are shown for both layers. Both tangent and secant moduli are compared at stress levels of 0, 150, and 300 psi. Since the nominal, expected peak stress σ was 250 psi, the last two stress levels correspond to 0.6σ and 1.2σ .

It is seen from Table 11-1 that the ratios of the several moduli considered there span a considerably larger range than the nominal range of 0.5 to 2.0 initially specified for the CBMI test series.

11.3 CONCLUSIONS FROM CBMI TEST SERIES

The conclusions from each of the CBMI test calculations have been discussed in Sections 6 through 8. Each of the calculations, CBMI-12, CBMI-13-1, and CBMI-14 showed very good agreement between the velocities calculated at the gage and free-field locations. Even in CBMI-12, the agreement was surprisingly good in spite of the large punchdown in the test. The test results also showed a similar agreement between the borehole and free-field measurements in every case except for the top gage location in the anomalous CBMI-12 test.

Sections 6 through 8 pointed out that this correlation is attributed to the bond at the grout/matrix interface. Perfect bonding was assumed in the calculations; while in the tests it is presumed that a moderately strong bond existed, probably as a consequence of the use of expansive cement in the matrix. This hypothesis is further substantiated by considering the other

TABLE 11-1. STIFFNESS COMPARISON OF BOREHOLE AND FREE-FIELD MATERIALS IN TESTS CBMI-14 AND CBMI-12

Test, Modulus and Stress Modulus Ratio at Level	CBMI-14			CBMI-12				
	Borehole, ksi	Free Field, ksi	Borehole Free Field	Borehole, ksi	Free Field, Layer 1, ksi	Free Field, Layer 2, ksi	Borehole Free Field Layer 1	Borehole Free Field Layer 2
Tangent Modulus at 0 psi	200	92.50	2.16	2	30	56	0.07	0.036
Tangent Modulus at 150 psi	200	22.87	8.74	2.75	11	5.57	0.25	0.49
Secant Modulus at 150 psi	200	92.50	2.16	0.33	9.57	24.44	0.03	0.01
Tangent Modulus at 300 psi	69.81	22.87	3.05	13.2	22.27	5.57	0.59	2.37
Secant Modulus at 300 psi	166	40.54	4.10	0.62	12	10	0.05	0.06

Note: Moduli are in ksi and are taken from stress/strain data supplied by WES except in the case of the free-field matrix of CBMI-14 where the properties were generated, accounting for the stiffened condition of the matrix (see Sec. 7 and Fig. 7-3a in particular).

extreme, i.e., the case of zero bond between the borehole grout and the matrix. In this case, the borehole and matrix would move more or less independently of each other under the applied input, and their motions can be approximated by performing one-dimensional calculations on columns with appropriate material properties.

Such one-dimensional calculations were indeed performed for each of the tests and have been described in Sections 6 through 8. A comparison of the responses of the borehole grout and matrix columns in these calculations shows the considerable differences in the velocity responses arising from the wide disparity in stiffness properties. Thus, Figures 7-7 and 7-9 can be compared for Test CBMI-14 and, similarly, Figures 8-4b and 8-5b for CBMI-12. Although the comparison is somewhat hindered by numerical problems in the latter case, the point is still clear, i.e. that:

A strong bond at the grout/free-field interface renders the velocity gage response relatively insensitive to large impedance mismatches between the grout and free field; the velocity gage under these circumstances records the free-field motion faithfully.

The above conclusion has far-reaching implications with regard to field practices, for it suggests that efforts need not be made to ensure that the borehole grout has the same stiffness properties as the free field. The expense and effort involved in preparing the borehole grout are therefore considerably reduced.

11.4 GAGE EMPLACEMENT RECOMMENDATIONS

Good interface bond between the borehole and free-field materials has been identified in Section 11.3 as the primary contributor to ensuring accuracy in velocity gage measurements. It follows, therefore, that efforts must be made to ensure strong interface bond between gage and free field. In the CBMI tests, as stated earlier, moderately strong bond was probably achieved without deliberate effort. In a real free-field event, such a bond should be

guarded by locking the velocity canisters in place. This leads to the following recommendation for gage placement:

In order to ensure that the velocity gage records free-field motion faithfully, the canister should be locked in place by surrounding its immediate vicinity with a stiff, expansive grout. Under these circumstances, considerable mismatch between the stiffness properties of the grout and the free field will not significantly affect the accuracy of the response of the velocity gage.

With the velocity gage canisters locked in place, the remainder of the borehole may be filled with grouts that are reasonable approximations (perhaps within an order of magnitude) of the soils at the test site. It is recommended that extremely soft grouts such as those used in the CBMI-12 test be avoided.

SECTION 12

REFERENCES

1. Isenberg, J; Van Dillen, D.; and Bhaumik, A.K. *Response of a Velocity Gage Canister to Free-Field Ground Shock (Draft)*, R-7255-2831. El Segundo, CA: Agbabian Assoc., Jun 1973.
2. Ingram, J.K. *Laboratory Investigation of Canister/Backfill/Medium Interaction*, paper presented at the Ground Motion and Blast Instrumentation Conference, 28-29 Oct 1975. Vicksburg, MS: USAE Waterways Experiment Station, (in press)
3. Ingram, J.K. and Ford, M.B. *Effects of Backfill Properties on Ground Shock Measurements*. Vicksburg, MS: USAE-Waterways Experiment Station, Apr 1976.
4. Van Dillen, D.E. and Reddy, D.P. *Analysis of Test CBMI-5 of the Canister/Grout/Soil Interaction Study*, I.R., R-7364-1-3836. El Segundo, CA: Agbabian Assoc., Apr 1975.
5. Van Dillen, D.E. and Reddy, D.P. *Analysis of Control Test i of the Experimental Canister/Grout/Soil Interaction Study*, Rev. 1, R-7364-1-3663. El Segundo, CA: Agbabian Assoc., May 1975.
6. *User's Guide for FEDRC Code*, U-4700-3868. El Segundo, CA: Agbabian Assoc., May 1975.
7. Bhaumik, A.K. and Reddy, D.P. *Material Models for Joints and Interfaces*, R-7354-3602. El Segundo, CA: Agbabian Assoc., Apr 1975.
8. Ingram, J.K. "Revised Properties for SBLG Test CBMI-10," memo from WES to D.P. Reddy, Agbabian Assoc., 10 Sep 1975.
9. Ingram, J.K. "Calculational Properties for Model V, CBMI-12, CBMI-13, and CBMI-14," memo from WES to J.A. Malthan, Agbabian Assoc., 17 Oct 1975.
10. Balachandra, M.B.; Chuang, K.P.; and Workman, J.W. *HARDPAN I-3, Traveling Wave Response (Simulated by Axisymmetric Calculation)*, R-6917-11G-3913. El Segundo, CA: Agbabian Assoc., Jul 1975.
11. Zelasko, J.S. "Recommended Interface Slip Mechanism Properties for Small Blast Load Generator (SBLG) Experiments," memo from WES to M.B. Balachandra, Agbabian Assoc., 19 Feb. 1976.

12. Cole, J. and Huth, J. "Stresses Produced in a Half Plane by Moving Loads," *Jnl Appl. Mech., Trans. ASME*, Vol. 80, Dec 1958, p. 433-436.
13. Brode, H.L. *A Review of Nuclear Explosion Phenomena Pertinent to Protective Construction*, R-425-PR. Santa Monica, CA: Rand Corp, May 1964.
14. Agbabian Assoc. (AA). Minutes of meeting between DNA, WES, and AA. E-7364-1-3896. at AA, El Segundo, CA, 17 Jun 1975.

DISTRIBUTION LIST

DEPARTMENT OF DEFENSE

Director
Defense Advanced Rsch. Proj. Agency
ATTN: Technical Library
ATTN: NMRO
ATTN: PMO
ATTN: STO

Defense Documentation Center
12 cy ATTN: TC

Director
Defense Nuclear Agency
ATTN: STSI Archives
ATTN: DDST
2 cy ATTN: SPSS
3 cy ATTN: STTL, Tech. Library

Commander
Field Command
Defense Nuclear Agency
ATTN: FCT
ATTN: FCTMOF
ATTN: FCPR

Chief
Livermore Division Fld. Command, DNA
ATTN: FCPRL

DEPARTMENT OF THE ARMY

Dep. Chief of Staff for Rsch. Dev. & Acq.
ATTN: Technical Library

Commander
Harry Diamond Laboratories
ATTN: DRXDO-NP
ATTN: DRXDO-TI, Tech. Lib.

Director
U.S. Army Ballistic Research Labs.
ATTN: Tech Lib., Edward Baicy
ATTN: J. H. Keefer, AMXBR-TL-IR
ATTN: DRXBR-X, Julius J. Meszaros

Director
U.S. Army Engr. Waterways Exper. Sta.
ATTN: F. Hanes
ATTN: Leo Ingram
ATTN: Technical Library
ATTN: William Flathau
ATTN: J. K. Ingram

Commander
U.S. Army Materiel Dev. & Readiness Cmd.
ATTN: Technical Library

DEPARTMENT OF THE NAVY

Chief of Naval Research
ATTN: Technical Library

Officer in Charge
Civil Engineering Laboratory
ATTN: R. J. Odello
ATTN: Technical Library

DEPARTMENT OF THE NAVY (Continued)

Commander
Naval Facilities Engineering Command
ATTN: Technical Library

Commander
Naval Ship Engineering Center
ATTN: Technical Library

Commander
Naval Ship Rsch. and Development Ctr.
ATTN: Code L42-3, Library

Commander
Naval Ship Rsch. and Development Ctr
Underwater Explosive Research Division
ATTN: Technical Library

Commander
Naval Surface Weapons Center
ATTN: Code WX21, Tech. Lib.
ATTN: Code WA501, Navy Nuc. Prgms. Off.

DEPARTMENT OF THE AIR FORCE

AF Geophysics Laboratory, AFSC
ATTN: SUOL, AFCRL Rsch. Lib.

AF Institute of Technology, AU
ATTN: Library, AFIT Bldg. 640, Area B

AF Weapons Laboratory, AFSC
ATTN: SUL
ATTN: DES, M. A. Flamondon
ATTN: DEX, J. Renick
ATTN: DEX

Hq. USAF/IN
ATTN: INATA

U.S. ENERGY RESEARCH AND DEVELOPMENT ADMINISTRATION

University of California
Lawrence Livermore Laboratory
ATTN: Tech. Info. Dept. L-3

Sandia Laboratories
Livermore Laboratory
ATTN: Doc. Con. for Tech. Library

Sandia Laboratories
ATTN: Doc. Con. for Luke J. Vortman
ATTN: Doc. Con. for A. J. Chaban
ATTN: Doc. Con. for Org. 3422-1,
Sandia Rpt. Coll.

U.S. Energy Rsch. & Dev. Admin.
ATTN: Doc. Con. for Tech. Library

U.S. Energy Rsch. & Dev. Admin
Division of Headquarters Services
ATTN: Doc. Con. for Class. Tech. Lib.

U.S. Energy Rsch. & Dev. Admin.
Nevada Operations Office
ATTN: Doc. Con. for Tech. Lib.

U.S. ENERGY RESEARCH AND DEVELOPMENT ADMINISTRATION
(Continued)

Union Carbide Corporation
Hoflund National Laboratory
ATTN: Civ. Def. Res. Proj., Mr. Kearny

DEPARTMENT OF DEFENSE CONTRACTORS

Aerospace Corporation
ATTN: Tech. Info. Services
ATTN: PREM, N. Mathur

Agbabian Associates
ATTN: M. Agbabian
ATTN: Mysore B. Balachandra
ATTN: James A. Malthan

ARTEC Associates, Inc.
ATTN: D. W. Baum

Civil/Nuclear Systems Corp.
ATTN: Robert Crawford

EG&G, Inc.
ATTN: Technical Library

General Electric Company
Tempo-Center for Advanced Studies
ATTN: DASIAC

IIT Research Institute
ATTN: Technical Library

Kaman Sciences Corporation
ATTN: Donald C. Sachs
ATTN: Library

Merritt Cases, Incorporated
ATTN: Technical Library
ATTN: J. L. Merritt

The Mitre Corporation
ATTN: Library

Nathan M. Newmark
Consulting Engineering Services
ATTN: W. Hall
ATTN: Nathan M. Newmark

Physics International Company
ATTN: Doc. Con. for Coye Vincent
ATTN: Doc. Con. for Charles Godfrey
ATTN: Doc. Con. for Fred M. Sauer
ATTN: Doc. Con. for Tech. Lib.

DEPARTMENT OF DEFENSE CONTRACTORS (Continued)

R&D Associates
ATTN: J. G. Lewis
ATTN: Technical Library
ATTN: Bruce Hartenbaum

Science Applications, Inc.
ATTN: Technical Library

Southwest Research Institute
ATTN: Wilfred E. Baker
ATTN: A. B. Wenzel

Stanford Research Institute
ATTN: Burt R. Gasten
ATTN: George R. Abrahamson
ATTN: P. De Carli

Systems, Science and Software, Inc.
ATTN: Technical Library
ATTN: Donald R. Grine

TRW Systems Group
ATTN: Tech. Info. Center, S-1930
2 cy ATTN: Peter K. Dai, R1-2170

TRW Systems Group
ATTN: E. Y. Wong, 527/712

The Eric H. Wang Civil Engineering Rsch. Fac.
ATTN: G. Lane
ATTN: Neal Baum

Weidlinger Assoc. Consulting Engineers
ATTN: Melvin L. Baron

Weidlinger Assoc. Consulting Engineers
ATTN: J. Isenberg